From Alloy to Oxide: Capturing the Early Stages of Oxidation and Corrosion on Ni and Ni-Cr Alloy Surfaces

A

Dissertation

Presented to
the faculty of the School of Engineering and Applied Science
University of Virginia

in partial fulfillment
of the requirements for the degree

Doctor of Philosophy in Materials Science and Engineering

by

William Harrison Blades

May 2021

Approval Sheet

This

Dissertation

is submitted in partial fulfillment of the requirements
for the degree of

Doctor of Philosophy

Author: William Blades

This Dissertation has been read and approved by the examining committee

Advisor: Petra Reinke

Committee Member: John Scully

Committee Member: Stephen McDonell

Committee Member: Ian Harrison

Committee Member: Líney Árnadóttir

Accepted for the School of Engineering and Applied Science:

Craig H. Benson, School of Engineering and Applied Science

May 2021

This dissertation was defended December 3rd, 2020

Table of Contents

Acknowledgments ... ***viii***

List of Publications ... ***ix***

Abstract ... ***x***

Chapter I: Introduction ... ***12***

1.1 Chapter I References ... **17**

Chapter II: Background and Motivation ... ***20***

2.1 Metal Surface: Oxygen Adsorption to Oxide Saturation ... **20**

2.2 Oxidation of Low-index Ni-Cr Surfaces ... **23**

2.3 Low temperature Oxidation of Ni-Cr(100) ... **26**

2.4 Electrochemical Corrosion of Ni-Cr Alloys ... **29**

2.5 From Alloy to Oxide: The Experimental Approach ... **32**

2.6 Chapter II References ... **34**

Chapter III: Methods ... ***39***

3.1 Scanning Tunneling Microscopy and Spectroscopy ... **39**

3.1.1 Bardeen Tunneling Theory ... 41

3.1.2 Tersoff-Hamann Model ... 44

3.1.3 Scanning Tunneling Spectroscopy ... 46

3.2 Atomic Force Microscopy ... **48**

3.3 Photoelectron Spectroscopy ... **49**

3.3.1 X-ray Photoelectron Spectroscopy ... 50

3.3.2 Valence Band Spectroscopy ... 52

3.3.3 X-ray absorption Spectroscopy ... 53

3.4 Spectroscopic Photoemission & Low Energy Electron Microscopy ... **56**

3.4.1 XPEEM ... 58

3.4.2 Low Energy Electro Diffraction (LEED) ... 59

3.4.3 Mirror Electron Microscopy (MEM) ... 59

3.5 Density Functional Theory 60

3.6 Electrochemical Techniques 61

3.7 Scanning Electron Microscopy 62

3.8 Sample Preparation 64

3.8.1 Thin Film Deposition 64
3.8.2 Polycrystalline Bulk Sample Preparation 65

3.9 Data Processing 66

3.9.1 Spectroscopy Data and MATLAB codes 66
3.9.2 DOS and Band gap maps 66
3.9.3 Conduction and Valence band maps 68
3.9.4 Topographical Data Processing using Gwyddion and MATLAB 69

3.10 Chapter III References 71

Chapter IV: Understanding the Early Stages of Oxidation on Ni-Cr(100) Alloys Surfaces 75

4.1 Technical Background 75

4.2 Methods 79

4.3 Results 81

4.3.1 Ni(100) vs Ni-Cr(100) at 500 °C 81
4.3.2 Trends in the oxidation of Ni-Cr(100) surfaces 83
4.3.3 Oxidation of a Ni-12Cr(100) surface: The Ni oxidation pathway 85
4.3.4 The NiO superlattices 90
4.3.5 The nanoscale origins of electronic heterogeneity at alloy-oxide interfaces 93

4.4 Discussion 98

4.5 Conclusions 99

4.6 Chapter IV References 101

4.7 Supplemental Data and Supporting Information 105

Chapter V: Initial Oxidation Pathways on a Ni-15Cr(100) Alloy Surface 111

5.1 Technical Background 111

5.2 Methods 115

5.3 Results 117

5.3.1 General trends in surface oxidation 117
5.3.2 Cr oxidation pathway: Growth of the a chromia layer 119
5.3.3 Next layer NiO growth: Chemical fluctuations across the superlattice 127

5.4 Discussion 129

5.5 Conclusions 132

5.6 Chapter V References 133

5.7 Supplemental Data and Supporting Information 137

Chapter VI: The Evolution of Nanoscale Oxides on Ni(111) and Ni-Cr(111) Surfaces 147

6.1 Technical Background 147

6.2 Methods 148

6.3 Results and Discussion 148

6.4 Conclusions 156

6.5 Chapter VI References 158

Chapter VII: The Oxidation of Low-index Ni-22Cr Surfaces Captured in operando with SPELEEM 159

7.1 Technical Background 159

7.2 Methods 161

7.3 Results and Discussion 162

7.4 Conclusions 171

7.5 Chapter VII References 173

7.6 Supplemental Data and Supporting Information 174

Chapter VIII: Influence of Chloride on Nanoscale Electrochemical Passivation Processes 175

8.1 Technical Background 175

8.2 Methods 181

8.3 Results 186

8.3.1 Overall Electrochemical Performance under Potentiostatic Conditions 186
8.3.2 Chemical Identity and Oxidation State Characterization of the Passive Films 190

8.3.3 Evolution of Surface Topography 193
8.3.4 Effect of Surface Pretreatment on Film Stability 199

8.4 Discussion 201

8.5 Conclusions 209

8.6 Chapter VIII References 211

8.7 Supplementary Data and Supporting Information 219

Acknowledgments

First, I would like to thank my advisor Professor Petra Reinke for giving me the opportunity to work in her lab. Her insatiably-inquisitive nature and positive attitude made conducting research a pleasant experience, and I am very grateful for her help and guidance these past 4 years. Outside of the lab, Petra has also been an excellent teacher and has spent a significant portion of her valuable time helping me acquire a deeper understanding of both physics and chemistry. Without her advice and instruction, I would not have smoothly navigated this path. I would also like to thank my undergraduate research advisor Professor James McLeskey and my master’s advisor Professor Shiv Khanna. Both have provided excellent advice and support during in my career, and I greatly appreciate the opportunities each has given me. Last but certainly not least, I would like to thank my high school physics teacher Michael Fetsko for nurturing my interest in physics. To all of my advisors and mentors, thank you all for believing in me even when I didn’t believe in myself. I am beyond grateful. Outside the academic circle I would like to thank my family and friends for their unwavering support while I have chased my dreams.

List of Publications

The work presented in dissertation is the culmination of four and a half years of work, resulting in the following publications. Some have been accepted, submitted or are under preparation. Each are marked accordingly.

[1] *On the Repassivation Behavior of Individual Grain Facets on Dilute Ni-Cr and Ni-Cr-Mo Alloys in Acidified Chloride Solution:* ***Journal of Physical Chemistry C****, (2018)*

[2] *From Alloy to Oxide: Capturing the Early Stages of Oxidation on Ni-Cr(100) Alloys:* ***ACS Applied Materials & Interfaces*** *(2018)*

[3] Influence of Chloride on Nanoscale Electrochemical Passivation Processes: ***Journal of Physical Chemistry C****, (2020)*

[4] *Thermally Induced Defects on* WSe_2*:* ***Journal of Physical Chemistry C****, (2020)*

[5] Initial Oxidation Pathways on a Ni-15Cr(100) Alloy Surface: **submitted to *npj Materials Degradation***

[6] The Evolution of Nanoscale Oxides on Ni(111) and Ni-Cr(111) Surfaces: **under preparation**

[7] Effect of alloy heterogeneity on the initiation of oxide formation: **under preparation**

[8] Oxidation of Low-index Ni-22Cr Surfaces Captured in operando: **under preparation**

Abstract

The realization of superior corrosion-resistant alloys requires a detailed understanding of surface oxidation to mitigate the impact of corrosion. To this end, we have studied the nanoscale evolution of surface oxides prior to the formation of a complete layer. The oxidation of Ni(100), Ni(111), and Ni-Cr(100), Ni-Cr(111) surfaces was captured by sequential oxidization and measured with scanning tunneling microscopy/spectroscopy (STM/STS) *in situ*. Alloy thin films (8-18 wt.% Cr) were prepared on MgO(100/111) and exposed to oxygen up to 400 L at 500 ^{o}C. NiO was found to undergo anisotropic growth and drive step-edge faceting on Ni-Cr(100), while NiO initiated across the terraces on the Ni-Cr(111) samples. On both surfaces the chromia initially nucleated as flat disks and eventually coalesced as large nodules. Several novel Cr(100)-O surface reconstructions were observed on the FCC Ni-Cr(100) surface, indicating surface segregation and phase separation of BCC Cr. Each aforementioned surface oxide presented a unique electronic signature, and STS maps were used to spatially resolve and assess local fluctuations in the DOS.

To understand how the presence of grain boundaries and crystallography affect the initial stages of oxidation, a polycrystalline Ni-22wt.%Cr alloy was oxidized under UHV conditions. The surface was exposed to O_2 and studied as a function of time and crystallographic orientation *in operando* with a Spectroscopic Photoelectron and Low Energy Electron Microscope, which can also perform XAS and XPS measurements in the valence band and core level regime. The oxidation across (104) and (212) alloy grains was simultaneously acquired with 25×25 nm^2 resolution by monitoring the XAS Cr-L-edge peak during a cumulative 65 L O_2 exposure at 500 ^{o}C. Initial changes in image contrast showed anisotropic surface oxide growth, and as oxidation

continued each grain became saturated with oxide at different rates. The grain boundary influenced the oxide growth on the (104) grain, while the (212) grain was unperturbed and oxidation proceeded more uniformly. After further oxidation, chromia nodules appeared across the (104) grain, their area growing linearly with time. These experimental results, when combined with computational level-set image characterization and DFT, underscore the importance of electronic heterogeneity and crystallographic orientation in driving kinetic behavior during surface oxide growth within the pre-Cabrera-Mott regime.

The corrosion of binary Ni-Cr and ternary Ni-Cr-Mo alloys was considered under a variety of different electrochemical conditions and their surfaces measured *ex-situ* with AFM. The data analysis was informed by *in operando* single-frequency electrochemical impedance spectroscopy (SF-EIS) measurements, taken by the Scully group (UVA), on the electrochemically grown passive film in either a chloride or sulfate solution as a function of time. Our results found that oxide nucleation occurs in the form of islands, which form on newly passivating surfaces with seconds of the establishment of an electrochemical potential driving force favoring oxidation of both Cr and Ni. Oxides tend to grow first as islands and coalesce to form nm-scale coverages on metallic surfaces consistent with the sharp decrease in oxidation rates commensurate with thin film-field driven passivation. At the same time, it is found that chemical driving forces favor simultaneous oxide dissolution, especially in the case of Ni^{2+} oxides. The balance between these two processes is argued to govern morphologies and thickness evolution. Roughness and topographical heterogeneity evolve with time and depend critically on anion identity. Cl^- is shown to enhance the spread in oxide island radii, heights, and Cr/Ni ratio compared to SO_4^{2-}. The possible impacts of morphology and chemical composition on oxide instability and breakdown are discussed.

Chapter I: Introduction

Oxidation and corrosion are ubiquitous phenomena that initiate at the surface of a material. Elicited by interactions with the surrounding environment, these processes result in the degradation of a material and its properties.[1] The ecological and economic cost of material breakdown due to oxidation and corrosion is staggering, therefore corrosion resistance is an important design parameter for technical alloys. The study of corrosion processes, which includes dry as well as aqueous corrosion reactions, is motivated by the need to increase the functional lifetime of materials, enhance public and environmental safety and reduce the overall economic burden incurred by materials degradation. When a material displays corrosion resistant behavior it is assumed the degradation is slow and the material and its properties have a comparatively long lifecycle. This resistance to degradation can come down to a relatively small number of atoms at the surface and the manner in which their electrons interact with the environment (e.g. air, water, etc.). For example, the oxidation of most metals initiates with the growth of a metal-oxide interface at the surface, where the oxide covers the surface and can act as a barrier to further oxidation. Exactly which oxide forms, its stability and growth rate are important parameters in determining a metal's corrosion resistance.

Depending on operational need, metal components used in practical applications can be alloyed with other elements to enhance their corrosion properties. Transition-metal alloys are a particular class of alloys with high technical relevance, and the complex processes that govern the reactions of molecular oxygen and corrosive solutions with these alloys have garnered significant interest for many decades.[4–14] Specifically, this dissertation considers the initial thermal oxidation

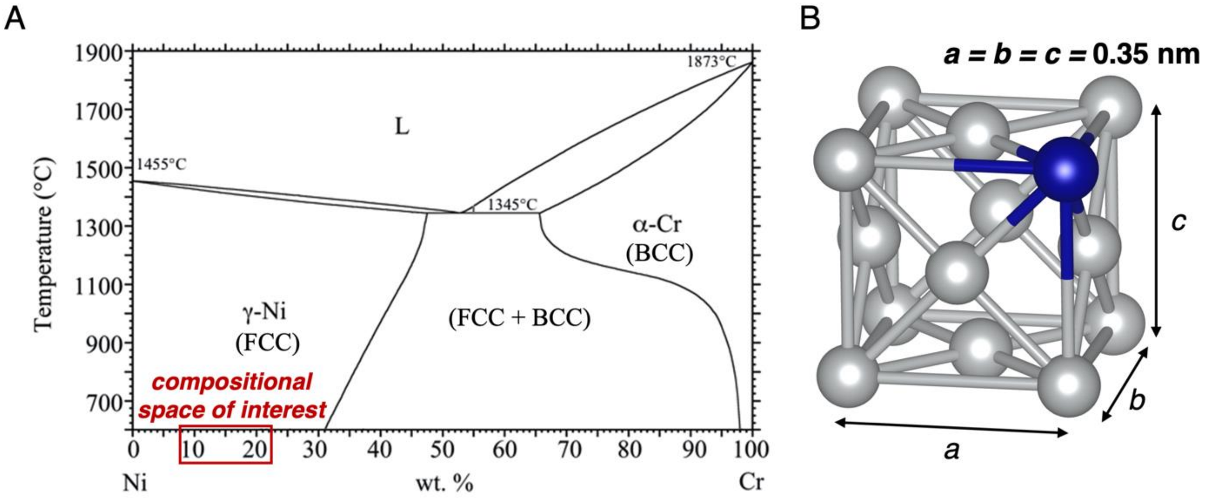

Figure 1-1. The phase diagram[15] (A) of Ni-Cr alloys and the crystal structure (B) of interest in this dissertation, where the silver atoms are Ni and the blue atom is Cr.

on Ni-Cr alloys, which possess excellent mechanical properties, a high degree of corrosion resistance and have practical application in an array of industrial and military systems.[16–19] These properties also make Ni-Cr useful for high temperature applications such as aerospace turbine blades and thermocouples.[17,18,20] Ni-Cr alloys of this technical class normally have a Cr concentration that is [Cr] < 30wt.% (weight precent). At this composition Ni-Cr alloys form a solid solution, where the Cr atoms are randomly substituted with the remaining Ni atoms, Figure 1–1(A). Within this compositional space the crystal lattice is determined by the Ni, which forms a face centered cubic (FCC) lattice, Figure 1–1(B). Therefore, the initial stages of oxidation on Ni-Cr alloy surfaces need to be considered as a heterogeneous reaction that occurs between the oxidation pathways of both the Ni and Cr atoms, and the different oxide phases that develop as oxidation progresses.

The corrosion resistance afforded by Ni-Cr alloys is attributed to the Cr atoms, which can form a passive Cr_2O_3 layer when exposed to oxygen at elevated temperatures.[4,5,21,22] The origin of

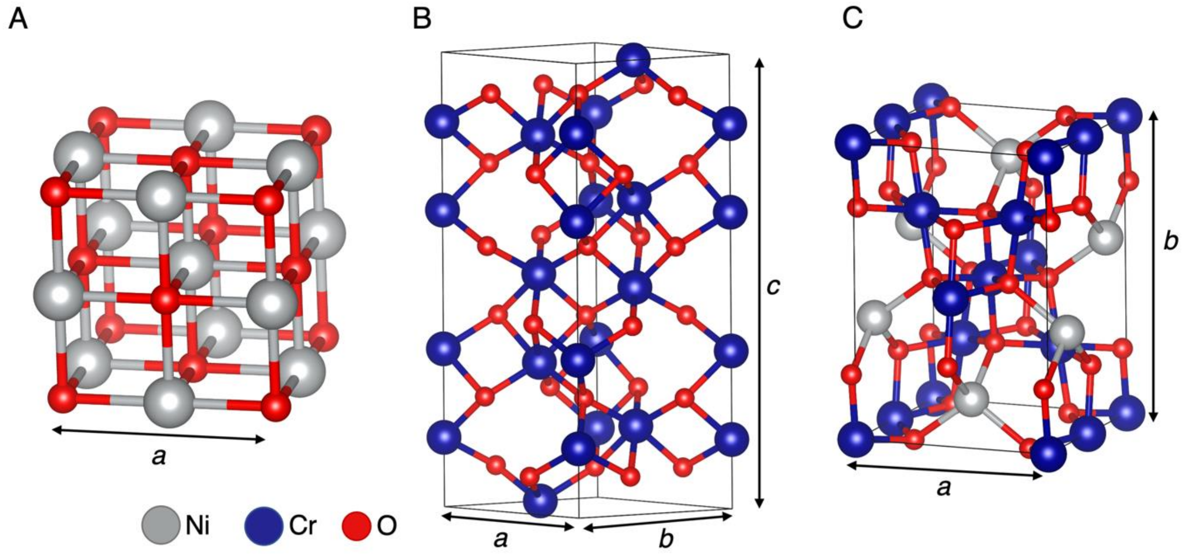

D

	NiO	Cr_2O_3	$NiCr_2O_4$
Crystal lattice	Cubic[23]	Hexagonal[24]	*Tetragonal[25,26]
Lattice parameters (nm)	a = 0.417	a = b = 0.495 c = 0.136	a = 0.851 b = 0.582
Band gap (eV)	4.3[27]	3.4 – 5[28,29]	4.1 – 4.3[30]

Figure 1-2. The different thermodynamically stable oxide species possible on Ni-Cr alloys: (A) NiO, (B) Cr_2O_3, and (C) $NiCr_2O_4$. The gray atoms are Ni, the blue atoms Cr, and the red atoms O. The table (D) provides some general information about their geometry and electronic structure. *A cubic structure has also been measured.

chromia's protective nature comes from its limiting thickness and adhesive quality. Effectively, once the oxide forms a complete layer with a particular vertical thickness, it inhibits the depletion of metal atoms from the underlying alloy and does not delaminate from the surface. This behavior is advantageous to material longevity and is why Ni superalloys are alloyed with Cr. However, Cr is expensive compared to Ni and consequently makes up a minority constituent component of most technical Ni-Cr alloys. The Ni atoms will also react to the presence of oxygen by forming NiO, which continues to grow and thicken in the presence of oxygen at elevated temperatures unless a complete passive chromia layer develops at the alloy-oxide interface.[9] The mixed spinel phase $NiCr_2O_4$ can also grow during thermal oxidation, however it is much less common than the phases previously mentioned. Examples of the crystal structure of these three oxides is provided in Figure 1–2, as well as some basic properties of each oxide relevant to this dissertation.[23–30]

The early stages of oxidation are complex, and synergistic interactions between the alloying elements, oxygen and each oxide phase are at the heart of understanding the alloy-to-oxide transformation. A large body of work exists on performance, passivation and break-down of complete oxide layers, but attention has turned only recently to the early stages of alloy oxidation.[4,10,12,14,31,32] It is therefore important to consider the initial stages of oxidation by targeting length and times scales during the nucleation and growth of partial oxide layers or islands on the surface, Figure 1–3. At these early stages significant structural and chemical changes at the alloy-oxide interface are observed.[4,33–37] These changes can bias the continued growth of the protective oxide and are therefore presumed to critically influence the passivity and performance of the oxide at these initial stages.

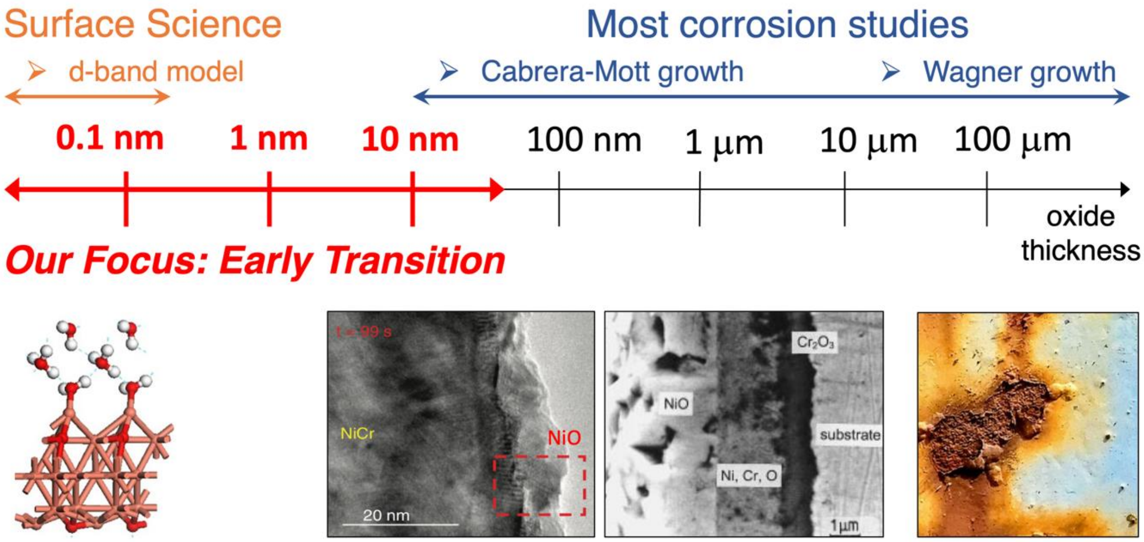

Figure 1-3. The different length scales typically considered when describing absorption and oxide growth on metal systems. The focus of this dissertation is marked relative to these different regimes, each of which will be discussed in Chapter II.

The initial oxidation behavior at the surface is highly sensitive to the alloy composition, oxidation temperature and crystallographic orientation.[13] To better understand the physics and chemistry of these early stage oxidation pathways, this dissertation targets the oxidation of single-grain Ni-(8-22)wt.%Cr alloy surfaces at 500-600 °C. As growth of the alloy-oxide interface initiates at the surface, a variety of different scanning probe microscopy, photoelectron spectroscopy and electron microscopy techniques will be synergistically paired with theoretical modeling to provide an atomistic understanding of the oxidation process. These results will be used to develop a mechanistic understanding of the initial reaction steps at the nanoscale. This approach will facilitate a deeper understanding of the relationship between initial oxide formation, oxide growth and properties, which will be useful in the design of future alloys.

1.1 Chapter I References

(1) Shaw, B. A.; Kelly, R. What Is Corrosion? *Electrochem. Soc. Interface* **2006**, *15*, 24–26.

(2) Mazumder, M. A. J. Global Impact of Corrosion: Occurrence, Cost and Mitigation. *Glob. J. Eng. Sci.* **2020**, *5* (4), 5. https://doi.org/10.33552/GJES.2020.05.000618.

(3) Koch, G.; Varney, J.; Thompson, N.; Moghissi, O.; Gould, M.; Payer, J. International Measures of Prevention, Application, and Economics of Corrosion Technologies Study. *NACE Int. Impact* **2016**, 216.

(4) Atkinson, A. Transport Processes during the Growth of Oxide Films at Elevated Temperature. *Rev. Mod. Phys.* **1985**, *57* (2), 437–470. https://doi.org/10.1103/RevModPhys.57.437.

(5) Wood, G. C.; Chattopadhyay, B. Transient Oxidation of Ni-Base Alloys. *Corros. Sci.* **1970**, *10* (7), 471–480. https://doi.org/10.1016/S0010-938X(70)80032-4.

(6) Chattopadhyay, B.; Wood, G. C. The Transient Oxidation of Alloys. *Oxid. Met.* **1970**, *2* (4), 373–399.

(7) De Los Santos Valladares, L.; Ionescu, A.; Holmes, S.; Barnes, C. H. W.; Bustamante Domínguez, A.; Avalos Quispe, O.; González, J. C.; Milana, S.; Barbone, M.; Ferrari, A. C.; Ramos, H.; Majima, Y. Characterization of Ni Thin Films Following Thermal Oxidation in Air. *J. Vac. Sci. Technol. B Nanotechnol. Microelectron. Mater. Process. Meas. Phenom.* **2014**, *32* (5), 051808. https://doi.org/10.1116/1.4895846.

(8) Mohanty, P.; Rath, C.; Mallick, P.; Biswal, R.; Mishra, N. C. UV–Visible Studies of Nickel Oxide Thin Film Grown by Thermal Oxidation of Nickel. *Phys. B Condens. Matter* **2010**, *405* (12), 2711–2714. https://doi.org/10.1016/j.physb.2010.03.064.

(9) Luo, L.; Zou, L.; Schreiber, D. K.; Baer, D. R.; Bruemmer, S. M.; Zhou, G.; Wang, C.-M. In-Situ Transmission Electron Microscopy Study of Surface Oxidation for Ni–10Cr and Ni–20Cr Alloys. *Scr. Mater.* **2016**, *114*, 129–132. https://doi.org/10.1016/j.scriptamat.2015.11.031.

(10) Luo, L.; Zou, L.; Schreiber, D. K.; Olszta, M. J.; Baer, D. R.; Bruemmer, S. M.; Zhou, G.; Wang, C.-M. In Situ Atomic Scale Visualization of Surface Kinetics Driven Dynamics of Oxide Growth on a Ni–Cr Surface. *Chem. Commun.* **2016**, *52* (16), 3300–3303. https://doi.org/10.1039/C5CC09165A.

(11) Unutulmazsoy, Y.; Merkle, R.; Fischer, D.; Mannhart, J.; Maier, J. The Oxidation Kinetics of Thin Nickel Films between 250 and 500 °C. *Phys. Chem. Chem. Phys.* **2017**, *19* (13), 9045–9052. https://doi.org/10.1039/C7CP00476A.

(12) Lutton, K.; Gusieva, K.; Ott, N.; Birbilis, N.; Scully, J. R. Understanding Multi-Element Alloy Passivation in Acidic Solutions Using Operando Methods. *Electrochem. Commun.* **2017**, *80*, 44–47. https://doi.org/10.1016/j.elecom.2017.05.015.

(13) Gusieva, K.; Cwalina, K. L.; Blades, W. H.; Ramalingam, G.; Perepezko, J. H.; Reinke, P.; Scully, J. R. Repassivation Behavior of Individual Grain Facets on Dilute Ni–Cr and Ni–Cr–Mo Alloys in Acidified Chloride Solution. *J. Phys. Chem. C* **2018**, *122* (34), 19499–19513. https://doi.org/10.1021/acs.jpcc.8b04306.

(14) Blades, W. H.; Reinke, P. From Alloy to Oxide: Capturing the Early Stages of Oxidation on Ni–Cr(100) Alloys. *ACS Appl. Mater. Interfaces* **2018**, *10* (49), 43219–43229. https://doi.org/10.1021/acsami.8b15210.

(15) Miller, C.; Field, R.; Kaufman, M. Phase Stability of Γ′-Ni2Cr and α-Cr in the Ni-Cr Binary. *Acta Mater.* **2018**, *157*, 1–10. https://doi.org/10.1016/j.actamat.2018.07.015.

(16) Strudel, J.-L. Mechanical Properties of Multiphase Alloys. In *Physical Metallurgy (Fourth Edition)*; Cahn, R. W., Haasen†, P., Eds.; North-Holland: Oxford, 1996; pp 2105–2206. https://doi.org/10.1016/B978-044489875-3/50030-2.

(17) Perepezko, J. H. The Hotter the Engine, the Better. *Science* **2009**, *326* (5956), 1068–1069. https://doi.org/10.1126/science.1179327.

(18) Superalloys for Gas Turbine Engines. In *Introduction to Aerospace Materials*; Mouritz, A. P., Ed.; Woodhead Publishing, 2012; pp 251–267. https://doi.org/10.1533/9780857095152.251.

(19) Horke, K.; Meyer, A.; Singer, R. F. Metal Injection Molding (MIM) of Nickel-Base Superalloys. In *Handbook of Metal Injection Molding (Second Edition)*; Heaney, D. F., Ed.; Woodhead Publishing Series in Metals and Surface Engineering; Woodhead Publishing, 2019; pp 575–608. https://doi.org/10.1016/B978-0-08-102152-1.00028-3.

(20) Poch, S.; Wyckoff, R. W. G.; Lewis, J. C. Thermocouple Element Composition. 2,691,690.

(21) Hoflund, G. B.; Epling, W. S. Oxidation Study of a Polycrystalline Ni/Cr Alloy II. *Chem. Mater.* **1998**, *10* (1), 50–58. https://doi.org/10.1021/cm970174o.

(22) Hoflund, G. B.; Epling, W. S. Oxidation Study of a Polycrystalline Ni/Cr Alloy II. *Chem. Mater.* **1998**, *10* (1), 50–58. https://doi.org/10.1021/cm970174o.

(23) Rooksby, H. P. Structure of Nickel Oxide. *Nature* **1943**, *152* (3854), 304–304. https://doi.org/10.1038/152304a0.

(24) Belokoneva, E. L.; Shcherbakova, Y. K. Electron Density in Synthetic Escolaite Cr~2O~3 with a Corundum Structure and Its Relation to Antiferromagnetic Properties. *Russ. J. Inorg. Chem. CC ZHURNAL NEORGANICHESKOI KHIMII* **2003**, *48*, 861–869.

(25) Pausescu, P.; Manaila, R. The Phase Transition in NiCr2O4. *Sov. Phys. Crystallogr.* **1965**, *13*, 533–535.

(26) Ivanov, V. V.; Talanov, V. M.; Shabel'skaya, N. P. Phase Relations in the NiFe2O4-NiCr2O4-CuCr2O4 System. *Inorg. Mater.* **2001**, *37* (8), 839–845.

(27) Sawatzky, G. A.; Allen, J. W. Magnitude and Origin of the Band Gap in NiO. *Phys. Rev. Lett.* **1984**, *53* (24), 2339–2342. https://doi.org/10.1103/PhysRevLett.53.2339.

(28) Crawford, J. A.; Vest, R. W. Electrical Conductivity of Single-Crystal Cr2O3. *J. Appl. Phys.* **1964**, *35* (8), 2413–2418. https://doi.org/10.1063/1.1702871.

(29) Hong, S.; Kim, E.; Kim, D.-W.; Sung, T.-H.; No, K. On Measurement of Optical Band Gap of Chromium Oxide Films Containing Both Amorphous and Crystalline Phases. *J. Non-Cryst. Solids* **1997**, *221* (2), 245–254. https://doi.org/10.1016/S0022-3093(97)00367-0.

(30) Marchetti, L.; Perrin, S.; Wouters, Y.; Martin, F.; Pijolat, M. Photoelectrochemical Study of Nickel Base Alloys Oxide Films Formed at High Temperature and High Pressure Water. *Electrochimica Acta* **2010**, *55* (19), 5384–5392. https://doi.org/10.1016/j.electacta.2010.04.063.

(31) Sprowl, L. H.; Adam, B. M.; Tucker, J. D.; Árnadóttir, L. First-Principles Study of the Products of CO2 Dissociation on Nickel-Based Alloys: Trends in Energetics with Alloying Element. *Surf. Sci.* **2018**. https://doi.org/10.1016/j.susc.2018.06.011.

(32) Ramanathan, R.; Ramalingam, G.; Perepezko, J. H.; Reinke, P.; Voorhees, P. W. Evolution of NiO Island Size Distributions During the Oxidation of a Ni-5Cr Alloy:

Experiment and Modeling. *ACS Appl. Mater. Interfaces* **2018**. https://doi.org/10.1021/acsami.7b18539.

(33) Wood, G. C.; Chattopadhyay, B. Transient Oxidation of Ni-Base Alloys. *Corros. Sci.* **1970**, *10* (7), 471–480. https://doi.org/10.1016/S0010-938X(70)80032-4.

(34) Chattopadhyay, B.; Wood, G. C. The Transient Oxidation of Alloys. *Oxid. Met.* **1970**, *2* (4), 373–399. https://doi.org/10.1007/BF00604477.

(35) Mohanty, P.; Rath, C.; Mallick, P.; Biswal, R.; Mishra, N. C. UV–Visible Studies of Nickel Oxide Thin Film Grown by Thermal Oxidation of Nickel. *Phys. B Condens. Matter* **2010**, *405* (12), 2711–2714. https://doi.org/10.1016/j.physb.2010.03.064.

(36) Haugsrud, R. On the High-Temperature Oxidation of Nickel. *Corros. Sci.* **2003**, *45* (1), 211–235. https://doi.org/10.1016/S0010-938X(02)00085-9.

(37) Ma, L.; Wiame, F.; Maurice, V.; Marcus, P. Origin of Nanoscale Heterogeneity in the Surface Oxide Film Protecting Stainless Steel against Corrosion. *Npj Mater. Degrad.* **2019**, *3* (1), 1–9. https://doi.org/10.1038/s41529-019-0091-4.

Chapter II: Background and Motivation

2.1 Metal Surface: Oxygen Adsorption to Oxide Saturation

During oxidation significant structural and chemical changes occur at the alloy-oxide interface,[1–6] and these changes can influence the passivation process as they predicate the development of a complete and corrosion resistant oxide layer. To understand these changes, models have been developed that capture the subtleties governing the physics and chemistry of oxidation phenomena. These are typically employed to predict different stages of the oxidation sequence, such as the d-band model[7–13] or Cabrera-Mott model[1,14,15], which can predictively determine the adsorption behavior and growth kinetics of thin oxide layers, respectively. However, discrepancies in the oxide growth arise due to the assorted oxidation pathways exhibited by transition metal alloys, e.g. Ni-Cr.[16,17] To better understand the oxidation process, the general oxidation behavior of oxygen adsorption to oxide saturation will be considered within the context of currently available theoretical models. A description of electrochemical corrosion at alloy surfaces will be discussed separately in section 2.4, and the differences between dry oxidation and aqueous corrosion will be remarked upon.

The early stages of oxidation commence with the impingement, adsorption, and dissociation of a reactive species (e.g. H_2O or O_2) onto a surface. The initial interaction results in bonding between the reactive species and the metal atoms, whereby the adsorbate can dissociate and become physisorbed or chemisorbed on the surface, Figure 2–1.[18–20] If the exposure is

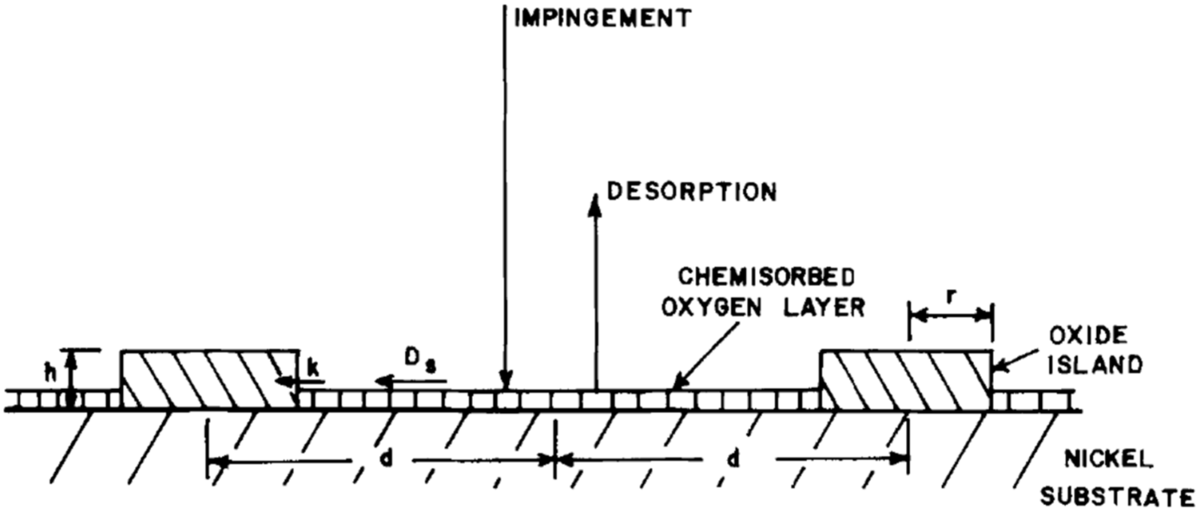

Figure 2-1. The general behavior of oxide growth on a Ni surface.[18,21]

sufficiently low, no metal to oxide phase is formed and instead oxygen adlayers typically are seen across the surface. The adsorption on transition metals and transition-metal alloy surfaces can be predicted by the d-band model.[7–13] In this model the electrons comprising the d-band of the transition-metal primarily determine the location and strength of the primary bonding to the adsorbate. For Ni-Cr alloys, the Cr atoms have been found to be preferential bonding sites for adsorption and can locally catalyze the reaction with the surrounding Ni atoms, thus enhancing the alloy's propensity for oxygen adsorption.[9,22–24] The partial pressure, temperature and crystallographic orientation can also have an effect on the manner in which surfaces react and will be discussed in detail in the next section. As exposure increases, the oxygen incorporates into the metal lattice and the nucleation and growth of an oxide layer or island occurs, Figure 2–1.[17,18,23,24] Chemical potentials develop at the alloy-oxide-oxygen interfaces and can drive the diffusion of metal cations and oxygen anions to the growth front, which happens faster at higher temperatures.

Cabrera-Mott and Wagner's theory are used as the basis to describe the growth of complete oxide layers at elevated temperatures, and are suitable to understand the growth kinetics of oxide

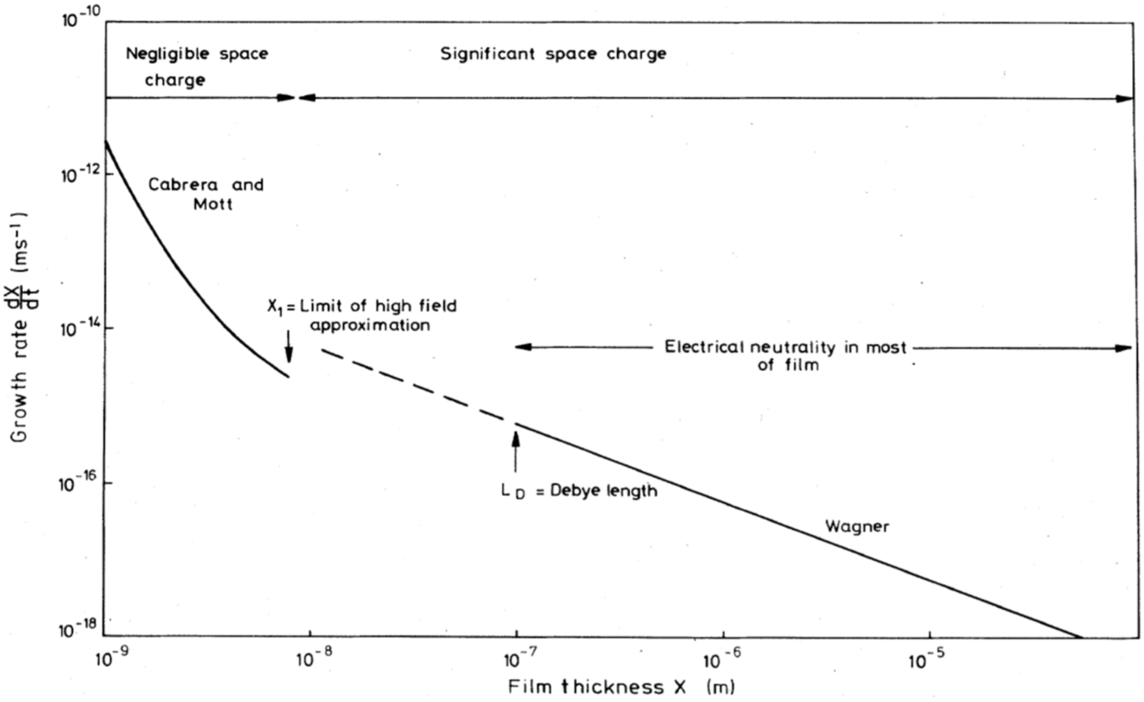

Figure 2-2. The growth rate of oxides as a function of film thickness.[1]

layers across different length scales.[1,25–27] Cabrera-Mott theory is applied to describe the growth kinetics of oxide layers that range from about 1 - 10 nm in thickness, Figure 2–2. At these length scales, growth is dominated by ion transport through the oxide layer, which is driven by the electric field between the metal-oxide and gas phase/adsorbate-oxide interfaces. This interaction controls oxide growth until a limiting vertical thickness is reached and the electric field is diminished.[1,25,27] Once the oxide reaches this limiting thickness Wagner's theory, which assumes a net charge neutral diffusion of ions and a field arising via ambipolar diffusion through the oxide, is suited to understand the growth rate.[28] This growth regime typically describes oxides growth on the micrometer length scale. The oxide growth rate as a function of oxide thickness within both the Cabrera-Mott and Wagner growth regimes is shown in Figure 2–2.[1] Both of these models assume that film growth is planar and homogenous across the surface, however the initial stages of growth before a complete oxide layer is formed are not fully understood. Indeed, many discrepancies have been observed during the thermal oxidation of transition metal surfaces.[17,29,30] Therefore, this dissertation specifically considers the transition from alloy to oxide during a growth regime prior to the Cabrera-Mott regime termed the “pre-Cabrera-Mott regime”, by capturing the initial stages of oxidation and corrosion on Ni-Cr alloy surfaces.

2.2 Oxidation of Low-index Ni-Cr Surfaces

To understand the role of crystallography in the early stages of oxidation Ni(100), Ni-Cr(100), Ni(111) and Ni-Cr(111) alloy surfaces are used as model systems. When oxidized above room temperature, Ni(100) oxidation begins with the dissociative chemisorption of O_2 and the formation of p(2×2)O and c(2×2)O ordered adlayers.[19,30–33] However, at elevated temperatures the formation of NiO is delayed and increasingly large oxygen exposures are required for its nucleation. Following the work by Kopatzki et al.[31] the incubation period can be attributed to the loss of preferential nucleation sites at the step edges due to faceting into {100} segments, which is driven by the reconstruction and achieved by the increased ad-atom mobility at higher temperatures, Figure 2–3(a). The NiO nucleation on Ni(100) relies on the availability of step edge nucleation sites, while nucleation on the terrace is suppressed. As a consequence, the Ni(100) surface requires relatively large doses of O_2 to initiate oxide formation.[30–32,34] The oxidation of Ni(111) also deviates from the expected oxide saturation thickening behavior predicted by the Cabrera-Mott model. Even after O_2 doses of up to 1000 L, clean areas of Ni(111) metal are still observed with patches of thin oxide between them.[29]

For Cr(100), a variety of different ordered oxygen adlayers and surface reconstructions have been reported after oxygen exposure.[20,35–39] It has been postulated that variations in sample

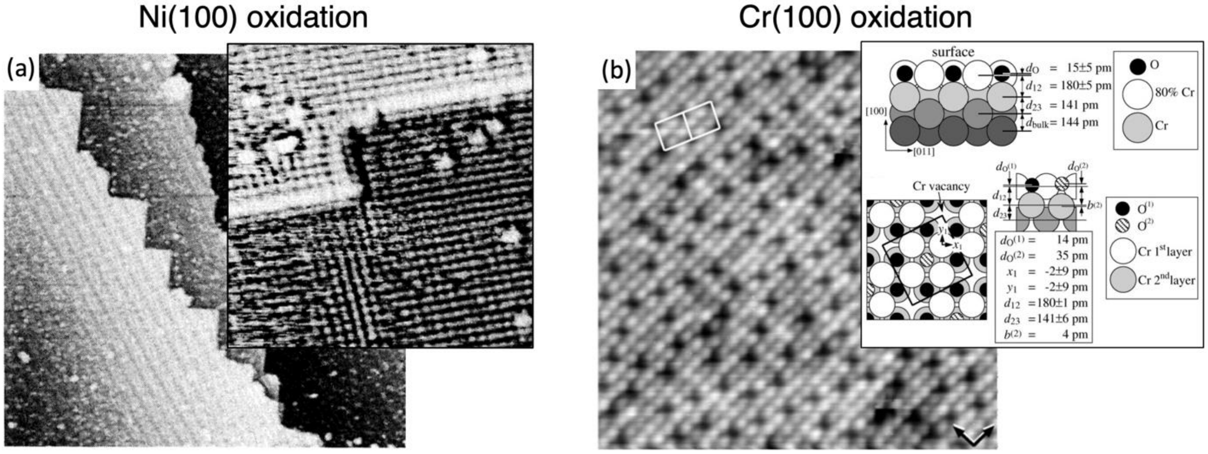

Figure 2-3. STM images of Ni(100) and Cr(100) surface after O_2 exposure. An STM image (a) of the Ni(100) surface (100×100 nm^2) after adsorption of 100 L of O_2 at 370 K.[31] A high resolution (12×12 nm^2) image inset is superimposed over the image, highlighting the c(2×2)O adlayer. (b) A 10×10 nm^2 STM image of the Cr(100) surface after O_2 exposure, showing the $(\sqrt{5}\times\sqrt{5})R27°$ reconstruction.[20] Superimposed over the image is a model of the surface determined by LEED. The STM image in (a) was measured at V_{bias} = 0.1-1.5V, $I_t < 1$ nA and the image in (b) was measured at V_{bias} = -0.19 V, I_t = 8 nA.

surface preparation are responsible for the disparities.[35] While the initial onset and progression of monolayer oxygen coverage is unresolved, the formation of chrome-oxide has been shown to initiate by the incorporation of oxygen atoms into the Cr(100) surface, Figure 2–3(b). This ad-layer is accompanied by small domains of a $(\sqrt{5}\times\sqrt{5})R27°$ sub-surface vacancy structure showing, at most, short range ordering of vacancies and not the long-range ordering of missing row reconstructions.[20] After a complete layer is formed the initial oxide growth is dominated by oxygen anion transport at $T_{ox} < 300$ °C and by metal cations at elevated temperatures.[39] The unique reaction pathways of the Ni and Cr surfaces suggests that alloying will result in distinctive oxidation processes different from those of the pure constituent metals.

The oxidation of Ni-Cr alloys is governed by the competing formation of NiO, Cr_2O_3, and mixed oxides such as the spinel $NiCr_2O_4$. Temperature, alloy composition, crystallographic orientation, and partial pressure of oxygen all influence the reaction pathways and consequently

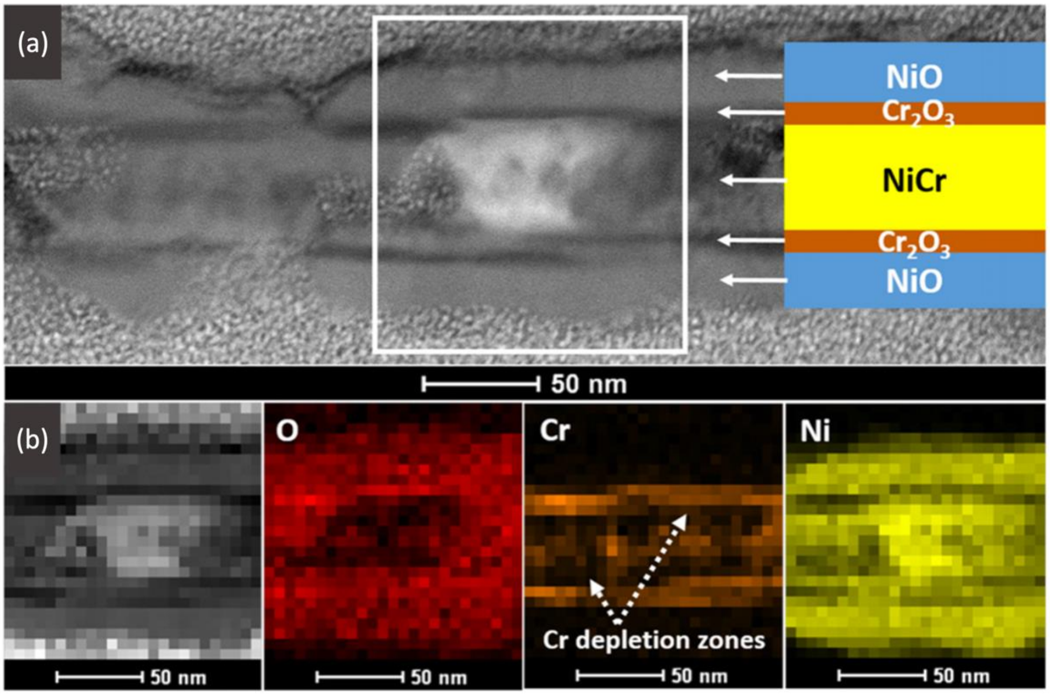

Figure 2-4. Cross sectional STEM and EDS analysis after oxidation of a Ni–20at.%Cr (atomic percent), where each phase was also determined by HRTEM. STEM image in (a) shows the cross-sectional view of layered oxide structure and (b) the corresponding EDS elemental maps of the area marked in the white block.[40]

the oxide products.[1,5,16,21,40–44] In general, the oxidation of Ni-Cr at or below 700 ºC, and for alloys with less than 20wt.%Cr, is dominated by the initial formation of NiO, which is generally attributed to the lower activation barrier for nucleation on a cube-on-cube epitaxy for the rock-salt structure.[16] NiO therefore dominates the initial oxide layer and Cr_2O_3 subsequently forms at the alloy-oxide interface by internal oxidation.[1,45–47] Luo et. al. specifically studied the oxidation of Ni-10at.%Cr(100) and Ni-20at.%(100) alloy surfaces at 450-700 ºC with high-resolution transition electron microscopy.[16,40] The in situ TEM and ex situ STEM results reveal the consequence of this reaction sequence is a layered oxide structure, Figure 2–4(a).[40] In conjunction with elemental mapping via EDS, evidence of Cr depleted zones were found in the alloy beneath the Cr_2O_3 layer, Figure 2–4(b). A limited supply of Cr in the Cr-poorer alloys impedes the formation of a continuous Cr_2O_3 layer thus diminishing the oxide's protective function.[40] However, the transition from alloy to complete oxide saturation on these surfaces is still not fully understood. To this end, more work is needed to understand how the alloy-oxide interface changes during oxidation and how crystallography effects the oxidation pathways this alloy system.

2.3 Low temperature Oxidation of Ni-Cr(100)

Previous work was conducted by Dr. Gopal Ramalingum, a former Reinke group member, on the oxidation of Ni-Cr(100) alloys at low temperatures (~300 °C). The oxide surface coverage of Ni-Cr(100) alloys after sequential oxidation steps was studied as a function of [Cr], Figure 2–5(a). The experimental results were paired with thermodynamic and kinetic modeling to understand how oxide islands grow and coalesce at low temperatures.[17] The post-nucleation and growth of oxides was captured on a Ni-wt.%5Cr(100) thin film using scanning tunneling microscopy (STM) after exposures between 7 and 130 L of O_2, Figure 2–5(b)–(e). Numerous STM

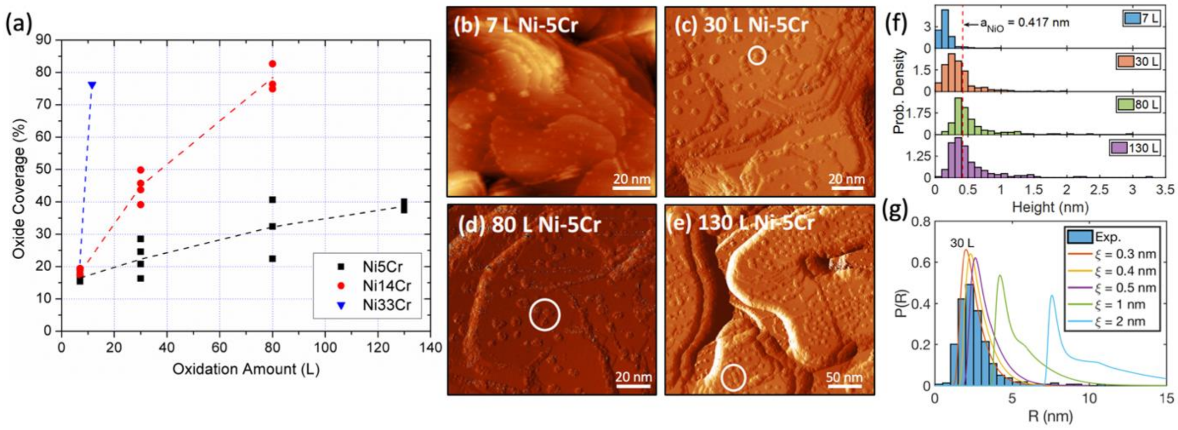

Figure 2-5. (a) Oxide coverage as a function of oxygen exposure given in Langmuir (L) for Ni-5wt.%Cr(100), Ni-14wt.%Cr(100) and Ni-33wt.%Cr(100) samples.[48] The sequential oxidation of a Ni-5wt.%Cr(100) sample is provided; an STM topography in (b) and current topography in (c)-(e). The STM images were recorded at V_{bias} = 2.0 V and I_t = 0.1 nA. The areas circled in white show instances of islands touching and coalescing into a larger island.[17]

images were analyzed, to evaluate the individual island sizes, the island number density, and oxide surface coverage as a function of oxygen exposure, Figure 2–5(f). STM data showed that changes in the oxide island height and oxide island radius are a separate, as opposed to a simultaneous, process. Essentially, the oxide islands were found to grow in height until they reach a critical thickness, after which the lateral growth dominated.

These experimental results were used to develop a surface diffusion model for oxide island growth. Figure 2–5(g) compares experimental oxide size distributions with those calculated from the surface diffusion model, using parameters that match the corresponding exposure from experiment. The initial growth of the surface oxide islands was shown to be controlled by short-range oxygen diffusion and was modeled using a screening length of approximately 0.4 nm, suggesting that growth and coalescence are localized to the edge of the oxide island at these oxidation temperatures and alloy compositions. Using this value of the screening length, excellent agreement between simulated and measured size distributions and island statistics is achieved, as shown in Figure 2–5(g). The results of the experimental and theoretical data set indicated the island growth rate is independent of the oxide island size, and is directly proportional to the gas pressure. Despite the success of these results, the nucleation behavior of the partial oxide layers was not fully understood and information on the oxide chemistry and composition was missing. Therefore, more work on the early stages of oxidation is needed to determine what oxide species form, how each oxide species nucleates, and in what manner does the oxidation pathway for each constituent alloying element evolve as a function of temperature and crystallographic orientation.

The electronic structure evolution of the Ni-Cr(100) surface after 300 ^{o}C oxidation was also obtained.[48] The STM topography data of a Ni-14wt.%Cr(100) surface after 30 L of oxidation and matching STS data are shown in Figure 2–6(a) and 2–6(b), respectively. The spatially resolved

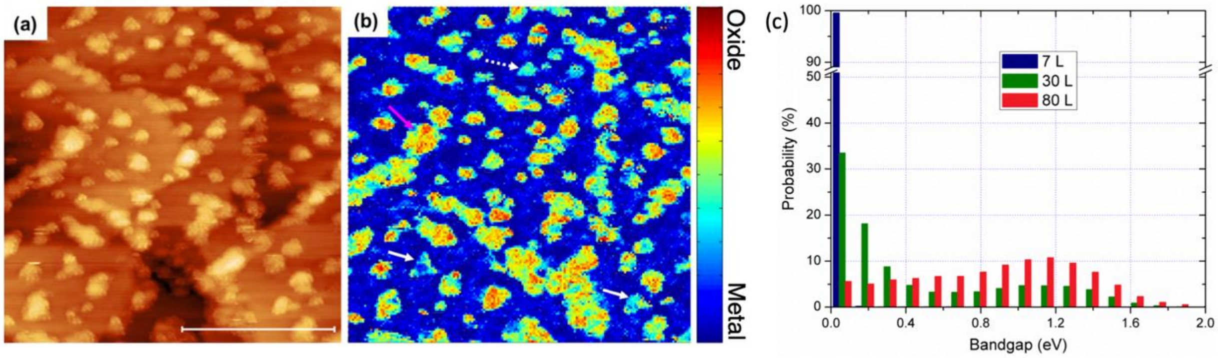

Figure 2-6. (a) The STM topography and accompanying band gap map (b) recorded on a Ni-14wt.%Cr(100) alloy thin film after 30 L oxidation at 300 °C.[48] The arrows in (b) point to oxide islands with different heights and respective band gaps. The band gap distributions in (c) shows the band gap evolution of a Ni-14wt.%Cr(100) surface after 7 L, 30 L and 80 L of O_2 exposure.[48] The scale bar in STM image is 25 nm and the color scale in the bandgap map is 0 eV (blue) to 2 eV (red).

band gap map distinguishes the alloy and oxide features across the surface. The thinner oxide features marked with the white arrows were found to have lower band gaps compared to the thicker islands around them, indicating a relationship between the oxide height and its band gap. The band gap of the surface was plotted as a function of exposure in Figure 2–6(c). As oxygen exposure is increased the oxide layer closes, as indicated by the increasing average band gap of the surface at greater exposures. While these data points indicate a relationship between the oxide height and their band gap, more work is needed to accurately determine the chemical nature of the oxide species and how the metal-oxide interface effects the electronic structure of the surface. It is also unclear how the conditions of the STS measurement itself effect the electronic structure of the oxide, thus the conditions of the STS mode will have to be carefully changed and their effect monitored.

2.4 Electrochemical Corrosion of Ni-Cr Alloys

Aqueous corrosion is experimentally studied by placing a metal in an electrochemical solution, applying a potential across that metal and monitoring the growth of the passive oxide film. During growth, the motion of the ions and defects is driven by an electric field across the film. Similar to the dry-oxidized alloys, the passivation of Ni-Cr alloys in aqueous environments is due to the formation of thermodynamically and kinetically stable passive Cr-rich oxides. NiO and hydroxides are also observed during aqueous corrosion and are stable over a broad range of potential and pH.[49–53] However, the passive oxide film that forms on the surface can be susceptible to breakdown and dissolution.[54–62] Models have been developed to understand the interplay between oxide growth and breakdown, specifically the Point Defect Model (PDM) and the Generalized Growth Model (GGM).[15,63] The PDM accounts for the diffusion of cations and anions through the oxide film and the reactions at the metal-film-solution interfaces. The dissolution of the oxide film is also explicitly accounted for, which allows the thickness of the steady-state film to be known. The general schematic of the PDM and the five reaction equations governing the oxide growth (1 & 2), metal dissolution (3 & 4) and passive film dissolution (5) are highlighted in Figure 2–7(a).[64] While the PDM has been used to successfully explain some experimental results, it assumes electric field strength across the film is constant and independent of both the anode potential and the film's thickness. The GGM, modifies this assumption by accounting for a change in the electric field across the oxide, as well as the potential drop at the oxide-solution interface, Figure 2–7(b).[15]

One of the assumptions of both these models is that the metal-oxide and oxide-solution interfaces are always planar, despite experimental results that contradict this notion.[64] For example,

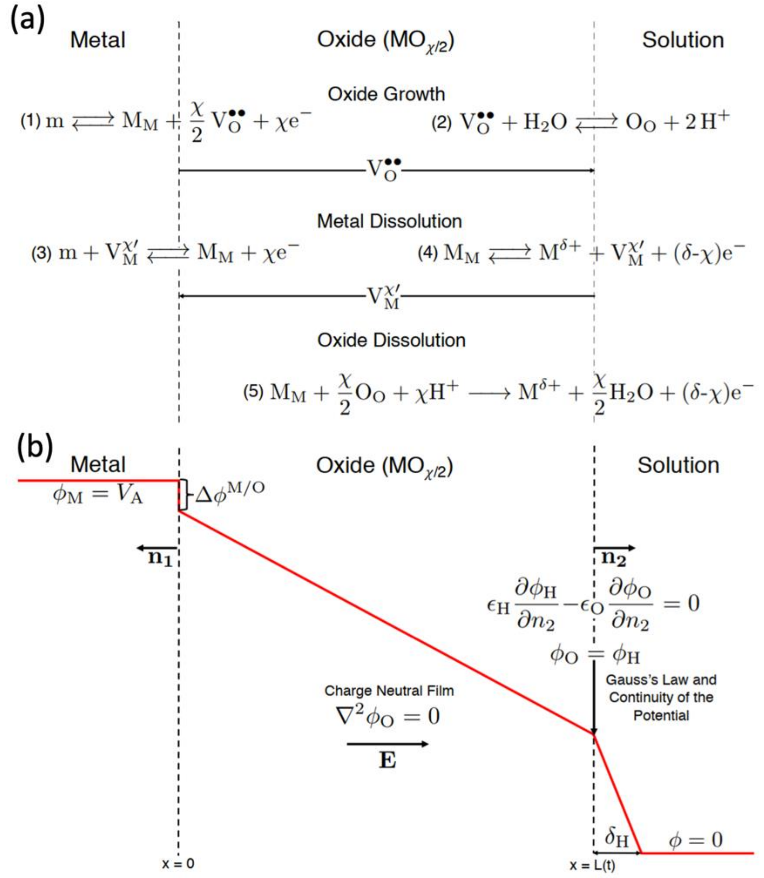

Figure 2-7. Diagrams of the metal-oxide-solution within the framework of the point defect model (PDM) and generalized growth model (GGM).[64] The different reactions possible (1)-(5) are given by the PDM in (a). χ is the charge of the cation in the oxide, while δ is the charge of the cation in the solution. Kröger-Vink notation is use to denote the point defects in the oxide, where a • is a positive charge relative to the host lattice, and a 0 is a negative charge relative to the host lattice. (b) The potential that arises between the metal-oxide-solution interfaces is described using the GGM and has been expanded by R. Ramanathan and P. Voorhees.[64]

in chloride solutions oxide films have been observed to undergo localized breakdown and dissolution in the form of pitting and crevice corrosion, which can lead to local dissolution and subsequent attacks at the interface of the metal or alloy.[54–62,65,66]Aside from changes at the interface, surface roughening can also occur by chemical processes including preferential chemical dissolution and/or oxidative dissolution across regions of the oxide that have not undergone a breakdown event. A model proposed by Ramanathan and Voorhees, adapted from the PDM and

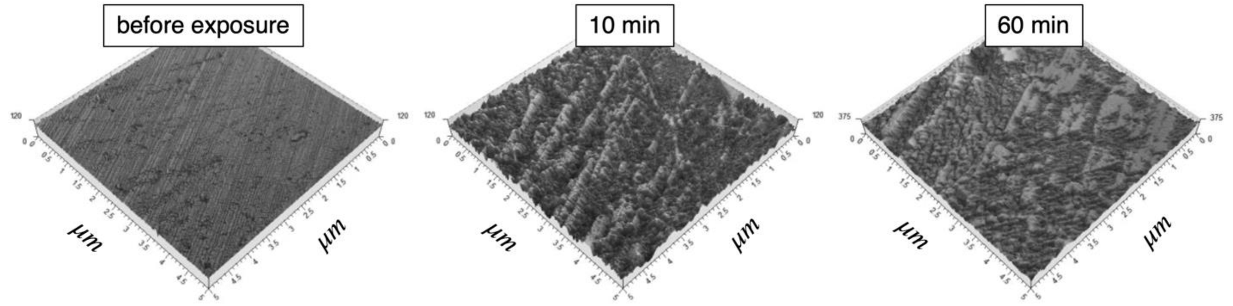

Figure 2-8. AFM images a carbon-steel (X65) surface after being electrochemically exposed to a CO_2-Saturated uninhibited NaCl solution at different times.[67] The vertical scale on the before and 10 min 3D images is 120 nm, while the vertical scale is 375 nm for the 60 min 3D image. All images are 5×5 μm.

GGM, has attempted to account for lateral variations and non-planar interfaces by assuming Gauss's law is preserved across the oxide-solution interface and the potential drop at the Helmholtz layer is linear.[64] Corrections to the chemical potentials of the cation and anion vacancies at the interfaces were made in order to account for the impact of interfacial energy and curvature on the defect concentrations.[64] This theoretical approach provided insight into passive film breakdown and pitting, but experimental confirmation is lacking partially because the quantitative assessment of length scale and amplitude of roughening at interface and surface due to morphological instabilities has not yet been achieved. Roughening in general is subject to competing mechanisms and as such is a significant challenge to unravel.

Measurements of oxidized and aqueous corroded metal and alloy surfaces have been made, and provide information on the surface roughness an example of which is provided in Figure 2–8, and numerous examples are included in the chapter VIII.[67] Other studies have also monitored the morphological changes and roughening of metal and alloy surfaces with AFM.[68–71] However, to the best of our knowledge AFM has not been applied to understand the nanoscale origins of roughening nor the impact of solution chemistry and grain orientation on nanoscale morphological changes. Therefore, the details of the oxidation process and passive layer evolution in Cl^- solution have been assessed by measuring the roughness of the film as it evolves during growth as a function of time and solution. This is achieved with a combination of electrochemical analysis *in operando* and quantitative assessment of surface roughness and oxide film composition *ex situ* by AFM and XPS, respectively. To date, few experiments have been published which offer a direct comparison between global and local morphologies and reactions, therefore more work is needed to understand the effect of the nanoscale passivation process.

2.5 From Alloy to Oxide: The Experimental Approach

To study the subtleties that govern the initial nucleation and growth of surface oxides Scanning Tunneling Microscopy/Spectroscopy is employed to gain insight into the evolution of oxide layers on Ni(100), Ni-Cr(100), Ni(111) and Ni-Cr(111) thin-film surfaces as they are exposed to O_2 under UHV conditions.[1,2] The work presented in this dissertation covers temperatures of 500 ºC and 600 ºC where the competition between Ni- and Cr-oxide formation is significant, and high-quality extended crystalline layers and interfaces are formed. The atomic processes that govern the growth of a passive oxide layer are studied, and the oxidation pathway of each constituent element is determined. Rigorous statistical treatment of the STS spectra is presented and significant electronic heterogeneity is observed within structurally identical regions. The *I(V)* characteristics of each oxide species and the effect of the measurement conditions on their electronic structure is also discussed.

To gain insight into the nucleation and growth of each oxide species, a polycrystalline Ni-22wt.%Cr alloy sample was oxidized under UHV conditions and studied as a function of time and crystallographic orientation *in operando* with a Spectroscopic Photoelectron and Low Energy

Electron Microscope (SPELEEM). The oxidation on (104) and (212) grains was simultaneously acquired with 25×25 nm^2 resolution by monitoring the XAS Cr-L-edge peak during a cumulative 65 L O_2 exposure at 500 ºC. Furthermore, valence band and core level spectroscopy were used to spatially resolve and identify the alloy and oxide chemistry, which displayed significant heterogeneities within local regions of the NiO and chromia. These methods are further informed by density function theory done by the Árnadóttir Group (Oregon State University) and level-set image characterization by the Voorhees group (Northwestern University).

In an attempt to better understand aqueous corrosion processes, the corrosion of binary Ni-Cr and ternary Ni-Cr-Mo alloys are also considered under a variety of different electrochemical conditions and their surfaces measured *ex situ* with AFM. The data analysis is informed by *in operando* single-frequency electrochemical impedance spectroscopy (SF-EIS) measurements, taken by the Scully group (University of Virginia), on the electrochemically grown passive film in either a chloride or sulfate solution as a function of time. This will allow for a detailed assessment of the topography, where nanoscale fluctuations between the alloy and the oxide can be measured. From this analysis the effect of the processing conditions on the oxide growth and stability can be delineated. This combined experimental and theoretical approach has offered greater insight into the progression of early-stage oxide growth on Ni-Cr alloys and underscores the dramatic impact of alloying on the oxidation process within the pre-Cabrera-Mott regime.

2.6 Chapter II References

(1) Atkinson, A. Transport Processes during the Growth of Oxide Films at Elevated Temperature. *Rev. Mod. Phys.* **1985**, *57* (2), 437–470. https://doi.org/10.1103/RevModPhys.57.437.

(2) Wood, G. C.; Chattopadhyay, B. Transient Oxidation of Ni-Base Alloys. *Corros. Sci.* **1970**, *10* (7), 471–480. https://doi.org/10.1016/S0010-938X(70)80032-4.

(3) Chattopadhyay, B.; Wood, G. C. The Transient Oxidation of Alloys. *Oxid. Met.* **1970**, *2* (4), 373–399. https://doi.org/10.1007/BF00604477.

(4) Mohanty, P.; Rath, C.; Mallick, P.; Biswal, R.; Mishra, N. C. UV–Visible Studies of Nickel Oxide Thin Film Grown by Thermal Oxidation of Nickel. *Phys. B Condens. Matter* **2010**, *405* (12), 2711–2714. https://doi.org/10.1016/j.physb.2010.03.064.

(5) Haugsrud, R. On the High-Temperature Oxidation of Nickel. *Corros. Sci.* **2003**, *45* (1), 211–235. https://doi.org/10.1016/S0010-938X(02)00085-9.

(6) Ma, L.; Wiame, F.; Maurice, V.; Marcus, P. Origin of Nanoscale Heterogeneity in the Surface Oxide Film Protecting Stainless Steel against Corrosion. *Npj Mater. Degrad.* **2019**, *3* (1), 1–9. https://doi.org/10.1038/s41529-019-0091-4.

(7) Takigawa, I.; Shimizu, K.; Tsuda, K.; Takakusagi, S. Machine-Learning Prediction of the d-Band Center for Metals and Bimetals. *RSC Adv.* **2016**, *6* (58), 52587–52595. https://doi.org/10.1039/C6RA04345C.

(8) Hammer, B.; Norskov, J. K. Why Gold Is the Noblest of All the Metals. *Nature* **1995**, *376* (6537), 238–240. https://doi.org/10.1038/376238a0.

(9) Sprowl, L. H.; Adam, B. M.; Tucker, J. D.; Árnadóttir, L. First-Principles Study of the Products of CO2 Dissociation on Nickel-Based Alloys: Trends in Energetics with Alloying Element. *Surf. Sci.* **2018**, *677*, 219–231. https://doi.org/10.1016/j.susc.2018.06.011.

(10) Hammer, B.; Nørskov, J. K. Electronic Factors Determining the Reactivity of Metal Surfaces. *Surf. Sci.* **1995**, *343* (3), 211–220. https://doi.org/10.1016/0039-6028(96)80007-0.

(11) Hammer, B.; Nørskov, J. K. Theoretical Surface Science and Catalysis—Calculations and Concepts. In *Advances in Catalysis*; Impact of Surface Science on Catalysis; Academic Press, 2000; Vol. 45, pp 71–129. https://doi.org/10.1016/S0360-0564(02)45013-4.

(12) Nørskov, J. K.; Abild-Pedersen, F.; Studt, F.; Bligaard, T. Density Functional Theory in Surface Chemistry and Catalysis. *Proc. Natl. Acad. Sci.* **2011**, *108* (3), 937–943. https://doi.org/10.1073/pnas.1006652108.

(13) Xin, H.; Vojvodic, A.; Voss, J.; Nørskov, J. K.; Abild-Pedersen, F. Effects of D-Band Shape on the Surface Reactivity of Transition-Metal Alloys. *Phys. Rev. B* **2014**, *89* (11), 115114. https://doi.org/10.1103/PhysRevB.89.115114.

(14) Cabrera, N.; Mott, N. F. Theory of the Oxidation of Metals. *Rep. Prog. Phys.* **1949**, *12* (1), 163. https://doi.org/10.1088/0034-4885/12/1/308.

(15) Seyeux, A.; Maurice, V.; Marcus, P. Oxide Film Growth Kinetics on Metals and Alloys I. Physical Model. *J. Electrochem. Soc.* **2013**, *160* (6), C189–C196. https://doi.org/10.1149/2.036306jes.

(16) Luo, L.; Zou, L.; Schreiber, D. K.; Olszta, M. J.; Baer, D. R.; Bruemmer, S. M.; Zhou, G.; Wang, C.-M. In Situ Atomic Scale Visualization of Surface Kinetics Driven Dynamics of Oxide Growth on a Ni–Cr Surface. *Chem. Commun.* **2016**, *52* (16), 3300–3303. https://doi.org/10.1039/C5CC09165A.

(17) Ramanathan, R.; Ramalingam, G.; Perepezko, J. H.; Reinke, P.; Voorhees, P. W. Evolution of NiO Island Size Distributions during the Oxidation of a Ni–5Cr Alloy: Experiment and Modeling. *ACS Appl. Mater. Interfaces* **2018**, *10* (10), 9136–9146. https://doi.org/10.1021/acsami.7b18539.

(18) Holloway, P. H. Chemisorption and Oxide Formation on Metals: Oxygen–Nickel Reaction. *J. Vac. Sci. Technol.* **1981**, *18* (2), 653–659. https://doi.org/10.1116/1.570847.

(19) Kopatzki, E.; Behm, R. J. STM Imaging and Local Order of Oxygen Adlayers on Ni(100). *Surf. Sci.* **1991**, *245* (3), 255–262. https://doi.org/10.1016/0039-6028(91)90028-Q.

(20) Schmid, M.; Leonardelli, G.; Sporn, M.; Platzgummer, E.; Hebenstreit, W.; Pinczolits, M.; Varga, P. Oxygen-Induced Vacancy Formation on a Metal Surface. *Phys. Rev. Lett.* **1999**, *82* (2), 355–358. https://doi.org/10.1103/PhysRevLett.82.355.

(21) Holloway, P. H.; Hudson, J. B. Kinetics of the Reaction of Oxygen with Clean Nickel Single Crystal Surfaces: I. Ni(100) Surface. *Surf. Sci.* **1974**, *43* (1), 123–140. https://doi.org/10.1016/0039-6028(74)90223-4.

(22) Samin, A. J.; Taylor, C. D. First-Principles Investigation of Surface Properties and Adsorption of Oxygen on Ni-22Cr and the Role of Molybdenum. *Corros. Sci.* **2018**, *134*, 103–111. https://doi.org/10.1016/j.corsci.2018.02.017.

(23) Das, N. K.; Shoji, T. Early Stage Oxidation of Ni–Cr Binary Alloy (111), (110) and (100) Surfaces: A Combined Density Functional and Quantum Chemical Molecular Dynamics Study. *Corros. Sci.* **2013**, *73*, 18–31. https://doi.org/10.1016/j.corsci.2013.03.020.

(24) Das, N. K.; Shoji, T. Adsorption and Diffusion of H and O on an Ni(111) Surface Containing Different Amounts of Cr. *Appl. Surf. Sci.* **2018**, *445*, 217–228. https://doi.org/10.1016/j.apsusc.2018.03.134.

(25) Cabrera, N. Theory of the Oxidation of Metals. **1949**, *12*, 163–184.

(26) Wagner, C. Equations for Transport in Solid Oxides and Sulfides of Transition Metals. *Prog. Solid State Chem.* **1975**, *10*, 3–16. https://doi.org/10.1016/0079-6786(75)90002-3.

(27) Seyeux, A.; Maurice, V.; Marcus, P. Oxide Film Growth Kinetics on Metals and Alloys: I. Physical Model. *J. Electrochem. Soc.* **2013**, *160* (6), C189–C196. https://doi.org/10.1149/2.036306jes.

(28) Lankhorst, M. H. R.; Bouwmeester, H. J. M.; Verweij, H. Thermodynamics and Transport of Ionic and Electronic Defects in Crystalline Oxides. *J. Am. Ceram. Soc.* **1997**, *80* (9), 2175–2198. https://doi.org/10.1111/j.1151-2916.1997.tb03107.x.

(29) Flege, J. I.; Meyer, A.; Falta, J.; Krasovskii, E. E. Self-Limited Oxide Formation in Ni(111) Oxidation. *Phys. Rev. B* **2011**, *84* (11), 115441. https://doi.org/10.1103/PhysRevB.84.115441.

(30) Bäumer, M.; Cappus, D.; Kuhlenbeck, H.; Freund, H.-J.; Wilhelmi, G.; Brodde, A.; Neddermeye, H. The Structure of Thin NiO(100) Films Grown on Ni(100) as Determined by Low-Energy-Electron Diffraction and Scanning Tunneling Microscopy. *Surf. Sci.* **1991**, *253* (1), 116–128. https://doi.org/10.1016/0039-6028(91)90585-G.

(31) Kopatzki, E.; Behm, R. J. Step Faceting: Origin of the Temperature Dependent Induction Period in Ni(100) Oxidation. *Phys. Rev. Lett.* **1995**, *74* (8), 1399–1402. https://doi.org/10.1103/PhysRevLett.74.1399.

(32) Smeenk, R. G.; Tromp, R. M.; Frenken, J. W. M.; Saris, F. W. The Oxidation of Ni(100) Studied by Medium Energy Ion Scattering. *Surf. Sci.* **1981**, *112* (3), 261–271. https://doi.org/10.1016/0039-6028(81)90374-5.

(33) Stuckless, J. T.; Wartnaby, C. E.; Al-Sarraf, N.; Dixon-Warren, St. J. B.; Kovar, M.; King, D. A. Oxygen Chemisorption and Oxide Film Growth on Ni{100}, {110}, and {111}: Sticking Probabilities and Microcalorimetric Adsorption Heats. *J. Chem. Phys.* **1997**, *106* (5), 2012–2030. https://doi.org/10.1063/1.473308.

(34) Norton, P. R.; Tapping, R. L.; Goodale, J. W. A Photoemission Study of the Interaction of Ni(100), (110) and (111) Surfaces with Oxygen. *Surf. Sci.* **1977**, *65* (1), 13–36. https://doi.org/10.1016/0039-6028(77)90289-8.

(35) Foord, J. S.; Lambert, R. M. Oxygen Chemisorption and Corrosion on Cr(100) and Cr(110) Single Crystal Surfaces. *Surf. Sci.* **1985**, *161* (2), 513–520. https://doi.org/10.1016/0039-6028(85)90824-6.

(36) Hope, G. A.; Ritchie, I. M. The Oxidation of Thin Chromium Films. *Thin Solid Films* **1976**, *34* (1), 111–114. https://doi.org/10.1016/0040-6090(76)90145-0.

(37) Salomonsen, G.; Norman, N.; Lonsjo, O.; Finstad, T. G. Kinetics and Mechanism of Oxide Formation on Cr Thin Films. *J. Phys. Condens. Matter* **1989**, *1* (42), 7843. https://doi.org/10.1088/0953-8984/1/42/006.

(38) Peter, R.; Saric, I.; Piltaver, I. K.; Badovinac, I. J.; Petravic, M. Oxide Formation on Chromium Metal Surfaces by Low-Energy Oxygen Implantation at Room Temperature. *Thin Solid Films* **2017**, *636*, 225–231. https://doi.org/10.1016/j.tsf.2017.06.011.

(39) Arlow, J. S.; Mitchell, D. F.; Graham, M. J. The Mechanism and Kinetics of the Oxidation of Cr(100) Single-crystal Surfaces Studied by Reflection High-energy Electron Diffraction, X-ray Emission Spectroscopy, and Secondary Ion Mass Spectrometry/Auger Sputter Depth Profiling. *J. Vac. Sci. Technol. A* **1987**, *5* (4), 572–576. https://doi.org/10.1116/1.574675.

(40) Luo, L.; Zou, L.; Schreiber, D. K.; Baer, D. R.; Bruemmer, S. M.; Zhou, G.; Wang, C.-M. In-Situ Transmission Electron Microscopy Study of Surface Oxidation for Ni–10Cr and Ni–20Cr Alloys. *Scr. Mater.* **2016**, *114*, 129–132. https://doi.org/10.1016/j.scriptamat.2015.11.031.

(41) Steffen, J.; Hofmann, S. Oxidation of NiCr and NiCrFe Alloys at Room Temperature. *Surf. Interface Anal.* **1988**, *11* (12), 617–626. https://doi.org/10.1002/sia.740111207.

(42) Jeng, S.-P.; Holloway, P. H.; Batich, C. D. Surface Passivation of Ni/Cr Alloy at Room Temperature. *Surf. Sci.* **1990**, *227* (3), 278–290. https://doi.org/10.1016/S0039-6028(05)80016-0.

(43) Hoflund, G. B.; Epling, W. S. Oxidation Study of a Polycrystalline Ni/Cr Alloy I: Room-Temperature Exposure to O2. *Thin Solid Films* **1997**, *307* (1), 126–132. https://doi.org/10.1016/S0040-6090(97)00300-3.

(44) Marcus, P.; Maurice, V. Atomic Level Characterization in Corrosion Studies. *Philos. Transact. A Math. Phys. Eng. Sci.* **2017**, *375*, 20160414. https://doi.org/10.1098/rsta.2016.0414.

(45) Chattopadhyay, B.; Wood, G. C. The Transient Oxidation of Alloys. *Oxid. Met.* **1970**, *2* (4), 373–399.

(46) Wood, G. C.; Chattopadhyay, B. Transient Oxidation of Ni-Base Alloys. *Corros. Sci.* **1970**, *10* (7), 471–480. https://doi.org/10.1016/S0010-938X(70)80032-4.

(47) Calvarin, G.; Molins, R.; Huntz, A. M. Oxidation Mechanism of Ni–20Cr Foils and Its Relation to the Oxide-Scale Microstructure. **2000**, *53*, 24–48.

(48) Ramalingam, G. Investigation of Semiconductor and Metal-Metal Oxide Surface Nanostructures by Scanning Tunneling Microscopy/Spectroscopy, University of Virginia, 2016.

(49) Lloyd, A. C.; Noël, J. J.; McIntyre, S.; Shoesmith, D. W. Cr, Mo and W Alloying Additions in Ni and Their Effect on Passivity. *Electrochimica Acta* **2004**, *49*, 3015–3027. https://doi.org/10.1016/j.electacta.2004.01.061.

(50) Lutton, K.; Gusieva, K.; Ott, N.; Birbilis, N.; Scully, J. R. Understanding Multi-Element Alloy Passivation in Acidic Solutions Using Operando Methods. *Electrochem. Commun.* **2017**, *80* (7), 44–47. https://doi.org/10.1016/j.elecom.2017.05.015.

(51) Zagidulin, D.; Zhang, X.; Zhou, J.; Noël, J. J.; Shoesmith, D. W. Characterization of Surface Composition on Alloy 22 in Neutral Chloride Solutions. *Surf. Interface Anal.* **2013**, *45* (6), 1014–1019. https://doi.org/10.1002/sia.5204.

(52) Lloyd, A. C.; Noël, J. J.; McIntyre, N. S.; Shoesmith, D. W. The Open-Circuit Ennoblement of Alloy C-22 and Other Ni-Cr-Mo Alloys. *JOM* **2005**, *57* (1), 31–35. https://doi.org/10.1007/s11837-005-0061-x.

(53) Jakupi, P.; Zagidulin, D.; Noël, J. J.; Shoesmith, D. W. The Impedance Properties of the Oxide Film on the Ni-Cr-Mo Alloy-22 in Neutral Concentrated Sodium Chloride Solution. *Electrochimica Acta* **2011**, *56*, 6251–6259. https://doi.org/10.1016/j.electacta.2010.07.064.

(54) Bocher, F.; Presuel-Moreno, F.; Scully, J. R. Investigation of Crevice Corrosion of AISI 316 Stainless Steel Compared to Ni–Cr–Mo Alloys Using Coupled Multielectrode Arrays. *J. Electrochem. Soc.* **2008**, *155* (5), C256. https://doi.org/10.1149/1.2883741.

(55) Bocher, F.; Huang, R.; Scully, J. R. Prediction of Critical Crevice Potentials for Ni-Cr-Mo Alloys in Simulated Crevice Solutions as a Function of Molybdenum Content. *Corrosion* **2010**, *66* (5), 1–15. https://doi.org/10.5006/1.3430462.

(56) Kehler, B. A.; Ilevbare, G. O.; Scully, J. R. Comparison of the Crevice Corrosion Resistance of Alloys 625 and C22. *Passiv. Localized Corros. Int. Symp. Honor Profr. Norio Sato* **1999**, *99*, 644–654.

(57) Kehler, B. A.; Ilevbare, G. O.; Scully, J. R. Crevice Corrosion Stabilization and Repassivation Behavior of Alloys 625 and 22. *Corrosion* **2001**, *57* (12), 1042–1065.

(58) Kehler, B. A.; Scully, J. R. Role of Metastable Pitting in Crevices on Crevice Corrosion Stabilization in Alloys 625 and 22. *Corrosion* **2005**, *61* (7), 665–684. https://doi.org/10.5006/1.3278202.

(59) Carranza, R. M.; Rodríguez, M. A. Crevice Corrosion of Nickel-Based Alloys Considered as Engineering Barriers of Geological Repositories. *Npj Mater. Degrad.* **2017**, *1* (1), 1–9. https://doi.org/10.1038/s41529-017-0010-5.

(60) Jakupi, P.; Noël, J. J.; Shoesmith, D. W. The Evolution of Crevice Corrosion Damage on the Ni-Cr-Mo-W Alloy-22 Determined by Confocal Laser Scanning Microscopy. *Corros. Sci.* **2012**, *54* (1), 260–269. https://doi.org/10.1016/j.corsci.2011.09.028.

(61) Jakupi, P.; Noel, J. J.; Shoesmith, D. W. Crevice Corrosion Initiation and Propagation on Alloy-22 under Galvanically-Coupled and Galvanostatic Conditions. *Corros. Sci.* **2011**, *53* (10), 3122–3130. https://doi.org/10.1016/j.corsci.2011.05.061.

(62) Mishra, A. K.; Shoesmith, D. W. Effect of Alloying Elements on Crevice Corrosion Inhibition of Nickel-Chromium-Molybdenum-Tungsten Alloys Under Aggressive

Conditions: An Electrochemical Study. *Corrosion* **2014**, *70* (7), 721–730. https://doi.org/10.5006/1170.

(63) Chao, C. Y.; Lin, L. F.; Macdonald, D. D. A Point Defect Model for Anodic Passive Films I. Film Growth Kinetics. *J. Electrochem. Soc.* **1981**, *128* (6), 1187–1194. https://doi.org/10.1149/1.2127591.

(64) Ramanathan, R.; Voorhees, P. W. Morphological Stability of Steady-State Passive Oxide Films. *Electrochimica Acta* **2019**.

(65) Marcus, P.; Maurice, V.; Strehblow, H. H. Localized Corrosion (Pitting): A Model of Passivity Breakdown Including the Role of the Oxide Layer Nanostructure. *Corros. Sci.* **2008**, *50* (9), 2698–2704. https://doi.org/10.1016/j.corsci.2008.06.047.

(66) Bouzoubaa, A.; Costa, D.; Diawara, B.; Audiffren, N.; Marcus, P. Insight of DFT and Atomistic Thermodynamics on the Adsorption and Insertion of Halides onto the Hydroxylated NiO(111) Surface. *Corros. Sci.* **2010**, *52* (8), 2643–2652. https://doi.org/10.1016/j.corsci.2010.04.014.

(67) Belarbi, Z.; Brown, B.; Singer, M.; Srdjan, N. Study of Adsorption of Corrosion Inhibitor 1-(2-Aminoethyl)-2-Oleyl-2-Imidazolinium Chloride on Carbon Steel Under CO2 Environment by Using In-Situ AFM Measurements. In *Corrosion Conference & Expo*; NACE International, 2017; p 15.

(68) Aurongzeb, D. Interface Evolution during Electrochemical Oxidation-Dissolution. *Appl. Surf. Sci.* **2005**, *252* (4), 872–877. https://doi.org/10.1016/j.apsusc.2005.01.032.

(69) Deng, X.; Galli, F.; Koper, M. T. M. In Situ Electrochemical AFM Imaging of a Pt Electrode in Sulfuric Acid under Potential Cycling Conditions. *J. Am. Chem. Soc.* **2018**, *140* (41), 13285–13291. https://doi.org/10.1021/jacs.8b07452.

(70) Li, X.; Jin, Y.; Liu, D.; Zeng, X.; Yang, R. Topographical Evolution of Magnetron Sputtering Ti Thin Films During Oxidatio Observed by AFM. *Surf. Rev. Lett.* **2011**, *18* (01n02), 61–69. https://doi.org/10.1142/S0218625X1101428X.

(71) Peng, X.; Li, L.; Wang, F. Application of AFM in a Study of the Selective Oxidation Behavior of Materials during the Early Oxidation Stage. *Scr. Mater.* **2009**, *60* (8), 699–702. https://doi.org/10.1016/j.scriptamat.2008.12.056.

(72) Bertrams, Th.; Neddermeyer, H. Growth of NiO(100) Layers on Ag(100): Characterization by Scanning Tunneling Microscopy. *J. Vac. Sci. Technol. B Microelectron. Nanometer Struct. Process. Meas. Phenom.* **1996**, *14* (2), 1141–1144. https://doi.org/10.1116/1.588416.

(73) Schintke, S.; Schneider, W.-D. Insulators at the Ultrathin Limit: Electronic Structure Studied by Scanning Tunnelling Microscopy and Scanning Tunnelling Spectroscopy. *J. Phys. Condens. Matter* **2004**, *16* (4), R49. https://doi.org/10.1088/0953-8984/16/4/R02.

(74) Castell, M. R.; Wincott, P. L.; Condon, N. G.; Muggelberg, C.; Thornton, G.; Dudarev, S. L.; Sutton, A. P.; Briggs, G. A. D. Atomic-Resolution STM of a System with Strongly Correlated Electrons:NiO(001) Surface Structure and Defect Sites. *Phys. Rev. B* **1997**, *55* (12), 7859–7863. https://doi.org/10.1103/PhysRevB.55.7859.

Chapter III: Methods

To capture the subtle changes at the surface during oxidation, a variety of experimental surface science techniques centered on scanning probe microscopy (SPM) and photoelectron spectroscopy were used. SPM includes an assortment of different methods and allows for the lateral measurement of surfaces and their accompanying topography and/or electronic structure. Scanning Tunneling Microscopy (STM) and Scanning Tunneling Spectroscopy (STS) are used to gather atomic scale information of early-stage oxidation, while Atomic Force Microscopy (AFM) is employed to capture both nanoscale and microscale corrosion processes at the surface. A selection of photoelectron spectroscopy techniques, specifically X-ray Photoelectron Spectroscopy (XPS), X-ray Absorption Spectroscopy (XAS) and Spectroscopic Photoemission and Low Energy Electron Microcopy (SPELEEM) are utilized to observe the initial oxidation process *in operando*. The use of all these techniques enabled us to connect these atomic scale and microscale oxidation processes, allowing for a deeper understanding of the effect of oxidation and corrosion at the surface of Ni-Cr based alloys.

3.1 Scanning Tunneling Microscopy and Spectroscopy

The primary experimental tool used in this dissertation is a scanning tunneling microscope (STM). Developed in 1981 by Gerd Binnig and Heinrich Rohrer, who were awarded the Nobel Prize in Physics for their work, STM allows for the atomic scale imaging of surfaces and the spectral analysis of its local density of states (LDOS) via a mode known as scanning tunneling

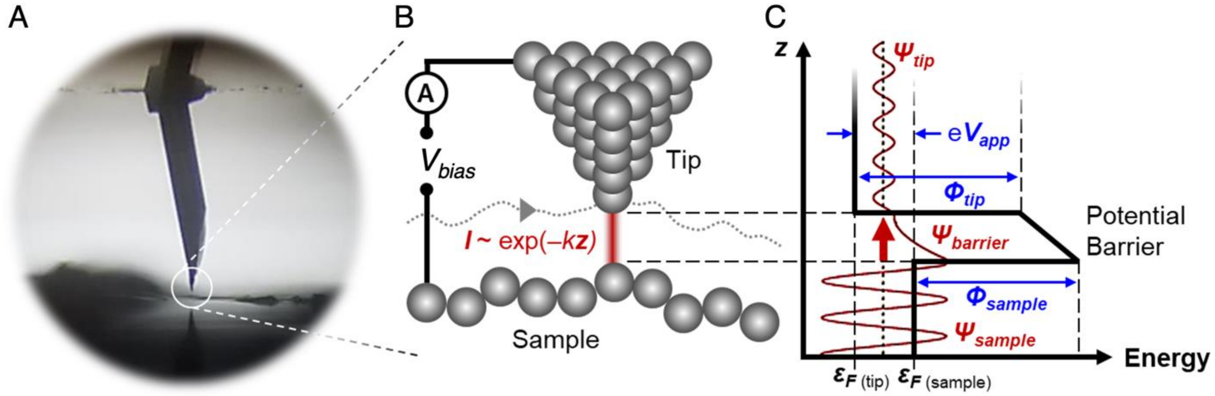

Figure 3-1. (A) depicts an image of a typical STM tip that is positioned just above a sample surface. (B) is a schematic for an STM tip drawing a tunneling current across the barrier region. (C) gives a general picture of how the position of the Fermi level, controlled by V_{bias}, effects the quantum tunneling, specifically the decay of the transmission probability, of electrons through the vacuum gap between surface and tip. [1]

spectroscopy (STS).[2–4] Based on the concept of quantum tunneling, STM/STS positions a sharp conductive tip, in our case tungsten, near a surface but not yet in electrical contact. The STM is commonly operated in what is known as a constant-current topographic mode. In this mode, the STM tip is rastered across the surface and a bias voltage (V_{bias}) of 0.1–5 V is normally applied. A tunneling current (I_t), typically on the order of 0.1–1 nA, arises across the vacuum gap between the tip and the surface. A feedback loop then adjusts the height of the STM tip to maintain a constant current across the tunneling barrier. This tunneling current is a function of V_{bias}, the LDOS of the surface, and the tip-sample distance. Depending on the polarity of V_{bias}, the filled or empty states of the surface can be probed. Therefore, the current flowing through the tip provides direct analysis of the surface's electronic structure. A schematic of the tunneling process can be seen in Figure 3-1.

The most elegant theoretical depiction of the tunneling process involves the application of John Bardeen's tunneling theory of metal-oxide-metal heterostructures.[5] This uses a first-order perturbation theory[6] and an adapted transfer Hamiltonian approach, i.e. a tunneling Hamiltonian.[7–

[9] While this theory was not explicitly designed to solve for the I_t of an STM, the assumptions and methodologies enabled two scientists at Bell Lab, Jerry Tersoff and Donald Hamann, to apply the equations and accurately model the STM tunneling current.[10] Each of these developments required a set of assumptions resulting in a reasonably accurate model of I_t. The entire set of assumptions and their respective mathematical consequences will be briefly summarized in the following subsections. Note, for the sake of clarity Bardeen's theories will be put into the context of a tip and sample, despite his model predating the development of the STM by many decades.

3.1.1 Bardeen Tunneling Theory

During the mid-20th century, electron tunneling between superconductor-oxide-superconductor heterostructures (oxide thickness ≈ 1.5-2.0 nm) was experimentally confirmed and served as the motivation to develop a better theoretical framework to describe the tunneling process.[11,12] To explain the results it was assumed that the only relevant factor was the density of states, and the transition probability for the tunneling of an electron should follow Fermi's Golden Rule.[5] Bardeen successfully demonstrated this assumption to be true in the case of electron tunneling by accurately breaking down the tunneling system into separate regions, ignoring electron-electron interactions and using a time-dependent perturbation theory, similar to one developed by Robert Oppenheimer to describe the field ionization of hydrogen.[6,8] The salient points regarding assumptions tied to these theories are briefly discussed below, however for more explicit treatment of these solutions, and detailed discussion on their derivation, the reader is directed to the following references.[8,9] The primary assumptions tied to the wave functions used to understand the tunneling process are, *i. the electron tunneling is weak enough to be described with a first order approximation*

ii. the tip and sample states are nearly orthogonal.

These assumptions fall directly out of the perturbation theory applied to a time-dependent electron wavefunction,

$$\psi(t) = \psi e^{-itE\,/\,\hbar} + \sum_{\mu} a_{\mu}(t)\phi_{\mu} \qquad 3-1$$

where t is time, E is the initial energy of an electron in the sample, and $\hbar$ Planck's reduced constant and the sum in the second term is over all bound states ϕ_{μ} of the tip. The symbols μ and ν are used for the tip and the sample, respectively. The coefficients $a_{\mu}(t)$ are then approximated, the electrons treated as experiencing a weak electric field. Mathematically this assumption requires all of the time dependent coefficients to "remain small" for a few picoseconds.[9] The second assumption approximates the electron transition probabilities by assuming orthogonality and taking the total derivative of the transition probability with respect to time. This leads to an expression for the approximate electron transition probability,[6,9]

$$P = \frac{d}{dt}\sum_{\mu}\left|a_{\mu}(t)\right|^{2} = \frac{2\pi}{\hbar}M^{2}\rho_{\mu}(E) \qquad 3-2$$

where M is a matrix element and $\rho_{\mu}(E)$ the density of states of the tip. This expression is similar Fermi's Golden Rule and effectively describes the behavior of electrons in the sample that tunnel into vacant tip states of comparable energy.[9] However, Bardeen needed to explicitly solve for the matrix element M in order to determine I_t.

To this end, Bardeen adopted a many-particle system with what is known as a transfer or tunneling Hamiltonian to solve for $M$and used Fermi-Dirac statistics to express I_t. The approach invoked another set of assumptions unique to Bardeen's theory,[9]

i. the electron-electron interactions can be ignored

ii. tip and sample occupation probabilities are constant and independent from each other

iii. there is electrochemical equilibrium between the tip and sample

The consequence of the first assumption falls out of Bardeen's set up of the tunneling problem, where the tunneling electron is independently governed by a single-electron Hamiltonian and the tunneling process is broken down into three separate regions with appropriate boundary conditions: sample, barrier, and tip. This piecewise approach means the tunneling process is a result of a transfer of electrons from the tip to the sample (or vice versa), and the matrix element is simplified and written,

$$M(\psi) = \frac{\hbar^2}{2m} \int \left(\psi_\nu^* \vec{\nabla} \psi_\mu - \psi_\mu \vec{\nabla} \psi_\nu^* \right) \boldsymbol{d\vec{S}} \qquad 3-3$$

where m is mass, ψ_μ the tip state, ψ_ν the surface state, and $\boldsymbol{\vec{S}}$ the "surface" between the barrier.

With the matrix element known, an expression for the transition probability of an electron is obtained. Bardeen used the second and third assumptions to express the tunneling current in the barrier region.[8,9] These assumptions lead to the what is known as the Bardeen tunneling current,

$$I_t = \frac{2\pi e}{\hbar} \sum_{\nu,\mu} f(E_\mu)[1 - f(E_\nu + eV)]|M(\psi)|^2 \, \delta(E_\mu - E_\nu) \qquad 3-4$$

where e is the charge of an electron, $f(E)$ the Fermi function, E_ν the energy of ψ_ν (energy of the sample state), E_μ the energy of ψ_μ (energy of the tip state) and V the applied voltage. To actually evaluate the current, the sums need to be calculated, which requires the matrix elements M to be determined. These can be calculated analytically when additional assumptions regarding the tip orbitals are made.

3.1.2 Tersoff-Hamann Model

After confirmation of STM's ability to provide atomic resolution using the tunneling current measurements by Rohrer and Binning in the early 1980s,[2] Jerry Tersoff and Donald Hamann proceeded to theoretically describe STM images and capture quantitatively I_t between the STM tip and sample.[3] In order to do this, they employed the tunneling Hamiltonian approach and adapted the matrix element M introduced by Bardeen.[3,5,7,10] To calculate Bardeen's matrix element, Tersoff and Hamann modified solutions to Schrodinger's equation for both the sample and tip and took the limit of small voltages and temperatures (~10 meV and 0 Kelvin). Due to the exponential decay of the wave function in the barrier region, only the orbitals localized at the outmost atom with respect to the surface was assumed to contribute to tunneling processing. Therefore, a *spherical-tip approximation* was introduced into the wave function, allowing the matrix element for an s-wave function to be properly evaluated.[10,13] Applying this approximation to the matrix element M and integrating over the energy the tunneling current becomes,

$$I_t \propto \int_{-\infty}^{\infty} \big(f(E_F) - f(E_F + eV)\big) \rho_\mu(E_F + eV) \rho_\nu(E_F, \vec{r_0}) \boldsymbol{dE} \qquad 3-5$$

where $f(E_F)$ is the Fermi function, $\rho_\mu(E_F + eV)$ the density of states of the tip and $\rho_\nu(E_F, \vec{r_0})$ the density of states of sample. It is worth noting that an extension of the model was provided by Chen to include d-wave function contributions to the tip.[14] To fully calculate the conductance, Tersoff and Hamann wrote an expression for the sample's DOS at the apex atom on the tip,

$$\rho_\nu(E_F, \vec{r_0}) = \sum_\nu |\psi_\nu(\vec{r_0})|^2 \delta(E_\nu - E_F) \qquad 3-6$$

which represents the local density of states of the sample at $\vec{r_0}$, the center of curvature at the outermost tip position. The squared modulus of the sample's wave function depends on the exponential, $|\psi_\nu(\vec{r_0})|^2 \propto exp[-2\kappa(R + d)]$ where κ is the vacuum decay constant, R the tip radius and d the barrier height. When the shape and DOS of the tip are assumed constant in the studied energy range, the energy dependent part of the tunneling current is determined,[7]

$$I_t \propto V_{bias} \rho_\nu(E_F, \vec{r_0}) \qquad 3-7$$

which highlights the tunneling current depends on the barrier distance, bias voltage and the sample's LDOS at the Fermi energy. Therefore, each STM image includes information on the topography and the electronic structure of the sample.

3.1.3 Scanning Tunneling Spectroscopy

The *I(V)* characteristics at the sample surface can be determined by using scanning tunneling spectroscopy (STS). In STS mode, the current-feedback loop is switched off in order to maintain a constant tip-sample distance. The voltage is then swept across a predetermined range (e.g. $V_{sweep} = \pm 3.0\ V$) and the current is measured as a function of voltage, producing an *I(V)* curve. The STS can be run in both point spectra and grid spectra modes. Fundamentally both rely on the same process, however the point spectra mode takes a single spectrum on the sample surface at a specific location, while the grid spectra mode measures the *I(V)* every 2nd, 3rd, 4th… etc. pixel and records an STM topography image (feedback loop on) for all pixels in between the grid array. All of the topography images in this body of work are constructed from a 512×512 px^2 (pixels squared) grid, and the STS grid is partitioned from this larger topography scan grid. An example of a 3×3 STS grid, where every third pixel is a spectroscopy measurement, is shown in Figure 3-2(A). In

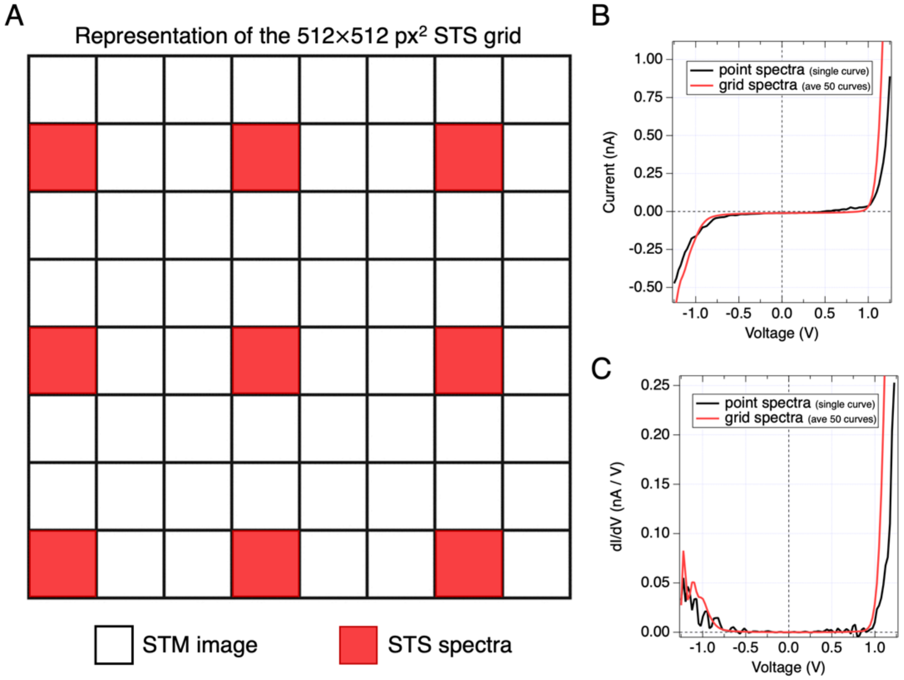

Figure 3-2. A representation of the 512×512 px^2 grid array (px = pixels) that makes up the STS spectra is provided in (A). Examples of both point averaged grid I(V) and dI/dV spectra taken from a WSe_2 surface are shown in (B) and (C), respectively.

this example a total of 28,900 spectra are taken over the scan area. This enables the grid STS mode to produce a better statistical representation and spatial mapping of the surface's electronic structure. A comparison between the point and average grid spectra is given in Figure 3-2(B)-(C). Indeed, most the STS data presented in this thesis were measured over a 3×3 or 4×4 grid and spatially resolved to allow topographic feature matching to a corresponding STM image. A MATLAB code was developed to handle the processing of grid STS and will be reviewed in section 3.9.

The treatment of our STS data follows the methodology developed by Randall Feenstra.[15,16] Feenstra et. al. improved upon the representation of STS data as LDOS by approximating the tip LDOS as a constant, taking the derivative of equation 2.1-5 with respect to voltage, and dividing that derivative by I/V.[4] In this dissertation, the *I(V)* curves are numerically differentiated to generate dI/dV curves. These spectra are then normalized by I/V to correct for the tip-sample distances, allowing the spectra from one part of the sample to be directly compared to another. This treatment generates (dI/dV)/(I/V) curves,

$$\text{normalized spectra: } \frac{\frac{dI}{dV}}{\frac{I}{V}+\varepsilon} \qquad 3-8$$

where ε is a rational number between 1–10 to avoid the singularity when $V = 0$. This normalization procedure is applied to the band gap map, conduction band map, and valence band map MATLAB codes discussed in section 3.9.

3.2 Atomic Force Microscopy

In 1986, G. Binnig et. al. expanded the concept of STM and introduced a new type of microscope called the atomic force microscope (AFM).[17] AFM involves rastering a mechanical probe, comprising a cantilever and tip, across a surface. The AFM tip interacts with the sample surface, where local tip-surfaces forces arise. Bending (and torsion) of the cantilever is initiated by the forces acting between tip and sample, whereas torsional motion is attributed to frictional forces. The motion of the cantilever in response to the tip-sample forces are monitored in our instrument by the reflection of a laser beam from the cantilever, which is measured quantitatively by a four-segment photodiode. The lateral and vertical variation in the laser intensity, determined by the local tip-surface forces, is then translated into a topography image, which can have a resolution ranging from microns to angstroms depending on the AFM tip and measurement mode. A general schematic of an AFM is shown in Figure 3-3(A). A review of the different AFM modes and their applications can be found in the following references.[18,19]

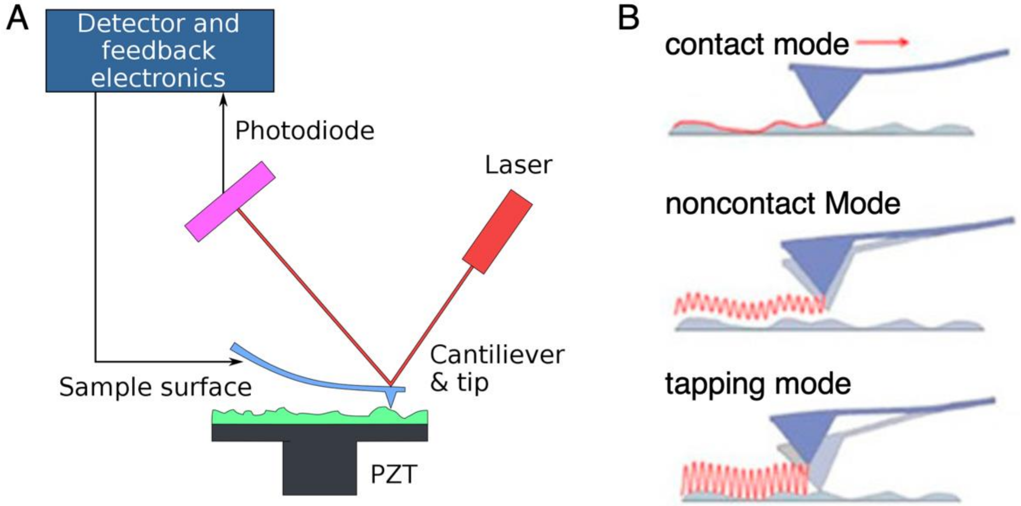

Figure 3-3. (A) A block diagram[20] of how an atomic force microscope measures a sample surface, whereby a mechanical tip is rastered across a surface (B)[21] and its deflection is measured as a function of position with a laser and a photodiode. Tapping mode was used in this dissertation.

In this dissertation, the morphology and surface roughness of electrochemically passivated Ni-Cr and Ni-Cr-Mo samples were studied. AFM enabled qualitative assessment of a surface's morphological features with the acquisition of 2×2 μm^2 to 50×50 μm^2 images after passivation. Quantitatively, the surface roughness of the samples surfaces was also determined from variations in the root mean square (RMS) of local surface areas (Chapter VIII). The RMS data in this study were calculated using Gwyddion, an open source software package used for scanning probe analysis.[22] The data processing is discussed in more detail in subsection 3.9.4. This dissertation uses an AFM with NT-MDT Solver Pro to measure the surface morphology of a variety of electrochemically corroded Ni-Cr samples. The AFM tip, ETALON HA/NC with a radius of curvature less than 10 nm, was kept in tapping mode during imaging, Figure 3-3(B).

3.3 Photoelectron Spectroscopy

Photoelectron spectroscopy relies on the general principles of the photoelectric effect. This phenomenon was described by Einstein during his *annus mirabilis* (miracle year) in 1905,[23] in an attempt to understand why the energy of emitted photoelectrons depended on the wavelength of light and not on the intensity. Using concepts developed by Max Planck,[24] Einstein proposed light is a collection of discrete wave packets, or photons, with energy hv (where v is the frequency and h Plank's constant). During photoemission, one packet of light is absorbed by one electron and the emitted electrons have an energy E which depends on the frequency of the light,

$$E = hv - \phi \qquad 3-9$$

where ϕ is a material dependent constant known as the work function. During experiments, because the Fermi energies of the sample and the collector are aligned, ϕ is the work function of the collector, also known as the spectrometer. Specific spectroscopy techniques have since been designed that exploit this effect and resolve the kinetic energies of the emitted photoelectrons, enabling chemically sensitive measures at a materials surface to take place. A large portion of this dissertation relied upon an assortment of spectroscopic techniques that use the photoelectric effect to excite electrons from the top layers of the alloy-oxide interface, and these will be discussed in the following sections.

3.3.1 X-ray Photoelectron Spectroscopy

Developed in the mid-1960s by Kai Siegbahn and his group at the University Uppsala,[25] X-ray Photoelectron Spectroscopy (XPS) is a technique that allows the chemical composition and electronic structure of surfaces to be measured. XPS measurements are typically made by irradiating a sample with low energy (~1.5 keV) X-rays, which triggers photoemission. The photoemission process can be described by a three-step model: i) a core electron becomes excited by a photon, ii) the photoelectron then travels to the surface and iii) it is then transmitted through the surface potential barrier into the vacuum and guided to the detector where its kinetic energy is measured.[26] A schematic for this process is shown in Figure 3-4(A) and (B). The binding energy (E_b) of the electron can then be calculated by,

$$E_b = hv - E_k - \phi \qquad 3 - 10$$

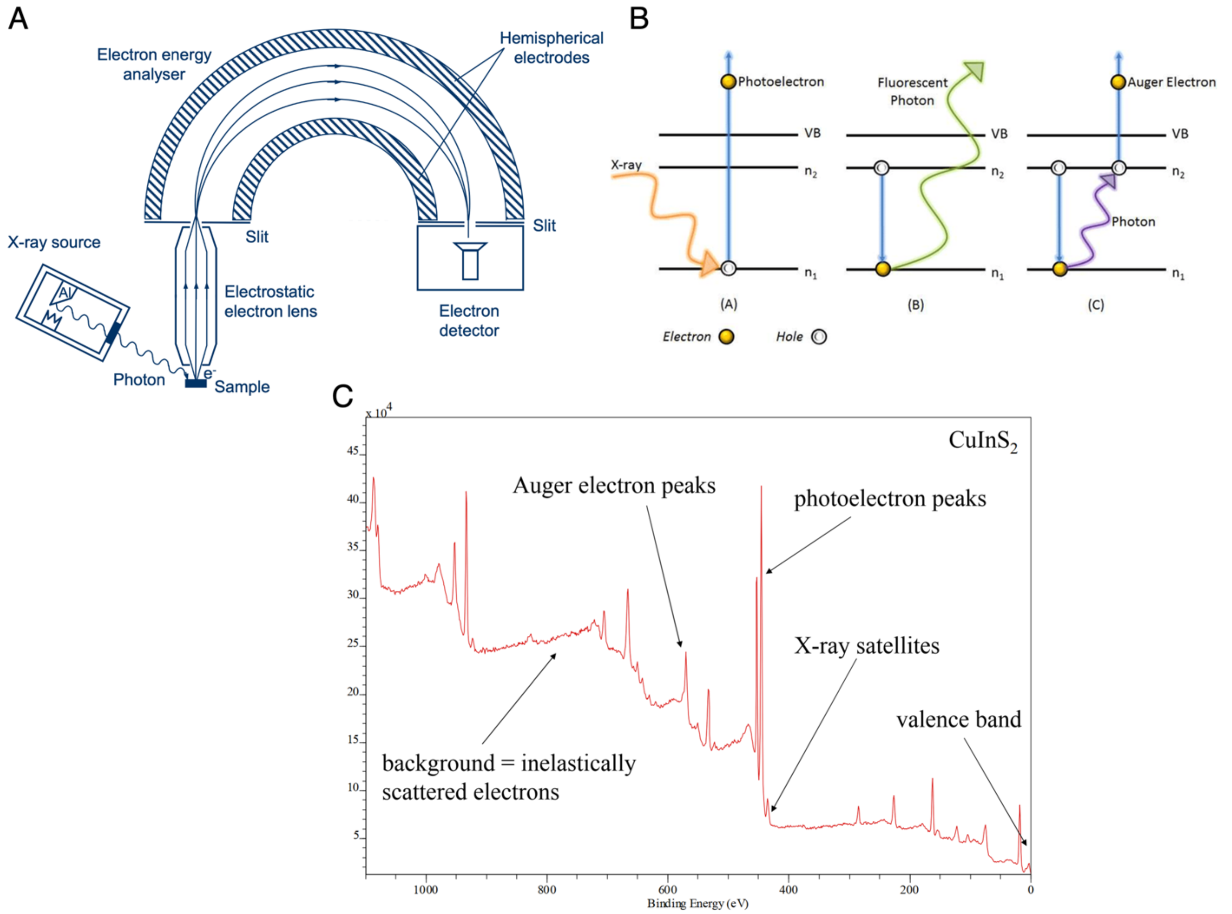

Figure 3-4. (A) A diagram of an XPS in operation as well as a general schematic for photoemission, (B).[27] An example of a spectrum taken from a $CuInS_2$ sample is shown in (C), where the different parts of the spectrum are labeled.[28]

where h is Plank's constant, v is the photon frequency (hv = photon energy), E_k the kinetic energy of the photoelectron and ϕ the work function of the spectrometer.

Each element and respective electron-core level has a characteristic binding energy, which leads to distinct peaks in the measured XPS data. Orbital quantum numbers are used to identify the respective electron peaks, specifically the principal quantum number n, the angular momentum ℓ and spin angular momentum j. The spin angular momentum is defined

$$j = 1 + s \qquad 3 – 11$$

where the spin *s* can either be ½ or -½. Spin-orbit splitting occurs, except when $\ell = 0$ (*s* orbital), via coupling between the spin and orbital angular momentums. This causes the *p*, *d*, and *f* orbitals to result in two possible states, each with a different binding energy.

An XPS spectrum is highlighted in Figure 3-4(C), where different characteristics of the spectra are labeled. As discussed in the above paragraphs, the primary excitation events yield element-specific peaks in the spectrum within the inelastically scattered background of secondary electrons. The shifts in the binding energy of the individual core levels are characteristic of small fluctuations in the local electron energy levels introduced by chemical bonding. XPS spectrum therefore does not only yield information on the elemental composition, but also provides detailed chemical information about a material. Auger electrons are due to emission following the relaxation of the core-hole following the emission of a photoelectron. The surface sensitivity provided by XPS is a consequence of a decrease in the flux of emitted photons via the inelastic mean free path (IMFP). The IMFP is a parameter that depends on the material and the photoelectron energy and is determined by collisions in which the photoelectron loses energy.[28] If the kinetic energy loss due to these collisions is sufficient, the photoelectron will contribute to the background rather than its characteristic peak. The photon energy and angle of the incident X-rays will also affect the escape probabilities[28] and most of the signal produced from the Ni-Cr alloys comes from the first ~10 nm of the surface.

3.3.2 Valence Band Spectroscopy

As XPS is a reflection of a material's band structure, the photoelectrons with lower binding energies near the Fermi energy come from occupied valence band states. Generally speaking, the valence band (VB) spectrum is the density of states, and in the work described in this thesis, the VB measurements are averaged over angle (and hence momentum) and do not offer detailed information about the band structure itself. The valence band spectra allow for distinction between the insulating oxide and conductive alloy substrate. [28] Quantum chemical theories (e.g. DFT) are often used in conjunction with VB measurements to aid in their interpretation, as the valence band spectra reflect the density of states modulated by the excitation cross section from the different bands. In this dissertation, valence band measurements were made on polycrystalline Ni-22wt.%Cr sample, and were spatially resolved between grains using an SPELEEM. Each measurement was made across the sample surface, and the grey-scale image corresponded to a specific energy slice across the valence band. More details on this specific measurement are provided in section 3.4.

3.3.3 X-ray absorption Spectroscopy

X-ray absorption spectroscopy (XAS) is a valuable technique used to determine a variety of different material characteristics such as the local geometric and electronic structure of the atoms in the sample. XAS is typically used at a beamline or synchrotron radiation facility, where tunable X-rays are provided and directed at the sample surface. These X-rays are absorbed by the atoms in the sample, and a core electron is promoted to an unoccupied level and measured by the detector. XAS can be broken down into two different ranges, Near Edge X-ray Absorption Fine Structure (NEXAFS or XANES – X-ray absorption near edge structure) and the Extended X-ray Absorption Fine Structure (EXAFS).[29–31] Different physical phenomena are visible in each specific energy range with respect to the absorption edge, such as the bonding symmetry, valency, nearest neighbor type and local geometric structure of a material.[32] In this dissertation NEXAFS was used to study the surface chemistry of Ni-Cr alloys during oxidation. Specifically, NEXAFS is integrated in the XPEEM experiments described below and afforded information on the progression of the oxidation reaction *in operando*.

XAS can measure the intensity of the electrons ejected from an absorption event as a function of energy and has a penetration depth of approximately 40 nm depending on measurement geometry. Generally, X-ray absorption is a process that obeys the Lambert-Beer law,

$$I = I_0 e^{-\mu L} \qquad 3 - 12$$

where I = transmitted light, I_0 = the incident light, μ = absorption coefficient and L = sample thickness.[33] An approximation for the absorption coefficient is made and the relationship between the material and the absorption process is written as,

$$\mu \cong {}^{\rho Z^4}\!/_{AE^3} \qquad 3 - 13$$

where ρ is the sample density, Z the atomic number, A the atomic mass and E the X-ray energy. The numerator dominates the absorption coefficient therefore, the absorption of X-rays is heavily dependent on the material. Indeed, while equation 3 – 13 gives a simplified view of this dependence it is sensible to give an overview of the physics of the absorption event and how it affects the XAS spectra.

During XAS operation an incoming X-ray is absorbed by the sample’s atoms, and a core electron is knocked out of its orbital, which is filled after a few femtoseconds by an electron from a higher energy state. Since the incident X-ray energy is larger than the binding energy of the core electron there is a sharp increase in absorption called the absorption threshold (or edge), Figure 3-

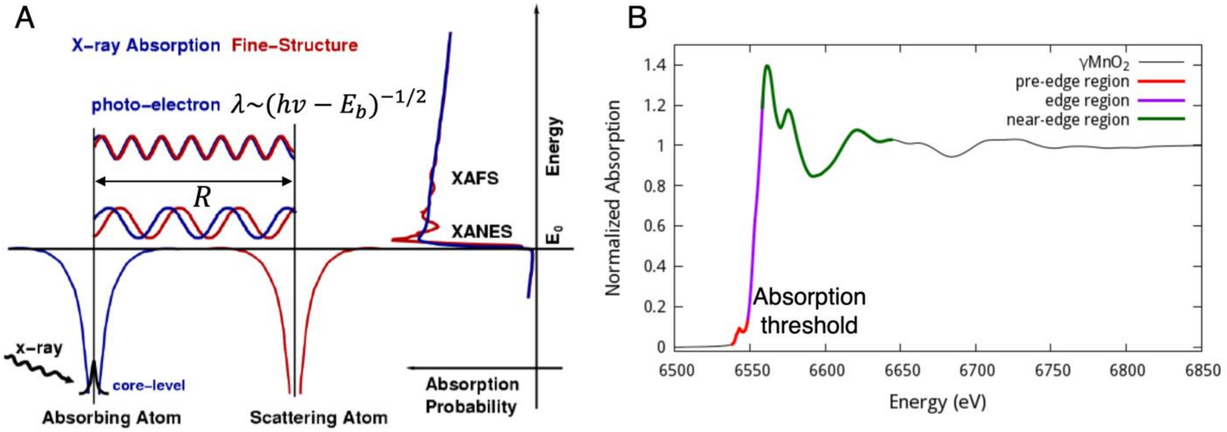

Figure 3-5. (A) The diagram of the ejected photoelectron and how scattering causes oscillations in the absorption coefficient.[34] (B) The absorption spectrum of MnO_2 taken at the Mn K-edge.[34] Each part of the spectrum around the absorption threshold is labeled, pre-edge (red), edge (purple), and near-edge (green).

5(A). The absorption edge is characteristic of the material and the electron core orbital level and is characterized by a sharp rise (or discontinuity) in the linear absorption coefficient of a specific element, where the energy of the photon corresponds to the specific energy (E_b) of an electron shell of that element.[34,35] Once the electron is kicked out, it leaves behind a core-hole which interacts with the photoelectron. As the photoelectron propagates through the surrounding material it can undergo scattering events from other electrons, grain boundaries, defects, etc. that will result in the attenuation of its energy. Eventually the photoelectron will make its way near the surface and exists in a final state ψ_f with some kinetic energy, where the absorption intensity is measured as a function of the photon energy, Figure 3-5(B).

These processes will cause oscillations in $\mu(E)$, which manifest as resonant scattering peaks in the spectra and cause changes the kinetic energy and final state of the photoelectron.[33,34] The contribution to the XAS absorption coefficient is then determined mathematically by the initial and final states of the system using Fermi's golden rule,[36]

$$\mu(E) = \frac{4\pi n\alpha}{\omega} \sum_{f} \left|\langle \psi_f | \boldsymbol{e} \cdot \hat{p} | \psi_i \rangle\right|^2 \delta(\hbar\omega + E_i - E_f) \qquad 3-14$$

where $n = N/V$ is the atomic number density, α the fine-structure constant, $\left|\langle \psi_f | \boldsymbol{e} \cdot \hat{p} | \psi_i \rangle\right|$ the X-ray coupled dipole approximation, $\hbar\omega + E_i$ the photoelectron energy, and E_f the final states energy. The initial state can be solved using something like Density functional theory (DFT), whereas the final state must consider a state with a core-hole and excited electron.[33] This is where multiple scattering theory comes into play, and an adapted version of Schrödinger's equation is evaluated,[36]

$$H\psi_f = \left[\frac{p^2}{2m} + V_{coul} + \Sigma(E)\right]\psi_f = E\psi_f \qquad 3-15$$

where H = Hamiltonian, V_{coul} = final state coulomb potential (in the presence of the screened core-hole potential) and $\Sigma(E)$ = photoelectron self-energy in the quasi particle approximation.[37] The peak positions and their shape come from the final state coulombic potential, which accounts for both the inelastic losses (final-state broadening) and systematic shifts in peak positions.

3.4 Spectroscopic Photoemission & Low Energy Electron Microscopy

The Spectroscopic Photoemission and Low Energy Electron Microscope (SPELEEM) is a unique microscopy technique that allows for the investigation of surfaces at the micrometer to nanometer scale and combines X-ray photoemission electron microscopy (XPEEM), low energy electron microscopy (LEEM) and low energy electron microscopy (LEED).[38,39] XPEEM is a chemically sensitive technique based on the photoelectron spectroscopic techniques of XAS and XPS. Used at synchrotron radiation sources, the energy-filtered imaging of the spectroscopic PEEM allows measurement of both the core and valence electrons of a sample and enables the direct spatially resolved imaging of the surface with chemical contrast. When these methods are combined with LEEM and LEED, the multi-method approach of SPELEEM supports the measurement of structural and chemical shifts *in operando*, making it highly useful for studying the oxidation of alloy surfaces.

The instrument used in this dissertation is located at the MAX IV facility in Lund, Sweden and the experimental station is shown in Figure 3-6(A). The experimental set-up at the MAXPEEM lab has two parts.[38] The first station facilitates the measurement of both X-ray photoemission and X-ray absorption spectroscopies, which are collected by a hemispherical electron analyzer.

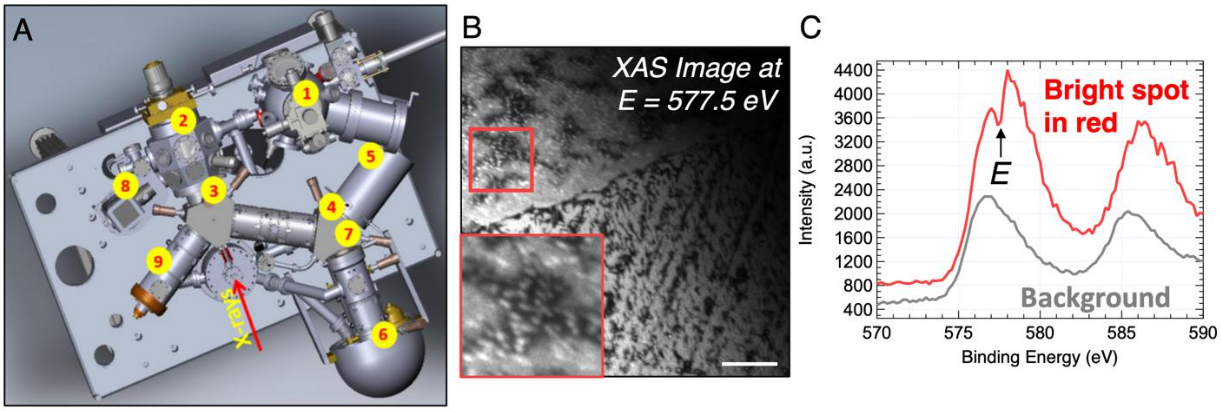

Figure 3-6. (A) The experimental station of the SPELEEM at the MAX IV lab in Lund, Sweden where 1 is the prep chamber, 2 the main chamber, 3 and 4 beam separators, 5 an AC mirror, 6 energy analyzer, 7 MCP detector, 8 UV-lamp, and 9 electron gun.[40] (B) is an XAS image in operando of a Ni-22%Cr sample surface by monitoring the Cr L edge during oxidation. A complete XAS spectra (C) is then taken, where the spectra are spatially resolved and matched to the image's features. In this example, the chromia appear as bright spots, whereas the background represents the underlying alloy.

Downstream from this analyzer is an experimental station that enables three operation modes using X-rays: i) energy filter imaging, ii) energy filtered micro-diffraction, and iii) micro-XPS or dispersive plane imaging.[38] The SPELEEM at the MAX-IV has a range of view of up to ~100 μm, with a resolution as small as 25 nm, and can monitor real-time dynamic processes up to that resolution. Given these resolutions, the emission and absorption spectroscopy measurements are often referred to as μ-XPS and μ-XAS and energy filter imaging can be achieved in both modes. A brief overview of XPEEM, LEED and Mirror Electron Microscopy (MEM) will be given in the sections below, as well as examples of the data produced.

3.4.1 XPEEM

X-ray photoemission electron microscopy uses energy-filtered imaging to monitor the active evolution of surfaces and interfaces during experiments with either μ-XPS or μ-XAS. In either mode, X-rays are used to excite core-electrons from the sample, which leave the surface with a specific kinetic energy that is selected by the hemispherical energy analyzer to form the XPEEM image, Figure 3-6(B). The kinetic energy of the electron can be varied, allowing the chemical states of a specific element within the material to be probed and utilized for elemental/chemical mapping.[40] This mode was used to monitor the evolution of the Ni-22wt.%Cr surface during oxygen exposure *in operando*, where the electrons from the Cr_2O_3 peak at E_{slice} = 577.5 eV were filtered from the μ-XAS. After each oxidation step the full XAS spectrum, Figure 3-6(C), was taken to allow feature matching with the corresponding XPEEM images. The XPEEM image filtering was also done with the μ-XPS in the valence band regime.

3.4.2 Low Energy Electro Diffraction (LEED)

Low Energy Electron Diffraction (LEED) is used for determining the crystal orientation of surface structures and its first uses traces back to the Davisson-Germer experiment which demonstrated the wave nature of electrons.[41] LEED measurements are made by directing a beam of low energy electrons (on the order of $10\text{-}10^2$ eV) normal to the sample. The electrons undergo Bragg diffraction where the elastically-scattered electrons contribute to a diffraction pattern and are measured by a detector, whilst the secondary electrons are filtered. The diffraction pattern, as a 2D representation of the reciprocal space of the surface, can be used to construct the real space image of the crystal surface. At the MAXPEEM lab, the LEED spot area can be as small as 250 nm, so diffraction patterns were taken in grains of interest on a polycrystalline Ni-22wt.%Cr sample and the relative orientation of each grain determined.

3.4.3 Mirror Electron Microscopy (MEM)

Images of the surface can be taken by using Mirror Electron Microscopy (MEM). A primary beam of electrons is directed at the sample surface and because the sample is held at a more negative potential than the electron source, the electrons are reflected away from the surface. The electrons get close enough to respond to the local field distribution just above the surface and are subsequently collected to show an MEM image.[40] These electrons make up an image, where the contrast is determined by the "field distribution" above the surface. The surface topography and the charge distribution at the surface contribute to the field distribution.[40] While the images are not a direct representation of a sample surface's topography, they do relay information that can enable feature matching when other techniques are used. In this dissertation, MEM was used to locate the grains and grain boundaries on a Ni-22wt.%Cr sample prior to oxidation.

3.5 Density Functional Theory

In collaboration with the Árnadóttir group at Oregon State University, the VB measurements conducted in the XPEEM microscope were analyzed using a first-principles density functional theory (DFT) approach. DFT is a state-of-the-art technique that enables users to calculate the electronic and geometric structure of many body systems. The cornerstone of DFT is the application of the Hohenberg-Kohn and Kohn-Sham theorems.[42,43] Pierre Hohenberg and Walter Kohn expanded the Hartree-Fock method in the spring of 1965 to more accurately account for the electronic nature of many particle systems.[42,44,45] Their work utilized functionals, which represent the spatially dependent density of electrons in a system. A year after the Hohenberg-Kohn paper was published; Kohn collaborated with Lu Sham to produce a scheme that allowed for the indirect minimization of the energy of a many electron system, otherwise known as the exact energy functional.[43,44] This allowed the energy to be minimalized with respect to electron density and yielded an adapted version of the many-body Schrodinger equation,

$$\left[-\frac{1}{2}\nabla_i^2 + v_{ext}(\vec{r}) + v_H(\vec{r}) + v_{xc}(\vec{r})\right]\Psi_i(\vec{r}) = E\Psi_i(\vec{r}) \qquad 3-16$$

where v_{ext} is the static ionic potential of the nuclei, v_H is the Hartree potential, and v_{xc} is the exchange-correlation potential.[42,43,45–50] This equation is known as the Kohn-Sham equation and is at the center of modern DFT.

As it pertains to this proposal, energy calculations of the ground state geometry, electronic structure, and transition states will be carried out using a first principles density functional approach carried out using the Vienna Ab initio Simulation Package (VASP). The Kohn-Sham equations were solved with a plane-wave basis set and core electrons were described using the projector augmented wave (PAW) method. Electron exchange and correlation were described within the Perdew-Burke Ernzerhof (PBE) generalized gradient approximation (GGA). Spin polarization was used for all calculations, and the cutoff energy for the plane wave basis set was 400 eV. The calculated Cr and Ni lattice constant was 2.82 Å and 3.52 Å. The Cr (104) surface was represented by a 16 atomic layer slab using a (3×2) unit cell, which is 192 atoms. The Cr (212) surface was represented by a 16 atomic layer slab using a (6×2) unit cell, which is 384 atoms. The Ni (104) surface was represented by a 20 atomic layer slab using a (2×2) unit cell, which is 320 atoms. The Ni (212) surface was represented by a 16 atomic layer slab using a (2×2) unit cell, which is 256 atoms. For Cr (104) and Cr (212), the six bottom layers were fixed, and remaining top layers were relaxed. For Ni (104) and Ni (212), the six bottom layers were fixed, and remaining top layers were relaxed. A total vacuum distance of 10 Å was used to separate the surface from its periodic slab in the direction along the surface normal. The convergence criteria for the maximum residual force for the geometry optimization is 0.03 eV/Å. A Monkhorst−Pack grid of 9 × 9 × 1 k-points was used for the density of states (DOS) calculations. The magnetic moment was included for all calculations.

3.6 Electrochemical Techniques

In collaboration with the Scully Group at UVA, two complementary electrochemical techniques were employed to measure film growth in operando: Single Frequency Electrochemical

Impedance Spectroscopy (SF-EIS) and Inductively Coupled Plasma Mass Spectrometry (ICP-MS). SF-EIS is used to monitor passive film growth by measuring variations in the imaginary impedance across the film. This is accomplished by superimposing an AC signal onto a constant applied DC potential (potentiostatic case) or current density (galvanostatic case), resulting in global measurements of the film growth. Specifically, the oxide thickness and oxidation current density are determined by using a constant phase element fit.[51] ICP-MS uses a polychromatic spectrometer combined with a plasma source to evaluate an electrolyte stream during film growth. From the electrolyte stream, the concentration and the related element-specific metal dissolution current density and is determined from the emission wavelength intensity, where each element has a unique wavelength. Information about the growth of the film (i_{ox}) is calculated by subtracting the sum of the dissolution rate from the total electrochemical current.[51] For the passivation experiments outlined in this dissertation the electrochemical cell used was a typical three-electrode flat cell with a Pt mesh counter electrode and a corresponding reference electrode [saturated calomel electrode (SCE) for the chloride experiments and mercury-mercury sulfate electrode (MMSE, +0.41 V vs SCE) for the sulfate experiments]. The quiescent solutions were deaerated using ultra-high purity N_2 gas throughout experimentation. A Gamry Reference 600 potentiostat was utilized for dc and ac tests.

3.7 Scanning Electron Microscopy

Scanning Electron Microscopy (SEM) uses a focused primary electron beam to raster across a sample, where inelastic (or elastic) collisions with the sample's electrons occur and generate secondary (or backscatter) electrons. The secondary electrons leave the surface of the sample and are collected by a detector which generates a signal. A high-resolution image of the sample morphology is constructed from the variations in the signal intensity. Another consequence of the inelastic collisions is the production of core-holes. Once a core-hole is generated, higher energy electrons recombine with it and during the electron-hole recombination transition an x-ray is emitted. These x-rays have energies that are characteristic of the element they come from, therefore energy dispersive x-ray spectroscopy (EDS) is often used in conjunction with SEM to provide chemical analysis of the sample. This mode allows quantitative analysis of the sample's composition and was used to confirm the composition of our alloy thin films (subsection 3.8.1).

Backscattered electrons are generated from the elastic collisions that occur between the primary electron beam and the sample. When the primary electrons are accelerated at the surface, they can be diffracted by the atomic layers in the material. This behavior enables the SEM to provide detailed information about the material's microstructure and is called electron backscatter diffraction (EBSD). Specifically, the diffracted electrons exit the sample and are detected by a phosphor screen within the SEM chamber which generates a projection of the lattice geometry via visible lines called Kikuchi bands.[52] These bands are then processed by the SEM software and a spatial "crystallographic map" is projected over the imaged area. To this end, EBSD was used to determine the crystallographic orientation of our polycrystalline bulk Ni-22wt.%Cr alloy surface (subsection 3.8.2).

3.8 Sample Preparation

3.8.1 Thin Film Deposition

Polished MgO(100) and MgO(111) single crystals are used as substrates for Ni-Cr thin film growth.[53] This approach allowed for the growth of alloy thin films with wide terraces and atomically flat surfaces. Before deposition, these MgO substrates are annealed and etched with acid to prepare the smoothest surface possible. First, the substrate is etched with 85% phosphoric acid for 30 s and then rinsed in two 30 s baths of deionized water to remove the residual acid. The substrate is then annealed in air in a box furnace at 1200 °C for 5 hr to remove defects and further smooth the surface. Following this step, Ca spires are usually found at the surface, which are removed with a second 30 s acid etch. The substrates are then annealed in air at 1000 °C for 8 hours. At this stage, AFM is used to check the surface morphology of the samples. If the surface does not appear smooth enough or if there are residual surface defects, a third anneal and/or acid etch is performed. After the MgO surface is comprised of wide terraces and monatomic steps, the substrate is mounted on a sample plate and is introduced into the UHV chamber for an overnight anneal at 200 °C to remove hydrocarbons and water. A more detailed explanation of the pretreatment is outlined in the following publication.[53]

The metallic thin films are then deposited on the MgO(100) and MgO(111) single crystal substrates by electron beam evaporation. Ni (Alfa Aesar 99.999% purity) and Cr (American Elements, 99.95% purity) were deposited using a Mantis EV mini e-beam quad-source. The deposition rates of Ni and Cr were measured using a quartz crystal monitor to accurately adjust the film composition. The deposition of the Ni(100), Ni−8wt.%Cr(100), Ni−12wt.%Cr(100), Ni−15wt.%Cr(100), Ni(111) and Ni−18wt.%Cr(111) thin films followed the procedure developed previously.[53] The composition of the Ni−Cr thin films was verified ex situ, after experimentation, by EDS with a Quanta LV650 SEM. Oxygen was introduced through a sapphire leak valve, and all oxidation experiments were performed at 500 °C to form a crystalline oxide layer. All Ni and Ni-Cr surfaces were imaged immediately after deposition, and then after each oxidation and annealing steps. STM experiments were concluded within 48 hours of sample preparation to avoid deleterious reactions on the sample surface.

3.8.2 Polycrystalline Bulk Sample Preparation

The polycrystalline Ni-11wt.%Cr, Ni-11wt.%Cr-6wt%Mo and Ni-22wt.%Cr samples used in this dissertation were fabricated at The University of Wisconsin, Madison by the Perepezko group. High purity Ni, Cr and Mo were arc-melted in an inert gas, where several melt-solidification steps were used to achieve homogeneity of the alloy components. The alloys were then cast and rolled to attain a uniform sample thickness. To obtain large grain sizes (100-1000 μm), the samples were further heat treated at UVA in air in a box furnace. The Ni-11wt.%Cr and Ni-11wt.%Cr-6wt%Mo samples were annealed at 1100 ^{o}C for 96 hr UVA, and the Ni-22wt.%Cr sample was annealed at 1150 ^{o}C for 150 hr. Both 11wt.%Cr samples were mechanically polished to 1 μm and metallographic indents were made to mark the area of interest for *in situ* electrochemical exposure and *ex situ* AFM analysis. The Ni-22wt.%Cr sample was polished to 0.1 μm, enabling the crystallographic mapping of the surface with EBSD.

3.9 Data Processing

3.9.1 Spectroscopy Data and MATLAB codes

Once a grid STS measurement is made (subsection 3.1.3), the files generated by the STM software MATRIX are formatted by Scienta Omicron's Vernissage software and then organized and exported as text files by WSxM.[54] The *.txt* files contain the X position, Y position, voltage and current of each point across the grid. The rows and columns of the *.txt* files are then formatted into spatial maps, reflecting the surface's local electronic structure, using a MATLAB code written by a previous Reinke group member, Dr. Ehsan Monazami. This code has been developed further to satisfy the needs of this dissertation, and the subsections 3.9.2 and 3.9.3 will discuss the approaches used to generate density of states (DOS), conduction band minimum (CBM), valence band maximum (VBM) and band gap maps.

3.9.2 DOS and Band gap maps

The data from the STS measurements are formatted into DOS and band gap maps using a MATLAB code, which organizes each *I(V)* curve into an array across a 2D color plane, matching them to the sample surface's X-Y position. The ordered spectra are then numerically differentiating by MATLAB to generate dI/dV curves. These were then normalized by I/V and expressed as (dI/dV)/(I/V) curves following the procedure described by Feenstra et al. (subsection 3.1.3).[15,16] Once normalized, the band gap of each curve is numerically determined by calculating the region where (dI/dV)/(I/V) is smaller than a threshold value, i.e. where the DOS is very close to zero. An example of this is shown in Figure 3-7(A). The (dI/dV)/(I/V) spectra and their corresponding band gap values are then displayed as spatially resolved DOS maps and band gap

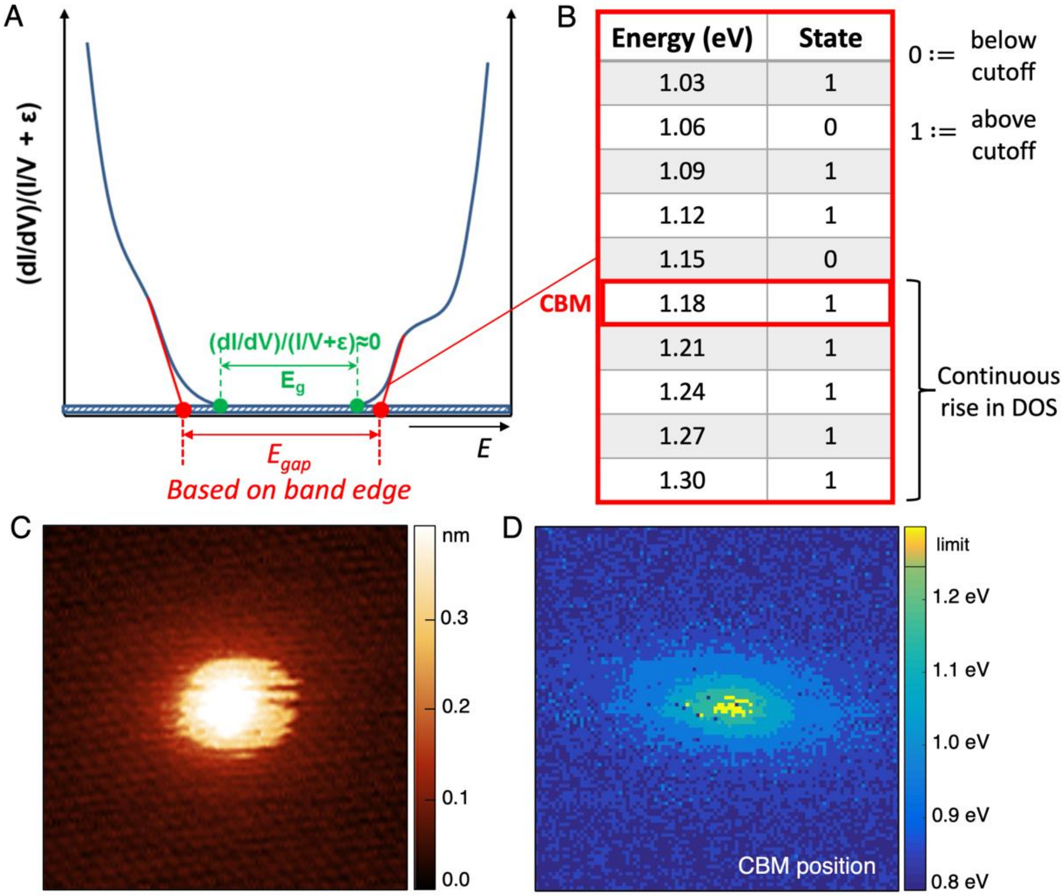

Figure 3-7. (A) Schematic representation of an STS curve and numerical determination of the band gap in the MATLAB code.[55] Two different methods were applied to calculate the band gap, the conduction band minimum (CBM) and valence band maximum (VBM). The threshold value used to determine DOS = 0 was chosen to best reflect the tangent method, outlined with the red markers in (A). The numerical representation an STS curve and the scheme used to determine the CBM and VBM values is highlighted in (B). These values are then spatially mapped to reflect the topography images as shown in (C) and (D). The topography (V_{bias} = -1.0 V, I_t = 100 pA) and the corresponding maps are each 8×8 nm^2.

maps, respectively, which allows for a direct comparison between topography and electronic structure. An example of one of these maps and accompanying topography images can be seen in Figure 3-7(C)-(D) and was taken from a defective WSe_2 surface after annealing.[56]

3.9.3 Conduction and Valence band maps

Additional routines have been developed to extract the conduction band minimum (CBM) and valence band maximum (VBM) values from the spectroscopy maps. After the *I(V)* spectra are differentiated and normalized, a threshold cutoff value is used to determine if a tunneling current can or cannot be reliably measured for each spectrum, i.e. is the DOS greater than or less than zero. Boolean logic is then used to assign 1's where the DOS is greater than the cutoff or 0's to where it is less than. The Boolean array is then paired with the corresponding energy values of the spectrum and a subroutine is used to define a "consistent rise" in tunneling current, i.e. when the current is continuously > 0, which marks the band edge in the DOS. This subroutine was chosen to mitigate the impact of noise or random fluctuations in current that can sometimes occur around the band edges.

The results of this step are then manually compared with the characteristics of the spectra, where a tangent method is used as a "sanity check" to determine the band edges. A cutoff value is then chosen to match the edges of the bands determined by the tangent method, Figure 3-7(A). The band edges now defined, the minimum value of the conduction array and the maximum value of the valence array are then selected by the code, Figure 3-7(B). The CBM and VBM values can also be spatially resolved across the STS grid, allowing for the construction of CBM and VBM maps. Additional subroutines were also implemented into this code to mark and remove spectra that showed no consistent rise in DOS, i.e. noisy spectra or spectra that deviated within the detection limit of our instrument.

3.9.4 Topographical Data Processing using Gwyddion and MATLAB

Prior to display and analysis of the STM and AFM topography images, each surface was leveled by mean plane subtraction and planarization. The use of these corrections is illustrated in the Figure 3-8(A), and only values not skewed by image processing are used in the subsequent analysis of step heights and other geometric features. The plots in Figure 3-8(B) show an example of the different correction methods in Gwyddion used to establish the most appropriate measure of apparent step height between the 1st layer and NiO (Chapter IV). To improve the overall visual quality of the images and accuracy of the measurements, the reported values in this dissertation were taken after plane leveling and feature matching were employed (as marked by the level and match line in Figure 3-8). For the plane leveling: points used for leveling are identified on the image, a plane between points is generated and subtracted from the all the data. This is effectively

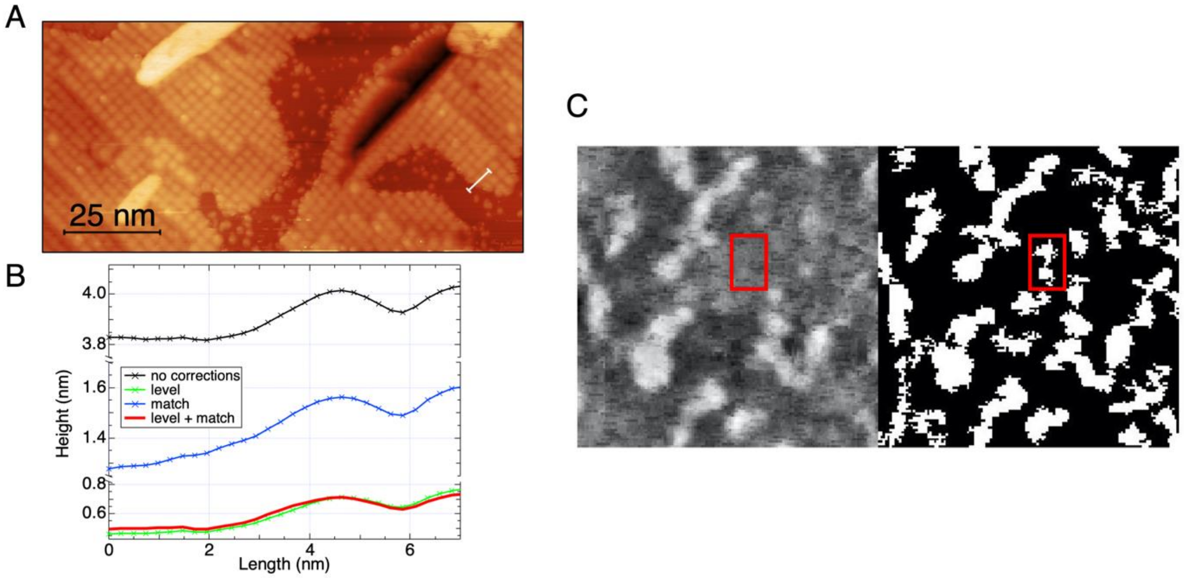

Figure 3-8. (A) STM topography of an oxidized Ni-12%Cr(100) sample and (B) the measured step height of 1st - Layer-NiO at -3.0 V and 0.1 nA, where the different image processing features are highlighted. (C) An example of the segmented oxide island data taken from an electrochemically exposed Ni22%Cr surface. Conditions for the marking code were based on what yielded the most consistent data for a particular image set. Points, indicated by the red box, that were not representative of the images were manually removed.

used to balance and equalize the corners of the image. For the feature matching: A representative height for each scan line (along the horizontal direction) is found and is subtracted from the background. As seen by the line profiles, no significant changes in the apparent step heights were observed after processing. Significant deviations where observed if line scans were taken over large portions of the image, but as shown above smaller and more localized scans were used in the collection of data.

A MATLAB code implementing routines for grey-scale segmentation was also used to analyze some of the surface features and is highlighted in Figure 3-8(C). The images shown in the aforementioned figure are of an electrochemically corroded Ni-Cr sample surface measured with AFM (Chapter VIII). Consistent masking procedures were used and any obvious over or under estimation of an oxide area was removed from the data set. The images in Figure 3-8(C) represent the greyscale segmentation process that was applied to an AFM image to obtain the area coverage of the oxide. The segmentation was done via the total image height, darker pixels representing the local minimum height and lighter pixels the local maximum height. To best match the topography of the line scans a cutoff was used to define the islands. This value was used to best match the true apparent height of the surface features with the segmented areas determined by the code.

3.10 Chapter III References

(1) Kirchhofer, N. Using Ambient STM on your Atomic Force Microscope https://afm.oxinst.com/learning/view/article/using-ambient-stm-on-your-atomic-force-microscope (accessed Nov 25, 2020).

(2) Binnig, G.; Rohrer, H. Scanning Tunneling Microscopy. *Surf. Sci.* **1983**, *126* (1), 236–244. https://doi.org/10.1016/0039-6028(83)90716-1.

(3) Tersoff, J.; Hamann, D. R. Theory of the Scanning Tunneling Microscope. *Phys. Rev. B* **1985**, *31* (2), 805–813. https://doi.org/10.1103/PhysRevB.31.805.

(4) Feenstra, R. M.; Stroscio, J. A.; Fein, A. P. Tunneling Spectroscopy of the Si(111)2 × 1 Surface. *Surf. Sci.* **1987**, *181* (1), 295–306. https://doi.org/10.1016/0039-6028(87)90170-1.

(5) Bardeen, J. Tunnelling from a Many-Particle Point of View. *Phys. Rev. Lett.* **1961**, *6* (2), 57–59. https://doi.org/10.1103/PhysRevLett.6.57.

(6) Oppenheimer, J. R. Three Notes on the Quantum Theory of Aperiodic Effects. *Phys. Rev.* **1928**, *31* (1), 66–81. https://doi.org/10.1103/PhysRev.31.66.

(7) Meyer, E.; Hug, H. J.; Bennewitz, R. *Scanning Probe Microscopy: The Lab on a Tip*; Physics and Anstronomy; Springer, 2004.

(8) Duke, C. B. *Tunneling in Solids*; Solid state physics; Academic Press: New York, 1969.

(9) Gottlieb, A. D.; Wesoloski, L. Bardeen's Tunnelling Theory as Applied to Scanning Tunnelling Microscopy: A Technical Guide to the Traditional Interpretation. *Nanotechnology* **2006**, *17* (8), R57–R65. https://doi.org/10.1088/0957-4484/17/8/R01.

(10) Tersoff, J.; Hamann, D. R. Theory and Application for the Scanning Tunneling Microscope. *Phys. Rev. Lett.* **1983**, *50* (25), 1998–2001. https://doi.org/10.1103/PhysRevLett.50.1998.

(11) Nicol, J.; Shapiro, S.; Smith, P. H. Direct Measurement of the Superconducting Energy Gap. *Phys. Rev. Lett.* **1960**, *5* (10), 461–464. https://doi.org/10.1103/PhysRevLett.5.461.

(12) Giaever, I. Electron Tunneling Between Two Superconductors. *Phys. Rev. Lett.* **1960**, *5* (10), 464–466. https://doi.org/10.1103/PhysRevLett.5.464.

(13) Wortmann, D. Interpretation of Scanning Tunneling Microscopy and Spectroscopy of Magnetic Metal Surfaces by Electron Theory, TU Dortmund University, Dortmund, Germany, 2000.

(14) Chen, C. J. Tunneling Matrix Elements in Three-Dimensional Space: The Derivative Rule and the Sum Rule. *Phys. Rev. B* **1990**, *42* (14), 8841–8857. https://doi.org/10.1103/PhysRevB.42.8841.

(15) Feenstra, R. M. Tunneling Spectroscopy of the (110) Surface of Direct-Gap III-V Semiconductors. *Phys. Rev. B* **1994**, *50* (7), 4561–4570. https://doi.org/10.1103/PhysRevB.50.4561.

(16) Feenstra, R. M.; Stroscio, J. A.; Fein, A. P. Tunneling Spectroscopy of the Si(111)2 × 1 Surface. *Surf. Sci.* **1987**, *181* (1), 295–306. https://doi.org/10.1016/0039-6028(87)90170-1.

(17) Binnig, G.; Quate, C. F.; Gerber, Ch. Atomic Force Microscope. *Phys. Rev. Lett.* **1986**, *56* (9), 930–933. https://doi.org/10.1103/PhysRevLett.56.930.

(18) Jalili, N.; Laxminarayana, K. A Review of Atomic Force Microscopy Imaging Systems: Application to Molecular Metrology and Biological Sciences. *Mechatronics* **2004**, *14* (8), 907–945. https://doi.org/10.1016/j.mechatronics.2004.04.005.

(19) Zhang, H.; Huang, J.; Wang, Y.; Liu, R.; Huai, X.; Jiang, J.; Anfuso, C. Atomic Force Microscopy for Two-Dimensional Materials: A Tutorial Review. *Opt. Commun.* **2018**, *406*, 3–17. https://doi.org/10.1016/j.optcom.2017.05.015.

(20) Atomic Force Microscopy. *Wikipedia*; 2020.

(21) Asmatulu, R.; Khan, W. S. Chapter 13 - Characterization of Electrospun Nanofibers. In *Synthesis and Applications of Electrospun Nanofibers*; Asmatulu, R., Khan, W. S., Eds.; Micro and Nano Technologies; Elsevier, 2019; pp 257–281. https://doi.org/10.1016/B978-0-12-813914-1.00013-4.

(22) Nečas, D.; Klapetek, P. Gwyddion: An Open-Source Software for SPM Data Analysis. *Open Phys.* **2011**, *10* (1), 181–188. https://doi.org/10.2478/s11534-011-0096-2.

(23) Einstein, A. On a Heuristic Point of View about the Creation and Conversion of Light]. *Ann. Phys.* **1905**, *322* (6), 132–148.

(24) Planck, M. On the Law of Distribution of Energy in the Normal Spectrum. *Ann. Phys.* **1901**, *4*, 553–563.

(25) Siegbahn, K.; Nordling, C.; Fahlman, A.; Nordberg, R.; Hamrin, K.; Hedman, J.; Johansson, G.; Bergmark, T.; Karlsson, S.-E.; Lindgren, I.; Lindberg, B. *ESCA: Atomic, Molecular and Solid State Structure by Mans of Electron Spectroscopy*; Nova acta Regiae Societatis scientiarum Upsaliensis; Almqvist snd Wiksells: Uppsala, Sweden, 1967; Vol. 20.

(26) Spicer, W. E. Photoemissive, Photoconductive, and Optical Absorption Studies of Alkali-Antimony Compounds. *Phys. Rev.* **1958**, *112* (1), 114–122. https://doi.org/10.1103/PhysRev.112.114.

(27) Diplas, S. X-Ray Photoelectron Spectroscopy - An Introduction. California Institute of Technology March 6, 2013.

(28) Paynter, R. XPS Theory. California Institute of Technology.

(29) Yano, J.; Yachandra, V. K. X-Ray Absorption Spectroscopy. *Photosynth. Res.* **2009**, *102* (2), 241. https://doi.org/10.1007/s11120-009-9473-8.

(30) Filipponi, A.; Di Cicco, A.; Natoli, C. R. X-Ray-Absorption Spectroscopy and n-Body Distribution Functions in Condensed Matter. I. Theory. *Phys. Rev. B* **1995**, *52* (21), 15122–15134. https://doi.org/10.1103/PhysRevB.52.15122.

(31) Fonda, L. Multiple-Scattering Theory of X-Ray Absorption: A Review. *J. Phys. Condens. Matter* **1992**, *4* (43), 8269–8302. https://doi.org/10.1088/0953-8984/4/43/004.

(32) XAS - Theory https://chem.libretexts.org/Bookshelves/Physical_and_Theoretical_Chemistry_Textbook_Maps/Supplemental_Modules_(Physical_and_Theoretical_Chemistry)/Spectroscopy/X-ray_Spectroscopy/XAS_-_Theory (accessed Oct 7, 2020).

(33) Casu, M. B.; Chassé, T. NEXAFS Studies at Surfaces. In *Handbook of Spectroscopy*; John Wiley & Sons, Ltd, 2014; pp 1485–1506. https://doi.org/10.1002/9783527654703.ch43.

(34) Ravel, B. Introduction to X-Ray Absorption Spectroscopy, 2015.

(35) Ascone, I. X-Ray Absoprtion Spectroscopy for Beginners, 2011.

(36) Rehr, J. J. Theory and Calculations of X-Ray Spectra: XAS, XES, XRS, and NRIXS. *Radiat. Phys. Chem.* **2006**, *75* (11), 1547–1558. https://doi.org/10.1016/j.radphyschem.2005.11.014.

(37) Rehr, J. J.; Ankudinov, A. L. Progress in the Theory and Interpretation of XANES. *Coord. Chem. Rev.* **2005**, *249* (1), 131–140. https://doi.org/10.1016/j.ccr.2004.02.014.

(38) Zakharov, A. A.; A.Mikkelsen; Andersen, J. N. Recent Advances in Imaging of Properties and Growth of Low Dimensional Structures for Photonics and Electronics by XPEEM. *J. Electron Spectrosc. Relat. Phenom.* **2012**, *185* (10), 417–428. https://doi.org/10.1016/j.elspec.2012.03.002.

(39) Locatelli, A.; Aballe, L.; Mentes, T. O.; Kiskinova, M.; Bauer, E. Photoemission Electron Microscopy with Chemical Sensitivity: SPELEEM Methods and Applications. *Surf. Interface Anal.* **2006**, *38* (12–13), 1554–1557. https://doi.org/10.1002/sia.2424.

(40) MAXPEEM Techniques https://www.maxiv.lu.se/accelerators-beamlines/beamlines/maxpeem/techniques/.

(41) Davisson, C. J.; Germer, L. H. Reflection of Electrons by a Crystal of Nickel. *Proc. Natl. Acad. Sci. U. S. A.* **1928**, *14* (4), 317–322.

(42) Hohenberg, P.; Kohn, W. Inhomogeneous Electron Gas. *Phys. Rev.* **1964**, *136* (3B), B864–B871. https://doi.org/10.1103/PhysRev.136.B864.

(43) Kohn, W.; Sham, L. J. Self-Consistent Equations Including Exchange and Correlation Effects. *Phys. Rev.* **1965**, *140* (4A), A1133–A1138. https://doi.org/10.1103/PhysRev.140.A1133.

(44) Scholl, D.; Steckel, J. A. *Density Functional Theory: A Practical Introduction*.

(45) Capelle, K. A Bird's-Eye View of Density-Functional Theory. *ArXivcond-Mat0211443* **2002**.

(46) Born, M.; Oppenheimer, R. Zur Quantentheorie Der Molekeln. *Ann. Phys.* **1927**, *389*, 457–484. https://doi.org/10.1002/andp.19273892002.

(47) Born, M.; Huang, K. *Dynamical Theory of Crystal Lattices*; Oxford classic texts in the physical sciences; Clarendon Press: Oxford, 1954.

(48) Hartree, D. R. The Wave Mechanics of an Atom with a Non-Coulomb Central Field. Part I. Theory and Methods. *Math. Proc. Camb. Philos. Soc.* **1928**, *24* (1), 89–110. https://doi.org/10.1017/S0305004100011919.

(49) Fock, V. „Selfconsistent field" mit Austausch für Natrium. *Z. Für Phys.* **1930**, *62* (11), 795–805. https://doi.org/10.1007/BF01330439.

(50) Amusia, M. Y.; Msezane, A. Z.; Shaginyan, V. R. Density Functional Theory versus the Hartree–Fock Method: Comparative Assessment. *Phys. Scr.* **2003**, *68* (6), C133. https://doi.org/10.1238/Physica.Regular.068aC0133.

(51) Lutton, K.; Gusieva, K.; Ott, N.; Birbilis, N.; Scully, J. R. Understanding Multi-Element Alloy Passivation in Acidic Solutions Using Operando Methods. *Electrochem. Commun.* **2017**, *80*, 44–47. https://doi.org/10.1016/j.elecom.2017.05.015.

(52) Swapp, S. Electron Backscatter Diffraction (EBSD) https://serc.carleton.edu/research_education/geochemsheets/ebsd.html (accessed Sep 22, 2020).

(53) Ramalingam, G.; Reinke, P. Growth of Ni and Ni-Cr Alloy Thin Films on MgO(001): Effect of Alloy Composition on Surface Morphology. *J. Appl. Phys.* **2016**, *120* (22), 225302. https://doi.org/10.1063/1.4971261.

(54) Horcas, I.; Fernández, R.; Gómez-Rodríguez, J. M.; Colchero, J.; Gómez-Herrero, J.; Baro, A. M. WSXM: A Software for Scanning Probe Microscopy and a Tool for Nanotechnology. *Rev. Sci. Instrum.* **2007**, *78* (1), 013705. https://doi.org/10.1063/1.2432410.

(55) Ramalingam, G. Investigation of Semiconductor and Metal-Metal Oxide Surface Nanostructures by Scanning Tunneling Microscopy/Spectroscopy, University of Virginia, 2016.
(56) Blades, W. H.; Frady, N. J.; Litwin, P. M.; McDonnell, S. J.; Reinke, P. Thermally Induced Defects on WSe2. *J. Phys. Chem. C* **2020**, *124* (28), 15337–15346. https://doi.org/10.1021/acs.jpcc.0c04440.

Chapter IV: Understanding the Early Stages of Oxidation on Ni-Cr(100) Alloys Surfaces

4.1 Technical Background

The complex processes that govern the reactions of molecular oxygen and corrosive solutions with transition metal alloys are of high technical relevance and have garnered significant interest for many decades.[1–9] The economic cost of materials breakdown due to corrosion and oxidation is staggering, and hence corrosion resistance is an important design parameter for technical alloys. The study of corrosion processes, including dry as well as aqueous corrosion reactions, is motivated by the need to reduce the overall economic burden incurred by materials degradation. A large body of work exists on performance, passivation and break-down of the oxide layers, but attention has turned only recently to the initial steps in alloy oxidation and, most importantly, formation of the alloy-oxide interface.[1,7,9–11] These initial reactions bias the continued growth of the protective oxide scale and therefore critically influence its passivity and performance. A mechanistic understanding of initial reactions steps and the formation of the alloy-oxide interface is therefore indispensable to future alloy design.

The initial reaction steps are complex, and synergistic interactions between the alloying elements and oxygen are at the heart of understanding the alloy-to-oxide transformation. Our work targets Ni-Cr alloys, which possess excellent mechanical properties and high degree of corrosion resistance, and have practical application in an array of industrial and military systems. The structure and composition of the oxide layer, which includes Ni and Cr-oxides, is highly sensitive to composition, temperature, and crystallographic orientation.[12] A deeper understanding of the relationship between initial oxide formation, oxide growth and properties, is therefore important to engineer passive layers and future alloys.

To study the subtleties that govern the initial nucleation and growth of surface oxides Scanning Tunneling Microscopy/Spectroscopy (STM/STS) is employed to gain insight into the evolution of oxide layers on Ni(100) and Ni-Cr(100) thin-film surfaces as they are exposed to O_2.[1,2] The work presented in this manuscript covers temperatures of 500 ºC and 600 ºC where the competition between Ni- and Cr-oxide formation is significant, and high-quality extended crystalline layers and interfaces are formed. In contrast, recent work modeled the oxidation of Ni-Cr(100) at 300 ºC, a relatively low temperature where Cr-supply from the bulk is severely limited, and short range surface diffusion controls oxidation.[11]

Cabrera-Mott and Wagner's theory are models that are frequently used as the basis to describe the growth of oxide layers, and are suitable to understand the growth kinetics of oxide layers across different length scales.[1,16–18] Cabrera-Mott theory is applied to describe the growth kinetics of oxide layers that range from about 1 - 10 nm in thickness. The growth of the oxide film is dominated by ion transport through the layer, which is driven by the electric field between the oxide-metal and gas phase/adsorbate-oxide interfaces. This interaction controls oxide growth until a limiting thickness is reached and the electric field is diminished.[1,16,18] Once the oxide reaches this limiting thickness Wagner's theory, which assumes a net charge neutral diffusion of ions and a field arising via ambipolar diffusion through the oxide, is suited to understand the growth rate.[19] Both of these models assume that film growth is planar and homogenous across the surface, however the initial stages of growth before a complete oxide layer is formed are not fully understood. To this end, the present study specifically considers the transition from alloy to oxide during a growth regime prior to the Cabrera-Mott regime tentatively termed the “pre-Cabrera-Mott regime”, by capturing the initial stages of Ni(100) and Ni-Cr(100) thin-film oxidation. Our report aims to gain a better understanding of the oxidation pathways for Ni(100), Ni-8wt.%Cr(100), and Ni-12wt.%Cr(100) at temperatures of 500-600 ºC, and the formation of the alloy-oxide interface.

The oxidation of Ni-Cr alloys is governed by the competing formation of NiO, Cr_2O_3, and mixed oxides such as $NiCr_2O_4$. Temperature, alloy composition, crystallographic orientation, and partial pressure of oxygen all influence the reaction pathways and consequently the oxide products.[1,6,7,20–25] In general, the oxidation of Ni-Cr below 700 ºC, and for alloys with less than 20wt.% Cr begins with the formation of NiO, which is generally attributed to the lower activation barrier for nucleation on a cube-on-cube epitaxy for the rock-salt structure. NiO therefore dominates the initial oxide layer and Cr_2O_3 subsequently forms at the alloy-oxide interface by internal oxidation. [1–3,26] A consequence of this reaction sequence is a layered oxide structure. A limited supply of Cr in the Cr-poorer alloys impedes the formation of a continuous Cr_2O_3 layer thus diminishing the oxide’s protective function.

In this work we use Ni(100) and Ni-Cr(100) alloy surfaces as model systems. The oxidation of Ni(100) itself is a rather peculiar process: dissociative chemisorption of O_2 leads to the formation of p(2 ×2)O and then c(2 ×2)O reconstructions which are followed at room temperature by the nucleation of oxide at the step edges.[27–31] However, at elevated temperatures the formation of NiO is delayed and increasingly large oxygen exposures are required for its nucleation. Following the work by Kopatzki et al.[27] the incubation period can be attributed to the loss of preferential nucleation sites at the step edges due to faceting into {100} segments, which is driven by the reconstruction and achieved by the increased ad-atom mobility at higher temperatures. The

NiO nucleation on Ni(100) relies on the availability of step edge nucleation sites, while nucleation on the terrace is suppressed. As a consequence, the Ni(100) surface requires relatively large doses of O_2 to initiate oxide formation.[27–29,32]

The oxidation of Cr(100) progresses via a Cr(100)–c(2×4)O chemisorbed structure followed by the formation of Cr_2O_3 when the Cr surface is oxidized and subsequently annealed.[33–37] Oxidation of Cr(100) at room temperature starts with the formation of p(1×1)O ad-layers, where the O-atoms are incorporated into in the four fold-site on the Cr(100) bcc lattice. This ad-layer is accompanied by small domains of a $(\sqrt{5}\times\sqrt{5})R27°$ sub-surface vacancy structure showing at most short range ordering of vacancies and not the long-range ordering of missing row reconstructions.[37] The p(1×1)O surface is structurally identical to a single layer of CrO, a surface stabilized oxide with NaCl structure where the O-atoms are fully integrated in the top metal layer. It is still unclear how the transformation from the CrO layer into the Cr_2O_3 oxide is achieved at the atomic scale. In contrast, Cr-atoms in Ni-Cr are embedded in an fcc bonding environment further complicating comparisons to the pure elements. The different reaction pathways between Ni(100) and Cr(100) surfaces raises the expectation that alloying results in a unique oxidation process that differs from the pure metals.

In a recent study we followed the initial steps in the oxidation of a Ni-5wt.%Cr(100) thin film at temperatures of 300 ^{o}C, which is in the regime of very limited bulk Cr-diffusivity.[11] This is a relatively low temperature for Ni-Cr oxidation and, in contrast to the present study performed at 500 ^{o}C and 600 ^{o}C, did not yield a high-quality crystalline oxide layer. The oxide islands grew to a critical height, propagated laterally and eventually formed a near complete oxide layer. The initial growth of the surface oxide islands was shown to be controlled by short-range oxygen diffusion and was modeled using a screening length of only a few nanometers, which suggests that growth and coalescence are localized to the edge of the oxide island.

The work presented here focuses on the comparison between Ni(100), Ni-8wt.%Cr(100), and Ni-12wt.%Cr(100) oxidation at 500 ºC using Ni-Cr(100) thin films grown under ultra-high vacuum conditions on MgO(100).[38] These alloy compositions and oxidation conditions favor NiO formation, and enable us to isolate the impact of Cr on the surface reactions within the pre-Cabrera-Mott regime. The evolution of surface oxides, and the alloy–oxide interface is measured using STM and STS, which deliver the geometric and electronic structure of the surface. We present a detailed analysis of the NiO-alloy interface, the evolution of surface oxides on Ni-Cr(100), and use STS to capture local variations in electronic structure and doping. The oxidation of this binary alloy relies on the intricate interplay between the chemistry of two highly reactive elements. The study of unique and often synergistic reaction pathways, as well as the geometric and electronic properties of ultra-thin oxides and interfaces will contribute to understanding how to improve the quality of passive layers on alloy surfaces.

4.2 Methods

The oxidation experiments were conducted under Ultra-High Vacuum (UHV) conditions using an Omicron Nanotechnology Variable Temperature Scanning Probe Microscopy (VT-SPM) system. A tungsten tip was prepared electrochemically and used for all experiments discussed herein. The base pressure was 2.5×10^{-10} mbar and imaging was done at ambient temperature. All metal thin films were deposited on MgO(100) single crystal substrates that had undergone pretreatment outlined in the following reference.[38] Ni (Alfa Aesar 99.999% purity) and Cr

(American Elements, 99.95% purity) were deposited on these MgO(100) substrates by electron beam evaporation using a Mantis EV mini e-beam quad-source. The deposition rates of Ni and Cr were measured using a quartz crystal monitor to accurately adjust the film composition. The deposition of Ni and Ni-Cr thin films followed the procedure developed previously.[38] The Ni-8wt.%Cr(100) and Ni-12wt.%Cr(100) alloys were deposited at a substrate temperature of 400 ºC. The composition of the Ni-Cr thin films was verified ex-situ, after experimentation, by energy dispersive spectroscopy (EDS) with a Quanta LV650 Scanning Electron Microscope (SEM). Oxygen was introduced through a sapphire leak valve, and all oxidation experiments were performed at 500 ºC to form a crystalline oxide layer. The Ni(100) and Ni-Cr(100) surfaces were imaged immediately after deposition, and then after all oxidation and annealing steps as summarized in Table 1. STM and STS were employed to gain insight into the surface topography and local density of states (LDOS) for all deposition and reaction steps. The spectra were recorded by measuring an I/V curve for every third image pixel with an open feedback loop, while topography information was recorded for the next two image pixels with a closed feedback loop set to a tunneling current of 0.1 nA and a bias voltage of 3.0 V. A voltage range of ±3.0 V was used for the STS spectra.

The data from the STS measurements were formatted into Density of State and Bandgap Maps using a MATLAB code. This was accomplished by numerically differentiating the I/V curves to generate dI/dV curves. These were then normalized by I/V and expressed as (dI/dV)/(I/V) curves following the procedure described by Feenstra et al..[39,40] Once normalized, the bandgap of each curve was numerically determined by calculating the region where (dI/dV)/(I/V) is smaller then a threshold value, i.e. where the DOS is very close to zero. This approach was particularly well suited for the analysis of a large number of data points. The distributions of valence/conduction band extrema and bandgap values were generated from these data. The tangent method for determining the bandgap, which takes into account variations in DOS slope at the band edges, was used when a smaller number of data points was considered and is illustrated in the Supporting Information 4-S1. The differences between the two methods were generally very small in this materials system, and confirmed the correct use of a threshold value for large data sets. The (dI/dV)/(I/V) spectra were then displayed as spatially resolved DOS and Bandgap maps, respectively, which allows for a direct comparison between topography and electronic structure. Prior to display and analysis of the topography images, each surface was leveled by mean plane subtraction and planarization. The use of these corrections is illustrated in the Supporting Information 4-S2, and only values not skewed by image processing are used in the subsequent analysis of step heights and other geometric features.

4.3 Results

4.3.1 Ni(100) vs Ni-Cr(100) at 500 ^{o}C

Figure 4-1 provides a comparison between the oxidation of Ni(100) and Ni-8wt.%Cr(100) surfaces to illustrate the impact of alloying on the oxidation process. Figure 4-1(A) shows the as-deposited Ni(100) thin film, which has wide terraces with curved step edges consistent with previous reports in literature.[36] The first oxidation step Figure 4-1(B) initiated a surface reconstruction and the steps faceted into parallel {100} segments. The step edge faceting can be attributed to the dissociative chemisorption of O_2 and formation of a c(2×2)O reconstruction on the Ni(100) surface.[27] Pure Ni(100) at very low exposures adopts the p(2×2)O reconstruction with

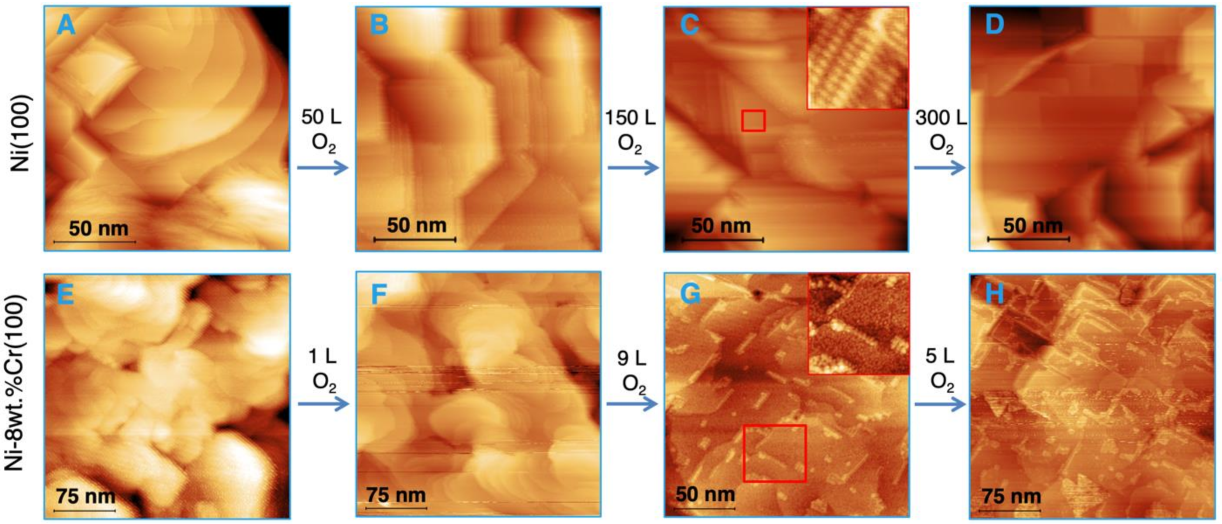

Figure 4-1. Topography images showing the progression of oxidation for Ni(100) (A-D), and Ni-8wt.%Cr(100) (E-H). The oxidation and annealing steps are indicated in the Figure, and summarized in Table 1. The image insets in C and G are 14×14 nm^2 and 50×50 nm^2, respectively. The oxidation steps were all performed at 500 ºC, and imaging conditions are U_{bias}= 2.0 V and I_t= 0.1 nA for all images in this series, except A, E, and F which were taken at U_{bias}= 0.15 V and I_t= 0.5 nA.

O atoms positioned in the 4-fold hollow sites, and with increasing exposure the center hollow site becomes occupied to form the c(2×2)O structure. The inset in Figure 4-1(C) shows a high-resolution image of the facet which is commensurate with the c(2×2)O reconstruction. An average spacing of 0.44 ± 0.05 nm separates the rows in the image inset confirming the c(2×2)O unit cell.

Reconstruction-induced step faceting removes reactive kink sites causing the surface to become nearly inert against oxide formation, which has been demonstrated in previous studies.[27] Indeed, no oxide islands are seen in Figures 4-1(C) and (D) even after a 300 L exposure of O_2 and is in stark contrast to the rapid development of oxide on the Ni-Cr alloys. According to the literature an oxygen exposure of at least 1000 L is required to grow NiO at elevated temperatures on Ni(100) surfaces.[28] The activation barrier for oxide nucleation increases significantly on faceted terrace edges compared to step edges with kink sites. The c(2×2)O reconstruction induced step edge faceting is held responsible for the extended induction period towards oxide formation.[27] Our observations of the Ni(100) thin film surfaces are in agreement with the literature, and the behavior of single crystal surfaces.[27,28,30]

4.3.2 Trends in the oxidation of Ni-Cr(100) surfaces

Four dominant types of surface features are observed on the alloy surfaces during oxidation and annealing and their relative abundance is determined by alloy composition, oxygen exposure, and temperature. The parameter space covered in the present manuscript is summarized in Table 1. Some features can be uniquely attributed to a specific oxide due to characteristic structural or

Alloy Composition	**Oxidation E_n** **Annealing A_n**	**T [ºC]**	**$p(O_2)$ [mbar]**	**Cumulative Exposure [L] (individual exposure step)**
i. Ni (100)	E_1	500 ºC	2.0×10^{-8} mbar	50 L (+50 L)
	E_2		6.0×10^{-8} mbar	200 L (+150 L)
	E_3		9.0×10^{-8} mbar	500 L (+300 L)
ii. Ni-8wt.%Cr	E_1	500 ºC	2.0×10^{-9} mbar	1 L
	E_2		1.0×10^{-8} mbar	10 L (+9 L)
	E_3		5.9×10^{-9} mbar	15 L (+5 L)
iii. Ni-12wt.%Cr	E_1	500 ºC	8.6×10^{-9} mbar	7 L (+7 L)
	A_1	600 ºC	-	annealed 1800s
	E_2	500 ºC	8.6×10^{-9} mbar	14 L (+7 L)
	A_2	500 ºC	-	annealed 1320 s
	A_3	600 ºC	-	annealed 1320 s
	A_4	600 ºC		annealed 5400 s

Table 1: Summary of oxidation and annealing steps for all alloys. All experiment and processing steps for a given alloy were completed within 24 hours of alloy deposition.

electronic signatures, while details of novel reconstructions are observed but not yet fully understood. The surface features in question are as follows:

1. NiO in a NiO-NiCr$(6\times7)_{terrace}$ or NiO-NiCr$(7\times8)_{step}$ coincidence lattices, which are seen in the STM images as moiré patterns, and appear on the terraces and at step edges, respectively. At higher oxygen exposure NiO extends far onto the terrace, and is observed on Ni-8wt.%Cr(100) and Ni-12wt.%Cr(100), and has also been reported for Ni(100) albeit at much higher oxygen exposures.[28]
2. Nanoscale oxide clusters tend to form early in the oxidation process and are located on the terraces.
3. Several different oxygen-induced reconstructions on the alloy surface and are distinct from any reconstructions reported for the pure metal surfaces.
4. Oxide nodules, which are several nanometers in width and length, and differ structurally and electronically from the surrounding NiO. The nodules have a relatively large apparent height that is highly dependent on bias voltage. The nodules are tentatively assigned to either Cr_2O_3 or spinel $NiCr_2O_4$ and are only observed on the Ni-12wt.%Cr(100) alloy surface at later oxidation and annealing steps.

The Ni(100) surface reaction is compared to Ni-8wt.%Cr(100) oxidation shown in Figure 4-1(E-H), which illustrates the impact of dilute amounts of Cr-alloying on oxidation. The pristine alloy surfaces consist of relatively large terraces up to several 10 nanometers in width, and step edges with an average apparent height of 0.17 nm ± 0.01 – half the unit cell height of Ni (a_{Ni}=0.35 nm). The modulation of surface morphology as a function of alloy composition is addressed in a previous publication.[38] The introduction of a small amount of oxygen, 1 L at 500 ºC, did not induce an observable reaction, while a cumulative exposure of 10 L (1 L +9 L) in a 2nd oxidation step initiated the formation of oxide islands and nanoscale clusters (Figure 4-1(G)). The oxide population is bimodal and consists of small clusters on the terraces and extended oxide segments along the step edges. The step edge oxide is NiO, which forms a coincidence lattice due to the lattice mismatch between Ni and NiO and is expressed as a characteristic moiré pattern in the STM images. The coincidence lattice is discussed in detail later in this manuscript. During the 3rd oxidation step depicted in Figure 4-1(H) the majority of the alloy step edges are decorated with oxide (NiO) and display faceting, which is consistent with the highly anisotropic surface free energy of oxides.[27,41] The oxide-induced step edge faceting is reminiscent of the reconstruction-induced faceting for Ni(100). The general evolution of surface features and oxides follows the same trend for the Ni-8wt.%Cr(100) and Ni-12wt.%Cr(100) alloys, although the oxidation is more rapid for the Ni-12wt.%Cr(100) alloy – especially the formation of NiO advances at a faster pace for the same oxygen exposure which is discussed in detail in the next paragraph. The preferential formation of NiO over Cr_2O_3 is in agreement with the work of Luo et al., who documented NiO

4.3.3 Oxidation of a Ni-12Cr(100) surface: The Ni oxidation pathway

The Ni-12wt.%Cr(100) alloy was oxidized and annealed in several sequential reaction steps as illustrated in Figure 4-2 and summarized in Table 4-1. Figure 4-2(A) shows the surface prior to oxidation.[38] The first oxidation step (Figure 4-2(B)) corresponds to reaction step E_1 as defined in Table 1, and leads to step edge decoration with NiO, and formation of an abundance of nanoscale clusters on the terraces. This reaction sequence is very similar to the Ni-8wt.%Cr(100) surface, and differs only in the amount of NiO. NiO starts to grow into the flat terrace as the oxygen exposure is increased. Line scans of the oxide on the terrace reveal an average spacing of the maxima of 2.50 ± 0.02 nm commensurate with the NiO-Ni(6×7) coincidence lattice along the [100]

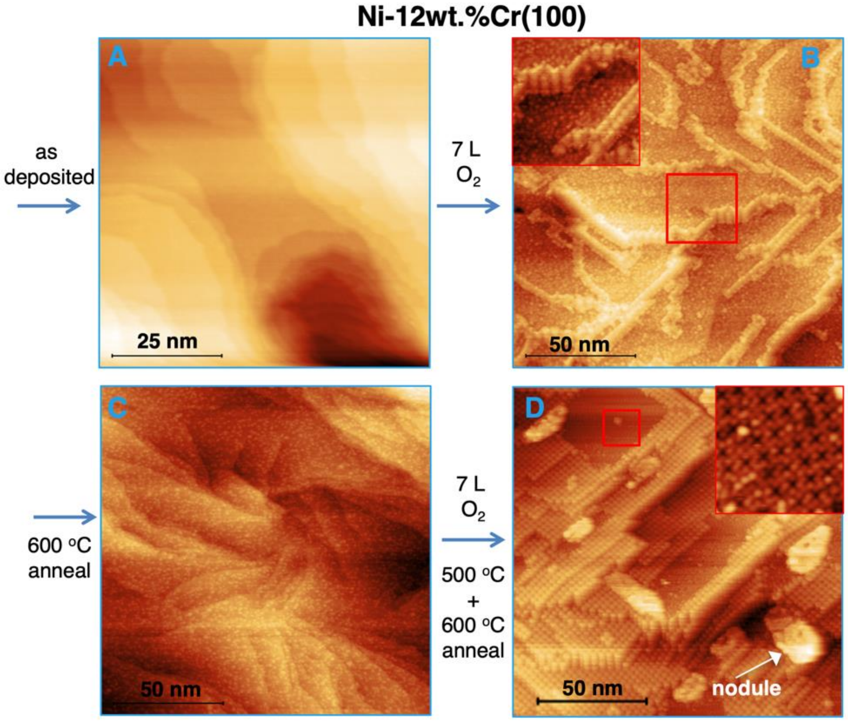

Figure 4-2. STM images captured for Ni-12wt.%Cr(100): (A) the as-deposited alloy surface, (B) after 7 L exposure at 500 ºC, and (C) subsequent annealing at 600 ºC (A$_1$ in Table 1). (D) is observed after the final annealing step at 600 ºC (A$_4$ in Table 1). The complete step edge decoration, and extended coverage of the terraces with NiO is seen in all samples after A$_1$ corresponding to the reaction steps E$_2$, A$_2$, A$_3$ and A$_4$. A direct comparison of the surface after A$_2$, A$_3$ and A$_4$ is included in the Supplemental Information Figure S3. (B) includes an inset with a higher resolution view of the step edge oxide, and (D) shows an inset with the cross-type reconstruction. Imaging conditions were U_{bias}= 2.0 V and I_t= 0.1 nA.

direction. The step edge oxide shows a more compact pattern with 2.01 ± 0.07 nm spacing measured edge-to-edge with respect to the repeat unit in NiO. This corresponds to NiO-Ni(7×8) along the [110] direction in both lattices. The supporting information includes a detailed illustration of the measurement directions. The increased NiO coverage in Ni-12wt.%Cr(100) in comparison to Ni-8wt.%Cr(100) shows that NiO nucleation and growth depends sensitively on the Cr content in the alloy.

The almost complete step edge decoration, and extended coverage of the terraces with NiO-NiCr(6×7) is seen in the reaction steps E$_2$, A$_2$, A$_3$ and A$_4$ (Figure 4-2(D)), which follow A$_1$ (Figure

4-2(C)). A direct comparison of the surface after A_2, A_3 and A_4 is included in the Supporting Information Figure 4-S3. Figures 4-6 and 4-7 show the surface after E_2. All statistical analysis of coincidence lattices on terraces and steps, step heights, their U_{bias} dependent behavior as well as the electronic characteristics of the different types of surface features has been performed for images recorded after all oxidation and annealing steps and are discussed in the next section. While the abundance of the surface features changes throughout the reaction sequence, their geometric and electronic characteristics remain unchanged. For example, all step edge NiO presents a NiO-Ni(7×8) coincidence lattice independent of whether it is observed after reactions step E_1 or E_4 for Ni-12wt.%Cr(100), or E_3 for Ni-8wt.%Cr(100).

In the early oxidation steps the terraces are covered by nanoclusters (Figure 4-2(B) and Figure 4-3), which form a dense layer. The relatively high cluster density precludes a reliable

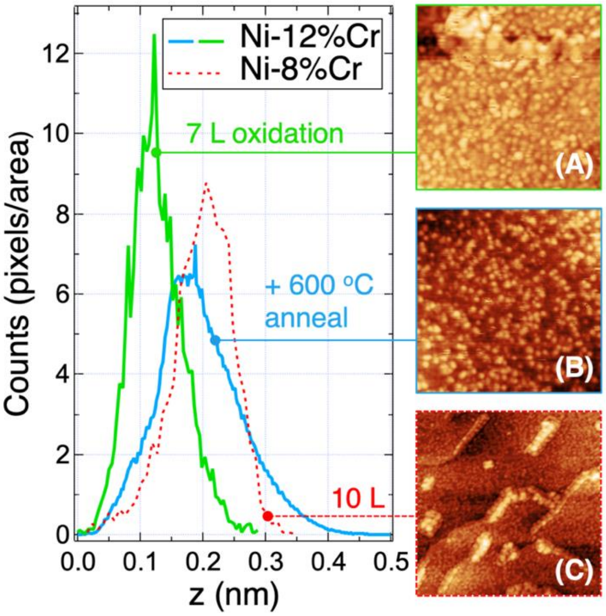

Figure 4-2. STM images captured for Ni-12wt.%Cr(100): (A) the as-deposited alloy surface, (B) after 7 L exposure at 500 °C, and (C) subsequent annealing at 600 °C (A_1 in Table 1). (D) is observed after the final annealing step at 600 °C (A_4 in Table 1). The complete step edge decoration, and extended coverage of the terraces with NiO is seen in all samples after A_1 corresponding to the reaction steps E_2, A_2, A_3 and A_4. A direct comparison of the surface after A_2, A_3 and A_4 is included in the Supplemental Information Figure S3. (B) includes an inset with a higher resolution view of the step edge oxide, and (D) shows an inset with the cross-type reconstruction. Imaging conditions were U_{bias}= 2.0 V and I_t= 0.1 nA.

measurement of the lateral size distribution due to tip convolution effects. Distributions of apparent height are therefore used for comparison and measured on 20×20 nm^2 areas on the terraces. The height distribution is measured as “apparent height above baseline” over the entire image with identical image sizes for all three oxidation steps. The baseline is defined as the positions with the smallest apparent height in the pockets between the clusters for each terrace individually. The baseline pockets might be the bare alloy, or an alloy with chemisorbed oxygen, and it was not possible to identify their chemical and bonding state unambiguously. The apparent height distributions reveal rather shallow clusters with a maximum around 0.12 nm and 0.21 nm for Ni-12wt.%Cr(100), and Ni-8wt.%Cr(100), respectively. The poorly defined cluster shape, and relatively large width of distributions, which can stem from variations in topographic height as well as local density of states, is commensurate with sub-oxides or amorphous oxide with variable composition formed on the surface of the random solid-solution Ni-Cr alloy. The nanocluster height distributions for the two alloys are nearly symmetric in the initial reaction step, although the average cluster height is larger for Ni-8wt.%Cr(100), which we attribute to the higher cumulative oxygen exposure. After the first 600 ^{o}C anneal step of Ni-12wt.%Cr(100) the clusters appear to ripen, which is expressed by a shift of the height distribution maximum to larger values and an increasing population at larger height. The STS spectra revealed a bandgap for the nanocluster-decorated terrace around 4.0 eV but the lack of well-defined geometric structure prevents attribution to a specific oxide.

The annealing step A_1 at 600 ^{o}C (Ni-12wt.%Cr) leads at the same time to the complete loss of step edge oxides (Figure 4-2(C)). The exposed alloy step edges revert to a more curved morphology and are reminiscent of the initial alloy surface shown in Figure 4-2(A). Hence, step edge motion in Ni-Cr alloys is relatively facile and straight edges are stabilized by NiO. The loss of step edge NiO can be attributed to a chemical reduction either due to the reducing ultra-high vacuum environment, or a solid-state reaction with Cr where the reaction products (Cr_2O_3 or $NiCr_2O_4$) are integrated in the nanocluster population. Reduction of NiO by either reaction can be facilitated by the abundance of under-coordinated edge sites along the narrow strips of edge-oxide. The solid state reaction pathway is also known to drive the internal oxidation of Ni-Cr in the later stages of the oxidation process.[1,26]

The second 7 L oxidation step at 500 ^oC (E_2, cumulative exposure of 14 L) drives a rapid increase in the NiO terrace coverage that now envelops a large part of the surface. At the same time nanoclusters, which previously dominated the terraces, have dissolved. Additional annealing steps at 500 ^oC and 600 ^oC have a negligible impact on the surface structure and only remove kinks in the edges of the NiO layer spreading over the terrace (Supporting Information 4-S3). The NiO boundaries often coincide with minima in the moiré pattern (Figure 4-2(D), A_4, final annealing step for Ni-12wt.%Cr) and therefore appear to be the most stable bonding site.

The image inset in Figure 4-2(D) shows that parts of the surface have undergone a surface reconstruction, which presents as a distinct cross-type pattern when the empty states are probed using $U_{bias} > 2$ V. The cross-type reconstruction is the dominant reconstruction among three distinct chemisorbed phases, which are seen on the surface but do not have an exact counterpart in either the pure Ni(100) and Cr(100) surfaces. The analysis of the reconstructions with density functional theory (DFT) calculations has not yet lead to a unique assignment, and will be pursued in a future publication. We propose that the cross-type reconstruction, which only forms after the 2nd annealing step, is created by transformation or dissolution of the nanoclusters observed in the initial oxidation step. The cross-type reconstruction is reminiscent of $\left(\sqrt{5}\times\sqrt{5}\right)R27°$ bcc Cr(100), but has a unit cell that is twice as large.[37] The cross-type reconstruction might be a surface oxide, or the first layer of $NiCr_2O_4$ or Cr_2O_3, and possibly includes an ordered vacancy structure. It is tentatively interpreted as a surface region with a relatively high Cr concentration, which is likely important for the nucleation of Cr_2O_3, and injection of Cr-dopants into the NiO layer.[8] Since surface diffusion is significant for oxide growth at this stage, it is very likely that regions with high Cr concentrations lead to locally doped oxides.[42] The lateral inhomogeneity in the Cr-concentration is hypothesized to play a critical role in connecting surface chemistry, and subsequent oxide layer growth.

In addition, the large oxide nodules appear after the 2nd oxidation step (E_2) of Ni-12wt.%Cr(100) and are readily apparent in Figure 4-2(D). Their long axis is along the [100] and [010] directions with respect to the Ni-Cr(100) and NiO(100) surfaces. The apparent height of the nodules is extremely sensitive to bias voltage, which is shown in the Supporting Information 4-S4.

4.3.4 The NiO superlattices

The NiO coincidence lattice, which figures so prominently in many of the images, is seen in the STM images as moiré patterns with a square symmetry due to cubic crystal structure of Ni and NiO. A detailed view of terrace and wedge (or step edge) NiO is given in Figures 4-4 and 4-5. Figure 4-4 addresses the coincidence lattice on the terrace, and Figure 4-5 describes the compressed wedge-like coincidence lattice across the step edges. Figure 4-4 shows the terrace-NiO obtained after a cumulative O_2 exposure of 14 L on the Ni-12wt.%Cr(100) sample and a 500 ^{o}C anneal period (step A_2 as classified in Table 1). The peak spacing is on average 2.5 nm and shows little variation with modulation of U_{bias}(Figure 4-4(A)). A representative line profile for U_{bias}= -2.0 V is shown in Figure 4-4(D) Based on the peak spacing a cube-on-cube epitaxial

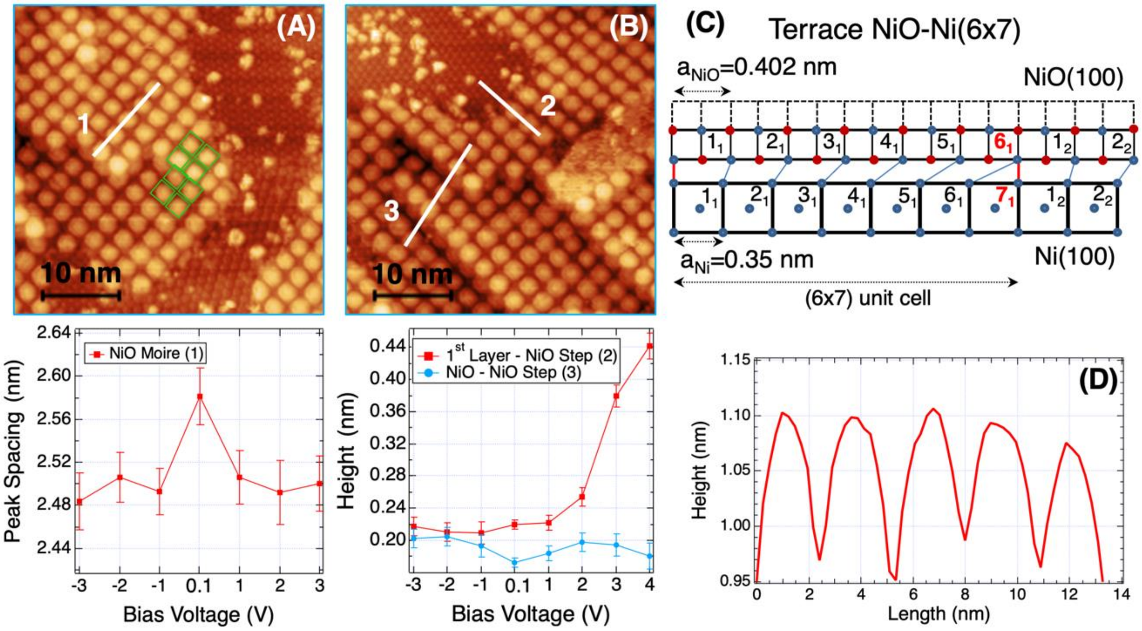

Figure 4-4. Assessment of the NiO moiré pattern and coincidence lattice measured for Ni-12wt.%Cr after a cumulative oxygen exposure of 14 L and annealing at 500 ºC (step A_2 as classified in Table 1). Images (A) and (B) were measured at -2.0 V and 0.1 nA. Height and distances were measured at the same image feature, which was recorded at different bias voltages maintaining a feedback current of 0.1 nA. The peak spacing (*line 1*) is acquired on the NiO moiré pattern, the height distributions are measured across *line 2* NiO-NiO, and *line 3* NiO-reconstruction. (C) Model of the 6×7 NiO-Ni cube-on-cube coincidence lattice, and (D) corresponding line scan along *line 1*.

relationship between the Ni-Cr alloy and NiO is confirmed. With a_{Ni}=0.35 nm, and a_{NiO}=0.402 nm,[7] a coincidence lattice with the unit NiO-NiCr(6×7) yields a period of 2.50 ± 0.02 nm and is in agreement with our STM data. The lattice constant of Ni-Cr alloys is for low Cr concentrations almost identical to the Ni-lattice constant.[43,44] A model for the NiO-NiCr(6×7) lattice match at the interface is proposed in Figure 4-4(C) As a side note: the chemisorbed structure (or reconstruction) at the endpoint of line scan 2 (Figure 4-4(B)) shows a square lattice~~.~~

The apparent height of the NiO steps between NiO-NiO, and NiO-NiCr with chemisorbed oxygen (oxygen-induced reconstruction), are summarized in Figure 4-4(B). The apparent step height NiO-NiO layer is 0.19 ± 0.01 nm and corresponds to the growth of NiO in layers of half unit cells (two atomic layers), and the coincidence lattice signature is conserved for several layers minimizing biaxial strain. Several (6×7) unit cells are marked in Figure 4-4(A) and are offset by half a (6×7) unit cell across a step edge. On the other hand, the apparent step height measured between the 1st layer chemisorbed phase on Ni-Cr, and NiO depends sensitively on the bias voltage and nearly doubles to reach 0.44 nm at U_{bias} = +4.0 V. At this bias voltage the antibonding p-states of the NiO[15] are probed, while the contributions from the chemisorbed domain are not yet understood. The tunneling current from NiO and the chemisorbed domains do not follow the same bias-voltage dependence, which leads to the strong variation in apparent step height between them. A future DFT calculation of the chemisorbed domains should provide the requisite LDOS and allow for a quantitative interpretation. Figure 4-6 includes STS spectra from both regions and underscores the differences in the LDOS between them.

Figure 4-5(A) and 4-5(B) show in more detail the NiO at the step edges, which presents as wedge-like structures first reported by Bäumer et al..[28] NiO nucleates first at the step edges and grows subsequently into the top and bottom terraces. The average spacing of the moiré maxima measured along the wedge incline (taken along the [110] and [1-10] directions) is 2.01 ± 0.07 nm and has an angle of 3.6-5.3º with respect to the [001] direction (Figures 4-5(D)). This reduced periodicity corresponds to a NiO-NiCr(7×8) coincidence lattice, where the lattice (110) lattice planes match at the aforementioned coincidence site. The wedge angle is achieved by introducing additional half-planes at the Ni-Cr(100)-NiO interface as shown schematically in Figure 4-5(C), and the geometric structure of the interface stabilizes a narrow range of wedge angles. These sites accommodate NiO formation by creating low-angle grain boundaries at the interface. In addition to the NiO wedge the formation of shorter, secondary wedges, is observed and they are marked by white arrows in Figure 4-5(B). These secondary wedges are a signature of a change in growth mode from Frank-van der Merve to Vollmer-Weber. Luo et al.[6] observed this transition with in-

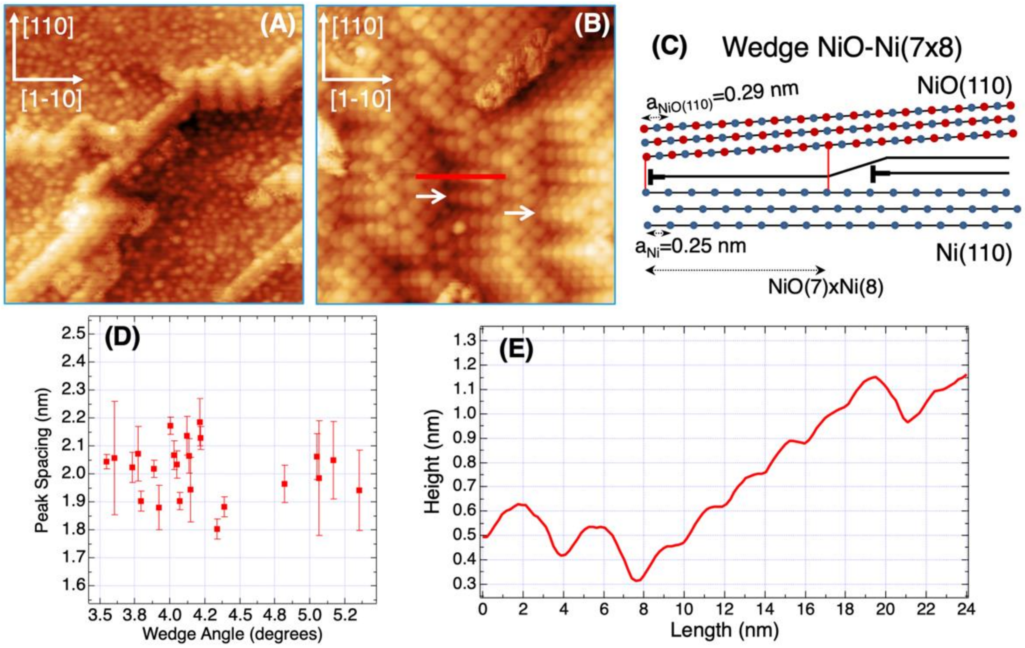

Figure 4-5. Images (A) and (B) show a selection of oxide wedges after processing steps E$_1$ and A$_2$, respectively for the Ni-12wt.%Cr sample. The arrow in (B) marks secondary wedges, which do not span the entire step edge. (C) model of the wedge structure with the dislocation plane introduced in the underlying substrate to support tilt in each wedge. (D) summarizes the spacing of the intensity maxima in the moiré structures across a large number of wedges from all different experimental steps for the Ni-12wt.%Cr sample. (E) is a representative line scan across a wedge marked in image (B) by a red line. Both images are 50×50 nm^2 with 2.0 V and a feedback current of 0.1 nA.

situ HRTEM (high resolution transmission electron microscopy) on Ni-10at.%Cr at 450 ºC, and a similar transition is seen on Cu with a shallow wetting layer of only two atomic layers.[45,46] The Ehrlich-Schwöbel barrier confines Ni atoms to a single NiO terrace where a new oxide layer nucleates. This results in the formation of stacked oxide islands and a new (110) facet.[7]

4.3.5 The nanoscale origins of electronic heterogeneity at alloy-oxide interfaces

The structural heterogeneity observed during the initial stages of oxidation is even more pronounced in the electronic heterogeneity, which is seen in the LDOS and bandgap maps. These maps reflect the LDOS of all surface features, and in addition show inhomogeneous distributions

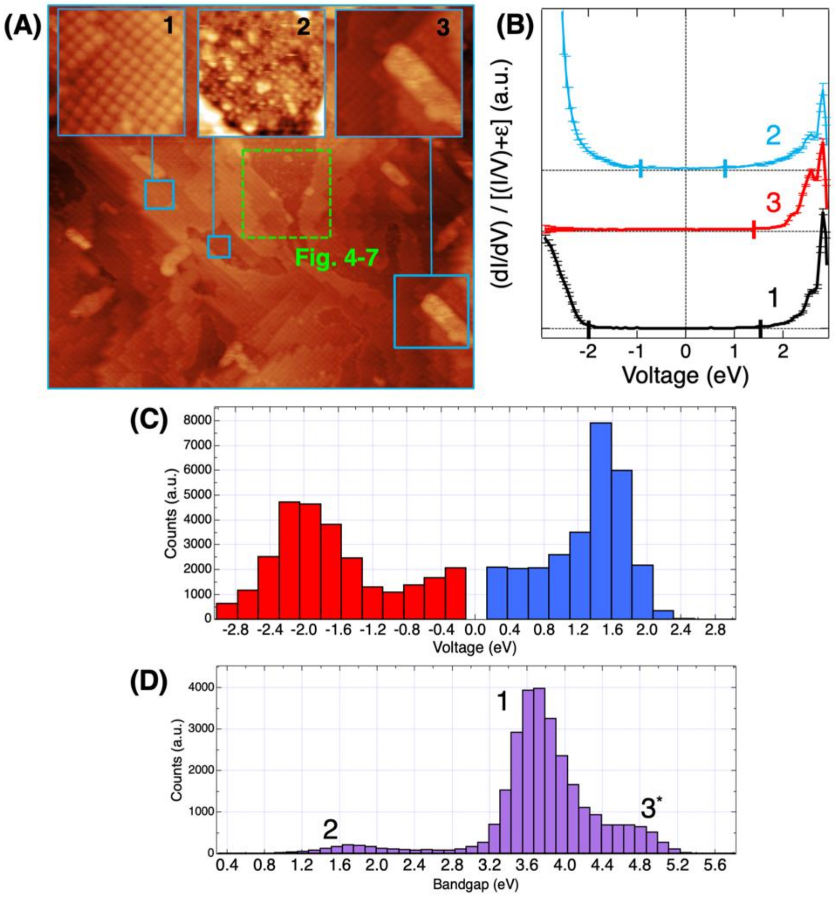

Figure 4-6. Topography images (A), bandgap and STS spectra (B) for Ni-12wt.%Cr after the 14 L O_2 at 500 ºC exposure (step E_2). (A) Large scale image 300×300 nm^2 in combination with higher resolution images of characteristic surface features. From left to right: moiré pattern from the coincidence lattice between Ni(100) and NiO(100), surface reconstruction labeled as "cross reconstruction" from its visual presentation, and oxide nodule. Images were recorded at 3.0 V and 0.1 nA. The green rectangle marks the region of the band gap and LDOS maps shown in Figure 7. (B) STS spectra for all characteristic regions shown in the high-resolution insets. The spectra are averaged over 20-40 individual spectra extracted from the STS maps recorded in the respective region. (C) This histogram summarizes VBM and CBM positions for all (dI/dV)/(I/V) spectra recorded in the STS map collection for the Figure 6.A surface area. (D) Histogram of the corresponding bandgaps collected for image area Figure 6.A and the labels correspond to the STS spectra (B) and images (A). Note that bandgaps larger than 4.1 eV (labeled 3^*) are positioned on the nodules and due to suppression of the tunneling current in the valence band it is not possible to assess the bandgap correctly.

of dopants within a single surface feature. Figures 4-6 and 4-7 are used to discuss the electronic structure of the surface after cumulative oxygen exposure of Ni-12wt.%Cr(100) with 14 L O_2 and annealing at 500 ºC (E_2 as classified in Table 1). Note that image resolution in the combined STS-

STM mode for the topography images is worse than for images recorded exclusively in topography mode. The topography image shown here was captured immediately after the STS map measurement, which allows for unambiguous feature matching.

Figure 4-6 summarizes characteristic regions and the STS spectra in Figure 4-6(B) are averaged over 20-40 individual spectra recorded within the marked areas in the topography image. Figure 4-6(A). *Region 1* corresponds to the NiO moiré pattern, *region 2* reflects the cross-type reconstruction, which is the dominant reconstruction observed on this sample, and *region 3* corresponds to one of the large oxide nodules.

The NiO layer (*region 1*) has on average a band gap of 3.6 eV, which is lower than the bulk value of 4.3 eV NiO.[47,48,49] The Fermi level is shifted towards the conduction band minimum (CBM) with respect to the intrinsic Fermi energy position and is commensurate with n-type doping. The reconstructed *region 2* has a smaller band gap, and the band edges are positioned at -1.0 eV and 0.9 eV, respectively. The shallower slope at the band edges is likely due to additional states specific for this reconstruction. The STS spectrum of the large oxide nodules in *region 3* shows a very small intensity for the valence band, which prevents a reliable determination of a bandgap.[50] The (dI/dV)/(I/V) values for the valence band show the reduction in the transmission function due to the insulating nature of the oxide nodule. The very low (dI/dV)/(I/V) is also reflected in bias dependent topography images included in the Supporting Information 4-S4. Figures 4-6(C) and (D) summarize all values for the valence band maxima (VBM) and conduction band minima (CBM), as well as bandgap values, respectively, for the entire image area of Figure 4-6(A). NiO dominates the surface and the position of the maxima for VBM and CBM histograms reflect the n-type doping we observed in the individual spectra. The most-probable bandgap value

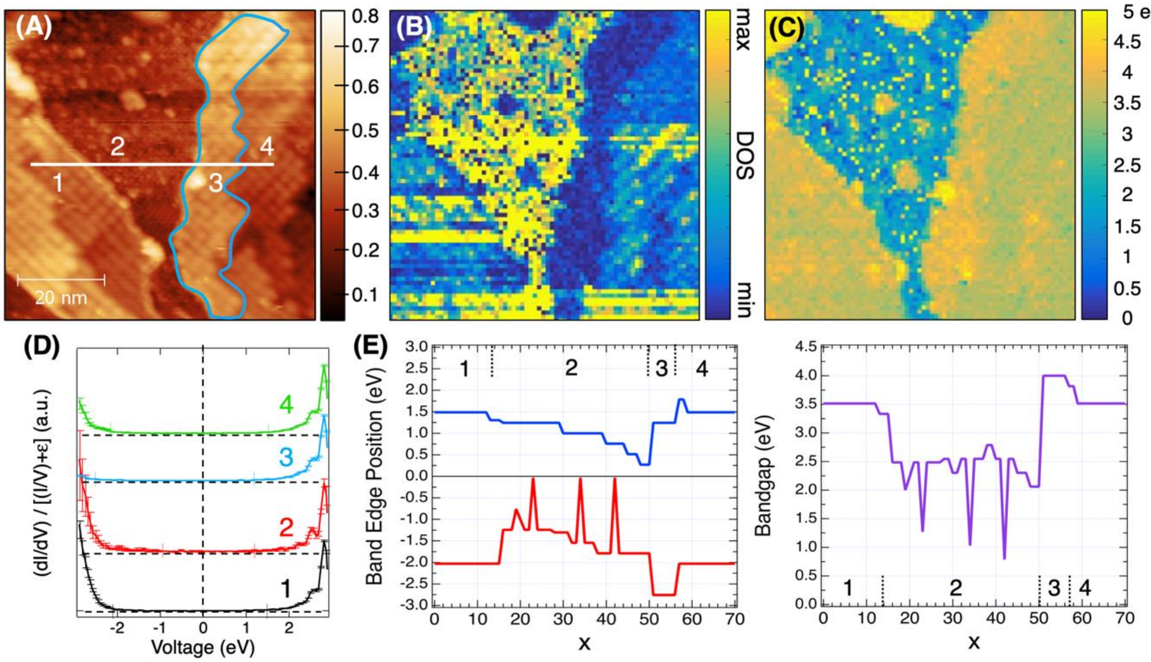

Figure 4-7. (A) Topography image of the region marked in Figure 6, and (B) is the corresponding density of states map at U_{bias}= - 2.39 V, and (C) bandgap map. (D) includes the spectra collected in the characteristic surface regions traversed along the line included in (A). *Region 3 and 4* show identical topography features and bandgaps, but present differences in doping. (E) includes the position of VBM, CBM and position of the Fermi level extracted from all spectra measured across *region 1 to 4* following the guiding line.

of 3.6 eV is attributed to the NiO layers, larger values correspond to oxide nodules, and values centered around 1.7 eV represent the chemisorbed regions.

To understand the heterogeneous electronic structure of the Ni-12wt.%Cr(100) surface after oxidation, a section of Figure 4-6(A) was selected that represented the spatial variation of the distinct surface oxides features. Figure 4-7 addresses the area marked with a green rectangle in Figure 4-6, and the image of this region is shown in Figure 4-7(A). Figure 4-7(B) includes the LDOS map – a cut through all spectra at U_{bias}=-2.39 V and the corresponding (dI/dV)/(I/V) value is displayed as a function of position. Figure 4-7(C) shows the band gap map for the same area. A few regions in the LDOS map have some streaks due to tip changes during measurement and are excluded from the discussion. The individual spectra in Figure 4-7(D) correspond to different segments along the line in the STM image, which crosses from the NiO region (1) onto the chemisorbed surface (2), and back onto a section of NiO, which is divided into segments 3 and 4. The bandgap, and band edge positions are summarized in Figure 4-7(E), and the different line segments are marked. The standard deviation for VBM (CBM) values is 0.2 eV (0.08 eV) for *segment 1 and 4*, 0.4 eV for VBM and CBM in *segment 2*, and 0.18 eV (VBM) and 0.16 (CBM) for *segment 3*. The standard deviation was calculated for datasets consisting of ±4 STS pixels around each data point positioned on the line and reflects the experimental variability. *Segment 2* is relatively inhomogeneous and shows significant local variations in its LDOS due to some very small clusters embedded in the cross-type reconstruction. *Segment 1 and 4* are very similar in terms of bandgap, VBM, and CBM values, and are both slightly n-doped. Note that the NiO section left of *segment 1* shows the identical band gap value and LDOS.

Segments 3 and *4* are particularly interesting: the bandgap is slightly larger in *segment 3*, and the position of the Fermi energy is shifted closer to the CBM indicating a stronger doping compared to NiO *segment 4*, and *segment 1*. NiO-*segment 3* is marked with a blue outline in the topography image and the corresponding region can clearly be identified in the LDOS map. Candidates for oxide doping are defects such as trivalent, substitutional Cr^{3+}, which increases the vacancy concentration and hence reduces the hole concentration.[42] The vacancies created by introduction of Cr^{3+} also provide a mechanism for the accelerated growth of NiO.[8] Additional gap states can arise from local O-deficiencies, or the presence of solute trapped Cr^{2}, and Cr^{3+}, which has recently been reported. [42,51] The overall position of the Fermi energy within the gap is determined by the entirety of the defect- and dopant inventory and cannot be attributed to one specific, dominant gap state at present. As a consequence, the assumption of a homogeneous electric field at the interface between alloys and oxide, which is commonly made in Cabrera-Mott growth models, should be revisited.

4.4 Discussion

The comparison between Ni(100) and Ni-Cr(100) oxidation demonstrates the significant changes in the formation of surface oxides caused by alloying even with relatively small amounts of Cr. NiO dominates the surface oxide during the early stages of oxidation, which is in agreement with the literature in the temperature regime of the present study.[6,7,11,51,8,52] The impact of Cr on NiO nucleation, and the wide range of surface features that emerge early in the oxidation process, illustrate the complexity of alloy surface chemistry. Consideration must be given to the preferred nucleation and growth site for each constituent metal in the alloy and their corresponding oxide phase, and the effects of the oxide growth on surrounding phases.

Introduction of Cr significantly enhances NiO nucleation and growth, but also contributes to the emergence of additional oxide features including novel reconstructions and large oxide nodules, which are not seen for pure Ni(100). Recent work has shown that substituting Cr for a Ni surface atom enhances the affinity for bonding between oxygen and Ni-Cr surfaces,[53,54] underscoring the role of Cr in promoting NiO formation. The enhanced NiO nucleation goes hand in hand with accelerated NiO growth, which is aided by Cr-doping. We propose two mechanisms for the enhanced NiO nucleation: (i) Cr segregates to the step edges and facilitates oxide nucleation by changing the reaction kinetics and local activation barriers, or (ii) Cr prevents reconstruction-induced step faceting by lowering step edge atom mobility and kink sites for nucleation are therefore retained. This question can be resolved in future work by targeting very low oxygen exposures and lower Cr-concentration alloys in conjunction with DFT calculations to assess the most likely Cr-position in the alloy surface.

The oxidation of Ni-Cr leads also to structural and compositional changes in the alloy surface itself and includes (i) faceting of step edges by NiO growth, which is driven by the epitaxial relationship between the Ni-Cr and NiO lattices, and (ii) the emergence of presumably Cr-rich regions within a novel cross-type reconstruction. The characteristic symmetry of the cross-type reconstruction has no counterpart in the fcc Ni(100) surfaces and is reminiscent of the oxygen-induced bcc Cr(100) [33,37] reconstructions. This lead us to propose that a Cr-rich surface region formed by lateral segregation of Cr. Consequently, we can not think about the Ni-Cr alloy surfaces as homogeneous with a random distribution of Cr-atoms which determines local oxidation reactions but should revise this picture to include lateral element segregation. One of the consequences of local variations in Cr-concentrations beyond the atomic-length scale of a solid solution is heterogeneity in oxide doping, which is likely the reason for the variations in electronic structure seen in Figures 4-6 and 4-7. The assumption of uniform oxide coverage is inadequate within the pre-Cabrera-Mott regime. As such, the description of the surface electronic structure and compositional variation can account for the heterogeneity observed and will be important for future work.

4.5 Conclusions

The surface reactions of binary Ni-Cr alloys were studied by nanoscale characterization of the geometric and electronic structure. The combination of STM and STS maps enabled us to deepen our understanding of the structural, compositional, and electronic heterogeneity that emerges in the initial stages of the oxidation process. Some aspects of the oxidation, which are controlled by geometric constraints and include the coincidence lattices formed by NiO at the step edges and on the terraces, have direct counterparts in the oxidation of Ni(100) surfaces. However, surface processes controlled by local chemistry and kinetics, such as reconstruction-driven step edge faceting, lateral segregation of Cr, and the formation of new reconstructions are uniquely changed by the addition of small amounts of Cr. The electronic heterogeneity is likely impactful for the continuation of NiO growth and is coupled to an established mechanism of NiO accelerated growth via Cr-dopant induced vacancies. The pre-Cabrera Mott regime sets the stage for the transition to Cabrera-Mott and field-controlled oxide growth, and the next step in this work is to understand this transition. It is particularly important to establish which features of pre-Cabrera Mott heterogeneity have an impact on the continued oxide growth and passive film performance.

4.6 Chapter IV References

(1) Atkinson, A. Transport Processes during the Growth of Oxide Films at Elevated Temperature. *Rev. Mod. Phys.* **1985**, *57* (2), 437–470. https://doi.org/10.1103/RevModPhys.57.437.

(2) Wood, G. C.; Chattopadhyay, B. Transient Oxidation of Ni-Base Alloys. *Corros. Sci.* **1970**, *10* (7), 471–480. https://doi.org/10.1016/S0010-938X(70)80032-4.

(3) Chattopadhyay, B.; Wood, G. C. The Transient Oxidation of Alloys. *Oxid. Met.* **1970**, *2* (4), 373–399.

(4) De Los Santos Valladares, L.; Ionescu, A.; Holmes, S.; Barnes, C. H. W.; Bustamante Domínguez, A.; Avalos Quispe, O.; González, J. C.; Milana, S.; Barbone, M.; Ferrari, A. C.; Ramos, H.; Majima, Y. Characterization of Ni Thin Films Following Thermal Oxidation in Air. *J. Vac. Sci. Technol. B Nanotechnol. Microelectron. Mater. Process. Meas. Phenom.* **2014**, *32* (5), 051808. https://doi.org/10.1116/1.4895846.

(5) Mohanty, P.; Rath, C.; Mallick, P.; Biswal, R.; Mishra, N. C. UV–Visible Studies of Nickel Oxide Thin Film Grown by Thermal Oxidation of Nickel. *Phys. B Condens. Matter* **2010**, *405* (12), 2711–2714. https://doi.org/10.1016/j.physb.2010.03.064.

(6) Luo, L.; Zou, L.; Schreiber, D. K.; Baer, D. R.; Bruemmer, S. M.; Zhou, G.; Wang, C.-M. In-Situ Transmission Electron Microscopy Study of Surface Oxidation for Ni–10Cr and Ni–20Cr Alloys. *Scr. Mater.* **2016**, *114*, 129–132. https://doi.org/10.1016/j.scriptamat.2015.11.031.

(7) Luo, L.; Zou, L.; Schreiber, D. K.; Olszta, M. J.; Baer, D. R.; Bruemmer, S. M.; Zhou, G.; Wang, C.-M. In Situ Atomic Scale Visualization of Surface Kinetics Driven Dynamics of Oxide Growth on a Ni–Cr Surface. *Chem. Commun.* **2016**, *52* (16), 3300–3303. https://doi.org/10.1039/C5CC09165A.

(8) Unutulmazsoy, Y.; Merkle, R.; Fischer, D.; Mannhart, J.; Maier, J. The Oxidation Kinetics of Thin Nickel Films between 250 and 500 °C. *Phys. Chem. Chem. Phys.* **2017**, *19* (13), 9045–9052. https://doi.org/10.1039/C7CP00476A.

(9) Lutton, K.; Gusieva, K.; Ott, N.; Birbilis, N.; Scully, J. R. Understanding Multi-Element Alloy Passivation in Acidic Solutions Using Operando Methods. *Electrochem. Commun.* **2017**, *80*, 44–47. https://doi.org/10.1016/j.elecom.2017.05.015.

(10) Sprowl, L. H.; Adam, B. M.; Tucker, J. D.; Árnadóttir, L. First-Principles Study of the Products of CO2 Dissociation on Nickel-Based Alloys: Trends in Energetics with Alloying Element. *Surf. Sci.* **2018**. https://doi.org/10.1016/j.susc.2018.06.011.

(11) Ramanathan, R.; Ramalingam, G.; Perepezko, J. H.; Reinke, P.; Voorhees, P. W. Evolution of NiO Island Size Distributions During the Oxidation of a Ni-5Cr Alloy: Experiment and Modeling. *ACS Appl. Mater. Interfaces* **2018**. https://doi.org/10.1021/acsami.7b18539.

(12) Gusieva, K.; Cwalina, K. L.; Blades, W. H.; Ramalingam, G.; Perepezko, J. H.; Reinke, P.; Scully, J. R. Repassivation Behavior of Individual Grain Facets on Dilute Ni–Cr and Ni–Cr–Mo Alloys in Acidified Chloride Solution. *J. Phys. Chem. C* **2018**, *122* (34), 19499–19513. https://doi.org/10.1021/acs.jpcc.8b04306.

(13) Bertrams, Th.; Neddermeyer, H. Growth of NiO(100) Layers on Ag(100): Characterization by Scanning Tunneling Microscopy. *J. Vac. Sci. Technol. B*

Microelectron. Nanometer Struct. Process. Meas. Phenom. **1996**, *14* (2), 1141–1144. https://doi.org/10.1116/1.588416.

(14) Schintke, S.; Schneider, W.-D. Insulators at the Ultrathin Limit: Electronic Structure Studied by Scanning Tunnelling Microscopy and Scanning Tunnelling Spectroscopy. *J. Phys. Condens. Matter* **2004**, *16* (4), R49. https://doi.org/10.1088/0953-8984/16/4/R02.

(15) Castell, M. R.; Wincott, P. L.; Condon, N. G.; Muggelberg, C.; Thornton, G.; Dudarev, S. L.; Sutton, A. P.; Briggs, G. A. D. Atomic-Resolution STM of a System with Strongly Correlated Electrons:NiO(001) Surface Structure and Defect Sites. *Phys. Rev. B* **1997**, *55* (12), 7859–7863. https://doi.org/10.1103/PhysRevB.55.7859.

(16) Cabrera, N. Theory of the Oxidation of Metals. **1949**, *12*, 163–184.

(17) Wagner, C. Equations for Transport in Solid Oxides and Sulfides of Transition Metals. *Prog. Solid State Chem.* **1975**, *10*, 3–16. https://doi.org/10.1016/0079-6786(75)90002-3.

(18) Seyeux, A.; Maurice, V.; Marcus, P. Oxide Film Growth Kinetics on Metals and Alloys: I. Physical Model. *J. Electrochem. Soc.* **2013**, *160* (6), C189–C196. https://doi.org/10.1149/2.036306jes.

(19) Lankhorst, M. H. R.; Bouwmeester, H. J. M.; Verweij, H. Thermodynamics and Transport of Ionic and Electronic Defects in Crystalline Oxides. *J. Am. Ceram. Soc.* **1997**, *80* (9), 2175–2198. https://doi.org/10.1111/j.1151-2916.1997.tb03107.x.

(20) Haugsrud, R. On the High-Temperature Oxidation of Nickel. *Corros. Sci.* **2003**, *45* (1), 211–235. https://doi.org/10.1016/S0010-938X(02)00085-9.

(21) Holloway, P. H.; Hudson, J. B. Kinetics of the Reaction of Oxygen with Clean Nickel Single Crystal Surfaces: I. Ni(100) Surface. *Surf. Sci.* **1974**, *43* (1), 123–140. https://doi.org/10.1016/0039-6028(74)90223-4.

(22) Steffen, J.; Hofmann, S. Oxidation of NiCr and NiCrFe Alloys at Room Temperature. *Surf. Interface Anal.* **1988**, *11* (12), 617–626. https://doi.org/10.1002/sia.740111207.

(23) Jeng, S.-P.; Holloway, P. H.; Batich, C. D. Surface Passivation of Ni/Cr Alloy at Room Temperature. *Surf. Sci.* **1990**, *227* (3), 278–290. https://doi.org/10.1016/S0039-6028(05)80016-0.

(24) Hoflund, G. B.; Epling, W. S. Oxidation Study of a Polycrystalline Ni/Cr Alloy I: Room-Temperature Exposure to O2. *Thin Solid Films* **1997**, *307* (1), 126–132. https://doi.org/10.1016/S0040-6090(97)00300-3.

(25) Marcus, P.; Maurice, V. Atomic Level Characterization in Corrosion Studies. *Philos. Transact. A Math. Phys. Eng. Sci.* **2017**, *375*, 20160414. https://doi.org/10.1098/rsta.2016.0414.

(26) Calvarin, G.; Molins, R.; Huntz, A. M. Oxidation Mechanism of Ni–20Cr Foils and Its Relation to the Oxide-Scale Microstructure. **2000**, *53*, 24–48.

(27) Kopatzki, E.; Behm, R. J. Step Faceting: Origin of the Temperature Dependent Induction Period in Ni(100) Oxidation. *Phys. Rev. Lett.* **1995**, *74* (8), 1399–1402. https://doi.org/10.1103/PhysRevLett.74.1399.

(28) Bäumer, M.; Cappus, D.; Kuhlenbeck, H.; Freund, H.-J.; Wilhelmi, G.; Brodde, A.; Neddermeye, H. The Structure of Thin NiO(100) Films Grown on Ni(100) as Determined by Low-Energy-Electron Diffraction and Scanning Tunneling Microscopy. *Surf. Sci.* **1991**, *253* (1), 116–128. https://doi.org/10.1016/0039-6028(91)90585-G.

(29) Smeenk, R. G.; Tromp, R. M.; Frenken, J. W. M.; Saris, F. W. The Oxidation of Ni(100) Studied by Medium Energy Ion Scattering. *Surf. Sci.* **1981**, *112* (3), 261–271. https://doi.org/10.1016/0039-6028(81)90374-5.

(30) Kopatzki, E.; Behm, R. J. STM Imaging and Local Order of Oxygen Adlayers on Ni(100). *Surf. Sci.* **1991**, *245* (3), 255–262. https://doi.org/10.1016/0039-6028(91)90028-Q.

(31) Stuckless, J. T.; Wartnaby, C. E.; Al-Sarraf, N.; Dixon-Warren, St. J. B.; Kovar, M.; King, D. A. Oxygen Chemisorption and Oxide Film Growth on Ni{100}, {110}, and {111}: Sticking Probabilities and Microcalorimetric Adsorption Heats. *J. Chem. Phys.* **1997**, *106* (5), 2012–2030. https://doi.org/10.1063/1.473308.

(32) Norton, P. R.; Tapping, R. L.; Goodale, J. W. A Photoemission Study of the Interaction of Ni(100), (110) and (111) Surfaces with Oxygen. *Surf. Sci.* **1977**, *65* (1), 13–36. https://doi.org/10.1016/0039-6028(77)90289-8.

(33) Foord, J. S.; Lambert, R. M. Oxygen Chemisorption and Corrosion on Cr(100) and Cr(110) Single Crystal Surfaces. *Surf. Sci.* **1985**, *161* (2), 513–520. https://doi.org/10.1016/0039-6028(85)90824-6.

(34) Hope, G. A.; Ritchie, I. M. The Oxidation of Thin Chromium Films. *Thin Solid Films* **1976**, *34* (1), 111–114. https://doi.org/10.1016/0040-6090(76)90145-0.

(35) Salomonsen, G.; Norman, N.; Lonsjo, O.; Finstad, T. G. Kinetics and Mechanism of Oxide Formation on Cr Thin Films. *J. Phys. Condens. Matter* **1989**, *1* (42), 7843. https://doi.org/10.1088/0953-8984/1/42/006.

(36) Peter, R.; Saric, I.; Piltaver, I. K.; Badovinac, I. J.; Petravic, M. Oxide Formation on Chromium Metal Surfaces by Low-Energy Oxygen Implantation at Room Temperature. *Thin Solid Films* **2017**, *636*, 225–231. https://doi.org/10.1016/j.tsf.2017.06.011.

(37) Schmid, M.; Leonardelli, G.; Sporn, M.; Platzgummer, E.; Hebenstreit, W.; Pinczolits, M.; Varga, P. Oxygen-Induced Vacancy Formation on a Metal Surface. *Phys. Rev. Lett.* **1999**, *82* (2), 355–358. https://doi.org/10.1103/PhysRevLett.82.355.

(38) Ramalingam, G.; Reinke, P. Growth of Ni and Ni-Cr Alloy Thin Films on MgO(001): Effect of Alloy Composition on Surface Morphology. *J. Appl. Phys.* **2016**, *120* (22), 225302. https://doi.org/10.1063/1.4971261.

(39) Feenstra, R. M. Tunneling Spectroscopy of the (110) Surface of Direct-Gap III-V Semiconductors. *Phys. Rev. B* **1994**, *50* (7), 4561–4570. https://doi.org/10.1103/PhysRevB.50.4561.

(40) Feenstra, R. M.; Stroscio, J. A.; Fein, A. P. Tunneling Spectroscopy of the Si(111)2 × 1 Surface. *Surf. Sci.* **1987**, *181* (1), 295–306. https://doi.org/10.1016/0039-6028(87)90170-1.

(41) W. Cahn, J.; A. Handwerker, C. Equilibrium Geometries of Anisotropic Surfaces and Interfaces. *Mater. Sci. Eng. A* **1993**, *162* (1), 83–95. https://doi.org/10.1016/0921-5093(90)90032-X.

(42) Yu, X.; Gulec, A.; Sherman, Q.; Cwalina, K. L.; Scully, J. R.; Perepezko, J. H.; Voorhees, P. W.; Marks, L. D. Nonequilibrium Solute Capture in Passivating Oxide Films. *Phys. Rev. Lett.* **2018**, *121* (14), 145701. https://doi.org/10.1103/PhysRevLett.121.145701.

(43) Karmazin, L. Lattice Parameter Studies of Structure Changes of L~i-Cr Alloys in the Region of Ni2Cr. *Mat. Sci. and Eng.* **1982**, *54*, 247–256.

(44) Chen, J. K.; Farkas, D.; Reynolds, W. T. Atomistic Simulation of an f.c.c./b.c.c. Interface in Ni□Cr Alloys. *Acta Mater.* **1997**, *45* (11), 4415–4421. https://doi.org/10.1016/S1359-6454(97)00159-6.

(45) Zhou, G.; Luo, L.; Li, L.; Ciston, J.; Stach, E. A.; Saidi, W. A.; Yang, J. C. In Situ Atomic-Scale Visualization of Oxide Islanding during Oxidation of Cu Surfaces. *Chem. Commun.* **2013**, *49* (92), 10862–10864. https://doi.org/10.1039/C3CC46684A.

(46) Li, L.; Luo, L.; Ciston, J.; Saidi, W. A.; Stach, E. A.; Yang, J. C.; Zhou, G. Surface-Step-Induced Oscillatory Oxide Growth. *Phys. Rev. Lett.* **2014**, *113* (13), 136104. https://doi.org/10.1103/PhysRevLett.113.136104.

(47) Sawatzky, G. A.; Allen, J. W. Magnitude and Origin of the Band Gap in NiO. *Phys. Rev. Lett.* **1984**, *53* (24), 2339–2342. https://doi.org/10.1103/PhysRevLett.53.2339.

(48) Schintke, S.; Schneider, W.-D. Insulators at the Ultrathin Limit: Electronic Structure Studied by Scanning Tunnelling Microscopy and Scanning Tunnelling Spectroscopy. *J. Phys. Condens. Matter* **2004**, *16* (4), R49. https://doi.org/10.1088/0953-8984/16/4/R02.

(49) Schintke, S.; Messerli, S.; Pivetta, M.; Patthey, F.; Libioulle, L.; Stengel, M.; De Vita, A.; Schneider, W.-D. Insulator at the Ultrathin Limit: MgO on Ag(001). *Phys. Rev. Lett.* **2001**, *87* (27), 276801. https://doi.org/10.1103/PhysRevLett.87.276801.

(50) Sommerhalter, Ch.; Matthes, Th. W.; Boneberg, J.; Leiderer, P.; Lux-Steiner, M. Ch. Tunneling Spectroscopy on Semiconductors with a Low Surface State Density. *J. Vac. Sci. Technol. B Microelectron. Nanometer Struct. Process. Meas. Phenom.* **1997**, *15* (6), 1876–1883. https://doi.org/10.1116/1.589571.

(51) Latu-Romain, L.; Parsa, Y.; Mathieu, S.; Vilasi, M.; Galerie, A.; Wouters, Y. Towards the Growth of Stoichiometric Chromia on Pure Chromium by the Control of Temperature and Oxygen Partial Pressure. *Corros. Sci.* **2017**, *126*, 238–246. https://doi.org/10.1016/j.corsci.2017.07.005.

(52) Jeng, S.-P.; Holloway, P. H.; Asbury, D. A.; Hoflund, G. B. Changes Induced at Ni/Cr Alloy Surfaces by Annealing and Oxygen Exposure. *Surf. Sci.* **1990**, *235* (2), 175–185. https://doi.org/10.1016/0039-6028(90)90792-7.

(53) Samin, A. J.; Taylor, C. D. First-Principles Investigation of Surface Properties and Adsorption of Oxygen on Ni-22Cr and the Role of Molybdenum. *Corros. Sci.* **2018**, *134*, 103–111. https://doi.org/10.1016/j.corsci.2018.02.017.

(54) Sprowl, L. H.; Adam, B. M.; Tucker, J. D.; Árnadóttir, L. First-Principles Study of the Products of CO2 Dissociation on Nickel-Based Alloys: Trends in Energetics with Alloying Element. *Surf. Sci.* **2018**, *677*, 219–231. https://doi.org/10.1016/j.susc.2018.06.011.

4.7 Supplemental Data and Supporting Information

4-S1. Bandgap measurements for STS Spectra

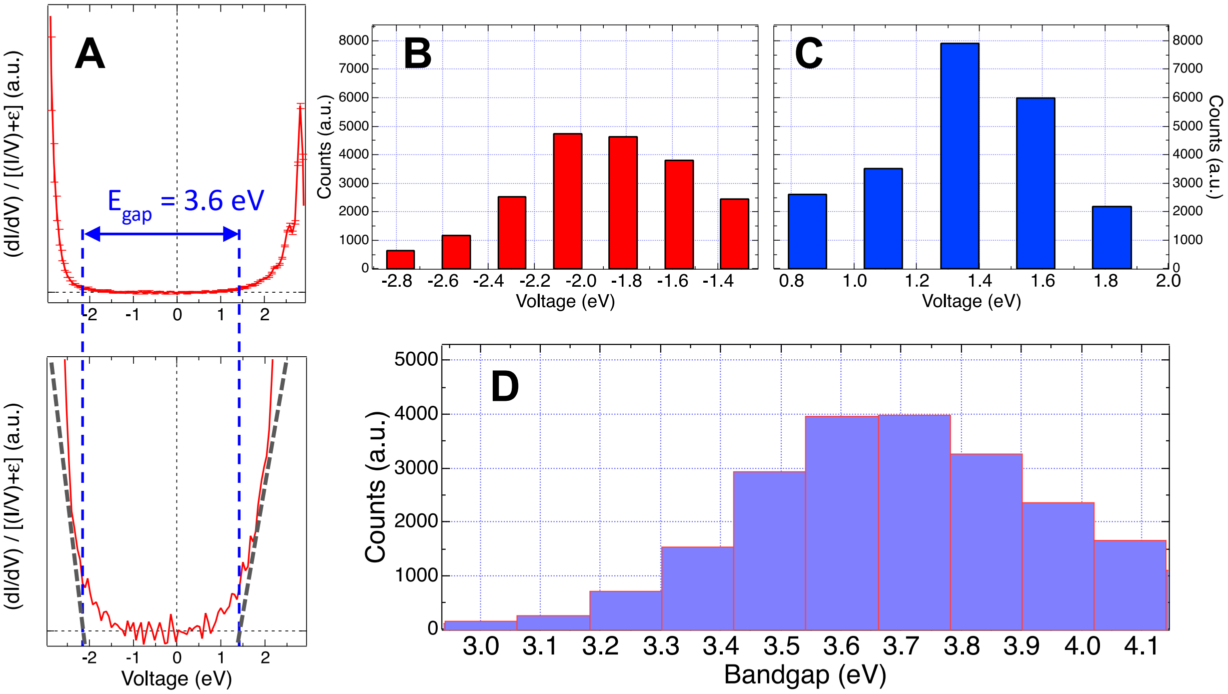

Figure 4-S1. (A) The cross-point of the tangent is used for determining the bandgap from STS data. The averaged STS curves (approx. 50 curves) were taken from NiO grown on Ni-12wt.%Cr. Distributions of the valence (B) band and conduction (C) band maxima and minima are computed from the STS spectra by numerically computing the voltage at which the current is above the threshold value reported in the method section. The bandgaps (D) are also acquired from the numerical differentiation routine and are in great agreement with the max/min of the valence/conduction bands.

This report uses the tangent method to establish specific bandgaps. This method relies on taking the derivative of the conduction and valence bands edges, and extending the slope across the x-axis. Statistical information regarding the edges of the conduction and valence bands yielded a bimodal distribution around 1.5 eV and -2.1 eV respectively, indicating that the tangent method was best suited for describing this surface. However, given the nature of room-temperature STS taken, absolute gaps are neither claimed nor suggested. Instead, relative differences in the electronic structure between various surface features are used as a measure of distinction.

4-S2. Ni-12%Cr metal surface topography of measurement at low V_{bias}

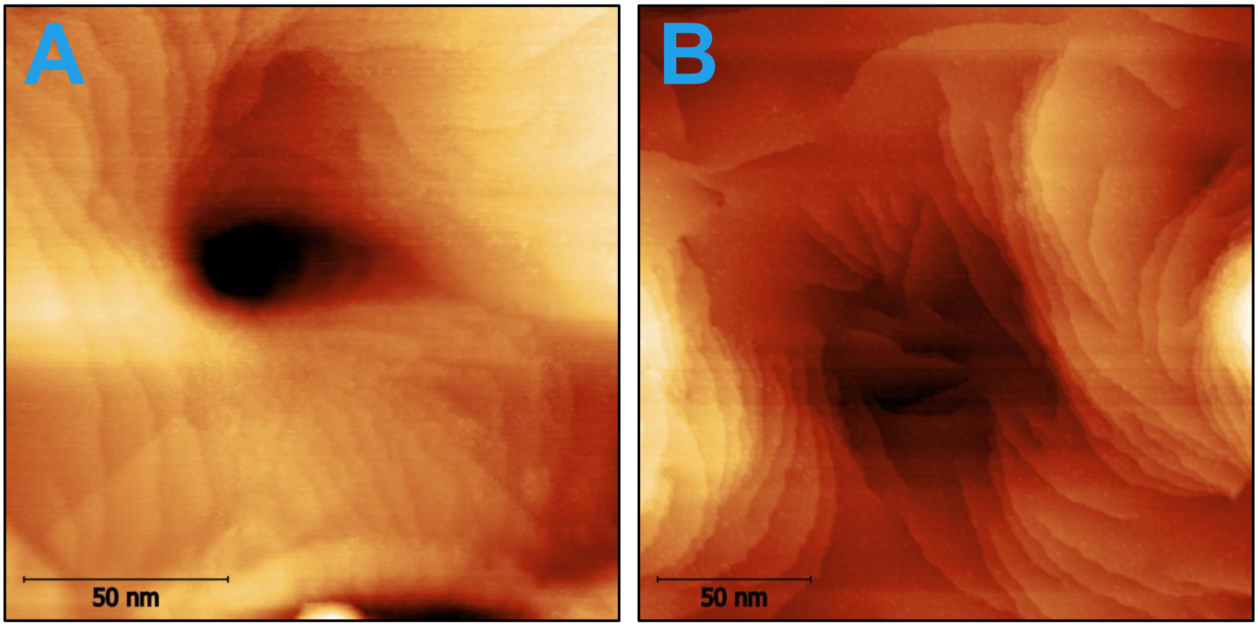

Figure 4-S2. STM image, both taken at 0.15V and 0.1 nA, of (A) Ni-12wt.%Cr before oxidation and (B) the same alloy after 7L + 600 ºC anneal.

The distinct and highly preferential step edge faceting observed post oxidation is no longer present after the crystalline NiO has been thermally removed by the 600 ºC anneal. Given the metal surface's circular terraces, one would expect Ni-Cr to have a relatively isotropic interfacial energy. Once the NiO was removed, removed, the surface would have lacked the surface energy curvature necessary to facilitate faceting, thus driving the surface to relax back to a similar orientation with round terraces.

4-S3. Image Data Processing and Correction

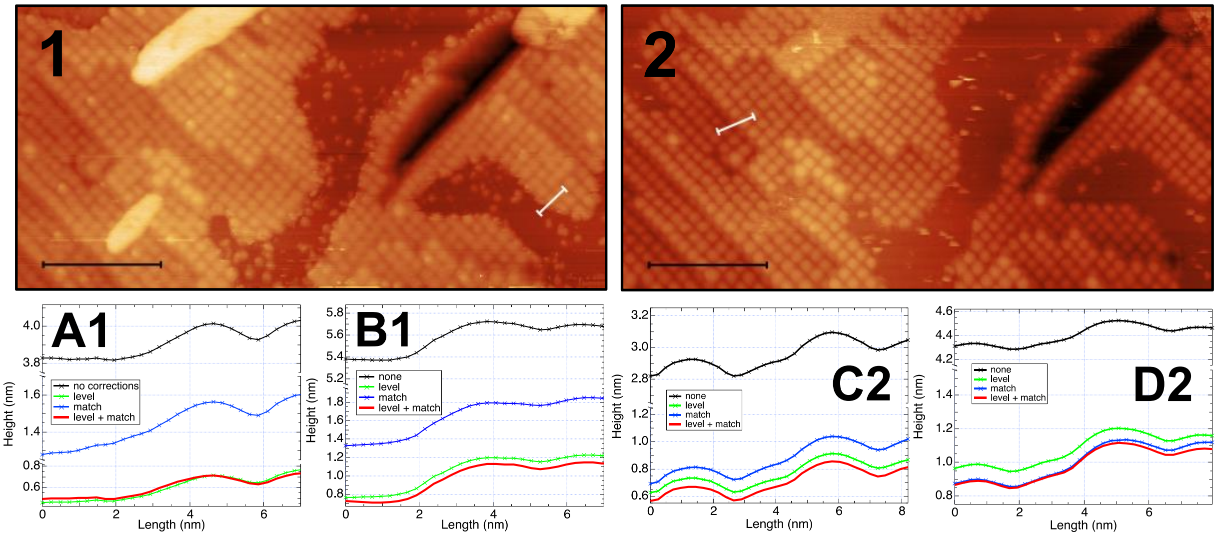

Figure 4-S3-(1-2). The measured step height of 1st - Layer-NiO at (A) -3.0 V and 0.1 nA and (B) 3.0 V and 0.1 nA. The image 1 was taken at the positive bias, while image 2 was taken at negative bias. Both scale bars are 25 nm.

The plots show the different correction methods in Gwyddion[1] used to establish the most appropriate measure of apparent step height between the 1st layer and NiO. To improve the overall visual quality of the images, the reported values in this paper were taken after plane leveling* and feature matching** were employed. As seen by the line profiles, no significant changes in the apparent step heights were observed after post processing. Significant deviations where observed if linescans were taken over large portions of the image, but as shown above smaller and more localized scans were used in the collection of apparent height data. The numerical values for the apparent heights reported in this work were taken from the difference between the surface features above and below a particular line scan, i.e. maximum to maximum.

* Leveled points are identified on the image; a plane between points is generated and subtracted from the data.

**A representative height for each scan line (along the horizontal direction) is found and is subtracted from the background.

4-S4. Apparent Height, and Periodic Rows in Oxide Nodules

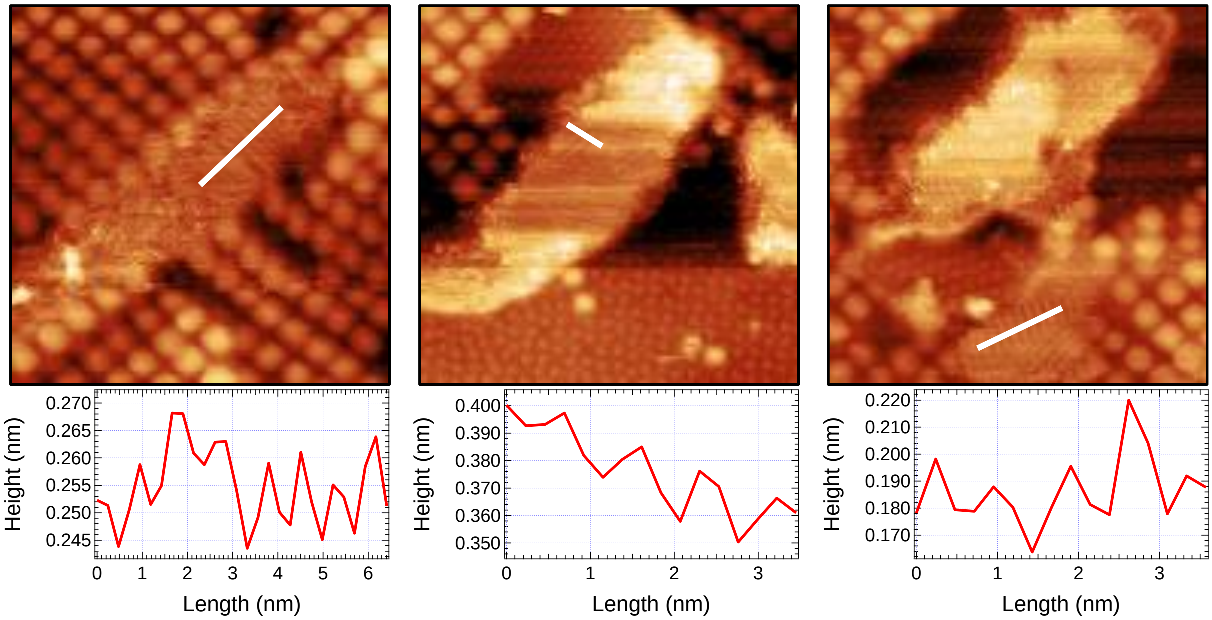

Figure 4-S4.1 Images of the oxide nodules taken at -3.0 V and 0.1 nA. Lines scans were performed across the periodic rows visible in parts of the nodules. Height vs. length of each respective profile were plotted to ascertain the peak distances between the rows.

At negative tip bias the filled states of the oxide nodules were probed and ordered rows were observed. Linescans were taken and the statistical average peak spacing was found to be 0.84 ± 0.03 nm. The lattice constant of the the spinel oxide, $NiCr_2O_4$, has been experimentally and theoretically determined to be 0.83 ± 0.07 nm.[2] Given this similarity and their characteristic surface position, never isolated from the NiO nor the phase separated Cr, it is possible that these nodules are the spinel. However, our current experimental techniques cannot confirm the specific nature of these nodules.

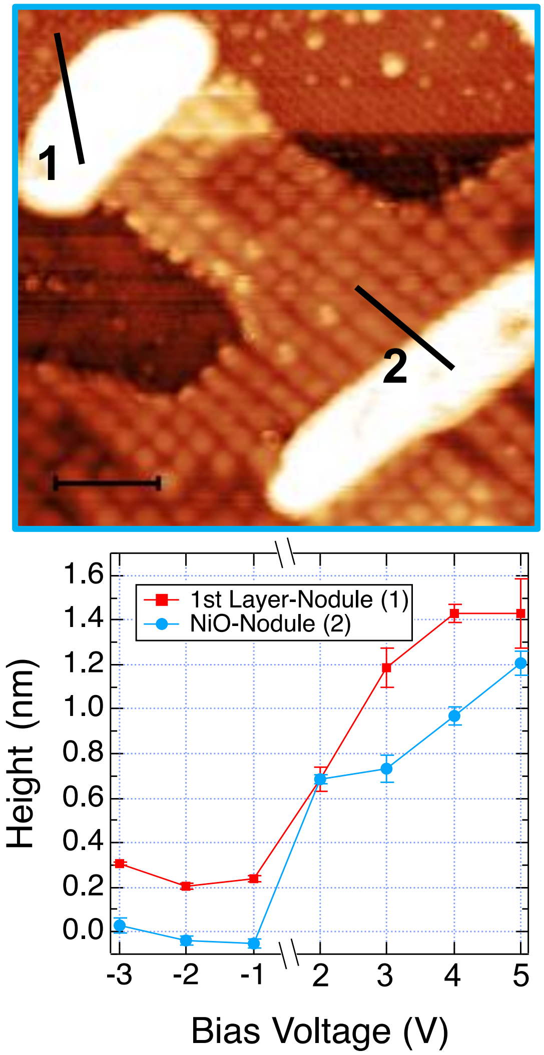

Figure 4-S4.2. The apparent step heights between the 1^{st} layer and the oxide nodules (line profile 1) and the NiO and the oxide nodule (line profile 2). The image was taken at 3.0 V and with a constant tunneling current of 0.1 nA. The scale bar is 10 nm.

Linescans of the oxide nodules reveal that when a negative tip bias is used, the nodules appear as depressions when measured from the NiO to the nodule (line profile 2) and as 0.25 nm protrusions when the apparent height is measured from the 1^{st} layer Ni-Cr-O surface (line profile 1). When positive tip bias is applied, there is a relatively linear increase in apparent height, which reaches a maximum of 1.4 ± 0.18 nm. It is likely that these nodules have reached a limiting thickness, and are this stage of the oxidation have begun to propagate laterally as there is a range in length of nodules varies from 10 nm up to 50nm, but all with relatively similar apparent heights.

S5. Coincidence Lattice – Measurement of NiO Periodicity on Terrace and Wedge

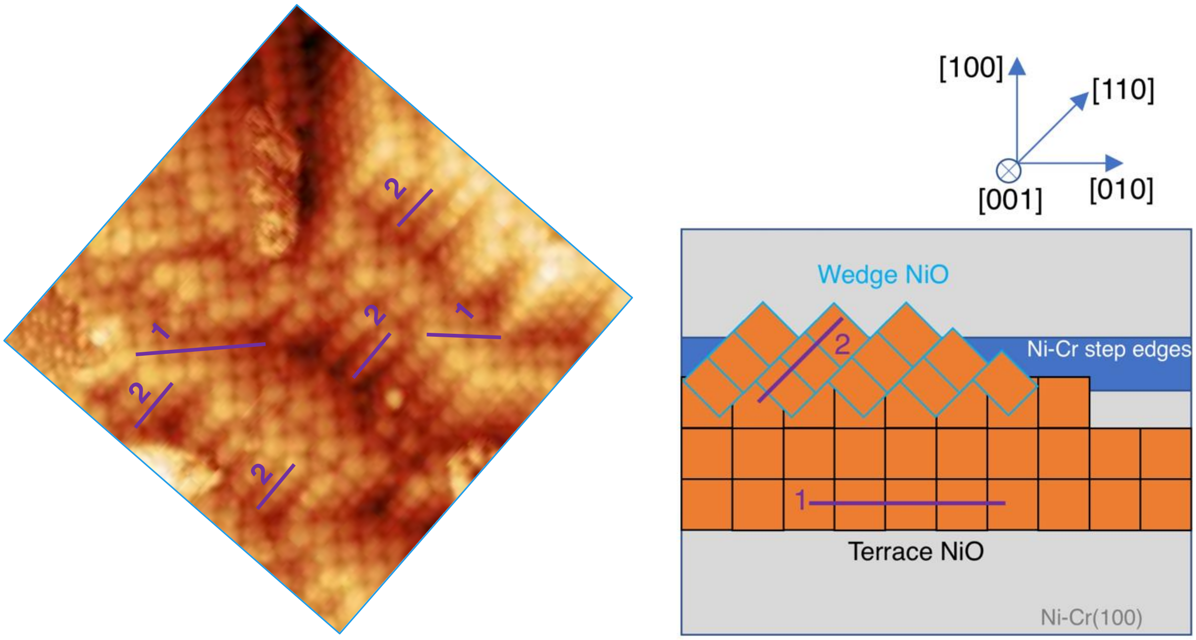

Figure 4-S5. Illustration of measurement of coincidence lattice on terrace (linescan in direction 1), and at step edges (linescan in direction 2). A few lines corresponding to 1 and 2 are icnluded as examples in the image on the left hand side.

This figure illustrates the surface crystallography as it pertains to the measurement of coincidence lattices on the terrace and the step edges. All linescans within the NiO lattice are measured edge-to-edge with respect to the repeat unit in the NiO. The image is identical to Figure 5.B in the main body of the manuscript and rotated to align line 1 and 2 to the schematics on the right-hand side. Line 1 is parallel to the [010] or equivalent [100] direction, and line 2 is parallel to the [110] direction.

Chapter V: Initial Oxidation Pathways on a Ni-15Cr(100) Alloy Surface

5.1 Technical Background

Early stage oxidation of metals commences with the nucleation and growth of partial oxide layers or islands on the surface and results in significant structural and chemical changes at the metal-oxide interface.[1–6] These changes to the metal-oxide interface can influence the passivation process as they predicate the development of a complete and corrosion resistant oxide layer. Specifically, Ni-Cr alloys have gained considerable attention in recent years due to their superior corrosion resistance and excellent mechanical properties.[7–15] Despite the increased focus on this alloy system, a significant gap still exists between the initial adsorption of oxygen and subsequent growth of a complete oxide layer. Models have been developed, such as the Cabrera-Mott model, that specifically consider the growth kinetics of oxide layers between 1 – 10 nm in thickness.[1,16,17] While Cabrera-Mott has been used to successfully describe the temperature-dependent thickening of oxide films and their growth via electric-field driven ion transport, discrepancies arise due to the assorted oxidation pathways exhibited by transition metal alloys, e.g. Ni-Cr. Therefore, by examining the growth of partial oxides during the pre-Cabrera-Mott regime, the fundamental phenomena that drive early-stage oxidation can be realized.

Given the chemically distinct nature of the Ni and Cr, oxide growth on Ni-Cr alloys is governed by the competing oxidation pathways of the two reactive elements. At elevated temperatures, oxidation of Ni(100) begins with the dissociative chemisorption of O_2 and the formation of p(2×2)O and c(2×2)O ordered adlayers.[18–22] The chemisorbed phases trigger step-edge faceting, which kinetically hinders oxide nucleation at the step edges and NiO is only observed after large O_2 doses.[18,19] For Cr(100), a variety of different ordered oxygen adlayers and surface reconstructions have been reported after oxygen exposure.[23–28] It has been postulated that variations in sample surface preparation is responsible for the disparities.[23] While the initial onset and progression of monolayer oxygen coverage is unresolved, the formation of chrome-oxide has been shown to initiate by the incorporation of oxygen atoms into the Cr(100) surface. After a complete layer is formed the initial oxide growth is dominated by oxygen anion transport at $T_{ox} < 300\ ^{o}C$ and by metal cations at elevated temperatures.[28] The unique reaction pathways of the Ni(100) and Cr(100) surfaces suggests that alloying will result in distinctive oxidation processes different from those of the pure constituent metals.

The complex interplay between thermodynamic and kinetic factors in the oxidation of the Ni-Cr system leads to competition between oxide species. Which oxide species will form, and their relative concentration with respect to the total oxide population, will depend on temperature, alloy composition, oxygen partial pressure, and crystallographic orientation. Notably, not all of these factors have been studied in detail, and the present work targets the initial oxidation steps where the competition between oxide species is readily apparent. The lower nucleation barrier for NiO due to cube-on-cube epitaxy is generally assumed to kinetically favor the nucleation of NiO compared to chromia albeit direct experimental observation of the initial oxidation steps as a function of crystallographic orientation is missing.[11] The oxidation of a Ni-5wt.%Cr(100) alloy at $300\ ^{o}C$ revealed oxide island growth after small sequential O_2 exposures, highlighting the addition of Cr removes the temperature induction period for oxide growth on Ni(100) surfaces.[10,18] A surface diffusion model, where oxygen atoms diffused to the oxide growth front, was developed and found a short screening length of 0.3-0.4 nm, suggesting oxide island growth at these temperatures is localized to the island edge.[10] At higher temperatures, oxidation is driven by the transport of metal atoms, as shown during the initial oxidation of a Ni-10at.%Cr(100) sample at 450 ^{o}C.[9] An operando high resolution transmission electron microscopy (HRTEM) study confirmed that NiO growth is kinetically favored, as compared to the more thermodynamically preferred Cr_2O_3, due to the rapid surface diffusion of Ni atoms across NiO within this compositional space.[8,9] Partially closed subsurface layers of Cr_2O_3 were observed beneath the NiO layers at T_{ox} = 700 ^{o}C, and when [Cr] = 20at.% these initially disjointed 'subsurface islands' form a complete Cr_2O_3 layer.[8] The manner in which the NiO and Cr_2O_3 evolve as a function of both temperature and composition reflect the diverse nature of oxide growth on Ni-Cr(100) surfaces and indicate that more work is required if the competition between the different oxidation pathways are to be fully understood.

Recently, our work has focused on the nanoscale observation of Ni(100) and Ni-Cr(100) surface oxidation by studying the sequential oxidation of alloy thin films (8-12wt.%Cr) grow in UHV with STM and STS.[7,29] The initial oxidation on Ni-Cr(100) commenced with the nucleation and growth of NiO along the step edges and a dense population of small oxide particles on the terraces. The NiO formed low-angle grain boundaries with respect to the Ni-Cr(100) surface and a distinct NiO-NiCr(7×8) superlattice lattice was observed across the step-edges, while a NiO-NiCr(6×7) superlattice was found on the terraces.[7,30] Concurrently, a variety of chemisorbed phases and large oxide nodules, assigned as Cr_2O_3 or $NiCr_2O_4$, grew on the terraces. The geometric structure of the chemisorbed phases, which is reminiscent of a Cr(100)-O reconstruction, strongly suggested the segregation of Cr at the surface, however no atomic spacing was observed. STS measurements combined with a statistical analysis of the surface's electronic structure revealed significant spatial variability in the surface band gap and confirmed the compositional and structural heterogeneity of the oxide-alloy interface and surface. The assumption of a homogenous electric field between the alloy and oxide surface is therefore insufficient to describe oxide growth once a complete oxide layer is formed.

Experiments that target the initial progression of oxide growth, combined with surface sensitive techniques, are necessary if the complex nature of early-stage oxidation is to be realized. To this end, STM and STS have been employed to capture the atomistic mechanisms of surface oxidation on a Ni-15wt.%Cr(100) sample at 500 ^{o}C. The Cr oxidation pathway starts by nucleating flat disk-like particles, their size driven by the local distribution of Cr-clusters in the first two (100) planes of the surface. As oxidation progresses phase separation of BCC Cr(100) is observed. Adjacent to these segregated regions are oxide rows and faceted oxide features, which are attributed to the passive Cr-oxide pathway. Initially nucleating at the step edges, the NiO rapidly saturates the surface and thickens, with the next layer initiating growth at the NiO superlattice groove site. Spatially resolved DOS maps reveal the origin of this behavior is attributed to the heterogeneity across the NiO superlattice, imprinted by the alloy-oxide interface. These data are used to build a model for the nanoscale growth of the partial oxide layers Ni-Cr(100) surfaces. Together, these details on the evolution of the surface's electronic and geometric structure have further illuminated the nuances of early-stage oxidation on Ni-Cr alloys within the pre-Cabrera-Mott regime.

5.2 Methods

Each step of the oxidation experiment was conducted *in-situ* under ultra-high vacuum (UHV) conditions using an Omicron Nanotechnology Variable Temperature Scanning Probe Microscopy (VT-SPM) system. The base pressure during measurements was kept at 3.0×10^{-10} mbar and imaging was conducted with an electrochemically prepared tungsten tip at ambient temperature. Using electron beam evaporation, the Ni-15wt.%Cr(100) thin film was grown using Ni (Alfa Aesar 99.999% purity) and Cr (American Elements, 99.95% purity), which were deposited on pretreated MgO(100) single crystal substrates.[29] Prior to the alloy thin film growth, the deposition rates of the Ni and Cr were measured using a quartz crystal monitor to accurately adjust the film composition. The deposition of the Ni-15wt.%Cr(100) thin film followed the procedure developed previously.[29] The starting alloy surface was found to have wide round terraces and the cleanliness and metallicity of the surface is confirmed by STS, supporting information Figure 5-S1. Oxygen was introduced through a sapphire leak valve while the Ni-Cr(100) sample was held at a constant elevated temperature of 500^{o} C and once the sample had cooled, the alloy surface was imaged at each oxidation step. Oxidation steps of +7 L ($p[O_2] = 7 \times 10^{-9}$ mbar, t = 1330 s), +7 L ($p[O_2] = 7 \times 10^{-9}$ mbar, t = 1330 s), and +4 L ($p[O_2] = 4 \times 10^{-9}$ mbar, t = 1330 s), for a cumulative of 18 L of O_2 exposure, were used to achieve partial oxide growth on the surface. 1 L (Langmuir) corresponds to 1 s exposure at 13.3×10^{-6} mbar of $p[O_2]$ and is equivalent to a monolayer of adsorbed molecules assuming a sticking coefficient of one. The composition of the alloy film was verified *ex-situ* by energy dispersive spectroscopy (EDS) with a Quanta LV650 Scanning Electron Microscope (SEM).

The surface topography and local density of states (LDOS) of the sample were measured before and after oxidation by STM and STS. The grid spectra were captured by sweeping the bias voltage (V_{bias}) from ±3.0 V and measuring an I/V curve for every fourth image pixel with an open current feedback loop. Simultaneously, the topography information was recorded for the next three pixels, where the tunneling current (I_t) was set at $I_t = 0.1$ nA and a bias voltage $V_{bias} = 3.0$ V was used. The I/V curves were numerically differentiated to generate dI/dV curves, which are then normalized by (dI/dV)/(I/V) following the procedure described by Feenstra et al..[31,32] The band gap was numerically determined from the normalized curves, by calculating the region where (dI/dV)/(I/V) is smaller than a threshold value, i.e. where the density of states (DOS) is effectively zero, and distributions of valence/conduction band extrema and band gap values were generated from these data. The (dI/dV)/(I/V) spectra are then spatially resolved by selecting a specific voltage slice (e.g. $V_{slice} = -2.7$ V) to highlight the contrast in local electronic structure at that particular voltage and displayed as a DOS map. This allows for the direct comparison between topography and electronic structure. Prior to display and analysis of the topography images, each surface was leveled by mean plane subtraction and planarization using the post processing software Gwyddion.[33] A MATLAB code implementing routines for grey-scale segmentation was also used to analyze some of the surface features and is highlighted in the supplementary information section Figure 5-S2.

To understand the clustering of Cr atoms within the Ni lattice, an in-house MATLAB code was written that modeled the first two surface planes of the lattice and identified clusters of adjacent Cr atoms. Matrices were used to represent atom planes of the (100) surface and a random number generator probabilistically assigned a 1 (Cr) or 0 (Ni) to each position in a square matrix corresponding to the atomic coordinates of an FCC Ni lattice (supporting information Figure 5-

S2). Two such planes were created representing the i) top surface plane and ii) the plane below the surface, properly offset to simulate an FCC (100) surface. Inter-atomic forces are not taken into account, so the occupation of each site is random, and the formation of clusters is therefore only a consequence only of probability. Clusters of Cr atoms were identified by finding Cr atoms and recursively checking all adjacent positions (8 positions in the same plane and 4 in the other plane) for other Cr atoms until no more are found. These clusters were then categorized by size (i.e. the number of Cr atoms in the cluster) and visualized via subroutines in the code. No distinction was made between Cr atoms that were adjacent laterally, diagonally, or from different planes, and a periodic boundary condition was used to eliminate edge effects. Only the Cr atoms in the top two (100) planes were considered, but the program mandated that at least one Cr atom in each cluster must be on the top surface plane to be counted since this is interpreted as the primary reaction site (supporting information Figure 5-S3).

5.3 Results

5.3.1 General trends in surface oxidation

STM images of the Ni-15wt.%Cr(100) surface prior to oxidation and after each exposure step are displayed in Figure 5-1. The onset of oxidation, **7 L of O_2** exposure at 500 ^{o}C, results in significant changes to the surface-free energy of the alloy. Oxide growth initiates with step-edge faceting driven by partial step-edge decoration of an angled NiO-NiCr(7×8) superlattice (i.e. NiO wedge), while oxide particles, tentatively assigned as Cr-oxide particles, have nucleated and grown across the terraces and some step edges, Figure 5-1(b)-(c).[7,18,19] After a **14 L cumulative exposure**

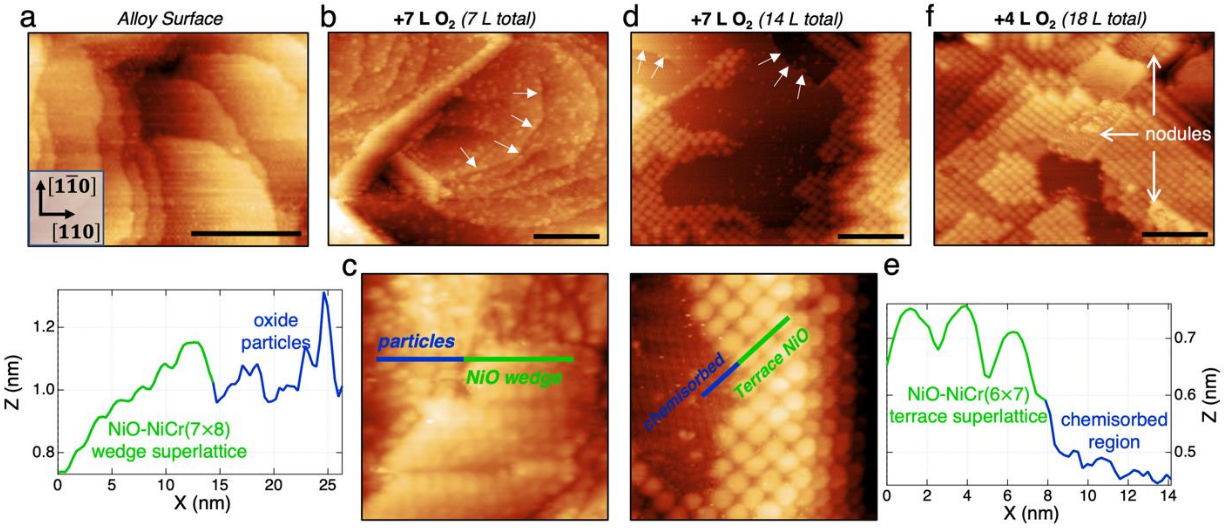

Figure 5-1. Topography of the alloy surface prior to oxidation is given in (a). The progression of oxidation after cumulative O_2 exposures at 500 °C of 7 L (b)-(c), 14 L (d)-(e), and 18 L (f). All scale bars are 20 nm. The white arrows indicate step edges that have not faceted, and are still curved despite oxygen exposure. Image (a) was measured at V_{bias} = 0.25 V, I_t = 0.5 nA, (b), (c), (d), and (e) at V_{bias} = 2.0 V, I_t = 0.1 nA and (f) at V_{bias} = 3.0 V, I_t = 0.1 nA. The images in figures (c) and (e) are both 30 ×30 nm^2 and show the different features after cumulative 7 L and 14 L exposures, respectively. Line scans of each feature at this oxidation steps are provided.

the NiO wedges have thickened and NiO has grown across the terraces, taking a different epitaxial relationship with the alloy by forming a NiO-NiCr(6×7) superlattice, Figure 5-1(d)-(e). The different NiO superlattices and their effect on the alloy surface have been discussed extensively in the following reference.[7] At this exposure, the Cr-oxide particles are no longer present on the surface and instead a variety of chemisorbed oxygen adlayers are found between the NiO layers, Figure 5-1(e). Additional oxidation, +4 L **(18 L cumulative)**, causes greater NiO surface coverage, the emergence of more 2nd layer NiO, a reduction in the surface area covered by ordered chemisorbed adlayers, and the growth of sizable oxide nodules,[7] Figure 5-1(f). It is evident from these images that the Ni-Cr(100) oxidation pathway is as complex as it is varied, and therefore will be discussed piecewise in this report starting with a closer look at the oxide clusters observed in the very early stages of oxidation.

5.3.2 Cr oxidation pathway: Growth of the a chromia layer

The NiO oxidation pathway presents clearly in the topography images post exposure, and the oxidation of Cr appears to begin with the nucleation and growth of oxide particles. To better understand the particle geometry, height and area distributions are taken over flat segments of the alloy surface, represented by the 3D topography image in Figure 5-2(a). The height distribution in Figure 5-2(b) reveals an apparent height of approximately 1.25 Å, while the area distribution obtained via the MATLAB segmentation code is relatively broad, Figure 5-2(c). Given the shallow apparent height another method for the quantification of particle dimensions was employed, and the particles were assumed to be flat disks, where the $Area = \pi r^2$ and r was determined by numerous line scans. This second method yielded an area distribution in excellent agreement with the distribution obtained by the segmentation code, therefore modeling the Cr-oxide particles as flat disks and islands is acceptable.

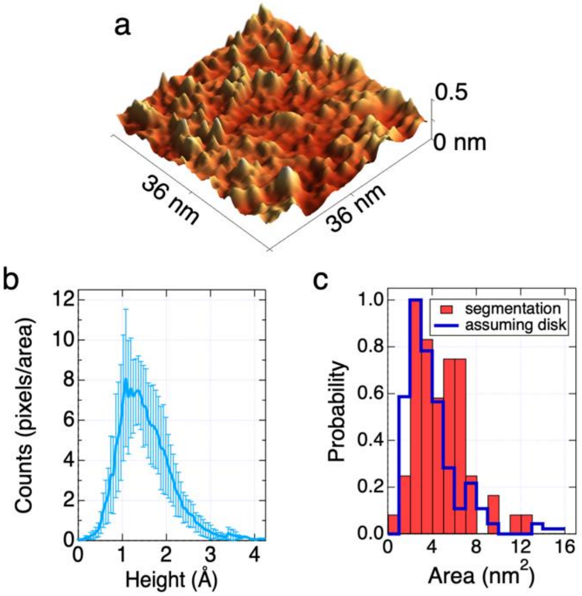

Figure 5-2. (a) 3D topography image showing the oxide particles present after 7 L of oxygen exposure along with (b) their height distribution. The area distribution of these particles is summarized (c) and was determined two different ways, i) via grey-scale segmentation (see supporting information) and ii) line scans combined with the assumption that the particles are disks ($A = \pi r^2$), which was used to translate radius into area distributions. The topography image was taken at V_{bias} = 2.0 V, I_t = 0.1 nA.

The Cr-oxide particles have been observed in our prior work on Ni-Cr(100) oxidation and are thermally stable with respect to annealing at 600 °C, contrasting the NiO which was reduced and thus removed from the surface during this heat treatment.[7] Similar particles have also been previously reported during thermal oxidation of pure Cr thin films.[34] Our STM results show the Cr-oxide particles preferentially populate across the alloy terraces and some step edges, marked by white arrows in the Figure 5-1(b). The extent of NiO step-edge coverage is found to be higher on Ni-Cr(100) samples with lower Cr concentration,[7] suggesting that step-edges with a higher local Cr concentration nucleate Cr-oxide particles instead of undergoing NiO driven step faceting. Essentially, NiO formation at the step edges competes with the nucleation of Cr-oxide particles. However, STM and STS do not deliver compositional information in the absence of a well-recognized surface structure (e.g. NiO), so we assign these features as Cr-rich oxide particles, as opposed to asserting they are purely Cr-based. Certainly, the initiation of Cr-oxidation is dominant on the terraces and step edges with higher Cr concentration, therefore we propose here that the presence of Cr-oxide particles can be linked to the distribution of Cr-atoms in the Ni-Cr(100) solid-solution surface.

To develop a qualitative understanding of oxide particle formation on the surface after the 7 L exposure, we developed a MATLAB code that describes the random distribution of Ni and Cr atoms within the first two layers of a substitutional solid-solution FCC(100) surface according to a predefined alloy stoichiometry. The population of dimer, trimer, tetramer, and pentamer sized Cr-clusters for a variety of different alloy compositions is displayed in Figure 5-3(a), where numerous simulations were run for each alloy composition, and the number of Cr-clusters (n) of a given atom size is shown as a function of at.%Cr. The details of cluster counting are given in the supplementary information Figure 5-S3. The number of Cr-clusters reaches a maximum when the

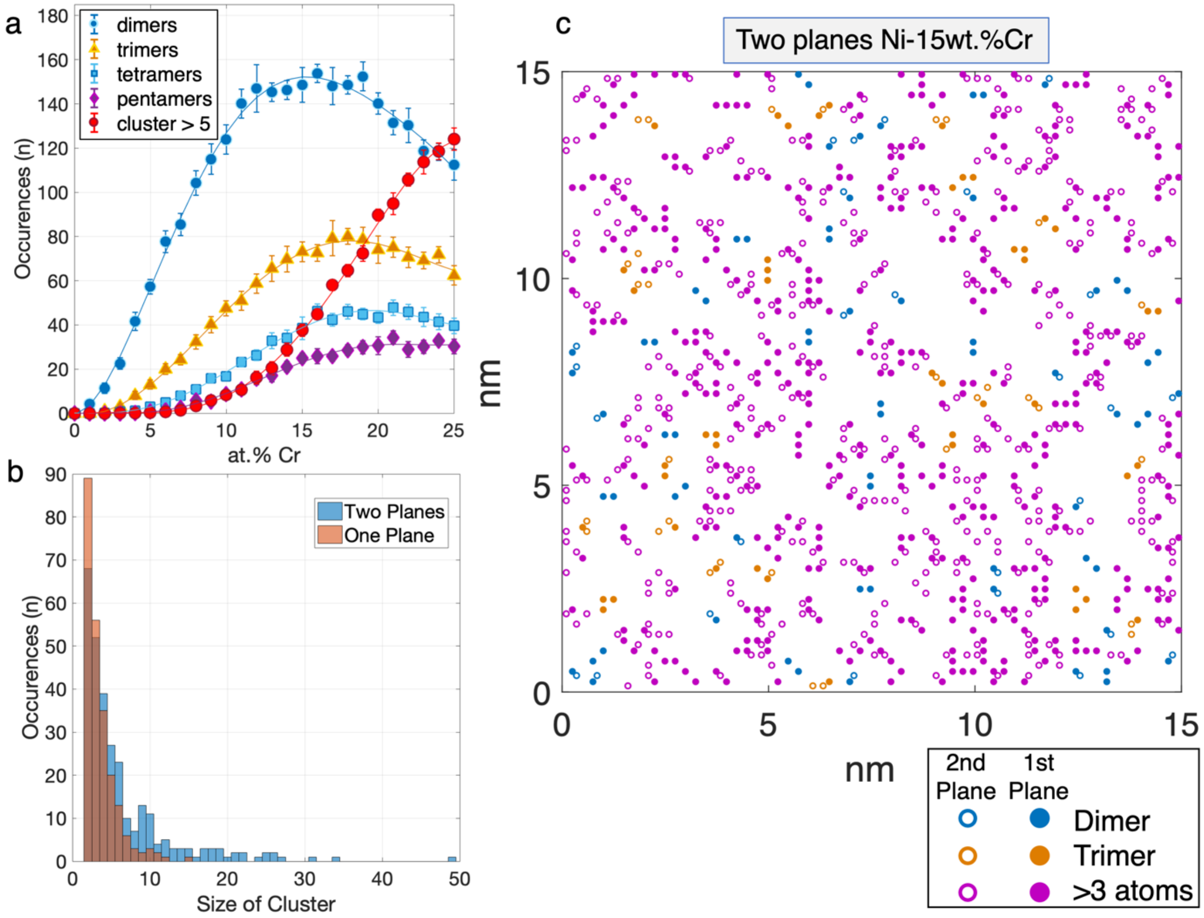

Figure 5-3. The graph (a) depicts the occurrences of different cluster sizes as a function of Cr concentration in the top two (100) planes (100x100atoms). The histogram in (b) displays the size distribution of Cr clusters on the surface of the Ni-15wt.%Cr alloy. A 15x15 nm^2 visual representation of Cr clusters in the first two planes of a Ni-15wt%Cr alloy is given in (c), with dimers shown as blue, trimmers as orange, and tetramers or larger as pink circles (1st plane) and open circles (2nd plane), where at least one atom had to be present on the top layer (1st plane) to be counted as a cluster for the 2nd plane.

composition (cluster-size) is 16at.%Cr (dimer), 19at.%Cr (trimers), 20at.%Cr (tetramer), and 22at.%Cr (pentamer). The contributions from clusters with n>5 increases rapidly for Cr concentrations exceeding 15at%. A closer look at the cluster distributions for a Ni-15wt.%Cr(100) alloy is provided in Figure 5-3(b)-(c).

The average cluster size increases with the addition of a second layer, which is summarized in the histogram presented in Figure 5-3(b). This result is expected given that the addition of a second layer increases the coordination number and inherently leads to larger and more realistic cluster sizes. The second layer can be interpreted as a Cr-atom reservoir that feeds the growth of nanoscale surface oxides at these temperatures. A spatial representation of the 1st and 2nd plane clusters on a Ni-15wt.%Cr(100) is provided in Figure 5-3(c). These filamentous Cr-surface clusters are the preferred oxygen adsorption sites, since DFT has shown that Cr is a preferential bonding site for oxygen in Ni-Cr alloys,[12,35] and consequently the precursors for islands and particles formed in the initial reaction steps. Indeed, the distribution of the Cr within the first few layers of the alloy is likely responsible for the initiation of the passive chromia layer, while the NiO is driven by epitaxial effects. A more detailed study of the re-organization of Cr within the surface layer in response to oxygen adsorption and development of chemical potential driven diffusion is in progress.

Once the sample is exposed to a **cumulative 14 L of O_2**, the oxide particles are no longer present. Instead, ordered chemisorbed oxygen adlayers have emerged across the surface and a complex mixture of different structures and domains are present. A few segments of curved alloy step edges are retained and covered with these adlayers, marked by white arrows in Figure 5-1(d). Unlike the c(2×2) reconstruction on pure Ni(100) the chemisorbed adlayers observed here do not induce step edge faceting. Images of these surface reconstructions/adlayers (generally referred to as ‘chemisorbed regions’ in ref.[7]) are provided in the supplementary information section Figure 5-S4. None of these surface structures exactly correspond to known chemisorption adlayers or surface oxides, however some have symmetries that are partially reminiscent of surface reconstructions observed on oxidized Cr(100) surfaces.[23–28] However, the inter-maxima distances deduced from the STM images are significantly larger and do not correspond to any known chemisorbed oxygen adlayer, alloy or oxide-alloy interface, and STS yields an unusually broad distribution of band gap values centered at about 1.8 eV.[7] Indeed, these chemisorbed structures

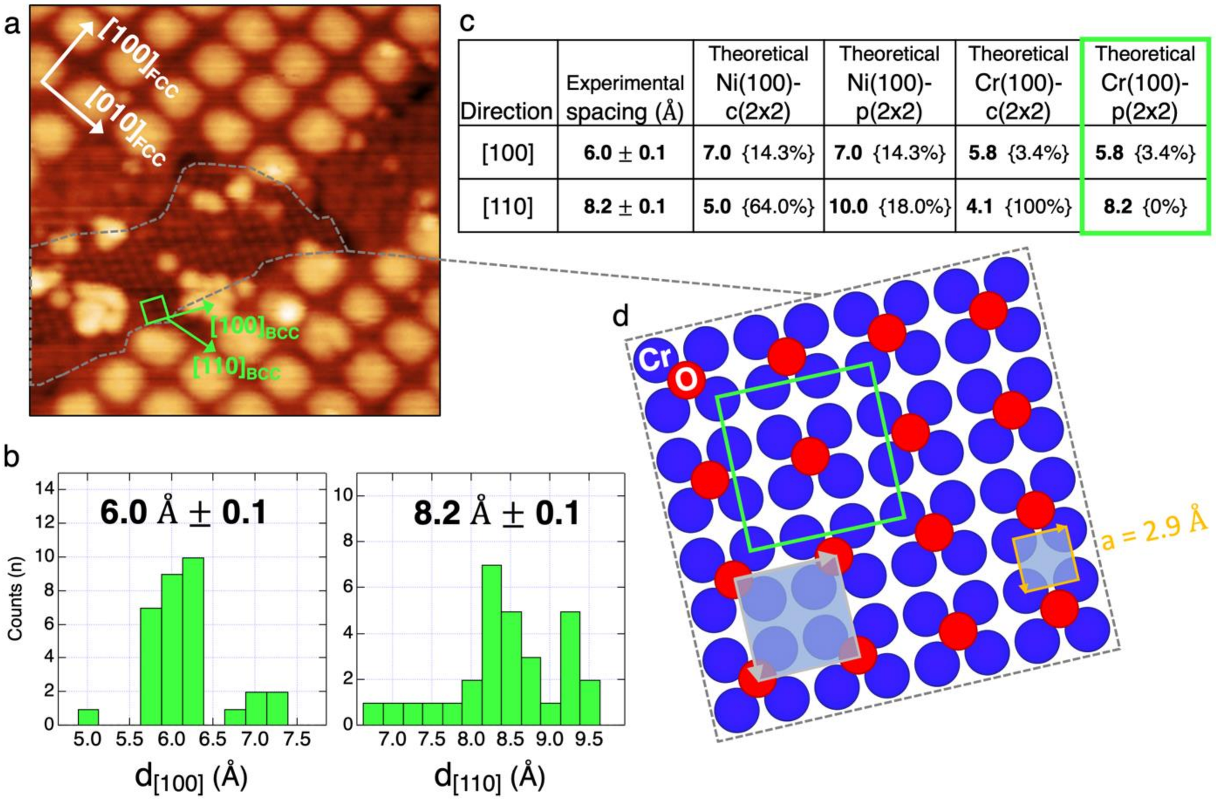

Direction	Experimental spacing (Å)	Theoretical Ni(100)-c(2x2)	Theoretical Ni(100)-p(2x2)	Theoretical Cr(100)-c(2x2)	Theoretical Cr(100)-p(2x2)
[100]	**6.0** ± **0.1**	**7.0** {14.3%}	**7.0** {14.3%}	**5.8** {3.4%}	**5.8** {3.4%}
[110]	**8.2** ± **0.1**	**5.0** {64.0%}	**10.0** {18.0%}	**4.1** {100%}	**8.2** {0%}

Figure 5-4. The topography image (a), 20×20 nm^2 after the 18 L oxidation step. This oxidation step illustrates the segregation of Cr(100) and the FCC and BCC surface orientations are superimposed over the image. The distributions in (b) represent the maximum-maximum spacing along the $[100]_{BCC}$ and $[110]_{BCC}$ directions, respectively, with the average spacing given in each plot. Using the geometry presented in the STM images, table (c) outlines the spacings {experimental error} expected for possible surface structures, assuming a variety of different coverages and orientations. A model of the Cr(100) surface for the Cr(100)-p(2×2) phase is provided in (d), which has an excellent agreement with the experimental data. The STM topography image was taken at V_{bias} = -3.0 V, I_t = 0.1 nA.

could be a collection defects or oxide nanocavities, which have been observed to form at oxide-metal interfaces.[36] Given these regions are most prominent after 14 L of exposure, but disappear with the addition of just 4 L of O_2, the chemisorbed oxygen adlayers are likely metastable, intermediate surface structures with unique oxygen coverages and distinctive interfacial relationships with the metal lattice below.

After an additional 4 L oxidation step **(18 L cumulative)**, the aforementioned chemisorbed oxygen adlayer regions disappear. Instead, a new set of surface structures emerge: a reconstruction/chemisorbed adlayer with a square unit cell, an oxide “row” structure, and a faceted oxide feature now dominate at this coverage and mark the progression of the oxidation process. Figure 5-4(a) shows a high-resolution image of one of these structures, whereby an ordered surface structure is atomically resolved in between the NiO edges. Taking line scans along the max-to-max positions reveals an average max spacing of 6.0 Å ± 0.1 and a diagonal spacing of 8.2 Å ± 0.1 confirming the square geometry of the structure. Distributions of these data are provided in Figure 5-4(b). The spacings were compared with a variety of possible O-adsorbate surface structures on both, Ni(100) and Cr(100) surfaces, and the theoretical spacings and respective percent error {%} are provided in the table included in Figure 5-4(c).[37] The Cr(100)-p(2×2)O ordered phase best fits the measured spacings, and a model surface structure is illustrated in Figure 5-4(d) where the p(2×2) unit cell is marked in grey. The green square illustrates correspondence between the model and topography image, also marked with a green square in Figure 5-4(a). The deviation between experiment and reported theoretical values for Cr(100)-p(2×2)O is well within the experimental error.

The presence of this atomically resolved adlayer highlights a BCC Cr(100) lattice region is embedded within the FCC Ni-Cr(100) alloy surface and emphasizes oxidation can induce phase separation of the alloy. The Cr(100)-p(2×2)O surface section is rotated by approximately 27^{o} with respect to the NiO lattice. It should be noted that we cannot see the oxide-alloy interface itself, therefore it is possible the BCC layer has a unique epitaxial relationship with respect to the surrounding FCC matrix.[38–41] The presence of this Cr(100) phase is evidence that the surface composition of the alloy changes significantly after O_2 exposure and the alloy surface can no longer be considered simply as a FCC Ni-Cr(100) random solid solution. This analysis confirms the formation of areas with pure Cr surface layers, which form by phase separation from the alloy and present the characteristic Cr(100)-p(2×2)O surface.

After **18 L** of O_2 the Cr(100)-p(2×2)O surface dominates the regions between the NiO, along with the oxide rows and faceted-oxide features. These oxides offer significant challenges in their assignment and are discussed in this paragraph in more detail. Both features are commonly seen adjacent to the Cr(100)-p(2×2)O surface structure, and examples can be seen in Figures 5-4(a), 5-5(a) and 5-5(b). Their proximity to known segregated regions of Cr(100), as well as their

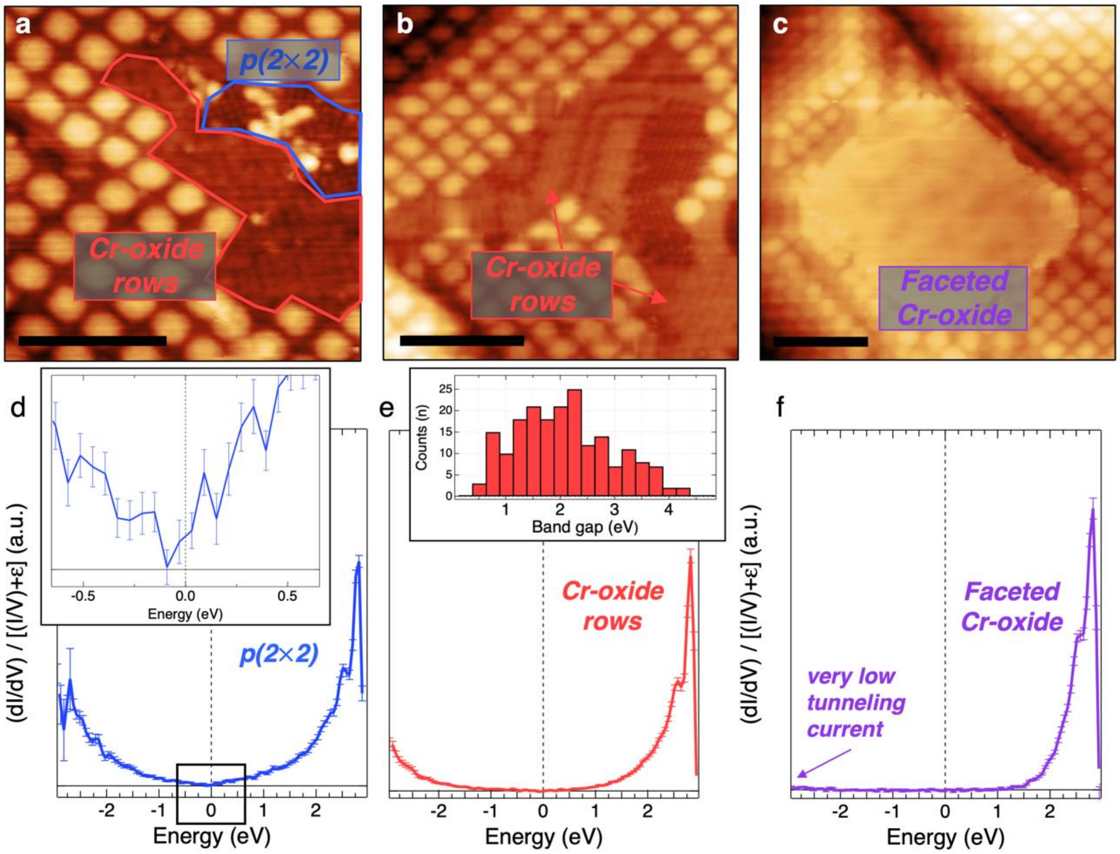

Figure 5-5. Topography of the oxide rows and faceted oxide feature (tentatively assigned as Cr-oxides) are provided in (a) and (b). The STS curves of each of these features is shown in (d)-(f). Specifically, the STS for the p(2x2) and oxide rows (Figure (d) and (e), respectively) were both taken from their respective regions shown in image (a). A close up of the normalized spectra near the Fermi energy is superimposed over (d) and a band gap distribution of the oxide rows is superimposed over (e). The STS for the Cr-oxide, (f), was taken from the topography image (c). The image in (a) was measured at V_{bias} = -3.0 V, It = 0.1 nA, while (b) and (c) were both measured at V_{bias} = -3.0 V, It = 0.05 nA. All scales bars are 10 nm.

distinctive geometric and electronic structures from that of the NiO, we assign them to the Cr-oxidation pathway and tentatively ascribe them as "Cr-oxide rows" and "faceted Cr-oxide" layers, respectively. The "Cr-oxide rows" are geometrically distinct from the NiO or previously reported chemisorbed adlayers, and the spacings between the rows are quite varied, supplementary information Figure 5-S5. The Cr(100)-p(2×2)O surface presents a nearly metallic signal, while the Cr-oxide rows have a significant variability in their electronic structure with an average band gap of 1.9 ± 0.1 eV, as shown in Figure 5-5(d) and 5-5(e) respectively. The band gap is smaller than that for the proper oxides, but higher than seen for the chemisorbed adlayer regions, indicates the presence of a surface oxide as a transition state between adsorbate and fully formed oxide. Figure 5-5(c) illustrates the "faceted Cr-oxide" features adjacent to the Cr(100)-p(2×2)O regions. The tunneling current from the filled states in STS is very small, and indicative of the insulating nature of the oxide feature, Figure 5-5(f). A periodic surface structure with rectangular symmetry is observed when their filled states are measured with a rather high V_{bias} = -3.5 eV, which is included in the supplementary information Figure 5-S6.

The chemical nature of these oxides remains open to interpretation, and is challenging to resolve like most oxide surface structures. It has been demonstrated that $Cr_2O_3(100)$ surface configurations are susceptible to local oxygen content and oxygen partial pressure variations,[42–46] and a simple feature matching approach might not be informative in this case. We propose that when taking into account both the electronic and geometric structure of the Cr-oxide rows and faceted Cr-oxide features, and their proximity to regions of segregated Cr(100), that they might be a manifestation of the intermediate stages of Cr-oxide growth on the Ni-Cr(100) surface. While we have assigned these two oxides to the overall Cr-oxidation pathway, we are hesitant to be more definitive about their stichometry and crystallography, hence the relatively vague nature of their labels as “Cr-oxides.” This result is in agreement with the generally reported observation that Cr_2O_3 growth on Ni-Cr alloys is slower than the formation of NiO during the initial stages of oxidation.[8,9,47]

5.3.3 Next layer NiO growth: Chemical fluctuations across the superlattice

The oxidation pathway of the NiO initiates at the alloy step edges, presenting as a NiO-NiCr(7×8) superlattice, and as oxidation progresses the terraces become saturated with the NiO-NiCr(6×7) superlattice following a cube-on-cube epitaxy.[7] As the total oxide coverage increases small areas of second and third layer NiO begin to appear. Figure 5-6(a) displays the topography image of the NiO after **18 L of oxygen exposure**, and an image inset showing the emerging next

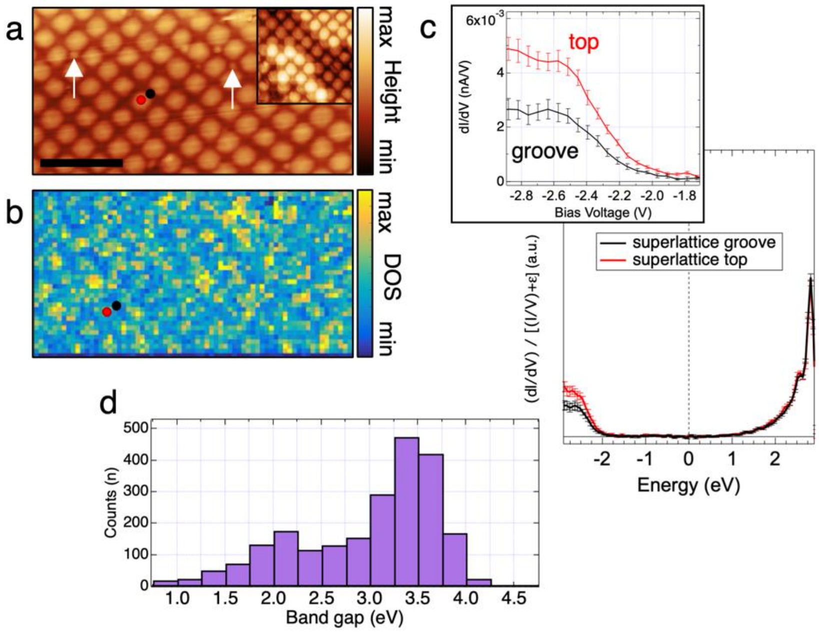

Figure 5-6. (A) is the topography of the NiO-NiCr(100) superlattice structure and an accompanying DOS map (B) at $V_{slice} = -2.7$ V. The image inset in (a), 20×20 nm^2, shows the orientation of the next NiO layer and is from a Ni-12wt.%Cr(100) sample. The white arrows point to small protrusions in the NiO found over the groove site of the superlattice. The red and black dots represent the superlattice top site and the groove site, respectively, where the averaged normalized dI/dV spectra (20 curves) were taken. The inset above the normalized spectra shows the difference in DOS of the respective sites. (D) is a distribution of the band gap values taken from the entire DOS map in (b). Image (a) was taken at $V_{bias} = 2.0$ V, $I_t = 0.1$ nA and the inset at $V_{bias} = -1.0$ V, $I_t = 0.1$ nA. The scale bar is 10 nm.

layer. The next layer is always seeded along the NiO-NiCr(6×7) superlattice groove site. Small spherical embedded protrusions can be seen between these grooves, as indicated by white arrows in the topography image, Figure 5-6(a) and could represent the nuclei of next layer growth. A line scan across these features is included in the supporting information Figure 5-S7. Indeed, the superlattice sites – grooves and top sites - differ subtly in the electronic structure of the valence band, which is seen in the grid STS DOS (density of states) map summarized in Figure 5-6(b).

This figure was formatted from the spectroscopy results and is shown for V_{slice} = -2.7 eV. The variation in DOS across the surface reflects the registry of the superlattice: averaged STS point spectra (~20 curves) comparing the groove sites (black dot) with the top sites (red dot) are shown in Figure 5-6(c), and illustrate that the local variation in DOS is tied to differences in the valence band. The dI/dV curves indicate a $2 \times 10^{-3}\ nA/V$ relative decrease in the differential conductance at the groove site, as compared to the top site. The corresponding band gap values from the entire DOS map are summarized in Figure 5-6(d), and a visualization of the corresponding band gap map can be found in the supplementary information section Figure 5-S8, along with a valence band maximum map. The majority of the spectra yield a band gap of about 3.5 eV, however the distribution is relatively broad. The electronic structure of the NiO across the superlattice is heterogeneous, and signifies chemical differences imprinted by bonding at the NiO and Ni-Cr(100) interface. We propose that the preference for the initial nucleation of the next NiO layer at the groove sites is connected to local electronic structure variations, and preferential diffusion paths for Ni created within the superlattice structure.

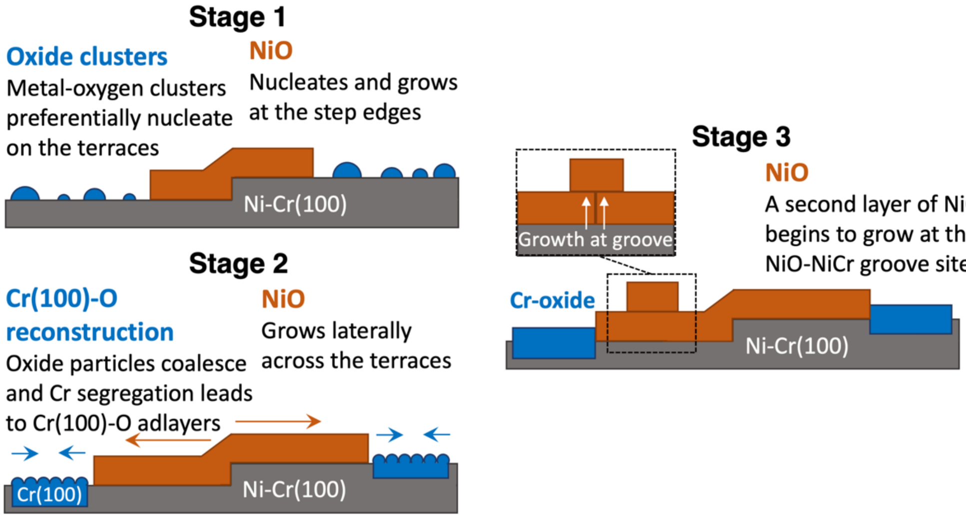

Figure 5-7. A model for the early stage oxidation of a Ni-Cr(100) alloy surface at 500 °C. Each stage of the oxidation process is highlighted with a diagram showing the evolution of each oxide product on the surface after low dosages of oxygen exposure.

5.4 Discussion

A general oxidation model is developed in Figure 5-7, where the oxidation pathways of the Ni and Cr are partitioned and described over 3 stages. The oxidation of Ni-Cr(100) surfaces has revealed the nucleation and growth of NiO begins at the step edges, while Cr-rich oxide particles form on the terraces (stage 1). As oxygen exposure increases, NiO grows laterally, across the terraces and a chromium rich phase nucleates and grows on the surface, which is (partially) covered in Cr(100)-O adlayers triggered by local Cr-segregation (stage 2). Further oxidation causes the Ni-Cr(100) surface to become saturated with oxide and the NiO begins to grow vertically, primarily via the transport of Ni cations through the groove site in the superlattice, while the Cr-oxide grows into the alloy as subsurface Cr-oxide layers begins to form.[8]

The early stage oxidation of Ni-Cr(100) alloy surfaces leads to structural and compositional changes along the alloy surface. After **7 L of O_2 exposure** at 500 °C, changes in surface free energy initiate step-edge faceting via the growth of NiO wedges, low-angle grain boundaries that mitigate strain at the oxide-alloy interface represented by the NiO-NiCr(7×8) superlattice, and the formation of oxide particles along the terraces and some of the step edges. At low partial pressures of O_2, these oxidation pathways will depend greatly on the adsorption of oxygen, which will be influenced by the d-bands of the Ni and Cr.[12,35,48–50] Recently, it has been shown that Cr hybridizes more readily with the oxygen on Ni-Cr surfaces.[12,35] These electronic effects enhance the propensity for oxygen adsorption at the Cr sites, supporting the assumption that the oxide particles on our Ni-Cr(100) surface are likely Cr-rich. Similar particles have also been observed on Cr(110) surfaces,[34] further bolstering this assignment, which indicates these clusters are a function of Cr and local chemistry, not of crystallographic orientation. As such, the local clustering and bonding of Cr atoms at or near the surface are important for initiating the growth of a passive layer on Ni-Cr alloys. This behavior contrasts NiO growth, whose formation depends considerably on epitaxy.

The distribution of Cr across the first two planes of a Ni-Cr(100) surface was evaluated using a MATLAB code, where Cr cluster sizes > 5 atoms increased significantly at about 15at.%Cr (~13wt.%). Given the size and shape of the oxide particles measured with our STM after 7 L, we can assume that the oxide particles are likely initiated on the filamentous Cr clusters, i.e. “strings” of Cr clusters. As a reaction to the initial O-adsorption event the local Cr diffusion is favored through a chemical potential gradient and leads to the formation of local clusters. While their formation is driven by the presence of Cr, they certainly can contain some Ni as a minor component.

After additional oxidation **(14 L cumulative)** the NiO extends across the terraces, presenting as a NiO- NiCr(6×7) superlattice, and the oxide particles are no longer visible. The oxide clusters are thermally stable[7] but transform into the (chemisorption) oxygen adlayers during continued exposure, lowering the surface free energy and wetting the alloy surface. A variety of new surface structures with variable electronic signatures are now present. These have been observed on Ni-Cr(100) surfaces with smaller Cr content, but are only marginally related to surface structures on the corresponding pure metal surfaces.[7] These chemisorbed adlayers are interpreted as metastable oxide phases, but their size and spacing disallow confident identification of the atomic scale structure (supplementary information Figure 5-S4).

Continued oxidation **(18 L cumulative)** and the NiO has begun to undergo next layer growth, always propagating from the superlattice groove of the layer below. A heterogenous electronic signature is measured at these sites and is a consequence of the registry at the NiO-NiCr interface. Given the next layer of the superlattice is always offset by half a superlattice cell,[7] the grooves are likely sites for the diffusion of metal atoms and defects. Distinct Cr(100)-p(2×2)O regions are also detected at this exposure, and are identified by their geometric spacing and mostly metallic electronic signature. Adjacent to the p(2×2) regions, Cr-oxide rows and faceted Cr-oxide regions are also found.

The Cr(100)-p(2×2)O reconstruction is the first step in the surface transformation to oxide and its structure analysis confirms the presence of BCC Cr(100) phase separated regions, which are embedded in the alloy surface and serve as nucleation centers for Cr-oxide growth. Always adjacent to these segregated regions are Cr-oxide rows and are interpreted as an intermediate stage of chromia growth preceding the formation of a closed Cr-oxide layer. The faceted oxide regions, also attributed to the Cr oxidation pathway, are similarly found near phase-separated Cr(100) regions, and are assigned to the advanced stages of Cr-oxide growth. The reaction pathway towards the passive chromia layer is then described as progression from BCC Cr(100) → Cr(100)-p(2×2)O → Cr-oxide rows → faceted Cr-oxide. These results support the formation of phase-separated BCC

Cr(100) layers on the surface which predicate the formation of a passive chromia layer on Ni-Cr(100).

5.5 Conclusions

The oxidation pathways of Ni-Cr alloys have been investigated by studying the evolution of partial surface oxides on a Ni-15wt.%Cr(100) sample. In this compositional space, the crystal structure of the alloy consists of a random solid solution of Cr atoms within a FCC Ni(100) lattice, however the progression of the Ni and Cr oxidation pathways drive changes to the crystal structure and chemistry of the Ni-Cr alloy. Step-edge faceting was observed where NiO growth initiated, while step edges with Cr-rich oxide particles remained curved. A greater number of these curved steps remained after 7 L of oxidation, as compared the oxidation of Ni-Cr(100) samples with lower Cr concentrations, suggesting that local compositional gradients need to be taken into account during the growth of partial surface oxides. As oxidation progressed, this point was further demonstrated by lateral segregation and phase separation of BCC Cr(100) via the observation of a Cr(100)-p(2×2)O phase. Neighboring these regions Cr-oxide rows and faceted Cr-oxide features were found, each displaying a unique electronic signature. As the alloy surface became increasingly saturated, next layer NiO growth initiated at the groove of the superlattice, which displayed electronic heterogeneity imprinted by the alloy-oxide interface. Understanding the oxidation pathways of partial oxide layers on Ni-Cr(100) alloys has given insight into the manner in which binary alloy systems undergo passivation within the pre-Cabrera-Mott regime.

5.6 Chapter V References

(1) Atkinson, A. Transport Processes during the Growth of Oxide Films at Elevated Temperature. *Rev. Mod. Phys.* **1985**, *57* (2), 437–470. https://doi.org/10.1103/RevModPhys.57.437.

(2) Wood, G. C.; Chattopadhyay, B. Transient Oxidation of Ni-Base Alloys. *Corros. Sci.* **1970**, *10* (7), 471–480. https://doi.org/10.1016/S0010-938X(70)80032-4.

(3) Chattopadhyay, B.; Wood, G. C. The Transient Oxidation of Alloys. *Oxid. Met.* **1970**, *2* (4), 373–399. https://doi.org/10.1007/BF00604477.

(4) Mohanty, P.; Rath, C.; Mallick, P.; Biswal, R.; Mishra, N. C. UV–Visible Studies of Nickel Oxide Thin Film Grown by Thermal Oxidation of Nickel. *Phys. B Condens. Matter* **2010**, *405* (12), 2711–2714. https://doi.org/10.1016/j.physb.2010.03.064.

(5) Haugsrud, R. On the High-Temperature Oxidation of Nickel. *Corros. Sci.* **2003**, *45* (1), 211–235. https://doi.org/10.1016/S0010-938X(02)00085-9.

(6) Ma, L.; Wiame, F.; Maurice, V.; Marcus, P. Origin of Nanoscale Heterogeneity in the Surface Oxide Film Protecting Stainless Steel against Corrosion. *Npj Mater. Degrad.* **2019**, *3* (1), 1–9. https://doi.org/10.1038/s41529-019-0091-4.

(7) Blades, W. H.; Reinke, P. From Alloy to Oxide: Capturing the Early Stages of Oxidation on Ni–Cr(100) Alloys. *ACS Appl. Mater. Interfaces* **2018**, *10* (49), 43219–43229. https://doi.org/10.1021/acsami.8b15210.

(8) Luo, L.; Zou, L.; Schreiber, D. K.; Baer, D. R.; Bruemmer, S. M.; Zhou, G.; Wang, C.-M. In-Situ Transmission Electron Microscopy Study of Surface Oxidation for Ni–10Cr and Ni–20Cr Alloys. *Scr. Mater.* **2016**, *114*, 129–132. https://doi.org/10.1016/j.scriptamat.2015.11.031.

(9) Luo, L.; Zou, L.; Schreiber, D. K.; Olszta, M. J.; Baer, D. R.; Bruemmer, S. M.; Zhou, G.; Wang, C.-M. In Situ Atomic Scale Visualization of Surface Kinetics Driven Dynamics of Oxide Growth on a Ni–Cr Surface. *Chem. Commun.* **2016**, *52* (16), 3300–3303. https://doi.org/10.1039/C5CC09165A.

(10) Ramanathan, R.; Ramalingam, G.; Perepezko, J. H.; Reinke, P.; Voorhees, P. W. Evolution of NiO Island Size Distributions During the Oxidation of a Ni-5Cr Alloy: Experiment and Modeling. *ACS Appl. Mater. Interfaces* **2018**. https://doi.org/10.1021/acsami.7b18539.

(11) Gusieva, K.; Cwalina, K. L.; Blades, W. H.; Ramalingam, G.; Perepezko, J. H.; Reinke, P.; Scully, J. R. Repassivation Behavior of Individual Grain Facets on Dilute Ni–Cr and Ni–Cr–Mo Alloys in Acidified Chloride Solution. *J. Phys. Chem. C* **2018**, *122* (34), 19499–19513. https://doi.org/10.1021/acs.jpcc.8b04306.

(12) Sprowl, L. H.; Adam, B. M.; Tucker, J. D.; Árnadóttir, L. First-Principles Study of the Products of CO2 Dissociation on Nickel-Based Alloys: Trends in Energetics with Alloying Element. *Surf. Sci.* **2018**, *677*, 219–231. https://doi.org/10.1016/j.susc.2018.06.011.

(13) Lutton, K.; Gusieva, K.; Ott, N.; Birbilis, N.; Scully, J. R. Understanding Multi-Element Alloy Passivation in Acidic Solutions Using Operando Methods. *Electrochem. Commun.* **2017**, *80*, 44–47. https://doi.org/10.1016/j.elecom.2017.05.015.

(14) Yu, X.; Gulec, A.; Sherman, Q.; Cwalina, K. L.; Scully, J. R.; Perepezko, J. H.; Voorhees, P. W.; Marks, L. D. Nonequilibrium Solute Capture in Passivating Oxide Films. *Phys. Rev. Lett.* **2018**, *121* (14), 145701. https://doi.org/10.1103/PhysRevLett.121.145701.

(15) Lutton, K.; Blades, W. H.; Scully, J. R.; Reinke, P. Influence of Chloride on Nanoscale Electrochemical Passivation Processes. *J. Phys. Chem. C* **2020**, *124* (17), 9289–9304. https://doi.org/10.1021/acs.jpcc.9b12050.

(16) Cabrera, N.; Mott, N. F. Theory of the Oxidation of Metals. *Rep. Prog. Phys.* **1949**, *12* (1), 163. https://doi.org/10.1088/0034-4885/12/1/308.

(17) Seyeux, A.; Maurice, V.; Marcus, P. Oxide Film Growth Kinetics on Metals and Alloys I. Physical Model. *J. Electrochem. Soc.* **2013**, *160* (6), C189–C196. https://doi.org/10.1149/2.036306jes.

(18) Kopatzki, E.; Behm, R. J. Step Faceting: Origin of the Temperature Dependent Induction Period in Ni(100) Oxidation. *Phys. Rev. Lett.* **1995**, *74* (8), 1399–1402. https://doi.org/10.1103/PhysRevLett.74.1399.

(19) Bäumer, M.; Cappus, D.; Kuhlenbeck, H.; Freund, H.-J.; Wilhelmi, G.; Brodde, A.; Neddermeye, H. The Structure of Thin NiO(100) Films Grown on Ni(100) as Determined by Low-Energy-Electron Diffraction and Scanning Tunneling Microscopy. *Surf. Sci.* **1991**, *253* (1), 116–128. https://doi.org/10.1016/0039-6028(91)90585-G.

(20) Smeenk, R. G.; Tromp, R. M.; Frenken, J. W. M.; Saris, F. W. The Oxidation of Ni(100) Studied by Medium Energy Ion Scattering. *Surf. Sci.* **1981**, *112* (3), 261–271. https://doi.org/10.1016/0039-6028(81)90374-5.

(21) Kopatzki, E.; Behm, R. J. STM Imaging and Local Order of Oxygen Adlayers on Ni(100). *Surf. Sci.* **1991**, *245* (3), 255–262. https://doi.org/10.1016/0039-6028(91)90028-Q.

(22) Stuckless, J. T.; Wartnaby, C. E.; Al-Sarraf, N.; Dixon-Warren, St. J. B.; Kovar, M.; King, D. A. Oxygen Chemisorption and Oxide Film Growth on Ni{100}, {110}, and {111}: Sticking Probabilities and Microcalorimetric Adsorption Heats. *J. Chem. Phys.* **1997**, *106* (5), 2012–2030. https://doi.org/10.1063/1.473308.

(23) Foord, J. S.; Lambert, R. M. Oxygen Chemisorption and Corrosion on Cr(100) and Cr(110) Single Crystal Surfaces. *Surf. Sci.* **1985**, *161* (2), 513–520. https://doi.org/10.1016/0039-6028(85)90824-6.

(24) Hope, G. A.; Ritchie, I. M. The Oxidation of Thin Chromium Films. *Thin Solid Films* **1976**, *34* (1), 111–114. https://doi.org/10.1016/0040-6090(76)90145-0.

(25) Salomonsen, G.; Norman, N.; Lonsjo, O.; Finstad, T. G. Kinetics and Mechanism of Oxide Formation on Cr Thin Films. *J. Phys. Condens. Matter* **1989**, *1* (42), 7843. https://doi.org/10.1088/0953-8984/1/42/006.

(26) Peter, R.; Saric, I.; Piltaver, I. K.; Badovinac, I. J.; Petravic, M. Oxide Formation on Chromium Metal Surfaces by Low-Energy Oxygen Implantation at Room Temperature. *Thin Solid Films* **2017**, *636*, 225–231. https://doi.org/10.1016/j.tsf.2017.06.011.

(27) Schmid, M.; Leonardelli, G.; Sporn, M.; Platzgummer, E.; Hebenstreit, W.; Pinczolits, M.; Varga, P. Oxygen-Induced Vacancy Formation on a Metal Surface. *Phys. Rev. Lett.* **1999**, *82* (2), 355–358. https://doi.org/10.1103/PhysRevLett.82.355.

(28) Arlow, J. S.; Mitchell, D. F.; Graham, M. J. The Mechanism and Kinetics of the Oxidation of Cr(100) Single-crystal Surfaces Studied by Reflection High-energy Electron Diffraction, X-ray Emission Spectroscopy, and Secondary Ion Mass Spectrometry/Auger Sputter Depth Profiling. *J. Vac. Sci. Technol. A* **1987**, *5* (4), 572–576. https://doi.org/10.1116/1.574675.

(29) Ramalingam, G.; Reinke, P. Growth of Ni and Ni-Cr Alloy Thin Films on MgO(001): Effect of Alloy Composition on Surface Morphology. *J. Appl. Phys.* **2016**, *120* (22), 225302. https://doi.org/10.1063/1.4971261.
(30) Saiki, R. S.; Kaduwela, A. P.; Osterwalder, J.; Fadley, C. S.; Brundle, C. R. Observation and Characterization of a Strained Lateral Superlattice in the Oxidation of Ni(001). *Phys. Rev. B* **1989**, *40* (3), 1586–1592. https://doi.org/10.1103/PhysRevB.40.1586.
(31) Feenstra, R. M. Tunneling Spectroscopy of the (110) Surface of Direct-Gap III-V Semiconductors. *Phys. Rev. B* **1994**, *50* (7), 4561–4570. https://doi.org/10.1103/PhysRevB.50.4561.
(32) Feenstra, R. M.; Stroscio, J. A.; Fein, A. P. Tunneling Spectroscopy of the Si(111)2 × 1 Surface. *Surf. Sci.* **1987**, *181* (1), 295–306. https://doi.org/10.1016/0039-6028(87)90170-1.
(33) Nečas, D.; Klapetek, P. Gwyddion: An Open-Source Software for SPM Data Analysis. *Open Phys.* **2011**, *10* (1), 181–188. https://doi.org/10.2478/s11534-011-0096-2.
(34) Maurice, V.; Cadot, S.; Marcus, P. XPS, LEED and STM Study of Thin Oxide Films Formed on Cr(110). *Surf. Sci.* **2000**, *458* (1–3), 195–215. https://doi.org/10.1016/S0039-6028(00)00439-8.
(35) Samin, A. J.; Taylor, C. D. First-Principles Investigation of Surface Properties and Adsorption of Oxygen on Ni-22Cr and the Role of Molybdenum. *Corros. Sci.* **2018**, *134*, 103–111. https://doi.org/10.1016/j.corsci.2018.02.017.
(36) Maurice, V.; Despert, G.; Zanna, S.; Bacos, M.-P.; Marcus, P. Self-Assembling of Atomic Vacancies at an Oxide/Intermetallic Alloy Interface. *Nat. Mater.* **2004**, *3* (10), 687–691. https://doi.org/10.1038/nmat1203.
(37) Wyckoff, R. W. G. *Crystal Structures - Volume 1.*, 2nd ed.; Interscience Publishers: New York, 1963; Vol. 1.
(38) Howe, J. M. 14 - Structure, Composition and Energy of Solid–Solid Interfaces. In *Physical Metallurgy (Fifth Edition)*; Laughlin, D. E., Hono, K., Eds.; Elsevier: Oxford, 2014; pp 1317–1451. https://doi.org/10.1016/B978-0-444-53770-6.00014-9.
(39) Chen, J. K.; Farkas, D.; Reynolds, W. T. Atomistic Simulation of an f.c.c./b.c.c. Interface in Ni-Cr Alloys. *Acta Mater.* **1997**, *45* (11), 4415–4421. https://doi.org/10.1016/S1359-6454(97)00159-6.
(40) Rigsbee, J. M.; Aaronson, H. I. A Computer Modeling Study of Partially Coherent f.c.c.:B.c.c. Boundaries. *Acta Metall.* **1979**, *27* (3), 351–363. https://doi.org/10.1016/0001-6160(79)90028-2.
(41) Hall, M. G.; Aaronson, H. I.; Kinsma, K. R. The Structure of Nearly Coherent Fcc: Bcc Boundaries in a Cu-Cr Alloy. *Surf. Sci.* **1972**, *31*, 257–274. https://doi.org/10.1016/0039-6028(72)90264-6.
(42) Bikondoa, O.; Moritz, W.; Torrelles, X.; Kim, H. J.; Thornton, G.; Lindsay, R. Impact of Ambient Oxygen on the Surface Structure of Alpha-Cr2O3(0001). *Phys. Rev. B* **2010**, *81* (20), 205439. https://doi.org/10.1103/PhysRevB.81.205439.
(43) Cao, S.; Wu, N.; Echtenkamp, W.; Lauter, V.; Ambaye, H.; Komesu, T.; Binek, C.; Dowben, P. A. The Surface Stability of Cr2O3(0001). *J. Phys. Condens. Matter* **2015**, *27* (25), 255003. https://doi.org/10.1088/0953-8984/27/25/255003.
(44) Lübbe, M.; Moritz, W. A LEED Analysis of the Clean Surfaces of Alpha-Fe2O3(0001) and Alpha-Cr2O3(0001) Bulk Single Crystals. *J. Phys. Condens. Matter* **2009**, *21* (13), 134010. https://doi.org/10.1088/0953-8984/21/13/134010.

(45) Rohr, F.; Bäumer, M.; Freund, H.-J.; Mejias, J. A.; Staemmler, V.; Müller, S.; Hammer, L.; Heinz, K. Strong Relaxations at the Cr2O3(0001) Surface as Determined via Low-Energy Electron Diffraction and Molecular Dynamics Simulations. *Surf. Sci.* **1997**, *372* (1), L291–L297. https://doi.org/10.1016/S0039-6028(96)01255-1.
(46) Rohrbach, A.; Hafner, J.; Kresse, G. Ab Initio Study of the (0001) Surfaces of Hematite and Chromia: Influence of Strong Electronic Correlations. *Phys. Rev. B* **2004**, *70* (12), 125426. https://doi.org/10.1103/PhysRevB.70.125426.
(47) Chattopadhyay, B.; Wood, G. C. The Transient Oxidation of Fe-Cr and Ni-Cr Alloys. *J. Electrochem. Soc.* **1970**, *117* (9), 1163. https://doi.org/10.1149/1.2407761.
(48) Hammer, B.; Norskov, J. K. Why Gold Is the Noblest of All the Metals. *Nature* **1995**, *376* (6537), 238–240. https://doi.org/10.1038/376238a0.
(49) Hammer, B.; Nørskov, J. K. Electronic Factors Determining the Reactivity of Metal Surfaces. *Surf. Sci.* **1995**, *343* (3), 211–220. https://doi.org/10.1016/0039-6028(96)80007-0.
(50) Hammer, B.; Nørskov, J. K. Theoretical Surface Science and Catalysis—Calculations and Concepts. In *Advances in Catalysis*; Impact of Surface Science on Catalysis; Academic Press, 2000; Vol. 45, pp 71–129. https://doi.org/10.1016/S0360-0564(02)45013-4.
(51) Belokoneva, E. L.; Shcherbakova, Y. K. Electron Density in Synthetic Escolaite Cr~2O~3 with a Corundum Structure and Its Relation to Antiferromagnetic Properties. *Russ. J. Inorg. Chem. CC ZHURNAL NEORGANICHESKOI KHIMII* **2003**, *48*, 861–869.

5.7 Supplemental Data and Supporting Information

5-S1 Alloy surface prior to oxidation

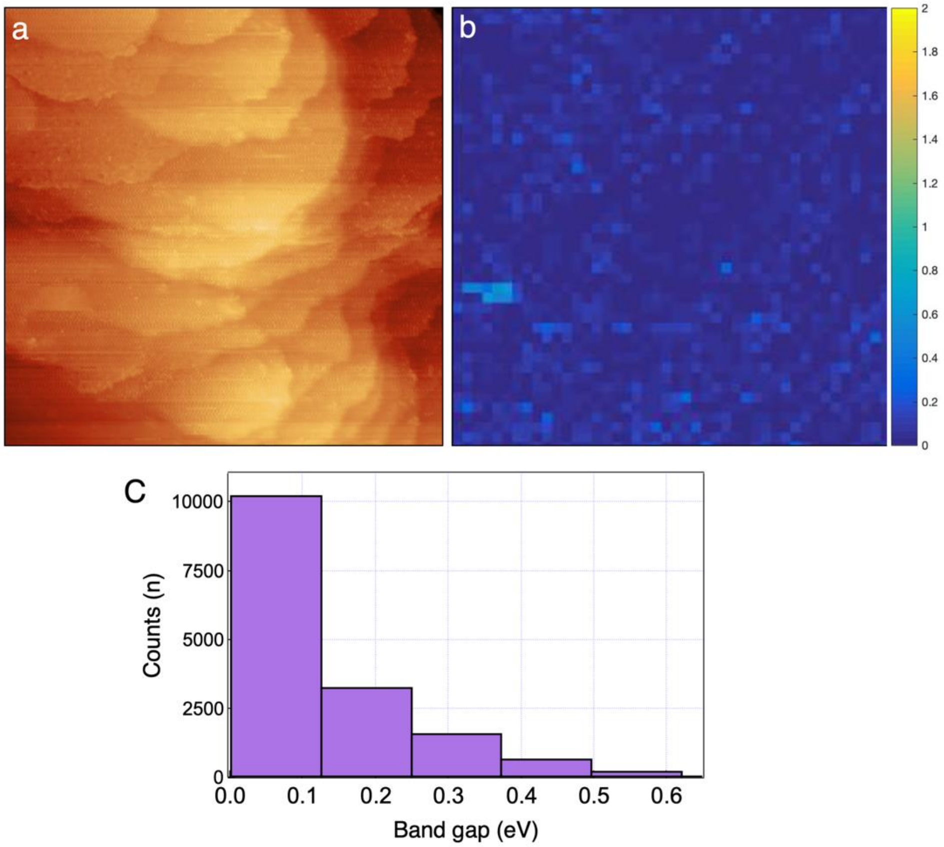

Figure 5-S1. The topography (a), and band gap map (b) of the Ni-15%Cr(100) surface before oxidation, and band gap distribution (c). The topography image was taken before the 4×4 grid (V_{sweep} = ±1 V) STS, and image and band gap map are 40×40 nm^2. The topography image was recorded with V_{bias} = 0.25 V, I_t = 0.5 nA. The scale bar on the band gap map is in eV.

STM and STS measurements summarized in Figure 5-S1 before oxidation confirm that the surface is metallic, and the band gap map illustrates the homogenous electronic structure in the surface. The band gap values extracted from the band gap map are summarized in the distribution in (c). This histogram, which shows the absence of a band gap in the metallic surface also serves as a test for the quality of the STS measurements.

5-S2 Image segmentation method used in cluster/island quantification

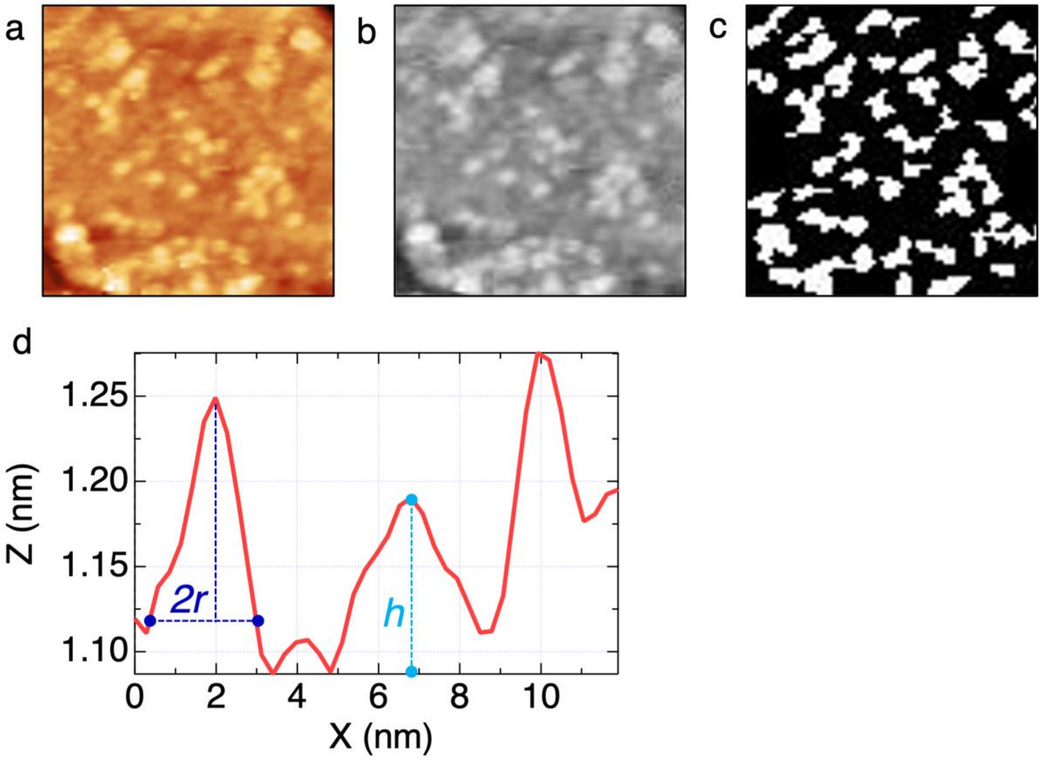

Figure 5-S2. Example of image segmentation used to capture the oxide particle areas. (a) is the original topography image (22×22 nm^2) measured at V_{bias} = 2.0 V, I_t = 0.1 nA. Images (b) and (c) represent the greyscale and segmented images, respectively. (D) is a line scan across the oxide particles.

Images (a)-(c) represent the greyscale segmentation process that was applied to 8 different images to obtain the area coverage with oxide clusters observed early in the oxidation process. The segmentation was done using the total image height, darker pixels representing the local minimum height and lighter pixels the local maximum height, (d). To best match the topography of the linescans a cutoff of approximately 20% above the minimum of the image apparent height (≥0.8 Å) was used to isolate the islands, (c). This value was used to best match the true apparent height of the oxide particles which is then used to isolate the particles within the image. (d) is a line scan of the clusters measured with the STM analysis software Gwyddion, and shows how the radius of the clusters was determined from images.[33]

5-S3 Model of the random solid solution NiCr surface

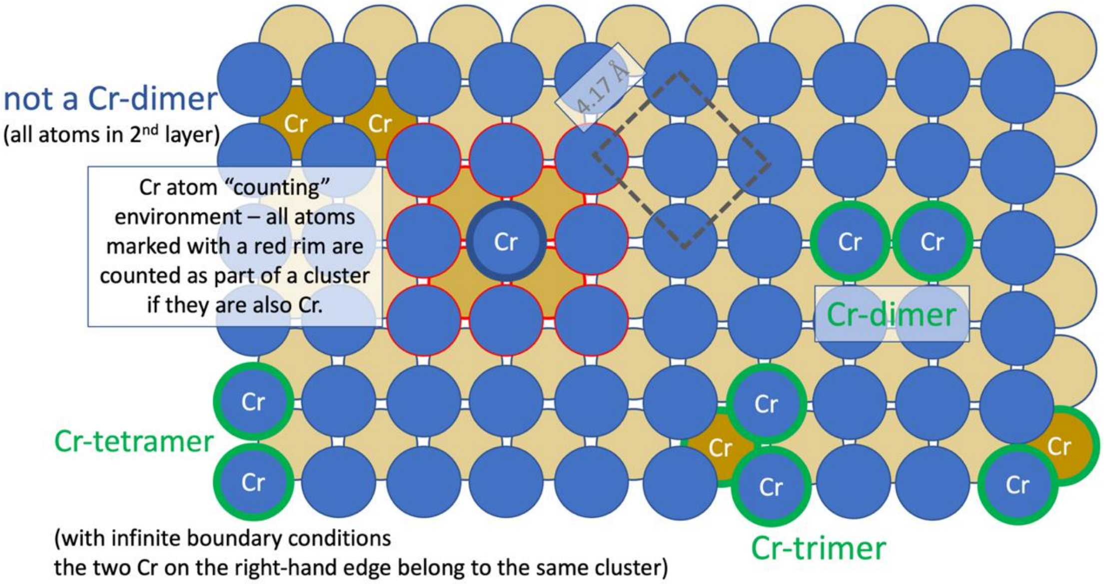

Figure 5-S3. Illustration of the rules used to define Cr-clusters on the Ni-Cr(100) surface, and the 2nd layer below the surface. Periodic boundary conditions are illustrated with the labeled tetramer that spans the boundary in the y direction. This is a model surface used to illustrate Cr-atom distributions in the NiCr surface. The actual Monte-Carlo simulation was done using surfaces with typically 10,000 atoms.

The alloy atomic layers were generated in MATLAB by using a random number generator to probabilistically assign Cr or Ni to each position in a matrix. Each matrix element corresponds to atomic coordinates and the matrix is typically around 100×100 atoms. Two such matrices were created representing the surface plane, and the plane below the surface (2nd layer). Once these matrices are generated, the atoms in the 1st layer are scanned for Cr atoms, and when one is found, all positions adjacent to this atom (8 neighbors in the same layer, and 4 in the 2nd layer) are scanned for additional Cr atoms to identify a potential cluster. To define the cluster, the code is called recursively on any adjacent Cr atoms that are found until all atoms in the cluster have been identified. Note that the first step of this program only scans for Cr atoms in the 1st layer, mandating that all clusters have at least 1 Cr atom on the surface to be counted. No distinction was made between Cr atoms that were adjacent laterally, diagonally, or from different planes, and a periodic boundary condition was used to eliminate edge effects in cluster counting as illustrated for the tetramer which is positioned on the left-hand edge and continued on the right-hand edge in Figure 5-S3.

5-S4 Oxygen-chemisorption surface structures

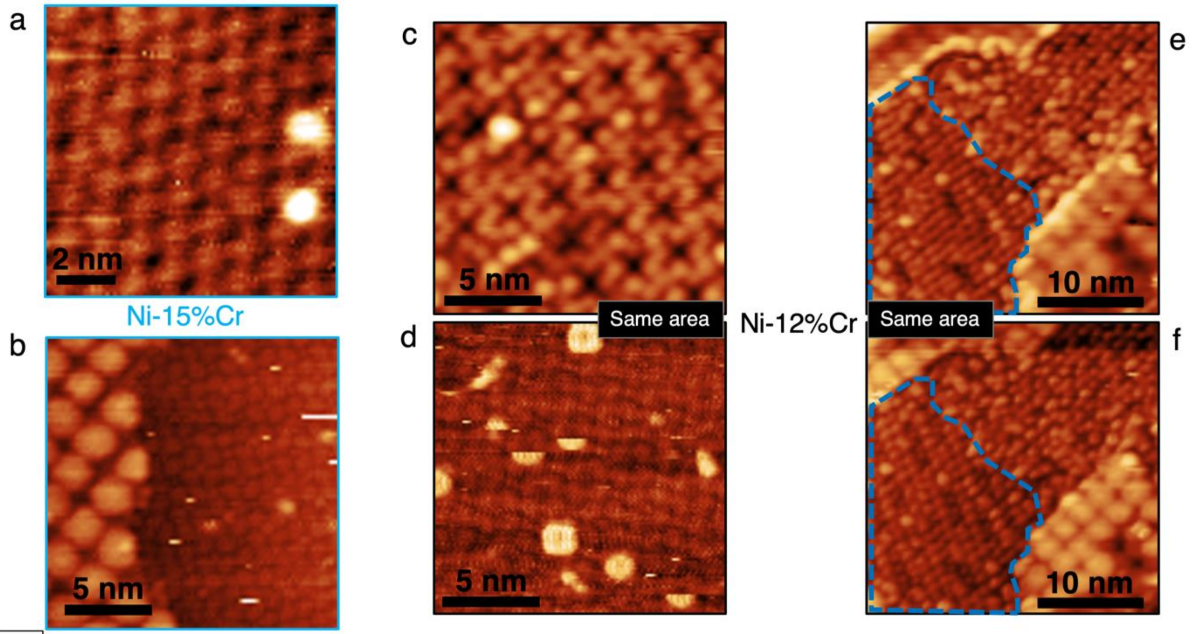

g

Oxygen adlayer / reconstruction	Observed in STM when… (V_{bias}, $I_{tunneling}$)
Hexagonal (a)	(V_b = ±3.0 V, I_t = 0.1 nA) & (V_b = ±2.0 V, I_t =0.1 nA)
Cross type (c)	(V_b = 3.0 V, I_t = 0.1-0.05 nA) & (V_b = 2.0 V, I_t = 0.05 nA)
Cross type (b & d)	(V_b = 2.0 V, I_t = 0.1 nA), (V_b = 0.1 V, I_t = 0.1-0.05 nA) & (V_b = 0.05 V, I_t = 0.05 nA)
Square (dashed in e & f)	(V_b = 3.0 V, I_t = 0.1-0.05 nA) & (V_b = 2.0 V, I_t = 0.05 nA)

Figure 5-S4. Topography images of the chemisorbed oxygen adlayers / surface reconstructions observed on Ni-Cr(100) alloys after **14 L** of oxidation at 500 °C. All the features shown above have been observed on both the Ni-15wt.%Cr(100) and Ni-12wt.%Cr(100) reported on an earlier publication, and we selected the highest quality images. The oxidation of 12wt.%Cr(100) was discussed in a prior publication where we focused on the Ni-NiO superlattices.[Ref. 7 in manuscript] Images (a) and (b) were taken from the Ni-15wt.%Cr(100) sample and images (c)-(f) on the Ni-12wt.%Cr(100) sample. These surfaces have been observed with different STM parameters, which are provided in table (g). Image (a) and (b) were both measured at V_{bias} = 2.0 V, I_t = 0.1 nA, image (c) at V_{bias} = 3.0 V, I_t = 0.05 nA, (d) at V_{bias} = 0.1 V, I_t = 0.1 nA, (e) at V_{bias} = 3.0 V, I_t = 0.1 nA, and (f) at 2.0 V, I_t = 0.05 nA.

After 14 L of O_2 exposure the Ni-Cr(100) surface is covered in a variety of chemisorbed oxygen adlayers. Images (a) and (b,c,d) are examples of the hexagonal and cross-type features, respectively, which are named here following their general appearance in the topography images. These are the two most frequently observed surface features, and were measured on different areas of the Ni-15wt%Cr(100) sample. The appearance of the cross-type reconstruction is strongly bias dependent, and has been observed repeatedly in our work on Ni-Cr(100) surface and presents periodic depressions that arranged in the shape of crosses at high positive bias voltages. Image (d) shows another example of the cross-type reconstruction from the same area as (c), but measured with a lower bias voltage and tunneling current than (b).

An oxide adlayer with square geometry is also occasionally observed adjacent to the cross-type reconstruction, and is marked with a dashed outline in (e) and (f). The spacings measured between the protrusions do not correspond any other reconstructions, surface oxides, or oxide layers described in the literature and remain at present unresolved in terms of their atomic structure. A variety of reconstructions have been observed during Cr(100) oxidation, [7,23–28] some of which have similarities in general appearance but not in dimension to the adlayers presented here. The effect of O_2 content on the lattice spacings of $Cr_2O_3(100)$ has also been reported.[42–46] We propose tentatively that these adlayers emerge due to the interplay of O, surface vacancies, fcc and bcc-Cr regions on the surface. The variability observed across Ni-Cr(100) surface strongly suggests the presence of metastable intermediate surface oxides that predate the formation of the chromia layer, and define ultimately the structure of the alloy-NiO and alloy-chromia interfaces. The variability in surface structures is particularly large at this oxidation step, and is reduced significantly after 18 L of exposure on Ni15wt%Cr.

5-S5 Geometry of oxide rows with E_{gap}>1 eV: companion to Figure 5-5 in main body of manuscript.

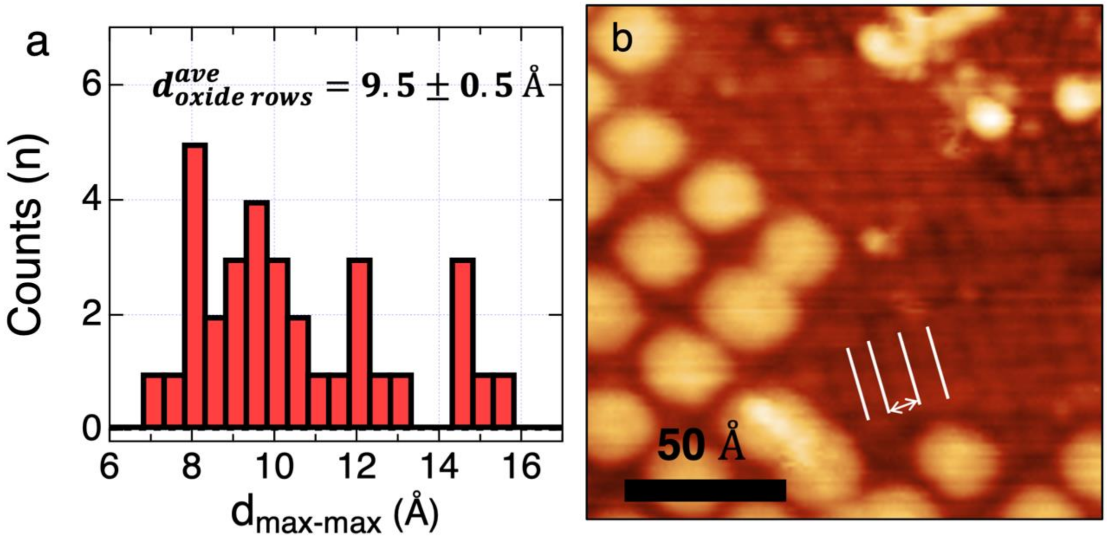

Figure 5-S5. **After 18 L exposure:** A histogram of the spacings between the oxide rows (a). The STM image (b), measured at V_{bias} = -3.0 V, It = 0.1 nA, shows the rows and the spacing between them is marked by white lines.

This histogram, (a), represents the spacings between the maximum heights, or protrusions, of the oxide rows found on the surface adjacent to segregated Cr(100)-p(2×2)O regions at **18 L** of oxidation. An example of these features is shown in (b), with white lines highlighting the distance between the rows. All line scans were done at either V_{bias} = -3.0 V, I_t = 0.1 nA or I_t = 0.05 nA. No measurable difference can be detected as a function of tunneling current. The average spacings between the rows was found to be $d^{ave}_{oxide\ rows} = 9.5 \pm 0.5$ Å. These spacings do not correspond to any known oxide feature, and cannot be explained with a poorly resolved reconstruction from the portfolio described in S4. Given their vicinity to the BCC segregated Cr(100)-p(2×2)O regions, these are tentatively interpretated as intermediate phase of the Cr-oxide, respectively a surface oxide which is positioned in the reaction timeline from Ni-Cr(100) → Cr(100)-p(2×2)O → “Cr-oxide row” → “faceted Cr-oxide” feature → chromia. Note that this interpretation remains speculative at present and our interpretation relies heavily on the time evolution of the different surface feature with oxygen exposure.

5-S6 Surface topography and structure of square nodules

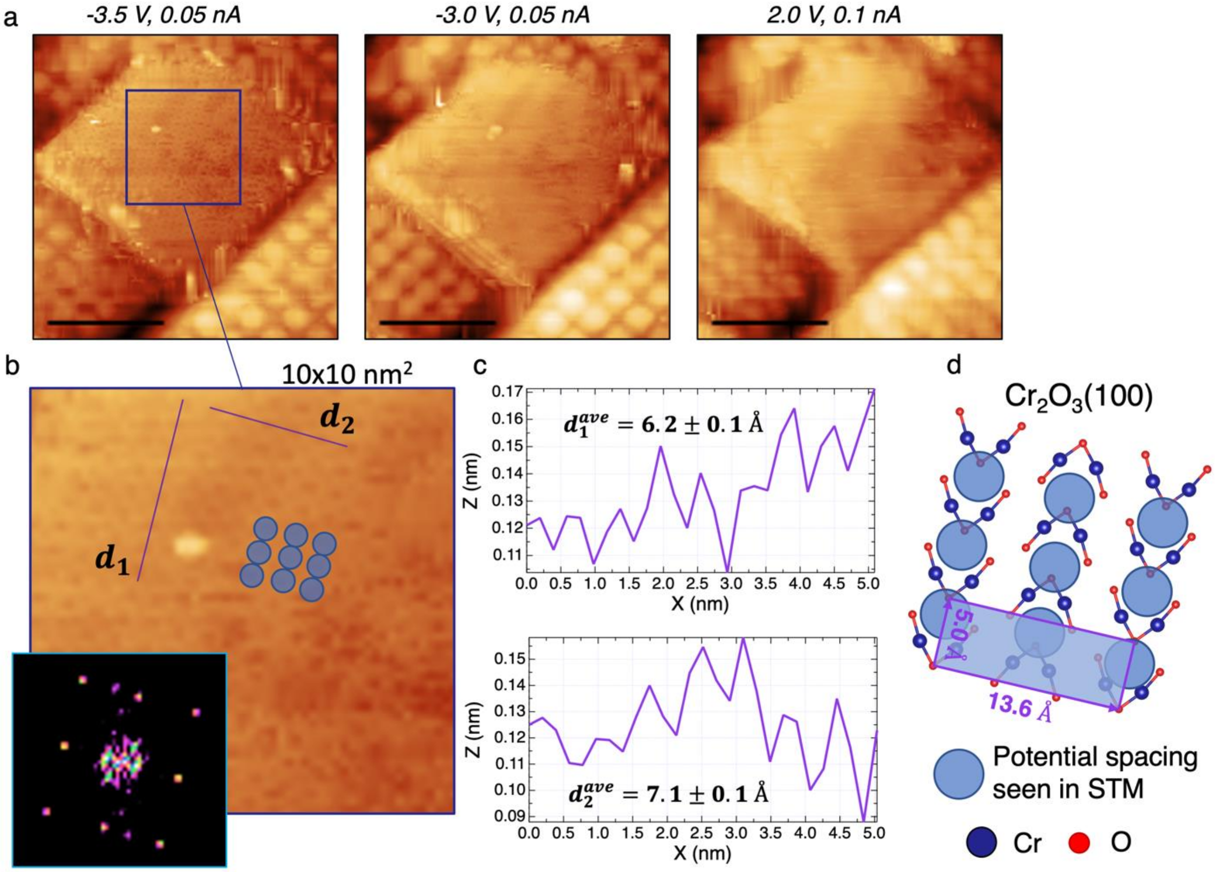

Figure 5-S6. (a) Bias dependent topography images for one of the faceted islands/nodules which are frequently observed at higher oxygen exposure. Image (b) corresponds to the 10×10 nm^2 area outlined by the dark blue box in (a), along with its corresponding FFT pattern. The line scans, (c) across the minima in the periodic structure. A ball and stick model, (d) of the $Cr_2O_3(100)$ surface. All scale bars are 10 nm.

The square, faceted nodules, are tentatively interpreted as Cr-oxides, and only observed on the Ni-Cr(100) surface later in the oxidation after a cumulative **18 L exposure**. The faceted structures are typically surrounded by a NiO step edge or NiO wedge and are found usually adjacent to the Cr(100)-p(2×2)O structure. Their vicinity to segregated regions of Cr(100), and appearance only at larger oxygen exposure suggest that they are connected to the initial growth stages of Cr_2O_3 which is characteristic behavior of initial grow on Ni-Cr[8,9,47]. The three topography images shown in (a) were recorded at different bias voltage. A periodic structure is observed when V_{bias} = -3.5 eV, I_t = 0.05 nA. The large bias voltage required to achieve a reasonable resolution is in agreement with an oxide surface. An FFT pattern highlights the rectangular symmetry of the periodic structure. The line scans in (c) across the minima also reflect this rectangular symmetry and an average spacing of $d_1^{ave} = 6.2 \pm 0.1$ Å and $d_2^{ave} = 7.1 \pm 0.1$ Å is observed.

A comparison with the $Cr_2O_3(100)$ surface [51] remains inconclusive, and challenging since this surface is subject to significant variations as a function of O_2 activity and partial pressure on the surface structure of Cr_2O_3 surface.[42–46] Alternatively, the peculiar square nodules can result from NiO layers, which are structurally decoupled from Ni-NiO interfacial structure and hence do not present the characteristic superlattice, although the rectangular surface features do not agree with this interpretation but are certainly subject to sub-optimal imaging conditions on an insulating surface.

5-S7 NiO-superlattice – 2nd layer growth

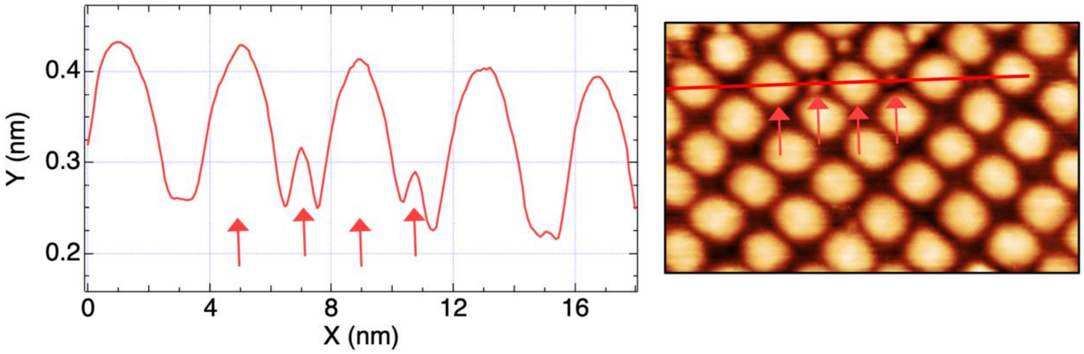

Figure 5-S7. A line scan and 20x12 nm^2 topography image (V_{bias} = -3.0 V, I_t = 0.1 nA), of the NiO-NiCr(6×7) superlattice structure.

A line scan and STM topography of the NiO-NiCr(6×7) superlattice structure. The line scan reveals the small protrusions between the overlap site of the NiO are approximately 1 nm in lateral size with an apparent height of 0.08 nm. These small features rest about 0.1 nm below the top of the superlattice structure of the NiO. Arrows are set over the image and line scan to guide the eye.

5-S8 NiO-superlattice – 2nd layer growth – complete set of STS maps

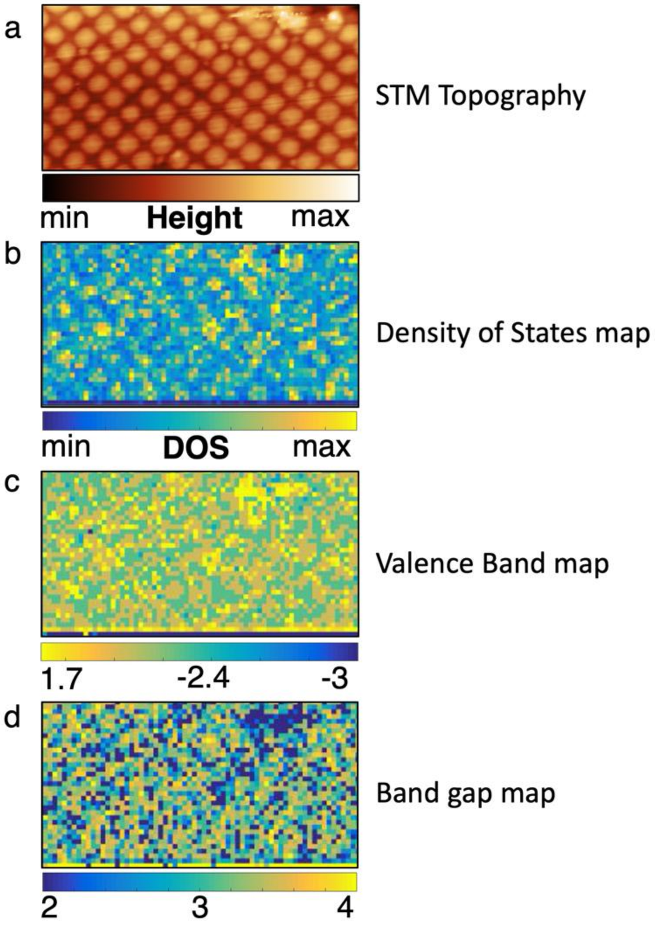

Figure 5-S8. (a) 40×20 nm^2 topography image taken at $V_{bias} = 2.0$ V, $I_t = 0.1$ of the NiO-NiCr(100) superlattice structure and the corresponding DOS map showing the local density of states at $V_{slice} = -2.7$ V. The map in (c) represents the same area visualizes energy position of the valence band minima, and (d) the band gap values in the window between 2 and 4 eV.

The area depicted in the main body of the manuscript in Figure 5-6, is shown here with its corresponding LDOS map (b), VBM map (c), and band gap map (d). There exists a contrast across the NiO-NiCr(6×7) superlattice, which is reflected in the STS measurements, and is a result of the presence of coincident Ni-NiO and non-coincident Ni-NiO sites in the superlattice. These sites present distinct electronic signature.

Chapter VI: The Evolution of Nanoscale Oxides on Ni(111) and Ni-Cr(111) Surfaces

6.1 Technical Background

An *in situ* STM study reported in the literature has previously considered the initial stages of Ni(111) oxidation.[1] When oxidized at 400 K or above, the adsorption of O_2 was found to commence with the formation of a Ni(111)-p(2×2)O reconstruction. After sequential oxidation steps, oxide growth initiated at the step edges and NiO(100) was observed, while triangular NiO(111) islands grew after larger O_2 doses.[1] The initial oxidation behavior of Ni(111) has also been observed with low-energy electron microscopy in conjunction with theoretical electron reflectively calculations, where both NiO(100) and NiO(111) grew at different temperature ranges.[3] At a temperature of 750 K, NiO(111) islands coexist with the unreacted metal surfaces after sequential oxidation up to about 1000 L. Rotated with respect to the underlying metal (111) surface, NiO(111) domains with a varying level of tilt are found to have nucleated at different areas across the sample. Theoretical calculations of the LEED patterns reveal the oxide layer grown at these temperatures is 2-3 atomic layers thick. DFT studies on Ni-Cr(111) alloys have shown the presence of Cr enhances oxygen absorption.[4–7] An increase in the maximum oxygen absorption energy is found when multiple Cr atoms are present at the surface,[7] suggesting that local segregation in the alloy will have an effect on this surface. To date, and the best of our knowledge no experimental studies have been conducted to observe the oxidation of Ni-Cr(111) surface and there exists a gap in our understanding of how these surfaces saturate with oxide and in what ways the crystallography effects the early stages of oxidation in comparison with NiCr(100).

6.2 Methods

Ni(111) and Ni-18wt.%Cr(111) thin films, approximately 30 nm thick, were deposited on MgO(111) substrates by electron beam evaporation. The rates prior to deposition were measured, and the composition of the Ni-18wt.%Cr(111) thin film verified ex-situ, by energy dispersive spectroscopy (EDS). The deposition and EDS measurements are described in chapter III. The sequential oxidation of both the Ni(111) and Ni-18wt.%Cr(111) thin films took place in our UHV chamber where oxygen was introduced through a sapphire leak valve while the thin films were held at 500 ºC. After each oxidation step the samples were allowed to cool before the surface evolution was measured with STM and STS. Each sample was deposited, measured and oxidized on different days but with the same tip. The topography data were analyzed using Gwyddion and MATLAB and the spectroscopy data was formatted into STS maps following the procedures outlined in sections 3.9. The experimental setup and oxidation conditions were identical to those used for the Ni-Cr(100) surfaces described in chapter IV and V.

6.3 Results and Discussion

After the Ni(111) and Ni-18wt.%Cr(111) thin films are grown, they were sequentially

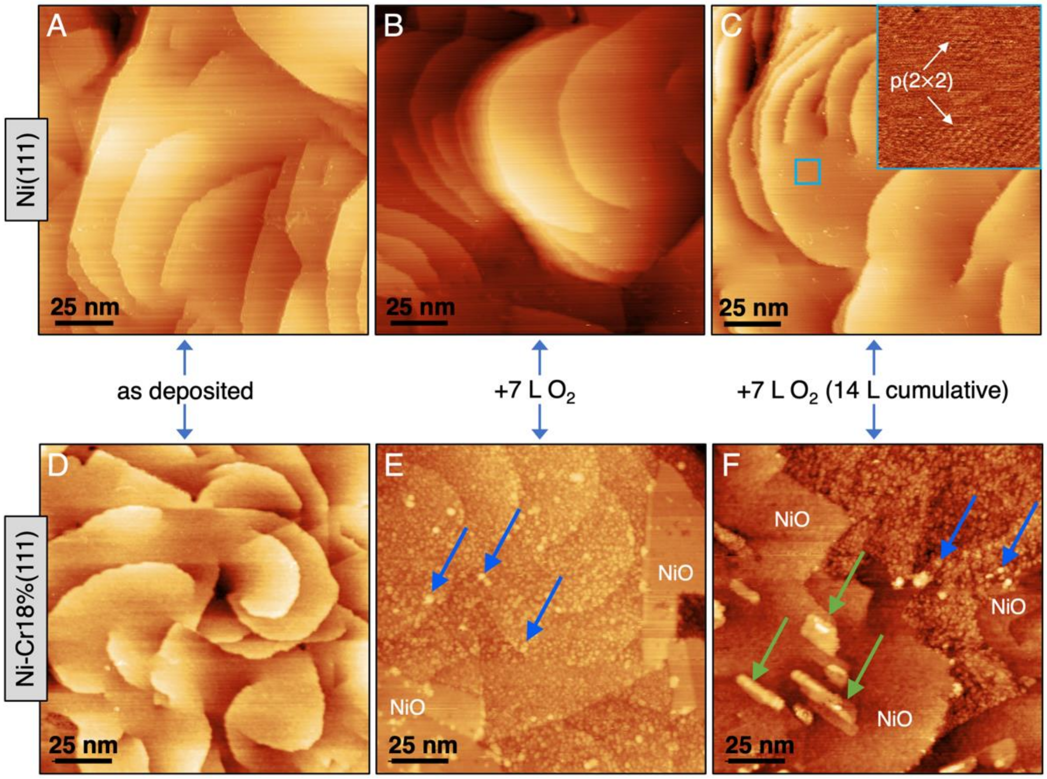

Figure 6-1. (A)-(C) STM images of the Ni(111) and (D)-(F) Ni-18wt.%Cr(111) surfaces before and after oxidation at 500 °C. The image inset in (C) highlights the ordered p(2×2) adlayer that forms on the surface (10×10 nm^2). The arrows in images (E) and (F) mark the Cr-oxide particles (blue) and larger Cr-oxide nodules (green). Ni(111): (A) was measured at V_{bias} = 0.25 V and I_t = 0.5 nA, image (B) at V_{bias} = 2.0 V and I_t = 0.1 nA, image (C) at V_{bias} = -1.0 V and I_t = 0.1 nA. Ni-Cr18wt.%Cr(111): image (D) was measured at V_{bias} = 0.15 V and I_t = 0.5 nA, while images (E) and (F) were measured at V_{bias} = 3.0 V and I_t = 0.1 nA.

oxidized at 500 °C, and STM images before and after each oxidation step are shown in Figure 6-1. The Ni(111) surface appears to saturate with oxide at a much slower rate compared to the Ni-Cr(111) sample. The Ni(111) surface presents as a clean metal surface until 14 L, and small islands of Ni(111)-p(2×2)O are observed on the surface, Figure 6-1(C). Areas of unreacted metal are found between the ordered oxygen adlayers, which is consistent with literature.[1,3] While no oxide islands were observed during these exposures, it is possible the STM tip was rastered between areas on the sample that had not yet undergone oxide growth.[3]

The oxidation of the Ni-18wt.%Cr(111) thin film results in oxide coverage after just 7 L of O_2, Figure 6-1(E). Small oxide particles have nucleated across both, the terraces and steps, and are marked with blue arrows. These particles resemble the disk-like Cr-oxide particles observed on other low-index Ni-Cr and Cr surfaces.[8,9] Smaller regions of "smooth" oxide, comprised of periodic rows, appear adjacent to these oxide particles. These patches extend across the terraces of the alloy and are pinned between its step edges. The oxidation of a Ni(111) surface studied with STM found NiO(100) presents a similar periodic structure and growth characteristics as this feature.[1] An additional +7 L oxidation (14 cumulative), the smaller oxide particles (blue arrows) remain, and larger oxide nodules (green arrows) are now visible across the surface, Figure 6-1(F). Areas that are still covered by these smaller particles appear to have laterally grown in size. Generally, after this oxidation step the regions of "smoother" oxide coverage is greater on terraces with the larger oxide nodules present, as compared to terraces populated with the smaller oxide particles. Initially, distinct oxide features are found across the surface, and to better understand the variation in the oxidation pathway of the Ni(111) and Ni-Cr(111) surfaces, each of these features will be discussed.

The initial oxidation of the Ni-18wt.%Cr(111) surfaces commences with the growth of smooth oxide patches and the formation of small oxide particles. These features present differently in the STM images and their size and shape vary significantly with bias voltage, Figure 6-2. When alloy-oxide surface is measured at V_{bias} = -3.0 V, the oxide particles appear as large protrusions and while a continuously smooth oxide patch extends between the step edges of the alloy, Figure 6-2(A). Once the bias voltage is changed to -1.0 V the surface appears completely devoid of these features, and the step edges and terraces of the alloy can be seen, Figure 6-2(B). The regions where the smooth oxide patches are present appear to have driven the step edges to facet (white arrows in B), which is comparable to the oxidation of NiO(100).[8] Differently spaced periodic rows across

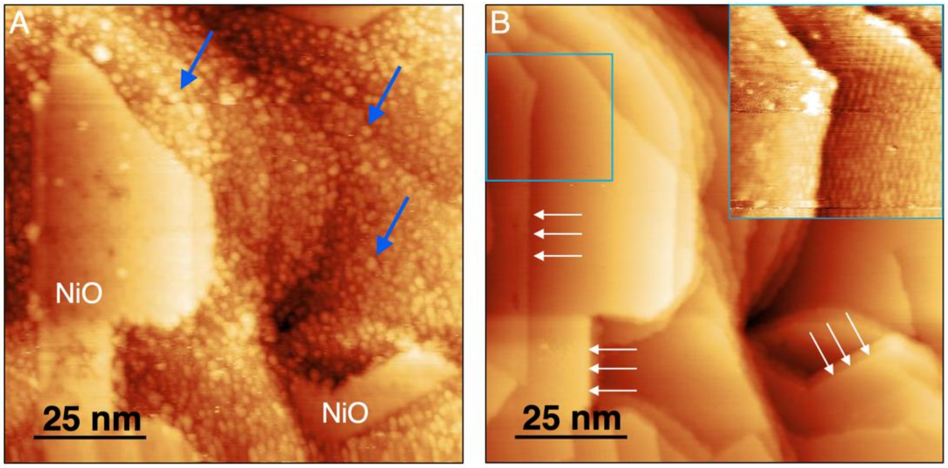

Figure 6-2. STM topography images of the Ni-18wt.%Cr(111) surface after 7 L of exposure. Image (A) was measured at V_{bias} = -3.0 V and I_t = 0.1 nA, while image (B) was taken at V_{bias} = -1.0 V and I_t = 0.1 nA. The variation in bias voltage has a clear effect on how the oxides visible on the surface, and at sufficiently low bias voltages the surface appears featureless. An image of the empty states, measured at V_{bias} = 1.0 V and I_t = 0.1 nA, is provided in the 25×25 nm^2 image inset in (B) and small periodic rows can be seen.

these regions are seen in the image inset in Figure 6-2(B), and present most prominently when measured at relatively low bias voltages 0.1-1 V. To better quantify each of these different oxides, more information is provided in the following paragraph about their geometric structure and how it evolves with increased oxygen exposure.

A high resolution STM image of smooth oxide patch can be seen in Figure 6-3(A), where periodic rows extend over the oxide. Line scans taken across the surface highlight the variation in periodicity and are provided adjacent to the STM image in Figure 6-3(B)-(D). Arrows, corresponding to the line scans, are overlaid on the image and point to the respective oxide features present. It is clear from the line scans that a number of differently ordered structures are present, and their average spacings are provided in each line scan. This varied periodicity is consistent with the a NiO(100)-Ni(111) structure measured with STM,[1,2] however the geometry and relative orientation this NiO structure to the Ni-Cr(111) surface will need to be explicitly solved. Indeed, the NiO(111) forms relatively thick triangular structures, which we do not observe at these

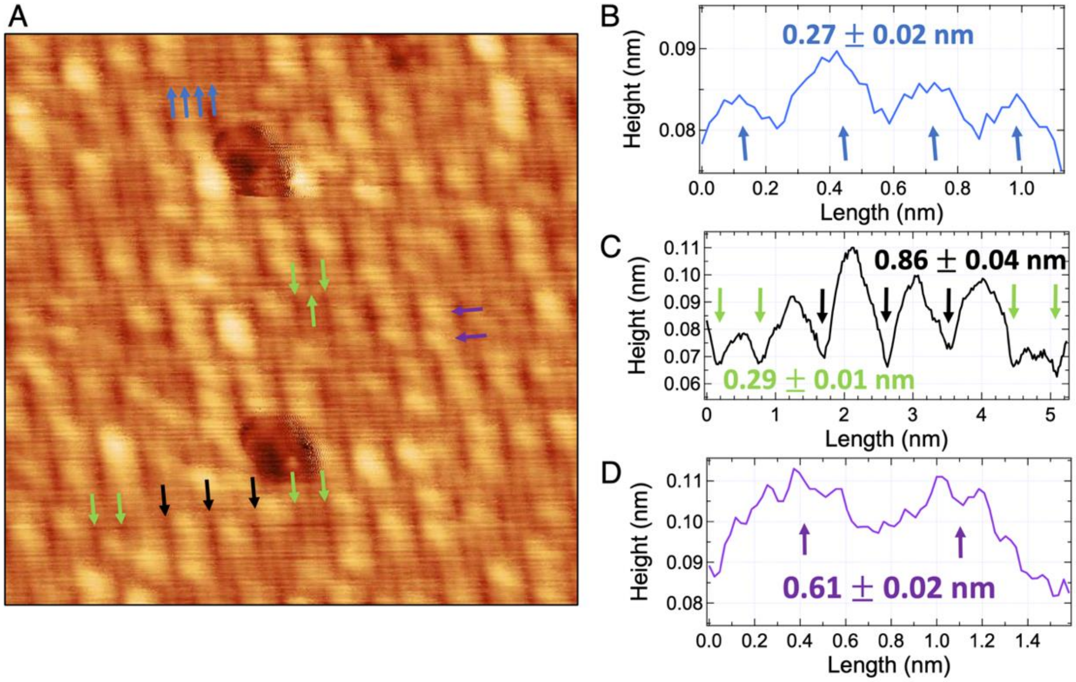

Figure 6-3. High resolution image of the NiO-NiCr(111) interface. (A) The topography image is 12×12 nm^2 and was taken at V_{bias} = -0.1 V and I_t = 0.5 nA. The colored arrows superimposed over the image accompany in the line scans in (B)-(D), which guide the readers eye to the various periodic structures found on the Ni-Cr(111) surface after oxidation.

exposures and temperatures. After a cumulative 14 L of oxidation, the NiO grows in total area coverage. The regions of increased coverage coincide with the growth of the larger Cr-oxide nodules, while the alloy step edges typically separate regions of NiO and the smaller Cr-oxide particles.

A quantitative assessment of the smaller oxide particles is given in Figure 6-4. These particles have been measured on a variety of different low-index Ni-Cr surfaces (chapter IV and V), as well as single grain Cr surfaces.[8,9] Their existence appears uniquely related to the presence of Cr, and was discussed in detail in chapter V. These Cr-rich oxide clusters present differently after the 7 L and 14 L O_2 cumulative exposures and grow in both height and lateral area, Figure 6-4(A)-(B). Line scans are also provided to highlight these changes, Figure 6-4(C)-(D). Taking numerous STM topography images (same imaging conditions), the change in apparent height and

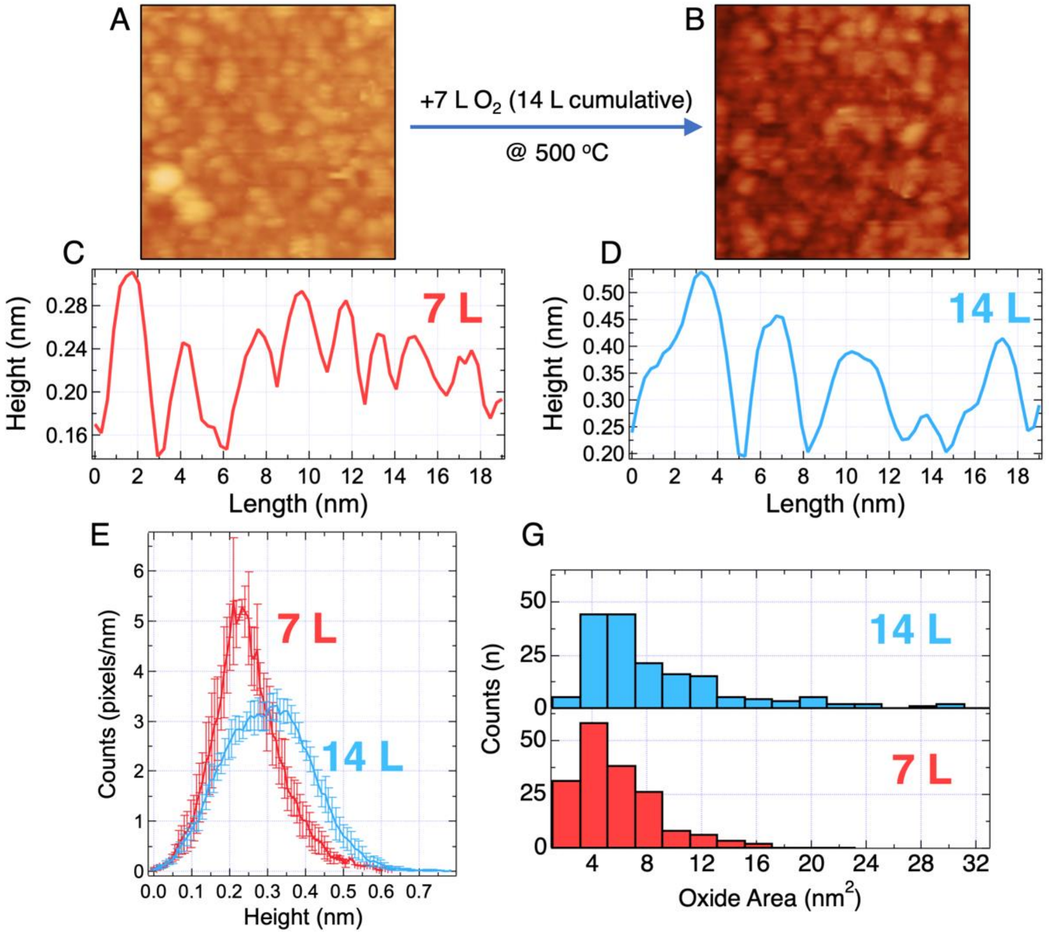

Figure 6-4. The growth of the smaller Cr-oxide particles after the 7 L and 14 L exposures on the Ni-Cr18wt.%Cr(111) surface. The STM images after 7 L (A) and 14 L (B) and accompanying line scans (C) and (D). The change in both height (E) and area (G) of these particles is also provided. Both images are 25×25 nm^2 and all data was taken at V_{bias} = 3.0 V, I_t = 0.1 nA.

lateral area was quantitatively determined, Figure 6-4(E)-(F). After the first 7 L oxidation step at 500 °C, the particles have a maximum apparent height centered at 0.21 nm, and an average oxide area of 4.99 ± 0.26 nm. An additional +7 L of oxidation (14 cumulative) and the particle's maximum apparent height increases slightly to 0.33 nm, while their lateral area swells to an average of 8.42 ± 0.50 nm. The change in lateral area has exposed the underlying alloy surface, and will be discussed in more detail in the next paragraph. Cr-rich oxide particles of similar shape and size are found on Ni-Cr(100), demonstrating initial growth the passive chromia layer initiates with the formation of these disk like particles at 500 °C. However, unlike the (100) surface these particles are still found on the surface after 14 L, where they undergo Ostwald ripening. More work is necessary to analyze the effects [Cr] on the initial stages of oxidation on Ni-Cr(111) surfaces and the growth of these particles.

From the STM results, it is clear that after a cumulative 14 L of the oxidation three distinct oxides are present, the NiO, Cr-oxide particles and the larger Cr-oxide nodules. The electronic structure of the surface was measured to gain more insight into these oxide features. A 3x3 grid spectrum was taken with ±3.0 V over a 200×200 nm^2 area, and the results were processed into DOS and band gap maps, Figure 6-5. A blue dashed box in the topography image in Figure 6-5(A) outlines the spatial region matching the DOS and band gap maps, Figure 6-5(B)-(C). Specific regions within these oxides are selected and the STS curves within that region are averaged (60-120 curves) for a better signal to noise ratio, Figure 6-5(D).

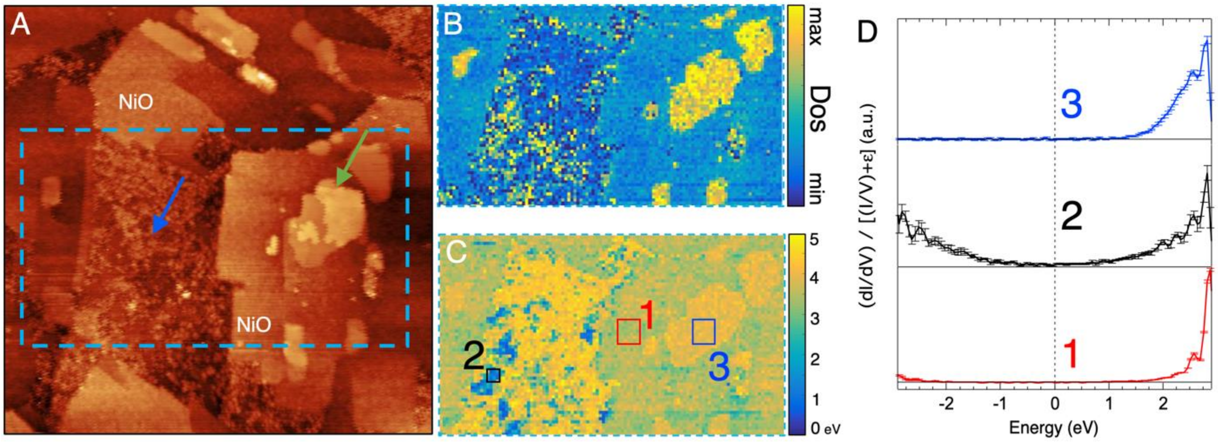

Figure 6-5. STS measurements of the Ni-18wt.%Cr surface after a cumulative 14 L. The STS data were taken from the blue-dashed square, marked in the topography image, and was formatted into an LDOS map (B) and a band gap map (C). The different oxides are marked accordingly in the STM image, the blue arrows pointing towards the smaller Cr-oxide particles and the green arrow pointing towards the larger Cr-oxide nodules. The averaged STS curves (30-60 curves) in (D) are marked with squares in (C) and provide details about the NiO (1), underlying Ni-Cr alloy (2), and the chromia layer (3). The STM topography was measured at V_{bias} = 3.0 V and I_t = 0.1 nA and is 200×200 nm^2.

The NiO in this region (1) appears to be electronically homogeneous across most of this area, while small variations in band gap can be seen near the edges of the Cr-oxide nodules. More work will be necessary to determine if these fluctuations are statistically relevant or tip induced. The smaller Cr-oxide particles have a relatively large band gap and there is some evidence that this scales with the height of the particle; however additional work is required to obtain a better signal to noise ratio that proves this. Nonetheless, patches of metallic alloy (2) can be seen near these smaller particles, which is a consequence of the Ostwald ripening – Ni surfaces are oxygen depleted for the benefit of Cr-oxidation. Region (3) corresponds to the Cr-oxide nodules, where the DOS and band gap maps emphasize their insulating nature. Similar to the Cr-oxide nodules on the Ni-Cr(100), the entire electronic structure was not captured. The average (dI/dV)/(I/V) curves show the valence band is suppressed and cannot be effectively measured due to insufficient conductivity within the nodule when the voltage sweep of ±3.0 is used. The lack of conductivity in the valence band, whether due to the oxide thickness, defects or a wide band gap, is a consequence of a low number of states available for tunneling.[10]

A schematic for the general oxidation behavior of a Ni-Cr(111) surface is provided in Figure 6-6. Given the distinctive manner in which each oxide phase developed across the surface, the oxidation pathways of the Ni and Cr are organized piecewise and described over 2 stages.

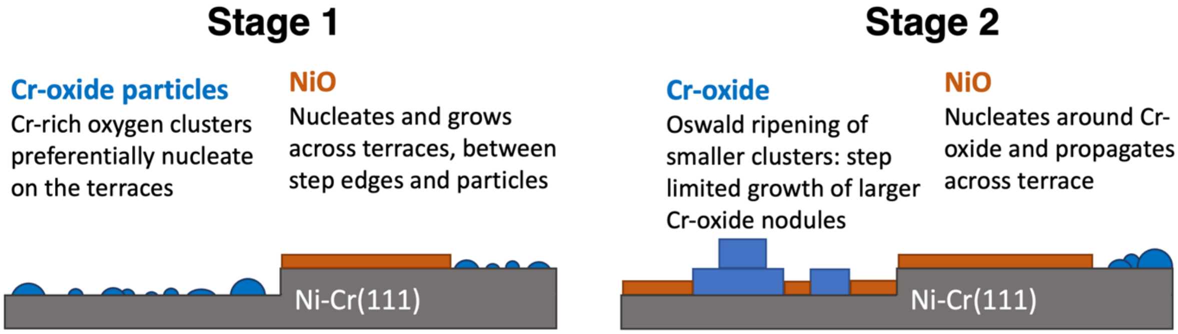

Figure 6-6. Schematic for the oxidation of Ni-Cr(111) surfaces, capturing both Ni and Cr oxidation pathways at each stage.

The initial onset of oxidation (stage 1) begins with the growth of NiO(100) layers across the terraces. These regions are typically pinned between the alloy step edges and the Cr-rich oxide particles, which nucleate and grow on both the step edges and terraces. As oxygen exposure increases (Stage 2), the Cr-oxide particles undergo Ostwald ripening and new Cr-oxide nodules are found surrounded by NiO, which grows laterally across the surface where there is an absence of the smaller Cr-oxide particles.

6.4 Conclusions

The sequential *in situ* oxidation of Ni(111) and Ni-18wt.%Cr(111) thin films at 500 ^{o}C has been studied with STM. The STM images before and after each oxidation step have highlighted the effect of crystallography and [Cr] on the initial oxidation pathways of these surfaces. The Ni(111) surface was found to saturate with oxide at a much slower rate than the Ni-Cr(111) sample. The Ni(111) surface remains mostly metallic during oxidation and islands of Ni(111)-p(2×2)O adlayers are observed on the surface.[1,3] The oxidation of the Ni-18wt.%Cr(111) alloy thin film commenced with the nucleation and growth two distinct oxide features after just 7 L of O_2. A NiO layer formed across the terraces as small Cr-oxide particles were observed to have nucleated across both the terraces and some of the alloy steps.[8,9] An additional +7 L oxidation (14 cumulative) lead to the growth of larger Cr-oxide nodules, similar to those found on Ni-Cr(100) surfaces after comparable exposures.. Some of the surface was covered by the smaller Cr-oxide particles, which grew in area and apparent height after the +7 L dose. Noticeably, greater NiO coverage was observed across areas adjacent to the larger Cr-oxide nodules, but almost no NiO was found to have grown directly neighboring the smaller particles. Instead, these smaller Cr-oxide particles and NiO were separated by step edges, suggesting the growth of the Cr-oxide nodules is step edge limited. These results support the significant role of crystallography on the oxidation pathways of low index Ni-Cr surfaces.

6.5 Chapter VI References

(1) Hildebrandt, S.; Hagendorf, Ch.; Doege, T.; Jeckstiess, Ch.; Kulla, R.; Neddermeyer, H.; Uttich, Th. Real Time Scanning Tunneling Microscopy Study of the Initial Stages of Oxidation of Ni(111) between 400 and 470 K. *J. Vac. Sci. Technol. A* **2000**, *18* (3), 1010–1015. https://doi.org/10.1116/1.582292.

(2) Kitakatsu, N.; Maurice, V.; Marcus, P. Local Decomposition of NiO Ultra-Thin Films Formed on Ni(111). *Surf. Sci.* **1998**, *411* (1), 215–230. https://doi.org/10.1016/S0039-6028(98)00372-0.

(3) Flege, J. I.; Meyer, A.; Falta, J.; Krasovskii, E. E. Self-Limited Oxide Formation in Ni(111) Oxidation. *Phys. Rev. B* **2011**, *84* (11), 115441. https://doi.org/10.1103/PhysRevB.84.115441.

(4) Das, N. K.; Shoji, T. Early Stage Oxidation of Ni–Cr Binary Alloy (111), (110) and (100) Surfaces: A Combined Density Functional and Quantum Chemical Molecular Dynamics Study. *Corros. Sci.* **2013**, *73*, 18–31. https://doi.org/10.1016/j.corsci.2013.03.020.

(5) Samin, A. J.; Taylor, C. D. First-Principles Investigation of Surface Properties and Adsorption of Oxygen on Ni-22Cr and the Role of Molybdenum. *Corros. Sci.* **2018**, *134*, 103–111. https://doi.org/10.1016/j.corsci.2018.02.017.

(6) Alexandrov, V.; Sushko, M. L.; Schreiber, D. K.; Bruemmer, S. M.; Rosso, K. M. Adsorption and Diffusion of Atomic Oxygen and Sulfur at Pristine and Doped Ni Surfaces with Implications for Stress Corrosion Cracking. *Corros. Sci.* **2016**, *113*, 26–30. https://doi.org/10.1016/j.corsci.2016.10.001.

(7) Das, N. K.; Shoji, T. Adsorption and Diffusion of H and O on an Ni(111) Surface Containing Different Amounts of Cr. *Appl. Surf. Sci.* **2018**, *445*, 217–228. https://doi.org/10.1016/j.apsusc.2018.03.134.

(8) Blades, W. H.; Reinke, P. From Alloy to Oxide: Capturing the Early Stages of Oxidation on Ni–Cr(100) Alloys. *ACS Appl. Mater. Interfaces* **2018**, *10* (49), 43219–43229. https://doi.org/10.1021/acsami.8b15210.

(9) Maurice, V.; Cadot, S.; Marcus, P. XPS, LEED and STM Study of Thin Oxide Films Formed on Cr(110). *Surf. Sci.* **2000**, *458* (1–3), 195–215. https://doi.org/10.1016/S0039-6028(00)00439-8.

(10) Sommerhalter, Ch.; Matthes, Th. W.; Boneberg, J.; Leiderer, P.; Lux-Steiner, M. Ch. Tunneling Spectroscopy on Semiconductors with a Low Surface State Density. *J. Vac. Sci. Technol. B Microelectron. Nanometer Struct. Process. Meas. Phenom.* **1997**, *15* (6), 1876–1883. https://doi.org/10.1116/1.589571.

Chapter VII: The Oxidation of Low-index Ni-22Cr Surfaces Captured *in operando* with SPELEEM

7.1 Technical Background

The data presented in this chapter were measured on a polycrystalline Ni-22wt.%Cr sample and are still undergoing analysis. Details of the current results and information about ongoing work is provided in the results and discussion section of this chapter. These data were recorded at the MAX IV synchrotron facility in Lund, Sweden, with a spectroscopic photoemission low energy electron microscope (SPELEEM) where the oxidation process was captured *in operando* across the grain boundary between two low-index surfaces. The SPELEEM at MAX IV has been used to measure the oxidation of an aluminum alloy surface *in operando* at a range of temperatures.[1] During oxidation an assortment of the SPELEEM's spectroscopic techniques (chapter III) were used to monitor the change in oxide thickness, chemical composition, and the lateral distribution of alloying elements. While not specific to our system of interest (Ni-Cr), the reader is pointed to the following reference if they desire more information about this technique and its ability to study the initial oxidation of surfaces.[1]

During our experiment, we used XPEEM (chapter III) and made additional measurements across our surface using X-ray absorption spectroscopy (XAS) and X-ray photoelectron spectroscopy (XPS) in the core and valence band regimes, respectively. Spectroscopic information taken with XAS or XPS on the oxidation phenomena across low-index Ni and Ni-Cr surfaces is available, and the details about these experiments is provided in the paragraphs below.[2,3] XPS and XAS have also been used to measure spectra from the bulk NiO or Cr_2O_3 phases, [4–6] which will be used as references for our measurements as the oxidation proceeds.

The effect of crystallography on the oxidation of Ni(100), Ni(110) and Ni(111) surfaces in UHV has been studied with photoelectron spectroscopy.[2] When oxidized between 295 and 485 K, XPS core-level measurements show the oxidation sequence begins with the dissociative chemisorption of oxygen followed by the nucleation and growth of NiO. The effect of O_2 exposure and temperature on the valence band of low index Ni surfaces and clean NiO has also been measured.[2,4] During repeated oxidation steps, the Ni(111) valence band spectra shifts to higher binding energy and grows a shoulder about 2 eV below the Fermi energy.[2] This shoulder eventually becomes the most prominent peak in the spectrum as the oxidation continues and corresponds to the NiO signal.[4] Once the film grows laterally across the surface it thickens to a limiting coverage of 3 NiO layers and the growth rate of the film was determined to be Ni(110) > Ni(111) > Ni(100).[2]

The chemical structure of Ni and Cr oxides has been measured with XAS. The Cr L-edge XANES spectra in a bulk Cr_2O_3 sample has been studied,[5] as well as the absorption spectroscopy of small chromia oxide particles.[6] XAS has also been used to measure the Ni L-edge XANES spectra of NiO.[7] Both XAS and XPS can provide useful information about the chemistry and oxidation state of surfaces, and when used in tandem with XPEEM (chapter III), the initial oxidation phenomena can be captured *in operando*. Therefore, a combination of these techniques will be used to study the early stages of oxidation simultaneously across two grains on a polycrystalline Ni-22wt.%Cr alloy surface at 500 ^{o}C.

7.2 Methods

The polycrystalline Ni-22wt.%Cr alloy sample was annealed for 150 hr at 1150 ºC to grow the grains of the sample, which facilitated measurements between the grains. After the anneal, the sample was polished to an EBSD finish (0.1 micron). The sample was then placed into the MAXPEEM lab prep chamber (Lund, Sweden) under UHV conditions (1.2×10^{-10} torr). The ambient oxide was removed by annealing for 1.25 hr at 600 ºC. A set of flash anneals was included, where the sample was held for 10 s at 700-800 ºC for 18 cycles to prepare a clean alloy surface. Prior to oxidation, a grain boundary on the Ni-22wt.%Cr sample surface was located by using the mirror electron microscopy (MEM) and EBSD measurements (made *ex situ*) provided crystallographic maps at this boundary, Figure 7-1. A green-dashed square superimposed over the MEM image in Figure 7-1(A) marks the area were the entire oxidation experiment was conducted. The EBSD map in Figure 7-1(A) aligns well with the grain boundary of the MEM mode. After the alloy was cleaned, the sample was held at 500 ºC during the oxidation steps: (1st oxidation) +**5 L** – [$p(O_2) = 7.5\times10^{-9}$ torr, 11 min], (2nd oxidation) +**15 L** – [$p(O_2) = 7.5\times10^{-9}$ torr, 33 min], (3rd oxidation) +**45 L** – [$p(O_2) = 7.5\times10^{-9}$ torr, 99 min]. Throughout the oxidation, XPEEM recorded the evolution of the surface *in operando* by monitoring the Cr-L edge (577.5 eV) with the μ-XAS and a spatial resolution of 25 nm per pixel. Both, XAS and XPS, spectra were recorded in the valence and core level regimes before and after each oxidation step. A complete table summarizing the different methods and reaction steps is provided below the MEM and EBSD map. Reference absorption spectra from the Ni and Cr L-edges before and after oxidation are provided in the supplemental data section, Figure 7-S1.

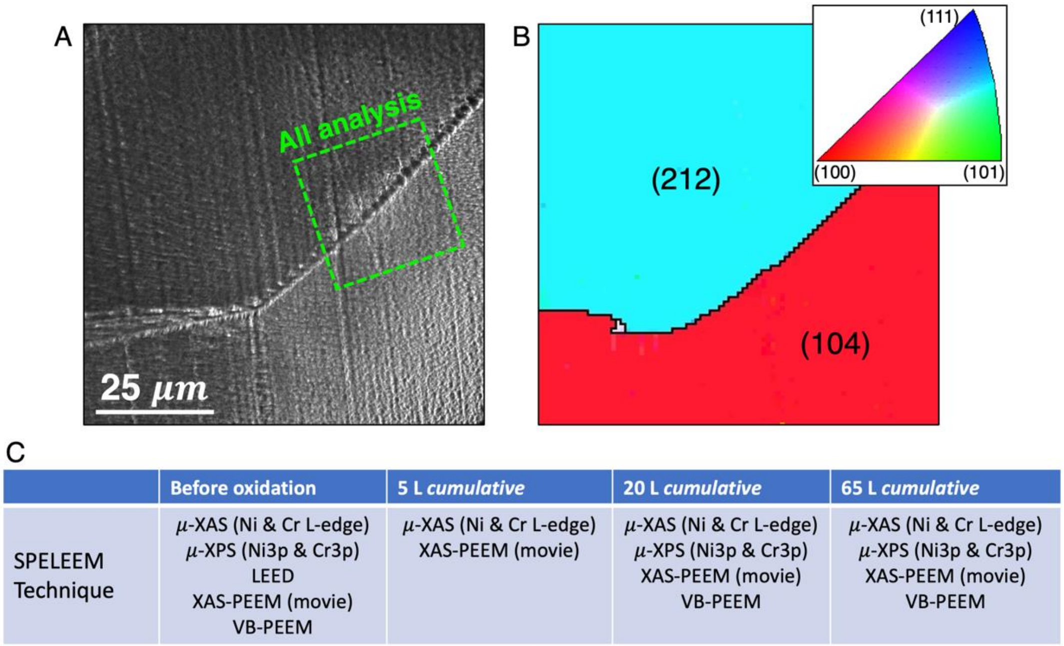

	Before oxidation	5 L *cumulative*	20 L *cumulative*	65 L *cumulative*
SPELEEM Technique	μ-XAS (Ni & Cr L-edge) μ-XPS (Ni3p & Cr3p) LEED XAS-PEEM (movie) VB-PEEM	μ-XAS (Ni & Cr L-edge) XAS-PEEM (movie)	μ-XAS (Ni & Cr L-edge) μ-XPS (Ni3p & Cr3p) XAS-PEEM (movie) VB-PEEM	μ-XAS (Ni & Cr L-edge) μ-XPS (Ni3p & Cr3p) XAS-PEEM (movie) VB-PEEM

Figure 7-1. The surface of our polycrystalline Ni-22wt.%Cr sample. MEM image is provided in (A) and a EBSD map of the grains across the GB. A table (C) of the experimental techniques used during the experiment. VB stands for valence band, which was measured in the μ-XPS mode with a photon energy of 100 eV. The XAS-movies refer to the in operando XAS measurements of the growth of the chromia. These were recorded during oxidation and energy filtered at 577.5 eV to monitor the the Cr L-edge.

7.3 Results and Discussion

To capture the relative crystallographic orientation of the grains at the grain boundary, we performed LEED measurements. The grains were identified as (212) and (104) surfaces, which are stepped surfaces with (111) and (100) terraces, respectively. The LEED patterns accompany an energy-filtered image from the μ-XAS measurements that shows the surface at the grain boundary prior to oxidation, Figure 7-2. The surface unit cell in reciprocal space is superimposed over the LEED patterns with a red dashed box, and the directions in the surface are deduced from the rotation of the diffraction pattern. The diffraction spots in the LEED pattern closer to the (000) reflection originate from the periodic terrace widths of each step on the surface (~0.7 nm on each

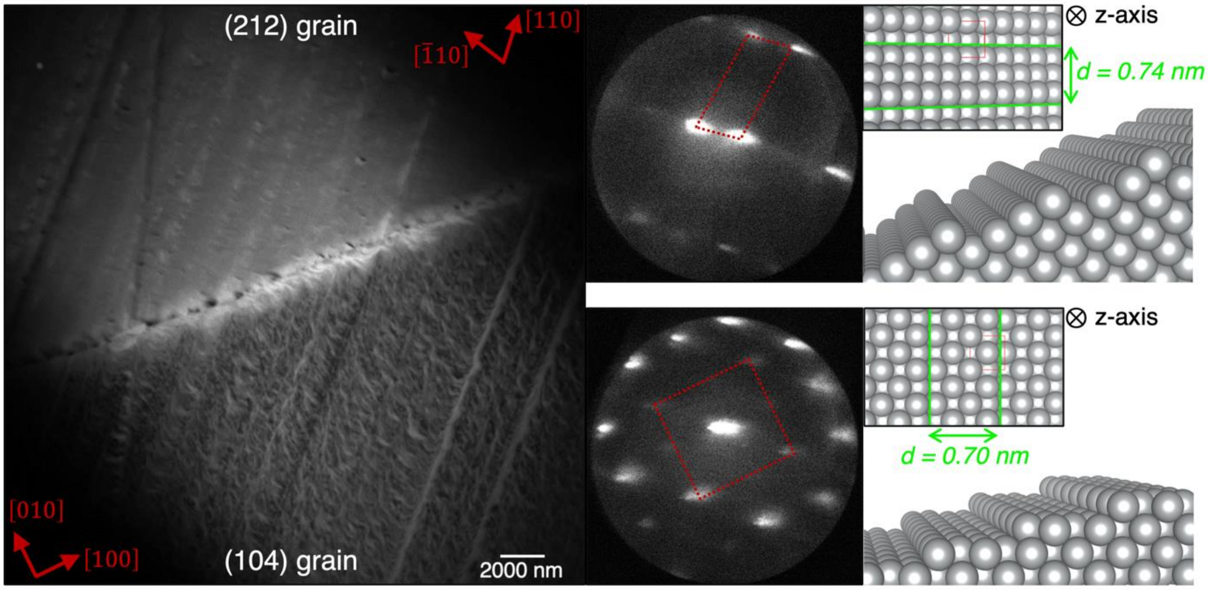

Figure 7-2. An XPEEM image of the (212) and (104) surfaces taken in the XAS-image mode ($E_{slice} \approx$ 580 eV). Next to each grain are the are the LEED patterns and hard-sphere models of each surface.

grain). Hard sphere models of these stepped surfaces are also provided in Figure 7-2. Prior to oxidation, XPEEM measurements were taken across area of interest in both the core-level and valence band regimes and spectra from the μ-XAS and the μ-XPS were generated. The μ-XPS was also used to probe the surface's valence band (*hv* = 100 eV), which provided information about

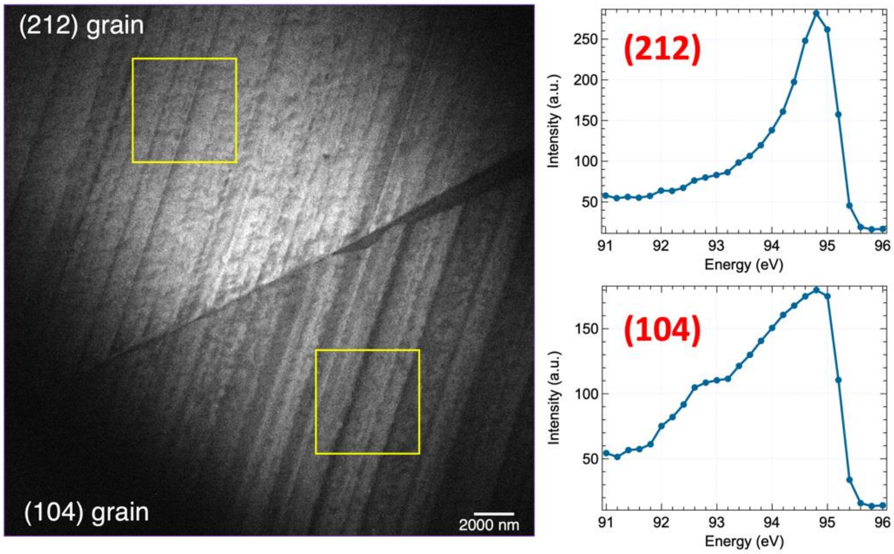

Figure 7-3. An XPEEM image ($E_{slice} \approx$ 95.2 eV) of each grain is constructed from the valence band spectra. The valence band spectra are taken from the areas marked by the yellow boxes in image.

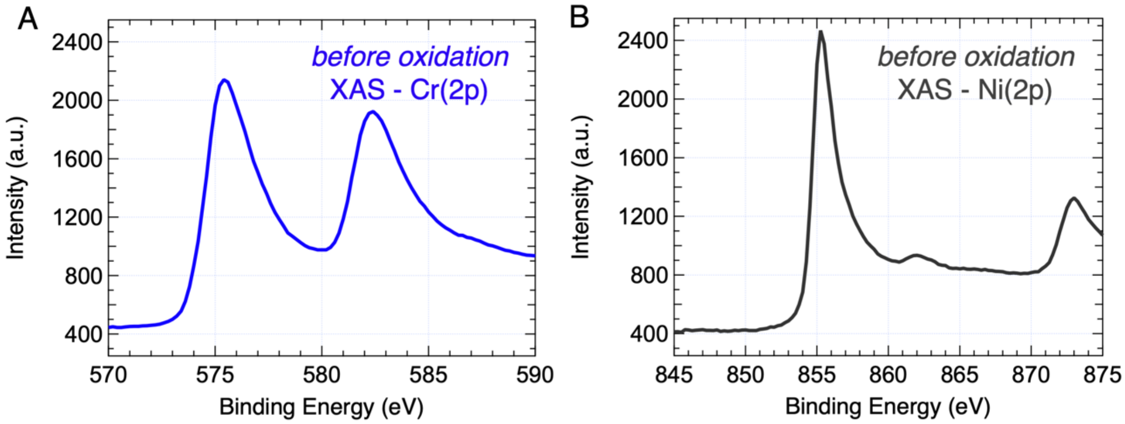

Figure 7-4. XAS spectra of the Ni and Cr L-edge (2p core) taken across both grains (including the grain boundary) before the oxidation.

the DOS of the alloy surface near the Fermi energy. The spectra from each grain, as well as an XPEEM image constructed from the valence band measurements, are provided in Figure 7-3. The valence band spectra highlight the electronic heterogeneity between each of the grains, and DFT calculations of these two surfaces are currently being compiled for interpretation of these results. The Cr(2p) and Ni(2p) μ-XAS measurement in Figure 7-4 reflect the metal spectra and no oxide is detected.

The oxidation commenced by leaking O_2 into the chamber and the changes to the surface were monitored the Cr-L edge using XPEEM (μ-XAS, E = 577.5 eV) *in operando*, Figure 7-5. This energy window was chosen to monitor the chromia growth and provide maximum contrast changes at the surface (see methods section 3.4.1). During the first oxidation step **(+5 L at 500 ^{o}C)** small bright spots appeared across each grain and are marked with blue arrows on the 665 s image. These spots (oxide islands, surface oxides, or reconstructions) are primarily concentrated around the grooves of the polishing marks, while a few are found to have populated between those grooves. After a **cumulative 20 L exposure** the bright spots begin to show signs of anisotropic growth, and the flat regions on the surfaces are now well-covered. A film, marked with arrows in

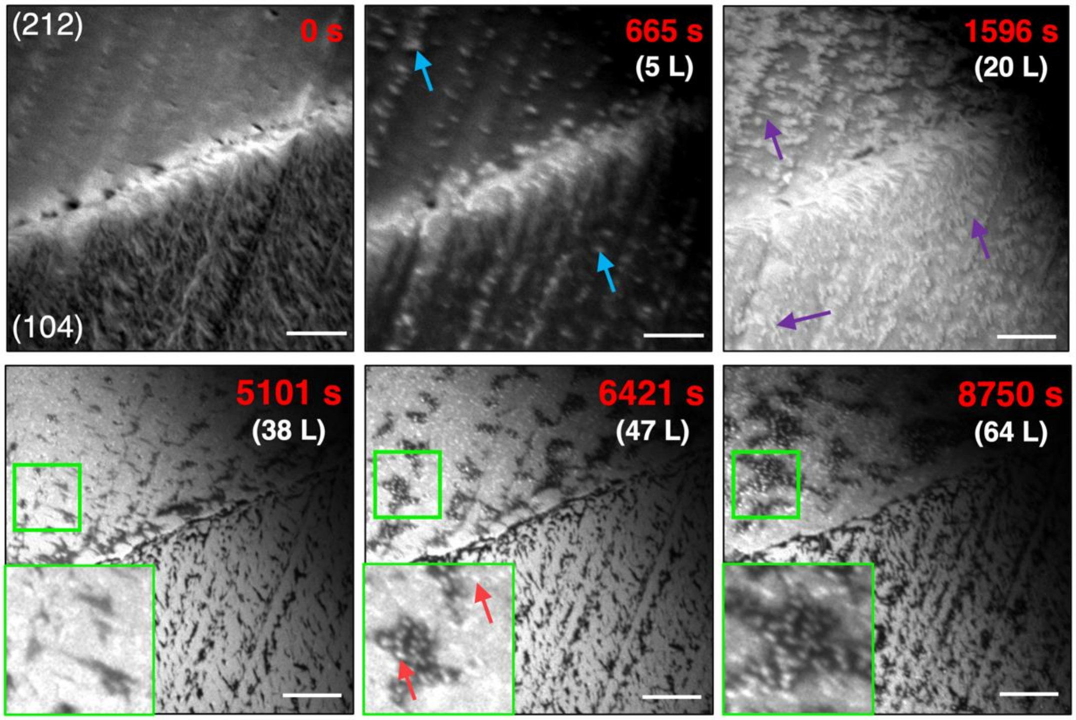

Figure 7-5. Select times during the *in operando* oxidation at 500 ^{o}C across the (212) and (104) surface taken with the XAS-PEEM imaging mode. Contrast is from the intensity of the Cr-O feature in the Cr-L edge as shown in Figure 7-6. The scale bars are all 2000 nm and the images insets are each 2000×2000 nm^2.

the 1596 s image, has begun to preferentially grown along different directions across each grain, and this behavior continues as the oxidation proceeds.

During the **+45 L exposure**, the film continues to grow, and the surface appears to reach full coverage around 5000 s. At this stage of the oxidation smaller features nucleate across the film and are marked on the 6421 s image inset in Figure 7-5. Initially, the size and shape of these nodules appear more isotropic, and they preferentially nucleate and grow on the (212) surface, where the number of nodules per nm^2 is greater on the (212) surface as compared to the (104). As the oxidation progresses, the crystallography affects the growth behavior of the nodules, and the underlying film begins to undergo a chemical change in some areas. The change in the film manifests as a increase in area of “dark patches” in the XPEEM images. To better understand the progression of the oxidation pathways on these two surfaces, chemical identification of the oxide phases is necessary.

To this end, μ-XAS spectra of the Cr(2p) and Ni(2p) core levels (L-edge) are measured after each oxidation step. μ-XPS measurements in the valence band regime are also measured after a cumulative 20 L and 65 L exposures. These spectra are then spatially resolved across both the (212) and (104) grains with XPEEM, enabling feature matching. Comparing the XAS spectra after the cumulative 5 L and 20 L exposures, no characteristic modulation of the L-edge is seen, which would indicate the presence of Cr_2O_3 or NiO.[6,7] At these low exposures, the only measurable difference in the XAS spectra is a change in relative intensity when spectra across the film (brighter areas in the XPEEM images) are compared to those taken from the darker background. The change in intensity is likely due a shift in work function that accompanies the formation of a thin oxide film on the surface, however the XAS signal surface-to-bulk ratio is too small to detect any chemical shifts. Indeed, our STM results (chapters IV, V, and VI) have shown that when low-index Ni-Cr alloy surfaces are exposed to low doses of oxygen ($\geq$ 20 L at 500 ^{o}C), the surface becomes saturated with an atomically thin oxide layer.[8] Consequently, at these exposures the oxygen dose is too small and the subsequent oxide phase too thin to accurately measure any shift in the XAS spectra. Valence band measurements were made after a cumulative 20 L of exposure and when coupled with DFT, these data should provide an avenue for chemically determining what oxide phase is present and how the O_2 adsorption changes the DOS of the surface. This work is still on going and will be discussed later in this section.

After 65 L of cumulative oxidation, changes to the absorption spectra indicate the presence of a significant amount of chromia. To determine the origins of this layer, a closer examination of the μ-XAS filtered XPEEM data is necessary, Figure 7-6(A). It has been discussed that as the

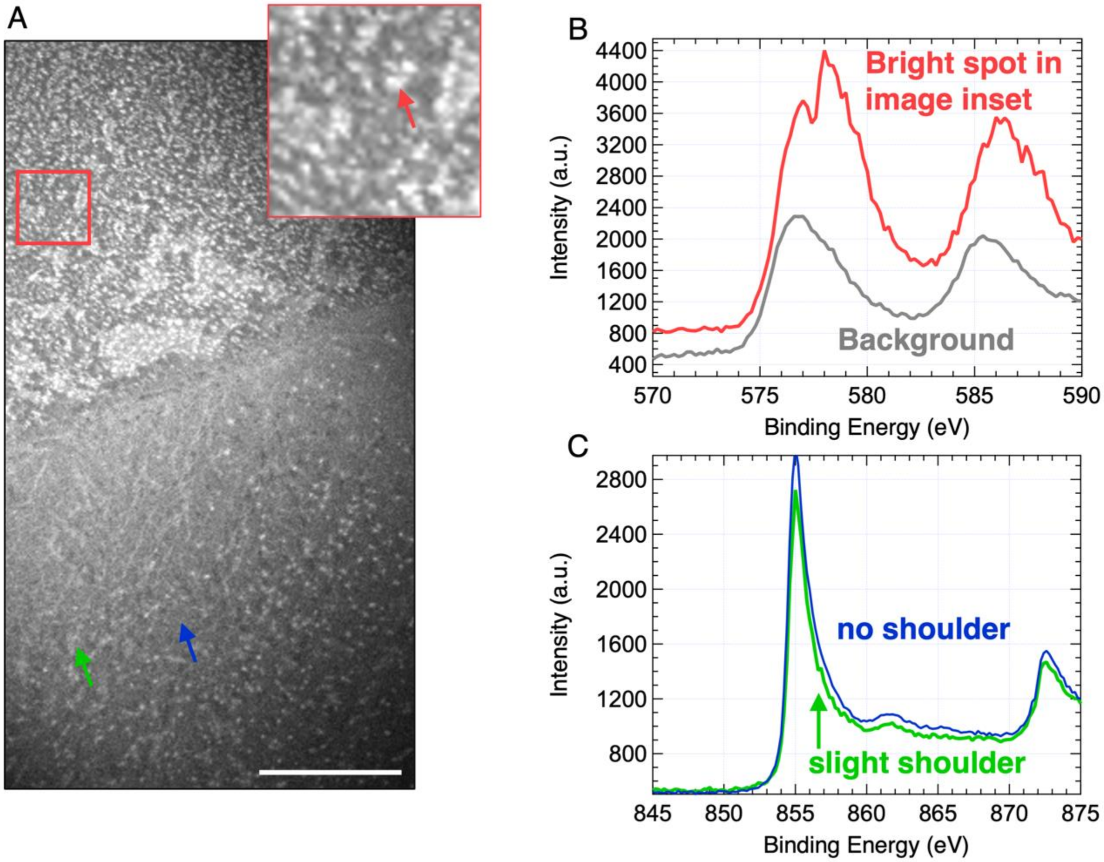

Figure 7-6. An XPEEM image (A) after a cumulative 65 L of exposure at 500 ^{o}C. The Cr L-edge XAS spectra (B) was taken from one of the nodules (red arrow in the image inset) and the surrounding background. The Ni L-edge spectra (C) was taken from the edge of one of the bright areas (green arrow) and one of the darker areas (blue arrow) on the (104) grain. For the XPEEM image the energy slice was taken at E_{slice} = 582 eV and the scale bar is 2000 nm.

oxidation of the Ni-22wt.%Cr sample progresses, a film initially grows across both grains of the Ni-Cr alloy. “Film” is used here as a general expression to include oxygen adsorbates, reconstructions, and surface oxides since the spectroscopic analysis has not yet been concluded. Once this film saturates the surface around 5000 s, smaller nodules nucleate and grow amongst the film. Isolating an area of about 5×5 pixels (25 XAS spectra) centered at these nodules and comparing a similar number of spectra from the background, confirm the nodules are indeed chromia islands, Figure 7-6(B). The spectra taken from the background, the area between the nodules, reflects the Cr(2p) absorption spectra measured from the alloy prior to oxidation. The μ-XAS Ni(2p) absorption spectra is provided in Figure 7-6(C) and seems almost unchanged after 65 L of oxidation. A small shoulder does appear on the right of the main peak and is consistent with NiO,[7] however this spectra cannot be matched to any specific features in the images. Although there are slight modulations to the shoulder of the absorption peak (evidence of an oxide), it is likely the NiO is too thin to be accurately detected with the μ-XAS at these exposures.

While the μ-XAS measurements show no chemical difference between the chromia nodules across the grains, the number of nodules per unit area is much greater on the (212) surface than on the (104). The μ-XAS filtered XPEEM image in Figure 7-6(A) also shows this density is uniform across the (212) while the density across the (104) surface is not. It appears this effect is most prevalent on the (104) surface near the grain boundary, while the density increases and becomes more uniform further away. Currently, the XPEEM data are still evaluated and more work is necessary to understand the dynamic changes induced by oxidation at the surface. Details about the work presently being undertaken is discussed in more detail below.

To better understand the nucleation and growth kinetics of the Cr-oxide islands of each grain, image segmentation with a level-set method has been employed in a collaboration with the Voorhees Group at Northwestern University. The level-set method is a computational method developed to numerically solve moving interface problems and can handle changes to the topography.[9,10] This method can be used to smooth the interfaces and shapes of the Cr-oxide islands from the movies generated by the XPEEM. The general flow chart of this method is provided in Figure 7-7. First the Cr-oxide islands are isolated from the image background via segmentation (subsection 3.9.4), and then the interfaces of each of the islands are identified. Once the interfaces of each island have been determined, functions that represent the changes to each

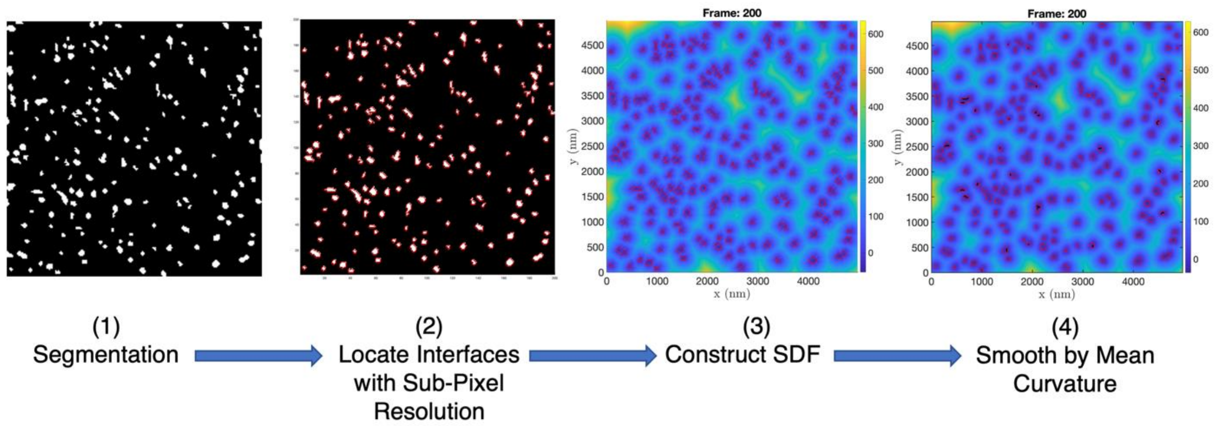

Figure 7-7. The work flow of image processing to use the Level-set method. The flow progression XAS-image segmentation and interfacial smoothing of the chromia islands on the (104) surface is provided above each step of the process.

interface are constructed. The curvature of each interface is then averaged and smoothed, which will enable each interface to be studied as a function of time.

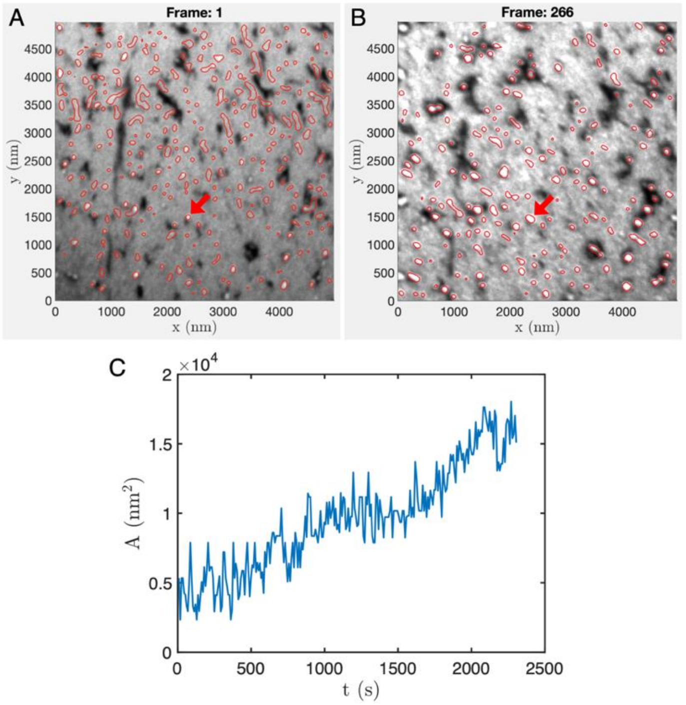

Figure 7-8. The change in chromia island area during oxidation. Image (A) was taken after about 48 L and image (B) after about 65 L. Some preliminary results from the level-set method are provided in (C), which shows the growth of the chromia nodule as a function of time.

The changes to each constructed interface relate to the interfacial changes the Cr-oxide island, which evolve as a function of O_2 exposure. This facilitates the direct analysis of Cr-oxide growth on each grain by determining changes to the oxide particle areas, particle interface lengths and the curvature and normal velocity of the growth fronts. An example of the growth of the chromia nodules on the (104) surface is highlighted in Figure 7-8. The images are taken from two different points during the oxidation, image (A) is after 48 L of O_2 and image (B) after about 65 L. One of the chromia nodules is marked with a red arrow in both images and its area changes linearly with time, Figure 7-8(C). While these results are preliminary, more work needs to be done to the image segmentation to accurately determine the velocities and curvatures of the growth fronts across each grain. This will enable a more complete understanding of how the crystallography effects the growth kinetics of the passive chromia layer at these temperatures.

The μ-XPS valence band measurements are also still under evaluation. After 65 L of cumulative O_2 exposure, the surface still shows a significant level of heterogeneity between the grains. Spectra were measured over known areas of chromia nodules and in between those areas (i.e. the background), Figure 7-9(A)-(B). Currently, these data are being coupled with DFT, which is being done by the Árnadóttir Group at Oregon State University. To date, a Ni(104) surface have been generated and the DOS calculated, Figure 7-9(C). This will provide a better understanding of how the surface changes during oxidation.

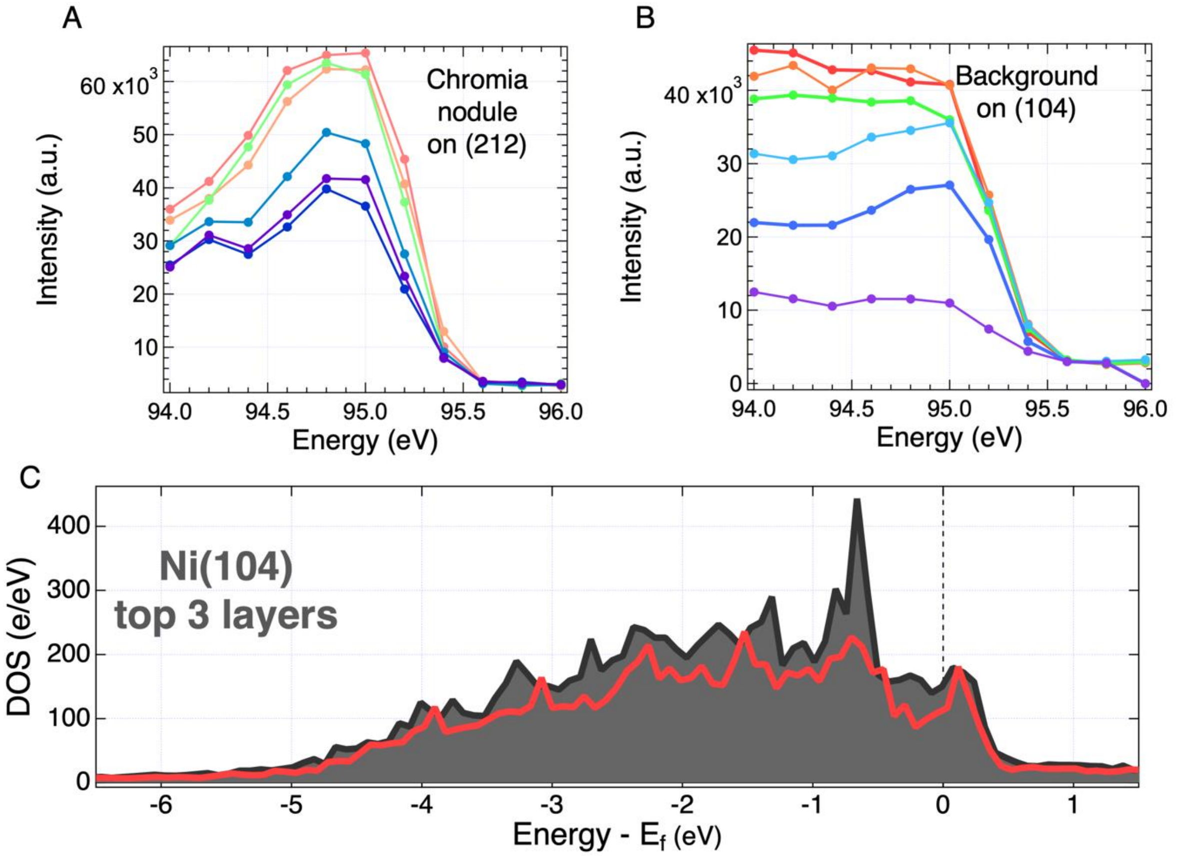

Figure 7-9. Valence band measurements from 6 chromia nodules on the (212) surface (A) and 6 areas between the nodules on the (104) grain (B). The density of states (C) from the top 3 atomic layers of a Ni(104) surface. The red line superimposed over the Ni(104) DOS is that of a Ni(100) surface, highlighting the effect of the steps on the electronic structure of the surface.

7.4 Conclusions

Studying the oxidation of a polycrystalline Ni-22wt.%Cr sample *in operando* with SPELEEM provided a wealth of information. Combining *in situ* LEED and *ex situ* EBSD yielded crystallographic information about our sample, and the experiment was conducted at the grain boundary of a (212) and (104) grain. The μ-XAS and the valence band μ-XPS measurements revealed a clean metal surface. After a cumulative 20 L oxidation at 500 ^{o}C, changes to our Ni-

22wt.%Cr surface were observed as a film grew across each surface, however little to no spectroscopic changes were measured and chemical identification of the oxide phases remains a challenge at these exposures. During the +45 L exposure, the initial film that grew saturated the surface and smaller nodules appeared across (212) and (104) grains. These nodules were confirmed with XAS to be chromia. A level-set method is used to monitor the growth of these nodules as a function of O_2 and is currently ongoing. The μ-XPS valence band measurements reveal a significant level of heterogeneity at the surface. Understanding what contributes to this heterogeneity requires the use of DFT and is still under evaluation.

7.5 Chapter VII References

(1) Rullik, L.; Evertsson, J.; Johansson, N.; Bertram, F.; Nilsson, J.-O.; Zakharov, A. A.; Mikkelsen, A.; Lundgren, E. Surface Oxide Development on Aluminum Alloy 6063 during Heat Treatment. *Surf. Interface Anal.* **2019**, *51* (12), 1214–1224. https://doi.org/10.1002/sia.6616.

(2) Norton, P. R.; Tapping, R. L.; Goodale, J. W. A Photoemission Study of the Interaction of Ni(100), (110) and (111) Surfaces with Oxygen. *Surf. Sci.* **1977**, *65* (1), 13–36. https://doi.org/10.1016/0039-6028(77)90289-8.

(3) Allen, G. C.; Tucker, P. M.; Wild, R. K. X-Ray Photoelectron/Auger Electron Spectroscopic Study of the Initial Oxidation of Chromium Metal. *J. Chem. Soc. Faraday Trans. 2 Mol. Chem. Phys.* **1978**, *74* (0), 1126–1140. https://doi.org/10.1039/F29787401126.

(4) Tjernberg, O.; Söderholm, S.; Chiaia, G.; Girard, R.; Karlsson, U. O.; Nylén, H.; Lindau, I. Influence of Magnetic Ordering on the NiO Valence Band. *Phys. Rev. B* **1996**, *54* (15), 10245–10248. https://doi.org/10.1103/PhysRevB.54.10245.

(5) Ünveren, E.; Kemnitz, E.; Hutton, S.; Lippitz, A.; Unger, W. E. S. Analysis of Highly Resolved X-Ray Photoelectron Cr 2p Spectra Obtained with a Cr2O3 Powder Sample Prepared with Adhesive Tape. *Surf. Interface Anal.* **2004**, *36* (1), 92–95. https://doi.org/10.1002/sia.1655.

(6) Neisius, Th.; Simmons, C. T.; Köhler, K. X-Ray Absorption Spectroscopy of Small Chromium Oxide Particles (Cr2O3, CrO2) Supported on Titanium Dioxide. *Langmuir* **1996**, *12* (26), 6377–6381. https://doi.org/10.1021/la960261f.

(7) Peng, H. Y.; Li, Y. F.; Lin, W. N.; Wang, Y. Z.; Gao, X. Y.; Wu, T. Deterministic Conversion between Memory and Threshold Resistive Switching via Tuning the Strong Electron Correlation. *Sci. Rep.* **2012**, *2* (1), 442. https://doi.org/10.1038/srep00442.

(8) Blades, W. H.; Reinke, P. From Alloy to Oxide: Capturing the Early Stages of Oxidation on Ni–Cr(100) Alloys. *ACS Appl. Mater. Interfaces* **2018**, *10* (49), 43219–43229. https://doi.org/10.1021/acsami.8b15210.

(9) Gibou, F.; Fedkiw, R.; Osher, S. A Review of Level-Set Methods and Some Recent Applications. *J. Comput. Phys.* **2018**, *353*, 82–109. https://doi.org/10.1016/j.jcp.2017.10.006.

(10) Osher, S.; Sethian, J. A. Fronts Propagating with Curvature-Dependent Speed: Algorithms Based on Hamilton-Jacobi Formulations. *J. Comput. Phys.* **1988**, *79* (1), 12–49. https://doi.org/10.1016/0021-9991(88)90002-2.

7.6 Supplemental Data and Supporting Information

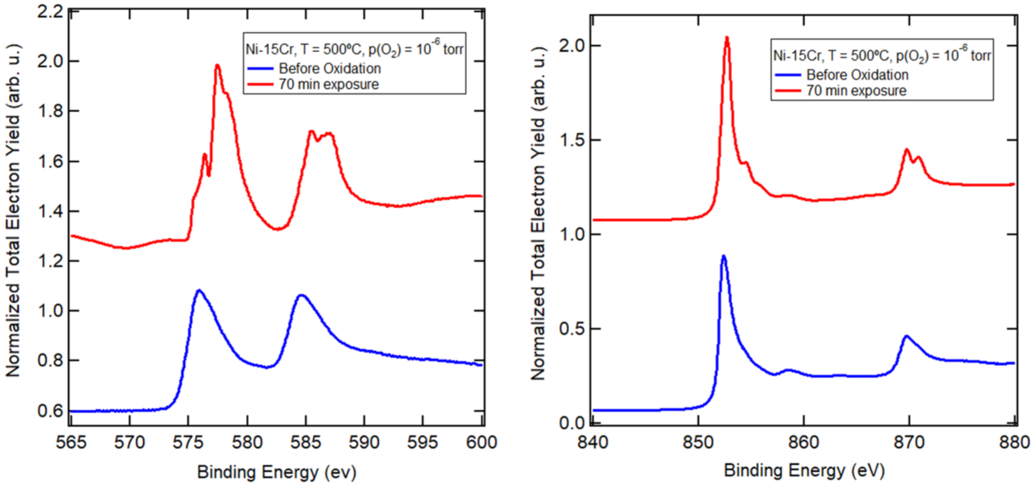

Figure 7-S1. Alloy and oxide XAS spectra of a Ni-Cr15wt.%Cr sample surface before and after exposure. These results were taken by a group member (Cameron Volders) at Brookhaven National Lab.

Chapter VIII: Influence of Chloride on Nanoscale Electrochemical Passivation Processes

8.1 Technical Background

Ni-Cr alloys are known for their robust corrosion resistance in a wide range of environments. This property is due to the formation of Cr-rich oxides, along with NiO and hydroxides, which are thermodynamically and kinetically stable over a broad range of potential and pH[1–5]. In chloride solutions, however, these oxide films have been observed to undergo localized breakdown and dissolution in the form of pitting and crevice corrosion[6–14]. The interaction of aggressive anions with the passive film during passivation, brought about by combinations of high applied potentials and Cl^- anions, initially causes local dissolution of oxide nanoparticles formed during passivation and consequently can lead to detrimental attack of the underlying alloy or metal[15,16]. In chloride environments in particular, this local attack manifests first as metastable pit events traceable to local instabilities in the oxide[17,18], which repassivate or lead to stabilization of more persistent forms of local attack such crevice or pitting corrosion[9,10,19,20]. The repassivation after these metastable events can lead to oxide film thinning and/or enhanced susceptibility to dissolution[21]. Notably such events are not seen in sulfate solution[2]. Preferential halide induced metastable pitting is more likely to occur at higher energy sites, such as a geometric or electronic surface inhomogeneities in the oxide, or local Cr-lean regions[15]. For metals and alloys, which are capable of initial passivation or healing by repassivation over a range of potentials in the passive range such as Ni-Cr alloys, the local breakdown-repair process is compensated by additional film growth at the metal/film interface[22,23]. The balance between film growth and dissolution at favored surface oxide sites will likely modify the composition of the oxide film and the surface and metal roughness over time.

In addition to breakdown-repassivation events and metastable pitting, surface roughening could also occur by other chemical processes including preferential chemical dissolution and/or oxidative dissolution of regions of the oxide without breakdown. Moreover, the overall evolution and presentation of film roughness is not solely controlled by surface chemical processes but is also linked to initial nucleation events, growth modes of the passive oxide layer, surface energy modulation by adsorbates, and morphological instabilities[18,24]. The surface roughness, independent of its cause, can exacerbate local variations in dissolution rates by preferential dissolution at geometric inhomogeneities, which locally modulate the electrostatic field such as edges, corners, and grain boundaries of oxides, and reactivity variations due to chemical inhomogeneities such as different oxide identities or variations in defect population[25,26]. This involves dissolution at the oxide-solution interface, which thins the oxide. In the same vein, local fluctuations in Cr-concentration, or variable orientation of the grains in the alloy can lead to modulation of the local oxide formation reaction[27]. However, both (chemical) roughening mechanisms, repassivation and chemical dissolution, are interdependent and repassivated pits might locally exhibit dissolution rates, which differ from those of the pristine film. Chloride adsorption has been observed in outer layer nickel hydroxides, as well as trapped at the oxide-metal interface when active Ni is passivated in Cl^- containing solutions[28]. The incorporation of Cl^- in the hydroxide is proposed to occur by a ligand exchange process[28]. It merits comment that sulfate does not adsorb on α-chromia nor Goethite by a ligand exchange process but instead adsorbs without ligand exchange [32,33].

Lastly, Cl^- adsorption can affect surface and interfacial energies and thus can modulate oxide morphology and consequently surface roughness developed during nucleation and growth[18,29,30]. If heterogeneity of structure, composition and electronic properties of oxides contribute to differences in Cl^- adsorption, which in turn alters the surface energy, then local oxide/hydroxide growth and morphology might be modified in even more complicated ways. The usual electrochemical description of passivation based on overall electrochemical current considers the global dissolution and growth kinetics averaged over the entire interfacial boundary, but neglects local rate fluctuations[2]. In these models, conformal oxide formation is assumed. Most models of aqueous passivation kinetics do not factor in the impact of lateral differences in dissolution rates and only a few models have started to take lateral variations and heterogeneity into account[18,22,23,31]. For example, recent theoretical models use the framework of morphological instabilities to describe oxide and oxide-alloy interface roughening[18].

We propose that the details of the oxidation process and passive layer evolution in Cl^- solution should be further scrutinized by examining oxide film formation and exposure aging by combining electrochemical analysis *in-operando* with a quantitative assessment of surface roughness and oxide film composition by atomic force microscopy and XPS, respectively. To isolate the impact of local fluctuations in morphology brought about by the collective impact of Cl^- on adsorption, repassivation, dissolution, changes in surface energy and possible changes in reaction rates, we compare passivation of the same Ni-22 wt% Cr alloy in solutions of equal pH but with variations in key anions: these include (a) a slightly acidified sulfate ion containing solution without intentional Cl^-, which does not lead to oxide breakdown, and (b) a slightly acidified chloride solution, which is known to be very aggressive and a challenging environment for retaining passivity in the presence of instabilities and local breakdown at high potential driving force. We also included a hybrid experiment where a smooth oxide layer initially formed in a Cl^- free sulfate solution is exposed to the aggressive chloride solution to test the role of surface topography on passivation and performance.

Few experiments have been published to date which offer a direct comparison between global and local morphologies and reactions, and we briefly summarize here the results of the most pertinent studies for aqueous as well as dry oxidation. For the pure Ni metal, electrochemical passivation in aqueous solution has been studied by scanning tunneling microscopy (STM)[34–38] and atomic force microscopy (AFM)[38,39]. It was found that Ni forms an inner layer of NiO and an outer, porous $Ni(OH)_2$ layer[40]. Pitting was observed preferentially at oxide grain boundaries with elongation of the oxide grains occurring in the direction of substrate terraces [36].

With regards to Ni-Cr alloys, dry oxidation at high temperatures[41–46] and passivation in various electrochemical environments[2,47–54] have been investigated. Oxidation in air at temperatures above 600 °C leads to rapid formation of NiO before reaching a constant film composition, whereas Cr_2O_3 accumulates over time via interfacial and internal oxidation[41,42,44]. Higher temperatures, and higher Cr concentration in the alloy will favor Cr_2O_3 formation and growth over NiO[55,56]. At lower concentrations of Cr in the alloy (<15wt%), NiO dominates and is observed as initial oxide nuclei, which eventually coalescence to produce a conformal layer[45]. Recent work using *in-situ* transmission electron microscopy (TEM) demonstrated that oxidation in this regime occurred through an adatom surface diffusion mechanism[44,45]. Upon increasing the bulk Cr concentration, the subsurface Cr_2O_3 coalesces and produces a continuous layer beneath the NiO thus greatly increasing protective function[57–62].

A local view of Ni-Cr dry oxidation was reported recently in an STM study[63], which compared single crystal Ni(100) and dilute Ni-Cr(100) alloy surfaces. This work illustrates how lateral heterogeneity in an oxide can already be introduced during the initial steps of oxidation. The surfaces were exposed to O_2 *in-situ* at 500 °C and characterized using scanning tunneling microscopy (STM) and scanning tunneling spectroscopy (STS) to develop an atomistic understanding of the oxidation process. The Ni(100) surface, under the aforementioned oxidation conditions, undergoes kinetically limited oxide growth requiring large oxygen fluences (> 500 Langmuir (L)), whereas NiO nucleation occurs along the step edges of Ni-Cr(100) alloy after just 7 L of O_2 exposure. These results indicate that the activation barrier for NiO nucleation is significantly lower for Ni-Cr(100) alloy surfaces than for Ni(100). Additional annealing and oxygen exposure promotes NiO growth along the terraces and is accompanied by step bunching and reconfiguration of the alloy-oxide interface. Concurrently, Cr-alloying leads to the initial formation of small oxide particles across the terraces, which are identified as Cr-rich oxide nuclei. Further oxidation introduces novel surface reconstructions and contributes to the formation of large oxide nodules identified as Cr_2O_3 or $NiCr_2O_4$ as a consequence of the laterally inhomogeneous distribution of Cr on the surface. Recent work shows the presence of a much larger variety of oxide, which structurally present as rocksalt and corundum but provide significant composition variations. This can be described in the framework of solute capture[55].

Electrochemical oxide film growth on Ni-Cr in aqueous solutions has been characterized using electrochemical impedance spectroscopy (EIS)[2,47,49–54], X-ray photoelectron spectroscopy (XPS)[64], X-ray absorption near edge structure (XANES)[48], Neutron Reflectometry[65] and recently, inductively coupled plasma mass spectroscopy (ICP-MS)[2,65]. In general, it has been found that in aqueous environments, the passive films are rich in $Cr(OH)_3$ and $Ni(OH)_2$. The growth progression is similar to those seen for dry oxidation; Ni-oxides nucleate first and coalesce rapidly whereas Cr-oxide enrichment is slower beneath the Ni-layer and eventually dominates the film composition[2,50]. Nickel oxide and hydroxide films are preferentially dissolved at pH 4, such that over 10^5 s of passivation, Cr cations are enriched[40]. Water molecules, however, hydrate the films and produce more defective hydroxide films[2]. Upon increasing the concentration of Cr in an alloy, the films are consequently enriched in Cr beyond the composition in the bulk alloy, which leads to more positive pitting potentials with a corresponding decrease in the frequency of metastable pitting events in chloride environments[27]. Prior literature has helped to identify the chemical, electronic, and physical structure of passive films on Ni-Cr, but very little work has been reported aimed at understanding the surface of Ni-Cr alloys during the early to intermediate stages of passivation and film growth in acidic and chloride-containing solutions[25,40]. Limited prior studies found Cl^- may interact with $Ni(OH)_2$ via a ligand exchange process where the hydroxide may form Ni(OH)Cl. Cl^- 2p XPS data suggest that $NiCl_2$ is not present, and Cl^- incorporation in the inner layer remains controversial[28,66,67].

We present herein an investigation where the time-dependent electrochemical passive film growth on binary Ni-22 wt% Cr is studied using single frequency EIS (SF-EIS) to examine passivation *in-situ*, coupled with *ex-situ* AFM imaging and analysis of the evolution of the surface topography and roughness. The passivation was achieved in dilute acidified NaCl solution, which was used in tandem with chloride-free acidified Na_2SO_4 at the same pH to understand the impact of chloride anions on the nucleation, growth, and of passive films and their resultant topography. A similar study with pure Ni has been reported previously[35]. Measurements of the surface roughness provide for a representation of the influence of chloride vs sulfate environments on localized passive film dissolution in acidic chloride solutions.

8.2 Methods

An arc-melted, cast, and rolled polycrystalline, solid solution Ni-22 wt% Cr alloy, which forms passive films, was used for all experiments. Metallographic indents marked the area of interest for *in-situ* electrochemical exposure, and *ex-situ* AFM analysis. The sample surface was metallographically prepared with mechanical polishing to 1 µm, followed by ion polishing.

The solutions used for electrochemical testing were 0.1 M Na_2SO_4 acidified to pH 4 using 1 M H_2SO_4, and 0.1 M NaCl acidified to pH 4 using 1M HCl, both prepared using reagent grade chemicals dissolved in 18.2 MΩ-cm resistivity deionized water. In addition, the electrochemical stability of a passive film formed in Na_2SO_4 in an NaCl environment was tested in a hybrid experiment: the sample was first subjected to the oxidation procedure in a sulfate solution at +0.2 V_{SCE} (potential with respect to a saturated calomel electrode) for 10^3 s in 0.1 M Na_2SO_4 pH 4, and was then removed and placed in another vertical cell that was filled with de-aerated 1.0 M NaCl pH 4. The same potential of +0.2 V_{SCE} was applied for an additional 10^3 s. The resulting surface was removed from the cell, cleaned, and analyzed with AFM.

The electrochemical cell for passivation experiments was a typical three-electrode flat cell with a Pt mesh counter electrode and a corresponding reference electrode (saturated calomel (SCE) for the chloride experiments and mercury-mercury sulfate (MMSE, +0.41 V versus SCE) for the sulfate experiments). The quiescent solutions were de-aerated using ultra-high purity N_2 gas throughout experimentation. A Gamry Reference 600 potentiostat was utilized for DC and AC tests. An initial cathodic reduction step at -1.3 V_{SCE} for 10 min was utilized to standardize subsequent oxidation condition and reduce air-formed oxides[68], followed by application of single frequency electrochemical impedance (SF-EIS) at +0.2 V_{SCE} conducted at 1 Hz frequency and a 20 mV_{rms} AC amplitude for up to 10^4 s. The measurement of the imaginary impedance, $Z_{imag}(t)$, enables calculation of the oxide thickness, l_{ox}, (Eq. 8-1) and determination of the corresponding oxidation current density, i_{ox}, (Eq. 8-2) as a function of exposure time. A set of reasonable assumptions regarding the dielectric behavior of the oxide thin film is made based on identifications of oxide/hydroxide species from XPS. The expressions to obtain l_{ox} and i_{ox} were used in the manner described in [2] and this publication includes an in-depth discussion of the validity and limits of this expression:

$$l_{ox}(t) = \frac{(2\pi\varepsilon\varepsilon_o f)^{\alpha}\left|Z_{imag}(t)\right|}{\rho_\delta^{1-\alpha}\sin\left(\frac{\alpha\pi}{2}\right)\left[1+2.88(1-\alpha)^{2.375}\right]} \qquad 8-1$$

$$i_{ox}(t) = \frac{zF\rho_{ox}}{M_{ox}}\frac{d(l_{ox})}{dt} \qquad 8-2$$

where ε is oxide dielectric constant, which is approximately 30 for typical oxides on Ni-based superalloys[69], ε_o is the vacuum permittivity, α is the constant-phase-element exponent determined by fitting a full EIS spectrum to a circuit model[5], ρ_δ is the boundary interfacial resistivity set to 450 Ω-cm based on [70], f is the frequency of 1 Hz used in the experiment, and F is Faraday's constant.

The following oxide-dependent parameters were weighted for oxide composed of 70% $Ni(OH)_2$ and 30% $Cr(OH)_3$, which yields an average metal cation valency of z = 2.3, ρ_{ox} is the approximate passive layer density of 3.8 g/cm^3, and M_{ox} is the molar mass of 95.8 g/mol[2]. These assumptions of oxide composition and dielectric constant were at first based on observations of steady-state films, rather than transient ones, and are a valid approximations during film growth which can be concluded from prior studies[40,55,65]. The analysis also assumes a single conformal oxide, and should therefore be regarded as an estimate of the absolute passive layer. This estimate is relatively insensitive to +/- 15% changes in the composition which is within the limits of the film composition measured with XPS.

Following electrochemical passivation, the samples were removed from the cell, rinsed with deionized water, and sonicated in ethanol to remove any residual salt from the surface that would obstruct imaging. The sample surface was probed with AFM consistently within 36 hours following passivation to minimize environmental impact on the surface topography, which can include ageing of the hydroxide surface layer. The surface topography of each sample was captured using an AFM with NT-MDT Solver Pro. The AFM tip, ETALON HA/NC with a radius of curvature less than 10 nm, was kept in tapping mode during imaging. The surface topography was quantified by using the RMS (root mean square) roughness measured on flat areas of the sample surface while avoiding distortions from polishing grooves. The RMS roughness was measured for several images (>5) positioned at different positions across the treated surface for each sample using Gwyddion[71], an open source software package used for scanning probe microscopy analysis.

To obtain consistent RMS values, each image was planarized by mean plane subtraction prior to RMS measurements. Line leveling artifacts in the horizontal scanning directions caused by exceptionally large particles were corrected by selective use of background corrections with linear or quadratic polynomials[71]. Area distributions were obtained by segmentation of the images using a threshold of approximately 50% of the largest surface feature height in a given image. Lower threshold values deliver pixelated images; the same is true for very smooth surfaces where thresholding and area distributions are no longer meaningful. These thresholds were used for samples passivated in sulfate solution for 10s and 100 s, and for passivation in chloride solution for 10 s, 100 s, and 500 s, which corresponds to times just prior to completion of the oxide layer as evident from current decays over time. It should be noted that all AFM images are convoluted with the tip shape, and the diameter (area) of small protrusions and features will be overestimated. Initial measurements were 5×5 μm^2 and 2×2 μm^2 image areas, followed by the assessment of a significant number of smaller image regions (100×100 – 500×500 nm^2), which are devoid of polishing marks, form the data set discussed in this work. Care was taken to probe several areas on the sample surface that in all likelihood include different surface orientations and grains with respect to the alloy. A selection of AFM images illustrating the process are includes in the Supporting Information as Figures 8-S2, 8-S3 and 8-S5.

Following the same cleaning procedure as applied prior to the AFM measurements post-passivation, XPS spectra were obtained using a Thermo Scientific™ K-Alpha™ XPS system equipped with a monochromatic Alk_α photon source (E = 1,486.7 eV). Samples were transported in an inert Ar environment immediately after cleaning in order to prevent additional oxidation, and contamination of the surfaces. The angle between the sample and detector was fixed at 90° and that between the detector and the X-ray source was 54.7°. Spectra were calibrated to the $4f^{7/2}$ binding energy of a metallic Au reference set to 83.98 eV. Survey spectra were recorded on all samples using a pass energy of 200 eV, followed by spectra of the Ni 2p, Cr 3p, and O 1s regions using a pass energy of 20 eV. Commercial CasaXPS software was used to perform Shirley background subtraction and peak fitting[72–74]. The concentration of Ni^{2+} and Cr^{3+} cations in the film were computed by fitting the spectra to the metallic peaks and the corresponding oxide and hydroxide species. The peak areas were corrected using the sensitivity factors for Ni and Cr: 4.044

and 2.427, respectively[74]. The equations used to obtain the metal cation concentrations are given as:

$$\chi_{Ni^{2+}} = \frac{\dfrac{A_{NiO}^{tot} + A_{Ni(OH)_2}^{tot}}{S_{Ni}}}{\left[\dfrac{A_{NiO}^{tot} + A_{Ni(OH)_2}^{tot}}{S_{Ni}} + \dfrac{A_{Cr_2O_3}^{tot} + A_{Cr(OH)_3}^{tot}}{S_{Cr}}\right]} \qquad 8-3$$

$$\chi_{Cr^{3+}} = \frac{\dfrac{A_{Cr_2O_3}^{tot} + A_{Cr(OH)_3}^{tot}}{S_{Cr}}}{\left[\dfrac{A_{NiO}^{tot} + A_{Ni(OH)_2}^{tot}}{S_{Ni}} + \dfrac{A_{Cr_2O_3}^{tot} + A_{Cr(OH)_3}^{tot}}{S_{Cr}}\right]} \qquad 8-4$$

where χ is the cation fraction, A^{tot} indicates the integrated peak area for the various chemical compounds in the passive film, and S is the atomic sensitivity factor for Ni and Cr.

The complexity of the Ni and Cr core level multiplet structures makes it challenging to obtain high quality and informative fits, which are suitable for a quantitative assessment of different oxide and hydroxide contributions[72,75]. In the same vein, the concentration of the $NiCr_2O_4$ spinel could not be extracted from the oxide contribution to the Ni2p and Cr2p core level peaks because we were not able to achieve reproducible and physically meaningful fit separating the NiO, Ni-hydroxide and spinel contributions. The integrated intensity of all oxide/hydroxide peaks on the other hand, can be reliably separated from the alloy/metal peaks for both elements due their larger binding energy difference, and deliver quantitative information on alloy and cation (oxide + hydroxide) contributions. The presence of hydroxide is confirmed in the O1s spectra, which have contributions from oxide (shoulder at ~529.3 eV), and hydroxides (main peak from ~531 eV to ~532.5 eV), and the highest binding energies (high binding energy tail) correspond to remnants of adsorbed water. The variability in hydroxide bonding leads to the rather broad main peak in the O1s spectra. The thickness of the passive layers was estimated using the Strohmeier method[76] (Supporting Information Figure 8-S4), which assumes a layer-by-layer growth, and can therefore be regarded only as a rough estimate of passive layer thickness.

8.3 Results

8.3.1 Overall Electrochemical Performance under Potentiostatic Conditions

An initial investigation into the different performance of Ni-Cr passivation in a chloride versus sulfate solution was conducted by cyclic polarization from -1.3 to +0.8 V_{SCE} at 1 mV/s following a 30 min hold at the system's open circuit potential (OCP) where a passive film is formed prior to the potential sweep. The effect of chloride anions is evident in Figure 8-1, which shows a direct comparison between sulfate and chloride potential sweeps. Schematics of representative cyclic polarization sweeps for chloride and sulfate solutions are included in the Supporting Information Figure 8-S1 and serve as a visual guide in the interpretation of the experimental data shown in Figure 8-1. The OCP is always more positive in sulfate compared to chloride solution whether recorded during upward or downward scans and is accompanied by a lower passive current density as low as ~8 $\times 10^{-7}$ A/cm^2, which is indicative of the formation of a more readily passivated and corrosion resistant film. Additionally, the positive hysteresis in the polarization sweep (i.e., increased current density upon downward sweep) in chloride above a value of about -0.1 V_{SCE} suggests localized damage to the surface, such as pitting or crevice corrosion, which is assisted by chloride anion attack at the solid-liquid interface between the aqueous solution and the passive film. The halide attack on the passive film during potentiostatic growth impacts passive

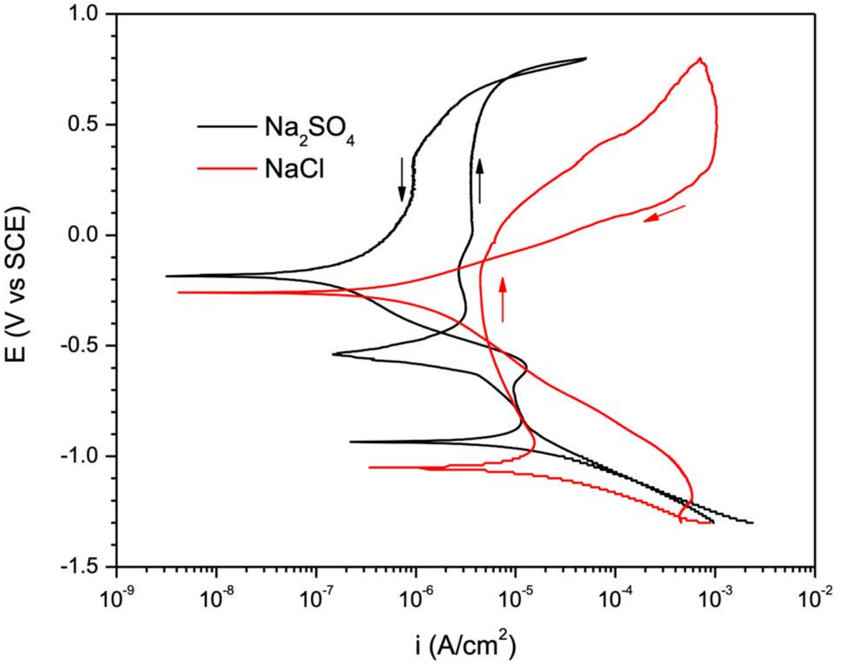

Figure 8-1: Cyclic polarization behavior of Ni-22 wt% Cr in 0.1 M Na_2SO_4 and 0.1 M NaCl, each acidified to pH 4. Current measurements were obtained using a cyclic potential sweep from -1.3 V_{SCE} to +0.8 V_{SCE} and reversed back to -1.3 V_{SCE} at 1 mV/s following a 30 min hold at the system's open circuit potential (OCP). The passive current density, i_{pass}, can be assessed in the constant current regions indicated by the up arrows. The OCPs are found around -1.0 V_{SCE}. For the E-log(i) behavior in the NaCl environment, the film breakdown potential, E_b (+0.1 V_{SCE}), is evident by the sudden increase in the measured current. Figure S1 in the Supporting Information includes a schematic representation of the cyclic polarization behavior in chloride and sulfate solution as a guide.

film stability, as well as growth and enrichment of certain cations like Cr^{3+} compared to Ni^{2+} in the oxide over time.

Additional tests were conducted on freshly polished samples by first reducing the film at the cathodic potential of -1.3 V_{SCE} for 10 min and then immediately polarizing to +0.2 V_{SCE} for up to 10^4 s. This anodic potential resides in the passive range and is well below potentials associated with breakdown and crevice or pitting corrosion, indicated by large increases in the measured current above i_{pass} with small increases in applied potential.

Figure 8-2 shows the overall electrochemical reaction current densities, i_{EC}, as well as EIS computed oxide thicknesses (right hand axis), and extracted current densities, l_{ox} and i_{ox},

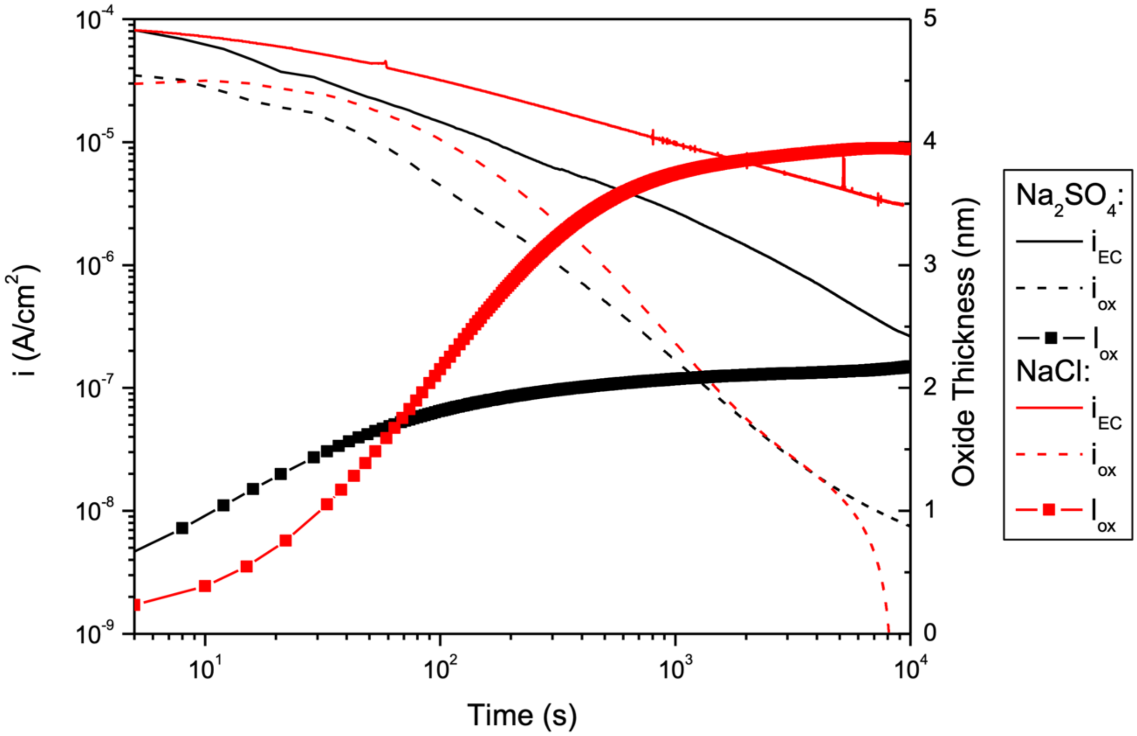

Figure 8-2: Comparison of the total electrochemical, i_{EC}, and oxidation, i_{ox}, current densities (e.g. reaction rates) along with oxide thickness, l_{ox}, growth calculated using the SF-EIS method (Eq. 1 and 2) for Ni-22 wt% Cr in 0.1 M Na_2SO_4 and 0.1 M NaCl acidified to pH 4 using H_2SO_4 and HCl, respectively, during potentiostatic passivation at +0.2 V_{SCE} with an applied AC frequency of 1 Hz and amplitude of 20 mV_{rms} .

respectively. The oxide thickness, l_{ox}, was obtained using the SF-EIS method described in the Experimental Procedure section. In general, i_{EC} decreases during film growth from approximately 10^{-4} to 10^{-6} A/cm^2, corresponding to an increase in film thickness l_{ox} with time. The i_{EC} in chloride is consistently larger than the value measured in sulfate solution. This indicates the significant contribution of dissolution reactions occurring during overall film growth in a chloride environment. Figure 8-2 shows a negligible difference between i_{EC} and i_{ox} at early times comparing both solutions, and oxide formation dominates i_{EC}. However, the difference between i_{EC} and i_{ox} increases with passivation time as the overall reaction kinetics expressed by i_{EC} decreases. Here the oxidation rate, i_{ox} , nearly equals the chemical dissolution rate of the oxide.

Therefore, a quasi-steady state film thickness is reached, and little further increases in l_{ox} can be observed. i_{ox} approaches 0 for the chloride solution at around 8×10^3 s where i_{EC} approaches a quasi-steady state often referred to as the passive current density of the alloy-electrolyte system. The film growth rate now becomes equivalent to the dissolution rate and a film thickness of ~3.8 nm is maintained. In other words, i_{EC} goes towards maintaining the steady-state oxide thickness which is continually dissolving at the oxide film-electrolyte interface, compensated by new oxide at the metal-electrolyte interface, with no net increase in l_{ox}. In sulfate, however, the small, but non-zero value for i_{ox} suggests that film growth is slow but continues even at 10^4 s.

The shape of the l_{ox} curves as a function of passivation time suggests that the passive films nucleate, cover the surface, and then thicken faster in sulfate than in chloride solutions, which is commensurate with the more rapid increase in l_{ox} from 5 to 300 s. Figure 8-2 also shows that the steady state film thickness is larger in chloride than in sulfate solution, which may be attributed to chloride anions either raising the driving force for the anodic passive film reactions or increasing cation vacancies, which enhances film growth[22,31,77]. Passive layer thicknesses estimated from the XPS data using the Strohmeier method yields similar relative increases in film thickness over time, and reflect the larger thickness of the passive films formed in the chloride solution (Supporting Information Figure 8-S4). This comparison includes the assumption of a layer-by-layer growth mode and as such should only be seen as in the case of EIS as a rough measure of passive film growth. The intent of this paper is to further explore these comparisons using atomic force microscopy.

8.3.2 Chemical Identity and Oxidation State Characterization of the Passive Films

The XPS spectra are summarized in Figure 8-3 and show the core level spectra for Ni $2p^{3/2}$, Cr $2p^{3/2}$, and O 1s as a function of passivation time. Cl 2p core levels peaks were observed for samples passivated in the chloride solution, and the concentrations were about 1.1% for 100 s, 1.4% for 10^3 s, and 1.8% for 10^4 s and no Na core level was seen. The presence of Na was taken as an indication of insufficient rinsing of the sample after extraction from the solution, and the experiment was repeated and is not included here. The signal-to-noise ratio of the Cl 2p core level

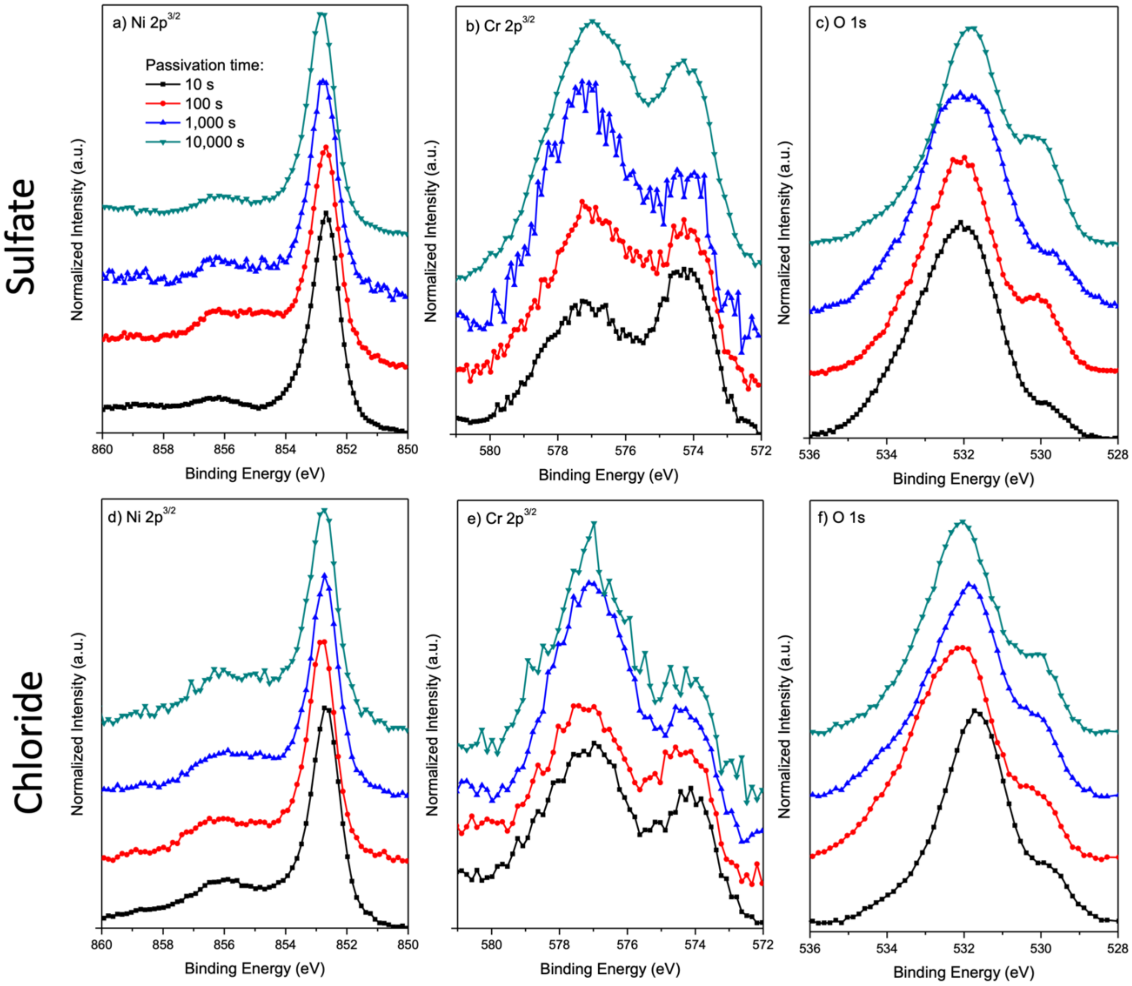

Figure 8-3: XPS spectra for (a,d) $Ni2p^{3/2}$, (b,e) $Cr2p^{3/2}$, and (c,f) O1s core levels for Ni-22 wt% Cr alloy. The spectra are normalized to the height of the respective alloy peak, and offset for clarity. Top row (a,b,c): spectra after passivation at +0.2 V_{SCE} for up to 10^3 s in de-aerated 0.1 M Na_2SO_4 pH 4 labeled "sulfate", and bottom row (d,e,f) 0.1 M NaCl pH 4 labeled "chloride".

is poor owing to the small concentration and does not offer any insight about bonding. The top row of spectra corresponds to passivation in de-aerated 0.1 M Na_2SO_4 pH 4 solution following Shirley background subtraction and normalization to unit height for the metallic peaks. The bottom row of spectra in Figure 8-3 shows the same core levels after passivation in the de-aerated 0.1 M NaCl pH 4 solution. The passive film was composed of predominantly Ni^{2+} and Cr^{3+}, both present as oxides and hydroxides, which formed following the hydration of the former species. The intensities at the maximum of the oxide/hydroxide contributions are used for this calculation and positioned at ~855.6 and ~577.3 eV binding energy for the Ni2p, and Cr2p core levels, respectively. This is close to the peak positions cited for the most intense hydroxide peaks $Ni(OH)_2$ and $Cr(OH)_3$, respectively, which are superimposed on the oxide multiplet structure leading to a complex peak shape. The metal peak positions agree with the literature values of 852.7 and 574.2 eV for Ni and Cr, respectively[72,75]. For the sake of simplicity in the text we will henceforth label the oxide-hydroxide films as "oxide" but are fully aware of the chemical complexity of the layers. The overall increase in oxide thickness with time, and the larger oxide layer thickness observed for passivation in chloride solution from *in-situ* SF-EIS are summarized in Figure 8-2.

The increase in the oxide thickness with passivation time is evidenced by the decreasing ratio of the metal-to-cation peak intensities for both core levels. The Ni-metal signal/oxide ratio is reduced from 10 to ~6 and Cr/Cr-oxide ratio is changed from 1.2 to 0.8 with increasing passivation time in sulfate solution; the Ni/Ni-oxide ratio decreases from ~6 to 4, and Cr/Cr-oxide from 0.7 to 0.4 with increasing passivation time in the chloride solution. These values reflect the increase in film thickness but are modulated by variation in oxide composition over time as shown in Figure 8-4. The higher Ni/Ni-oxide ratio is due to the Ni-rich alloy composition. The film thickness

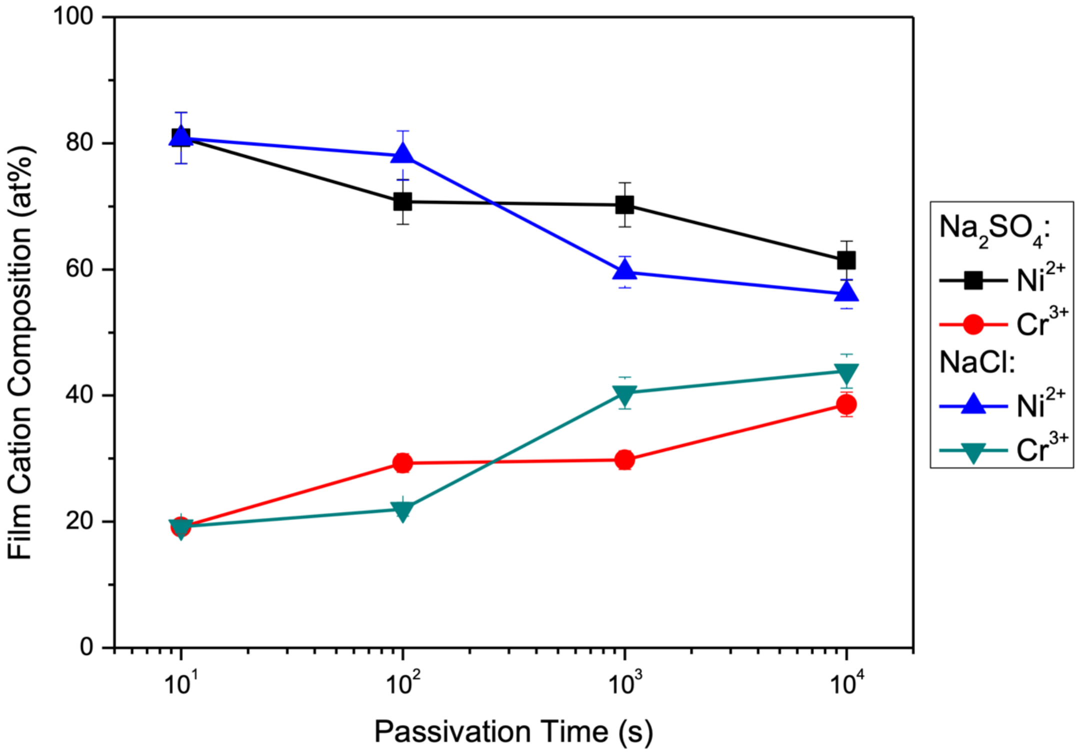

Figure 8-4: Cation composition in the passive films as a function of potential step passivation time on Ni-22% Cr alloys computed from XPS spectra using Eqs. [3] and [4].

estimate using the Strohmeier equation included in the Supporting Information Figure 8-S4 sums over all oxide and alloy contributions.

The change of cation composition of the passive film over time, which was calculated from the ratio of the oxide peak areas for Ni and Cr core levels using Eq. 8-3 and 8-4, is summarized in Figure 8-4. The films are initially rich in Ni^{2+} for both solutions, and their composition closely reflect the alloy composition. The Ni^{2+} contribution decreases with passivation time and is accompanied by Cr^{3+} enrichment. In the case of the chloride environment, the Ni^{2+} remains close to 80% until a relatively continuous oxide layer is reached at about 500 s and followed by an increase in the Cr^{3+} (chromia and hydroxides) contribution. The compositional variation in the passive layer during the entire passivation time is smaller for the sulfate solution compared to chloride. However, for shorter passivation times – before a continuous layer is formed - the oxide layer grown in chloride solution exhibits less Cr-enrichment and increases steadily between 100 and 10^3 s towards a Cr^{3+} concentration which exceeds the values measured for Na_2SO_4 solutions (Figure 8-4). At the longer times the passive film formed in NaCl is both richer in Cr^{3+} and thicker than that in Na_2SO_4.

8.3.3 Evolution of Surface Topography

The details of the passivation process are demonstrated in Figures 8-1 and 8-2, and the oxide surfaces were imaged with AFM at specific time intervals of exposure. The assessment of the surface topography and roughness yields information about the growth mechanisms of the oxide films. Clear trends are observed, albeit the complexity of the passivation process remains a challenge and defies easy interpretation. Figures 8-5 and 8-6 show representative linescans and the corresponding 3D AFM images of oxide films formed in sulfate and chloride solutions, respectively. A collection of images with different magnification is included in the Supporting Information as Figure 8-S2, and a selection of segmentation images, which are the basis for the area distributions, is shown in Figure 8-S3.1 and 8-S3.2. The image insets in S1 (500×500 nm^2) depict representative image areas as they were used to obtain the root mean square (RMS) roughness, oxide particle height distributions, and oxide area histograms shown in Figure 8-7 and 8-8. Figure 8-S5 illustrates the method used in the measurement of particle distributions, and 8-S6 includes a graph of height distribution parameters for the sulfate solution results.

Especially for shorter times the surfaces are visually rough and prominent features in the form of distinct protrusions can be identified. The line scans are selected to illustrate the difference between the protrusions and the smoother “background” which fluctuates by less than a nanometer in height across the sample. For sulfate solutions, the frequency of the larger protrusions is reduced

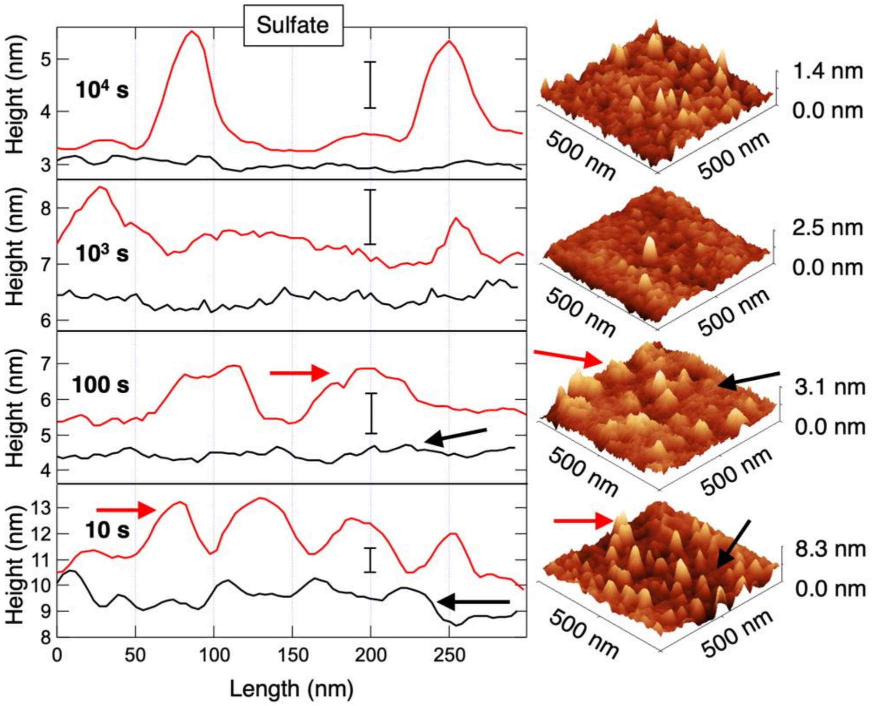

Figure 8-5: Representative line scans of the surface after passivation in *sulfate solution*. The red lines are crossing prominent protrusions on the surface, while the black lines represent the oxide surface in between the more prominent features. At 10^3 s the prominent features (protrusions) are rare and the majority of the surface shows a much flatter topography. 3D images are marked with arrows indicating the specific features included in the line scans. The height scales for the linescans were adapted to optimize visualization of features – the bar within each line scan panel corresponds to 1 nm in height to facilitate comparison.

over time (Figure 8-5) and RMS roughness is equally diminished (Figure 8-7). For passivation in chloride solution, the overall roughness of the surface is retained and larger local fluctuations persist (see Figure 8-6, 10^4 s). The oxide evolution can be put into context with the results from the electrochemical analysis in Figure 8-2. The oxide thickness, l_{ox}, for chloride and sulfate solutions levels off around 500 s, and 100 s, respectively, which is commensurate with formation of a continuous oxide layer, and establishing steady state conditions.

The AFM images for all exposure times were characterized by RMS values averaged over several images, and image regions. The RMS roughness values for both the chloride and sulfate

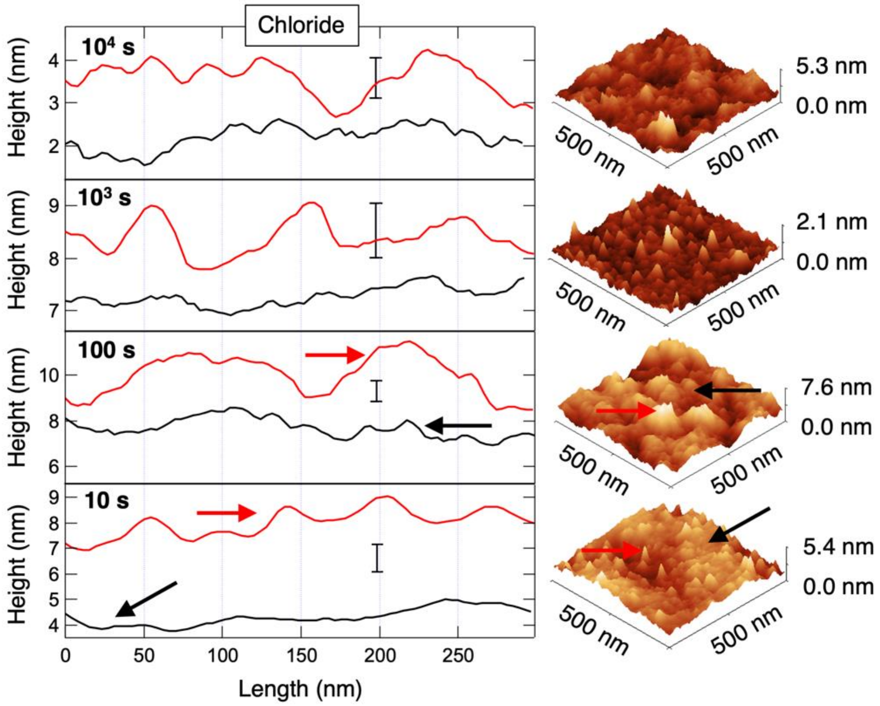

Figure 8-6: Representative line scans of the surface after passivation in 0.1 M *chloride solution at pH 4* for 10 to 10^4 s. The red lines represent the most prominent protrusion in the oxide surface, while the black lines reflect the roughness of the oxide surface in between. At and after 10^3 s the surface is overall very rough and the assignment of prominent features becomes moot – the red line scan features the highest roughness region within the image. The height scales for the linescans were adapted to optimize visualization of features – the bar within each line scan panel corresponds to 1 nm in height to facilitate comparison.

samples as a function of passivation time are summarized in Figure 8-7, height and area distributions are included in Figure 8-8. The surfaces studied here are covered by oxide islands and layers corresponding to specific passivation times. RMS roughness is an average value of features heights in a given image irrespective of the spatial distributions of the height values – it is a summation over all values displayed in the height histograms (see Figure 8-8A and C). The RMS values, and height distributions are complemented by area distributions (Figures 8-8(B) and (D)), which offer additional insight.

The RMS roughness of the chloride sample increases from 0.59 ± 0.14 nm at 10 s to 0.75 ± 0.17 nm at 100 s and remains unchanged for longer exposure times. The large error bar included

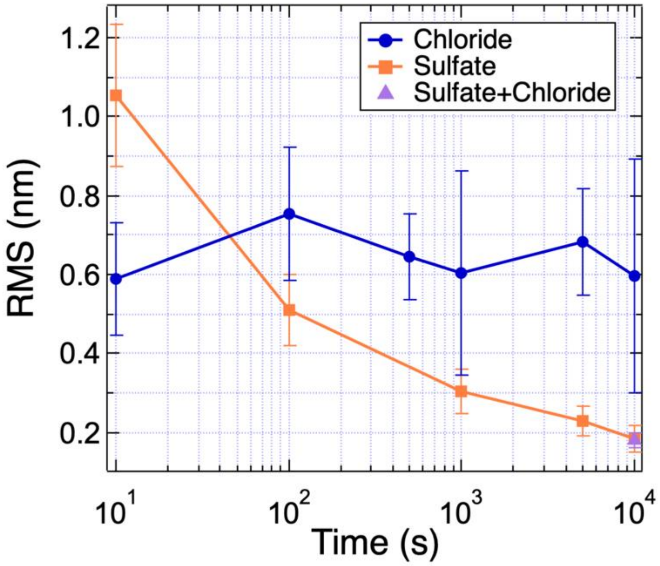

Figure 8-7: RMS roughness values for all samples used in the present work as a function of time. The large error bar for the chloride solution values stems from the inhomogeneity of the sample surface, which is not present in the oxides grown in sulfate solution. The data point for the hybrid experiment “sulfate+chloride” is located at 10^4 s and an RMS of 0.2.

in the figure represents the area-to-area variability in the sample and is consistently larger than for any of the sulfate samples. On the other hand, the sulfate samples show a clear downward trend in RMS towards a morphologically homogeneous sample surface. The RMS roughness for the chloride solution is initially lower than its sulfate counterpart at 10 s during the nucleation phase. The lower RMS value can be a consequence of a high density of small oxide nuclei, and a consequently smaller average oxide-feature height (Figure 8-8). For all other exposure times the chloride sample exhibits a much rougher surface. Indeed, numerous 100 s chloride samples were studied and consistently yielded rougher surfaces commensurate with the broader height distributions.

After 10 s of exposure the sulfate sample surface is relatively rough with an RMS value of 1.05 ± 0.18 nm, which is also reflected in the broad height distribution of the oxide particles (Figure 8-8(C)). After an exposure of 100 s the RMS value is reduced to 0.51 ± 0.09 nm, and

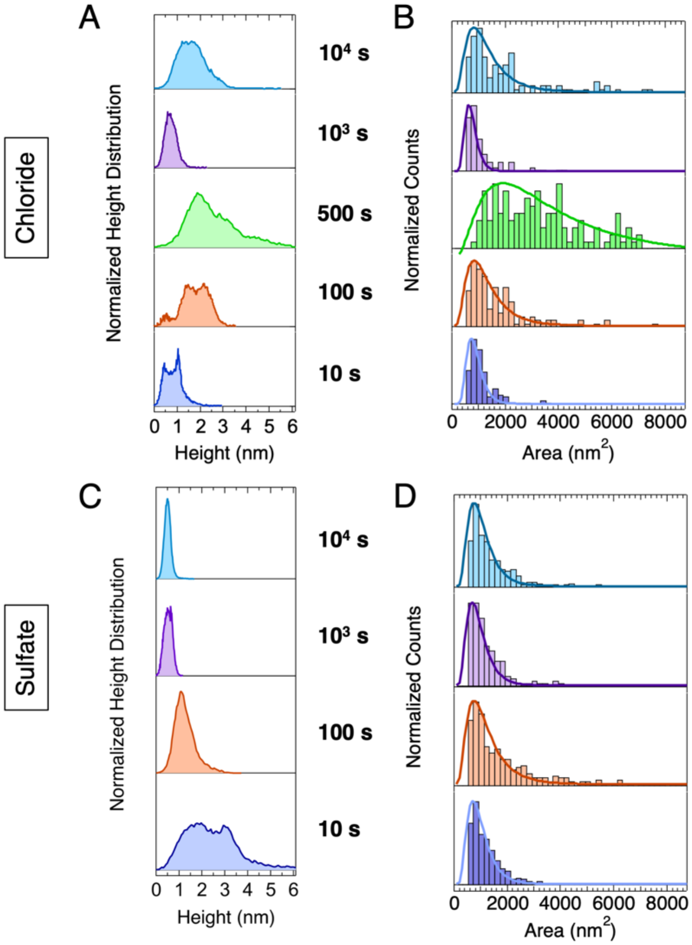

Figure 8-8: The oxide surface height distributions (A–chloride) and (C–sulfate), and area distributions (B–chloride) and (D–sulfate) obtained by segmentation. All distributions are normalized to unit height, and the area distributions are fit with a log-normal distribution. Several 500×500 nm^2 images were used in each case to derive both area and height data, and the bin size for the area distributions is 200 nm^2. The height distributions, which directly relate to the RMS calculation, were taken from images areas with zero slope. Figure S5 (Supporting Information) illustrates the method used for measuring the area distributions.

decreases rapidly for longer times. According to the *in-situ* passivation data summarized in Figure 8-2 a steady-state film thickness is reached shortly after 100 s in sulfate solution, and after 500 s in chloride solution. At the later stages of exposure (10^3 -10^4 s) segmentation of the images to obtain area distributions shows increasing coalescence (Figure 8-S2.1 and 8-S2.2). The height distributions in Figure 8-8(A) and 8-8(C) illustrate a rather different behavior for chloride and sulfate samples: for sulfate samples the height distribution of the oxide-film features rapidly narrows and moves to lower values with increasing exposure time. In contrast, the height evolution of the film features in the chloride solution is erratic, remaining relatively broad for all times with no clear trend even after reaching steady state conditions. These dissimilar behaviors are also reflected in the RMS values (Figure 8-7) and an expression of large local variations in roughness. The heterogeneity in roughness might be a function of surface orientation of alloy grains[27], or even local differences in the propensity of the alloy surface to react with Cl^-, and formation of an initially much rougher interface.

Figure 8-8 also includes the area distributions, which sum over all regions in the segmentation images with a height exceeding the threshold of ~50% of maximum height in a given image (Figures 8-8(B) and 8-8(D)). A schematic of this method is included in the Supporting Information Figure 8-S5. These distributions and the segmentation images reflect a degree of coalescence: isolated "protrusions" appear in the area histograms at lower values, while interconnected regions are counted in the "large area" tail of the distribution. The connectivity is not synonymous with RMS values, but adds to our understanding of surface topography evolution. For 10 and 100 s, the area distributions for the chloride samples broaden significantly, and the average oxide features cover 1000 nm^2 at 10 s, 1700 nm^2 after 100 s, and after 500 s the area distributions are relatively broad, and the average oxide feature size has increased to about 3500 nm^2. This is commensurate with coalescence and formation of a continuous layer as visualized in the segmentation images in Figures 8-S2.1 and 8-S2.2. The oxide features for sulfate samples show similar trends: as exposure time progresses from 10 s to 100 s, the average oxide feature area for sulfate samples increases from about 1000 nm^2 to 2600 nm^2, and then decreases for all longer passivation times. Overall, the broadening of the area distribution is more pronounced for chloride samples.

The increased width of the area distributions occurs close to times when steady state layer thicknesses are reached as deduced from SF-EIS (Figure 8-2). The largest breadth of island size distributions is observed before a continuous layer is achieved, and decreases again once a continuous layer is formed. In layer-by-layer growth modes the roughness oscillates with each added layer, but in our system the island type growth only allows to see this effect for the initial film coalescence. All area distribution for continuous layers reflect the continued evolution of the oxide during steady state conditions, where growth at the interface is equilibrated with reactions at the solid-liquid interface. The changes in area and height distributions are now more subtle, particularly for the sulfate, but still visible in both the area and height distributions. The overall RMS roughness evolution is mostly driven by the feature height modulations.

8.3.4 Effect of Surface Pretreatment on Film Stability

The influence of chloride on breakdown was studied in a hybrid experiment, and combined sulfate and chloride environments in a sequential manner: an alloy surface was exposed to 0.1 M Na_2SO_4 pH 4 environment for 10^4 s, which corresponds to the longest time used in the time evolution experiments, and delivers the smoothest film surfaces in the series. Following the production of this smooth oxide film, the samples were exposed to 1.0 M NaCl pH 4 at +0.2 V_{SCE} for 10^4 s to induce localized breakdown. However, no metastable pitting events were observed following this sulfate “pretreatment”, as shown in Figure 8-9 despite exposure to an even more concentrated chloride environment than discussed above. The subsequent AFM topography images do not show any additional roughening of the surface and identical RMS = $0.18 \pm 0.02\ nm$

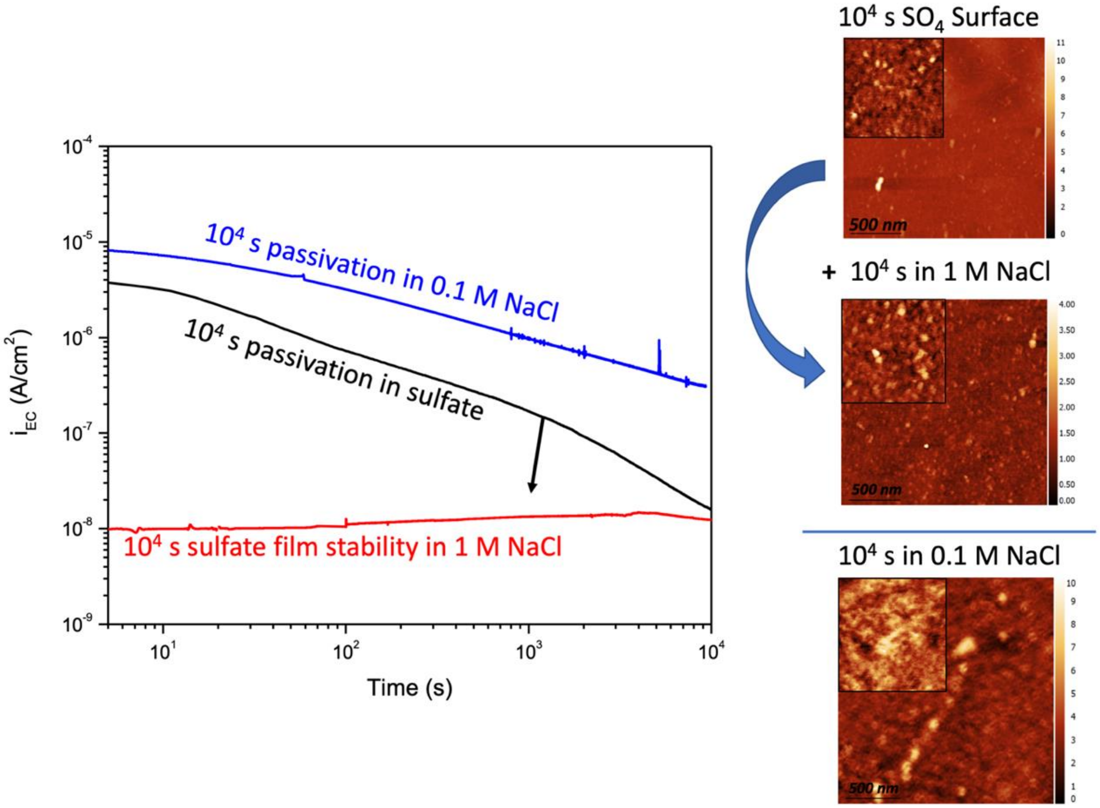

Figure 8-9: Passivation and pitting electrochemical current density vs time and corresponding surface topography in a sample pretreated/oxidized in *0.1 M* Na_2SO_4 *pH 4,* and subsequently exposed to *1.0 M NaCl* pH 4 for 10^3 s. Surface roughness, and topography are not changed by the second oxidation step in chloride solution, and no pitting events are seen; this data point is also included in Figure 8 at 10^4 s. For comparison, the surface roughness and Passivation and pitting electrochemical current density vs time of the same sample oxidized in *0.1 M NaCl pH 4* for 10^3 s is included - these are the typical conditions for oxidation used in the present work.

values are measured after chloride exposure (for comparison an image of the surface after exposure to the pure chloride solution for 10^4 s is included). The passivation current density for the pretreated surface remains low for the entire 10^4 s of exposure time despite significant exposure to chloride. In contrast, the surface oxidized solely in chloride solution, however, exhibits metastable breakdown events at longer times (Figure 8-9), significant dissolution during the entire passivation sequence, and a consistently rough surface. The presence of the smooth sulfate layer prior to chloride exposure limits the otherwise detrimental impact of chloride exposure with respect to film breakdown.

8.4 Discussion

Significant decreases in the observed film breakdown potential, E_b, where film dissolution occurs and the current increases, along with an increase in the passive current density, i_{pass} were observed during upward scans in Cl^- solution (Figure 8-1). This strongly implicates a significant interaction of Cl^- with the passive film, which regulates anodic current density. In the presence of chloride anions in the aqueous solution during application of potentials, Cl^- is expected to become adsorbed on both oxide and bare Ni-Cr alloy surfaces according to a potential and Cl^- activity dependent adsorption isotherm[78]. In a study on Ni, radiotracer methods show a strong increase in Cl^- coverage with potential in the active range interpreted to be Cl^- adsorption on bare Ni, followed by a drop in Cl^- coverage with passivation and then a slight increase with increasing potential in the passive range[28]. There is a strong effect of bulk [Cl^-] on coverage but the coverage at anodic potential may be convoluted with pitting, which is an added effect beyond interactions with oxides.

Understanding the effects of Cl^- on passivated oxide covered surfaces require closer inspection of the behavior in the passive range. Figure 8-2 shows a comparison from the electrochemical perspective between the development of passive films formed on Ni-22 wt% Cr in a sulfate versus chloride environment over a 10^3 s period at fixed potential in the passive potential region. The significant role of dissolution in Cl^- on the progression of passivation is indicated at a fixed potential in the passive region, and can be recognized because i_{ox} associated with new oxide formation falls to zero (Figure 8-2) but i_{EC} remains substantial in the latter stages of passivation. The film is thicker in Cl^- because, on balance, i_{EC} is much greater than in sulfate while i_{ox} is slightly greater at intermediate times. The surface morphology keeps evolving although at a slower pace in the latter stages of passivation. The driving force for oxide formation may be enhanced by Cl^- if the difference between the applied potential and the primary passivation or oxide formation potential, is greater in Cl^-. In addition, the chemical reactions between Cl^- and the oxide surface may enhance cation vacancy concentrations in the passive film which in turn enhances kinetic film growth processes as suggested recently on Fe by reactive force field molecular dynamics[79,80].

The overall electrochemical passivity is also impacted by the film composition, which is modified throughout the exposure time (Figure 8-3). The film becomes richer in Cr^{3+} with time, especially in the NaCl solution (Figure 8-4). This is because NiO ($Ni(OH)_2$) dissolves chemically with a greater thermodynamic driving force in acidic chloride solutions and this process occurs at faster rate than for Cr_2O_3 ($Cr(OH)_3$) at pH 4[15,81]. Thus, the film may both form by electrochemical oxidation faster but then also dissolve chemically on a selective basis (i.e. $Ni(OH)_2$) as soon as formed at a greater rate in Cl^-. Evidence of this is shown in Figure 8-2 where i_{EC} is $5x10^{-6}$ A/cm^2 in Cl^- but only $3x10^{-7}$ A/cm^2 in sulfate after 10 ks of passivation. The former current density would produce a dissolution rate of about 20 nm in 100 s, which must be overcome by fresh oxidation to continue to grow oxide films and allows for roughening or smoothing during the time frame of these experiments.

Surface topography reflects the complex interplay between competing mechanisms which roughen versus those which tend to level a surface during nucleation, coalescence of oxide islands, growth and dissolution[24]. It connects the global electrochemical measurements to local features and the nanoscale heterogeneity on the surface. The mechanisms and drivers to consider include surface and interfacial energies, chemical and electrochemical local reactions at the electrolyte-solid interface, which are coupled to transport processes through the passive film[18], and surface diffusion. Local electric fields are enhanced in thinner oxide regions which enhances i_{EC} which in turn exacerbates roughness and dissolution especially at sites with low coordination[15,16]. Film thickening (Figure 8-2) and surface topography measurements (Figures 8-5 and 8-6) suggest an early lag in oxide nucleation and initial growth in chloride compared to sulfate. Consequentially, nuclei and islands might form rapidly early in the growth process in the case of Cl^- but are also more susceptible to thermodynamically driven and kinetically rapid dissolution reactions thus prompting secondary nucleation events, and a divergent size distribution expressed in surface roughness at later times. The extended nucleation window prior to the formation of a continuous film is also commensurate with a more pronounced island growth mode, and can contribute to larger surface roughness. Note that the evolution in RMS over time is carried mostly by a modulation of the height distribution (Figure 8-8).

The sulfate solution, on the other hand, has significantly less dissolution reactions as shown in the electrochemical data presented in Figures 8-1 and 8-2, and supports the faster transition to a closed oxide layer. In addition, the growth mode, which is influenced by the interfacial and surface energies, is according to the height distributions closer to a layer-by-layer mode, respectively shows less pronounced islanding. Recently, DFT calculations have demonstrated a decrease in the oxide surface energy when chloride is present[82], which might indeed promote island formation. The differences in the processes described here are argued to produce a narrowing distribution of surface structure heights during passivation, and lead to a lower RMS (Figure 8-7) in sulfate solution compared to chloride.

The early growth times are characterized by a slight preference for the formation of Cr-oxide/hydroxide over Ni-oxide/hydroxide layers in sulfate compared to chloride solution (Figure 8-4). This is an opposing influence to the frequent assumption that NiO nucleation is preferred since the interfacial energy is lowered due to the epitaxial relation between Ni and NiO[63].

However, a favorable interfacial energy at the solid-solid interface due to compatible oxide and substrate crystal structures can be offset by variations in the surface energy at the alloy surface, and at the solid-liquid interface due to Cl^- adsorption. In addition, as described earlier in the discussion the dissolution rate for Ni-oxides and hydroxides is larger in chloride solution[83], hence the enrichment in Cr in the oxide film over time of exposure to Cl^- exceeds the enrichment in Cr in the sulfate solution.

A common finding is that films rich in Cr^{3+} exhibit greater repassivation capabilities in Fe-Cr and Ni-Cr alloys.[1,4,12,14,84–87] However, in this study we find that oxides did not form conformal layers over flat metals surface as is often assumed in thin film high field models of passive film growth. The development of increasingly rough surfaces in the presence of chloride compared to smoothing in sulfate requires also consideration of the governing chemical and electrochemical thermo-kinetic factors that affect each stage of film formation. First it should be noted that by conducting experiments in 0.1 M NaCl solution at pH 4 and an applied potential at +0.2 V_{SCE}, the system is displaced far from the electrochemical equilibrium for both the Ni/Ni^{2+} and Cr/Cr^{3+} oxidation half-cell reaction regardless of whether $NiO/Ni(OH)_2$ or $Cr_2O_3/Cr(OH)_3$ formation are considered. The typical oxidation process during passivation considering relevant metastable products involves the direct transformation of the metallic substrate by the following parallel pathways forming either oxide or hydroxide with a parallel route to form soluble aqueous ions (where when $M/M^{n+} = Ni/Ni^{2+}$, n=2; and when $M/M^{n+} = Cr/Cr^{3+}$ n=3).

$$M = M^{n+} + ne^- \quad [1]$$

$$M + nH_2O = M(OH)_n + nH^+ + ne^- \quad [2]$$

$$M + mH_2O = MO_m^{(n-2m)} + 2mH^+ + ne^- \quad [3]$$

Once the oxide is formed chemical or oxidative dissolution might occur by reaction with [H^+] as covered by Pourbaix[81]. Note that both metastable NiO and Cr_2O_3 are predicted based on thermodynamics to chemically dissolve in pH 4 acid by the following reaction pathways:

$$NiO + 2H^+ = Ni^{2+} + H_2O \qquad [4]$$

$$Cr_2O_3 + 6H^+ = 2Cr^{3+} + 3H_2O \qquad [5]$$

It should be noted that oxidative dissolution is possible for these elements but the conditions tested herein do not allow this as the applied potential is less oxidizing than the equilibrium potential for these reactions.

NiO is thermodynamically unstable at a pH of less than 8 according to one source[88] and less than pH 5 according to another source[81]. Cr_2O_3 also is susceptible to chemical dissolution in acid but remains thermodynamically stable at a lower pH than NiO (i.e., at pH 5)[81]. Therefore, at pH 4, reactions [2] and [3] will produce metastable products. Metastable oxides are well known to form in aqueous corrosion systems[55], and the oxide or hydroxide will be present even though equilibrium conditions at pH 4 favor cations as soluble aqueous ions. Reactions [1-3] also depend on nanometer-scale curvature[89], crystal orientation , oxide thickness[92,93] and temperature, which affect the electrochemical equilibria for formation as well as the rates. Since reactions [2] and [3] are solid state reactions, there is no direct dependency on the chloride concentration in solution, but hydroxide may also form by precipitation at the aqueous-solid interface. The change in surface energy induced by Cl^- may be a factor as discussed earlier in 4.1. The chemical dissolution stability of the oxide is also affected by the complex interplay between oxide cation type, oxide crystallinity and crystal orientation, thickness, stress state and various environmental factors. All of these factors likely contribute to the significant heterogeneity in local morphology for chloride samples. Notably oxide dissolution is more likely when convex nanometer-scale curvature occurs as shown for oxides such as in the case of Zn[94], Cu and Pt[89,95]. More corrugated surfaces, which develop during the initial nucleation stage, are therefore more prone to evolve into rougher oxide surfaces if local dissolution rates are higher.

Moreover, attack of the outer $Ni(OH)_2$ film or $Cr(OH)_3$ film or inner oxides films with anions such as Cl^- but also SO_4^{2-} and other anions will produce a series of metal cation salt species, which are often soluble in water, and provide a pathway to dissolution:

$$Ni^{2+}(ox) + nCl^-(aq) \rightarrow NiCl^{2-n}(aq) \qquad [6]$$

Ni dissolution in acidic solutions containing Cl^- either forms Ni^{2+}, $NiCl^+$ or $NiCl_2$ according to speciation diagrams. It should also be noted that the thermodynamic stability of nickel chlorides is greater than that of nickel oxides[96]. It is argued that Cl^- attacks $Ni(OH)_2$ proceeds by a ligand exchange process (i.e., $Ni(OH)_2/Ni(OH)Cl/NiCl^+$)[15,28]. A similar process is described for $Fe(OH)_3$ and it is supported by ReaxFF-MD calculations, that $Fe(OH)_3$ undergoes ligand exchange with Cl^- and that this process is catalytic[80]. The reaction of iron oxides with SO_4^{2-} is also catalytic and it is argued that $FeSO_4^+$ is easier to transfer to solution than Fe^{3+} [97]. A similar reaction occurs in the case of Cr^{3+} hydroxides and oxides but complexation does not enhance release of Cr cations particularly. Upon chemical dissolution in Cl^- various soluble Cr-Cl species are predicted based on thermodynamics including Cr^{3+}, $CrCl^{2+}$, $CrCl_2^+$, $CrCl_3$. Ni^{2+} and Fe^{2+} are quite prone to this reaction in Cl^-, Br^-, I^- and HF with pK's of -0.25 and 0.62, respectively, in Cl^-. In contrast, the pK value in the case of Cr is -0.65[98,99].

The important points are that reactions 1-6 occur in parallel and simultaneously and that rates differ with both halides as well as cation and anion specificity. Reactions [2] and [3] contribute to oxide growth while [1] and [4-6] all release metal cations into aqueous solutions. Reactions [4-6] dissolves new oxide nuclei and mature oxides alike. Rate laws for cation dissolution in halides typically possess first order dependencies on bulk anion concentration, cation-halide intermediate coverage and Helmholtz potential (i.e. potential across the film/electrolyte interface)[100–102]. The selective etching of Ni^{2+} over Cr^{3+} containing oxides and hydroxides is highly likely but the difference in rates depends on anion, temperature as well as pH adding to the inherent complexity of the system. It should be noted that the NiO chemical dissolution rate is much faster than the Cr_2O_3 dissolution rate in H_2SO_4[83] and also especially in NaCl. Because of this competition, oxide formation and coalescence are very inefficient in the aqueous case, as seen in Figure 8-2. Moreover, given that Cl^- lowers the surface energy of oxides on Ni-Cr alloys[31,82], it stands to reason that the nucleation behavior of oxides is modified and the critical nuclei radii differ in the presence of chloride. In nanocrystal precipitation reactions, the nucleation of terraces on islands is governed by an Arrhenius expression where activation energy is a function of the surface energy of the new step edge created squared. The lowering of surface energy lowers the activation energy, which in turn raises the nucleation rate in the nanoscale regime. This scenario and how it can relate to the observed modulation of area and height distributions is seen in Figures 8-5 through Figure 8-8 and discussed in previously.

The morphologies of the oxide covered surfaces likely depend on all of the factors described above, including differences in electrochemically-driven nucleation and growth of oxide as well as the chemical dissolution of oxides in Cl^- versus SO_4^{2-}. If dissolution leads to surface roughening, the effect of Cl^- adsorption on surface energy mitigates an otherwise energetically unfavorable increase in surface area, and perturbations in the film are facilitated because of the chloride-assisted decrease in surface energy. Thus rougher morphologies can become energetically possible[18] and are expressed in the development of RMS and surface features. Even if a smooth morphology is energetically favorable, limited surface diffusion can kinetically stabilize a rough surface and lead to its propagation over time[103–105]. In addition, greater dissolution has been theorized to occur within the oxide troughs compared to the peaks due to electric field differences across the oxide, resulting in the exaggeration of any existing surface perturbations[18].

It is tempting to attribute the variation in surface roughness as illustrated in Figures 8-5 to Figure 8-8 solely to the enhanced oxide dissolution kinetics by Cl^- of the continuous passive film. However, this deceptively simple interpretation can be called into question by the observation that a smooth oxide layer formed in sulfate solution is not susceptible to pitting events or roughening by dissolution as described in Section 8.3.4. Oxides grown in sulfate for 10^3 s and then exposed to 1 M NaCl for another 10^3 s (Figure 8-9) do not roughen during the time frame of the exposure and do not undergo breakdown and pitting nearly as readily as those grown in Cl^- solution.

This implies that roughening owing to oxide formation, growth and dissolution can be connected with the resistance to oxide breakdown afforded by a protective oxide. Therefore, the surface roughness development has to be coupled to the initial nucleation and growth steps and is then propagated throughout the continuation of oxide layer growth. This can be attributed to the interplay between surface and interfacial energies as a thermodynamic factor, and diffusive processes at the surface and through the growing oxide, or a concerted interface roughening as described in the morphological stability models developed by Ramanathan et al.[18]. Clearly both, kinetic and thermodynamic factors, contribute. The exact roles and even more critically, synergies, between surface energy and surface diffusion for hydroxide, oxides, sulfate, and chloride terminated surfaces in driving film smoothing remain open questions. However, while the interpretation of roughness evolution within a unified model remains at present elusive, and is challenging even in seemingly simple materials systems, the experimental findings illustrate clearly the significant differences in roughness evolution as a function of exposure time in chloride and sulfate solutions.

8.5 Conclusions

Oxide nucleation and growth of metastable oxides on a polycrystalline, solid solution Ni-22 wt% Cr alloy were studied in slightly acidic chloride solution and compared to sulfate solutions at the same pH. Oxide nucleation occurs in the form of islands, which develop on newly passivating surfaces with seconds of the establishment of electrochemical driving forces favoring the oxidation of both Cr and Ni. Oxides tend to grow and coalesce to “closed” surfaces, continuous passive layers, and also enrich in Cr^{3+} hydroxides and oxides consistent with the sharp decrease in oxidation rates commensurate with thin film field driven passivation. At the same time, it is found that chemical driving forces favor simultaneous oxide dissolution especially in the case of Ni^{2+} oxides. The balance between these two processes is argued to govern oxide morphology and thicknesses and propagate roughness parameters developed during the initial steps of passive film growth.

Surface roughness and topography evolve with time and depend critically on anion identity. Cl^- is shown to alter the distributions in oxide islands and their coalescence, and leads to significantly broader height distributions and surface roughness compared to more chemically benign species such as SO_4^{2-}. Factors responsible for topography development were identified. The impact of morphology and composition on oxide breakdown is discussed. Topologically smooth oxides grown in Cl^- free solutions resisted pit breakdown events once exposed to 1M NaCl (Figure 8-9). The features developed in Cl^- may be key factors in creating instabilities in passive films[18], which trigger local breakdown. These finding should be further considered in the context of oxide growth as well as breakdown where oxide roughening here-to-fore has not been broadly considered.

8.6 Chapter VIII References

(1) Lloyd, A. C.; Noël, J. J.; McIntyre, S.; Shoesmith, D. W. Cr, Mo and W Alloying Additions in Ni and Their Effect on Passivity. *Electrochimica Acta* **2004**, *49*, 3015–3027. https://doi.org/10.1016/j.electacta.2004.01.061.

(2) Lutton, K.; Gusieva, K.; Ott, N.; Birbilis, N.; Scully, J. R. Understanding Multi-Element Alloy Passivation in Acidic Solutions Using Operando Methods. *Electrochem. Commun.* **2017**, *80* (7), 44–47. https://doi.org/10.1016/j.elecom.2017.05.015.

(3) Zagidulin, D.; Zhang, X.; Zhou, J.; Noël, J. J.; Shoesmith, D. W. Characterization of Surface Composition on Alloy 22 in Neutral Chloride Solutions. *Surf. Interface Anal.* **2013**, *45* (6), 1014–1019. https://doi.org/10.1002/sia.5204.

(4) Lloyd, A. C.; Noël, J. J.; McIntyre, N. S.; Shoesmith, D. W. The Open-Circuit Ennoblement of Alloy C-22 and Other Ni-Cr-Mo Alloys. *JOM* **2005**, *57* (1), 31–35. https://doi.org/10.1007/s11837-005-0061-x.

(5) Jakupi, P.; Zagidulin, D.; Noël, J. J.; Shoesmith, D. W. The Impedance Properties of the Oxide Film on the Ni-Cr-Mo Alloy-22 in Neutral Concentrated Sodium Chloride Solution. *Electrochimica Acta* **2011**, *56*, 6251–6259. https://doi.org/10.1016/j.electacta.2010.07.064.

(6) Bocher, F.; Presuel-Moreno, F.; Scully, J. R. Investigation of Crevice Corrosion of AISI 316 Stainless Steel Compared to Ni–Cr–Mo Alloys Using Coupled Multielectrode Arrays. *J. Electrochem. Soc.* **2008**, *155* (5), C256. https://doi.org/10.1149/1.2883741.

(7) Bocher, F.; Huang, R.; Scully, J. R. Prediction of Critical Crevice Potentials for Ni-Cr-Mo Alloys in Simulated Crevice Solutions as a Function of Molybdenum Content. *Corrosion* **2010**, *66* (5), 1–15. https://doi.org/10.5006/1.3430462.

(8) Kehler, B. A.; Ilevbare, G. O.; Scully, J. R. Comparison of the Crevice Corrosion Resistance of Alloys 625 and C22. *Passiv. Localized Corros. Int. Symp. Honor Profr. Norio Sato* **1999**, *99*, 644–654.

(9) Kehler, B. A.; Ilevbare, G. O.; Scully, J. R. Crevice Corrosion Stabilization and Repassivation Behavior of Alloys 625 and 22. *Corrosion* **2001**, *57* (12), 1042–1065.

(10) Kehler, B. A.; Scully, J. R. Role of Metastable Pitting in Crevices on Crevice Corrosion Stabilization in Alloys 625 and 22. *Corrosion* **2005**, *61* (7), 665–684. https://doi.org/10.5006/1.3278202.

(11) Carranza, R. M.; Rodríguez, M. A. Crevice Corrosion of Nickel-Based Alloys Considered as Engineering Barriers of Geological Repositories. *Npj Mater. Degrad.* **2017**, *1* (1), 1–9. https://doi.org/10.1038/s41529-017-0010-5.

(12) Jakupi, P.; Noël, J. J.; Shoesmith, D. W. The Evolution of Crevice Corrosion Damage on the Ni-Cr-Mo-W Alloy-22 Determined by Confocal Laser Scanning Microscopy. *Corros. Sci.* **2012**, *54* (1), 260–269. https://doi.org/10.1016/j.corsci.2011.09.028.

(13) Jakupi, P.; Noel, J. J.; Shoesmith, D. W. Crevice Corrosion Initiation and Propagation on Alloy-22 under Galvanically-Coupled and Galvanostatic Conditions. *Corros. Sci.* **2011**, *53* (10), 3122–3130. https://doi.org/10.1016/j.corsci.2011.05.061.

(14) Mishra, A. K.; Shoesmith, D. W. Effect of Alloying Elements on Crevice Corrosion Inhibition of Nickel-Chromium-Molybdenum-Tungsten Alloys Under Aggressive

Conditions: An Electrochemical Study. *Corrosion* **2014**, *70* (7), 721–730. https://doi.org/10.5006/1170.

(15) Marcus, P.; Maurice, V.; Strehblow, H. H. Localized Corrosion (Pitting): A Model of Passivity Breakdown Including the Role of the Oxide Layer Nanostructure. *Corros. Sci.* **2008**, *50* (9), 2698–2704. https://doi.org/10.1016/j.corsci.2008.06.047.

(16) Bouzoubaa, A.; Costa, D.; Diawara, B.; Audiffren, N.; Marcus, P. Insight of DFT and Atomistic Thermodynamics on the Adsorption and Insertion of Halides onto the Hydroxylated NiO(111) Surface. *Corros. Sci.* **2010**, *52* (8), 2643–2652. https://doi.org/10.1016/j.corsci.2010.04.014.

(17) Strehblow, H. -H. Nucleation and Repassivation of Corrosion Pits for Pitting on Iron and Nickel. *Mater. Corros.* **1976**, *27* (11), 792–799. https://doi.org/10.1002/maco.19760271106.

(18) Ramanathan, R.; Voorhees, P. W. Morphological Stability of Steady-State Passive Oxide Films. *Electrochimica Acta* **2019**.

(19) Kobayashi, Y.; Virtanen, S.; Böhni, H. Microelectrochemical Studies on the Influence of Cr and Mo on Nucleation Events of Pitting Corrosion. *J. Electrochem. Soc.* **2000**, *147* (1), 155. https://doi.org/10.1149/1.1393169.

(20) Tobler, W. J.; Virtanen, S. Effect of Mo Species on Metastable Pitting of Fe18Cr Alloys-A Current Transient Analysis. *Corros. Sci.* **2006**, *48* (7), 1585–1607. https://doi.org/10.1016/j.corsci.2005.05.049.

(21) Schmuki, P.; Böhni, H. Metastable Pitting and Semiconductive Properties of Passive Films. *J. Electrochem. Soc.* **1992**, *139* (7), 1908–1913. https://doi.org/10.1149/1.2069520.

(22) Chao, C. Y.; Lin, L. F.; Macdonald, D. D. A Point Defect Model for Anodic Passive Films I. Film Growth Kinetics. *J. Electrochem. Soc.* **1981**, *128* (6), 1187–1194. https://doi.org/10.1149/1.2127591.

(23) Lin, L. F.; Chao, C. Y.; Macdonald, D. D. A Point Defect Model for Anodic Passive Films II. Chemical Breakdown and Pit Initiation. *J. Electrochem. Soc.* **1981**, *128* (6), 1194–1198. https://doi.org/10.1149/1.2127592.

(24) Evans, J. W.; Thiel, P. A.; Bartelt, M. C. Morphological Evolution during Epitaxial Thin Film Growth: Formation of 2D Islands and 3D Mounds. *Surface Science Reports*. April 2006, pp 1–128. https://doi.org/10.1016/j.surfrep.2005.08.004.

(25) Pang, Q.; DorMohammadi, H.; Isgor, O. B.; Árnadóttir, L. The Effect of Surface Vacancies on the Interactions of Cl with a α-Fe2O3 (0001) Surface and the Role of Cl in Depassivation. *Corros. Sci.* **2019**, *154*, 61–69. https://doi.org/10.1016/J.CORSCI.2019.03.052.

(26) Yu, X.; Marks, L. Combining the Physics of Metal/Oxide Heterostructure, Interface Dipole, Band Bending, Crystallography and Surface State to Understand Heterogeneity Contrast in Oxidation and Corrosion. *Corrosion* **2018**, *75* (2), 152–166. https://doi.org/10.5006/2794.

(27) Gusieva, K.; Cwalina, K. L.; Blades, W. H.; Ramalingam, G.; Perepezko, J. H.; Reinke, P.; Scully, J. R. Repassivation Behavior of Individual Grain Facets on Dilute Ni–Cr and Ni–Cr–Mo Alloys in Acidified Chloride Solution. *J. Phys. Chem. C* **2018**, *122* (34), 19499–19513. https://doi.org/10.1021/acs.jpcc.8b04306.

(28) Marcus, P.; Herbelin, J. M. The Entry of Chloride Ions into Passive Films on Nickel Studied by Spectroscopic (ESCA) and Nuclear (36-Cl Radiotracer) Methods. *Corros. Sci.* **1993**, *34* (7), 1123–1145. https://doi.org/10.1016/0010-938X(93)90293-P.

(29) Yates, D. E.; Healy, T. W. Mechanism of Anion Adsorption at the Ferric and Chromic Oxide/Water Interfaces. *J. Colloid Interface Sci.* **1975**, *52* (2), 222–228. https://doi.org/10.1016/0021-9797(75)90192-7.

(30) Davis, J. A.; Leckie, J. O. Surface Ionization and Complexation at the Oxide/Water Interface. 3. Adsorption of Anions. *J. Colloid Interface Sci.* **1980**, *74* (1), 32–43. https://doi.org/10.1016/0021-9797(80)90168-X.

(31) Yu, X.; Gulec, A.; Lutton Cwalina, K.; Scully, J.; Marks, L. New Insights on the Role of Chloride During the Onset of Local Corrosion: TEM, APT, Surface Energy, and Morphological Instability. *CORROSION* **2019**. https://doi.org/10.5006/2991.

(32) Zuo, Y.; Wang, H.; Xiong, J. The Aspect Ratio of Surface Grooves and Metastable Pitting of Stainless Steel. *Corros. Sci.* **2002**, *44* (1), 25–35. https://doi.org/10.1016/S0010-938X(01)00039-7.

(33) Seyeux, A.; Maurice, V.; Marcus, P. Oxide Film Growth Kinetics on Metals and Alloys: I. Physical Model. *J. Electrochem. Soc.* **2013**, *160* (6), C189–C196. https://doi.org/10.1149/2.036306jes.

(34) Maurice, V.; Klein, L. H.; Marcus, P. Atomic Structure of Metastable Pits Formed on Nickel. *Electrochem. Solid-State Lett.* **2001**, *4* (1), B1–B3. https://doi.org/10.1149/1.1344277.

(35) Scherer, J.; Ocko, B. M.; Magnussen, O. M. Structure, Dissolution, and Passivation of Ni(111) Electrodes in Sulfuric Acid Solution: An in Situ STM, X-Ray Scattering, and Electrochemical Study. *Electrochimica Acta* **2003**, *48*, 1169–1191. https://doi.org/10.1016/S0013-4686(02)00827-7.

(36) Seyeux, A.; Maurice, V.; Klein, L. H.; Marcus, P. In Situ STM Study of the Effect of Chloride on Passive Film on Nickel in Alkaline Solution. *J. Electrochem. Soc.* **2006**, *153* (11), B453–B463. https://doi.org/10.1149/1.2337768.

(37) Massoud, T.; Maurice, V.; Klein, L. H.; Wiame, F.; Marcus, P. Intergranular Effects on the Local Electronic Properties of the Passive Film on Nickel. *Corros. Sci.* **2013**, *69*, 245–251. https://doi.org/10.1016/j.corsci.2012.12.010.

(38) Maurice, V.; Nakamura, T.; Klein, L. H.; Marcus, P. Initial Stages of Localized Corrosion by Pitting of Passivated Nickel Surfaces Studyed by Scanning Tunneling Microscopy (STM) and Atomic Force Microscopy (AFM). In *Local Probe Techniques for Corrosion Research*; Oltra, R., Maurice, V., Akid, R., Marcus, P., Eds.; CRC Press LLC: Boca Raton, 2007; pp 71–83.

(39) Kowal, A.; Niewiara, R.; Peron, B.; Haber, J. In Situ Atomic Force Microscopy Observation of Change in Thickness of Nickel Hydroxide Layer on Ni Electrode. *Langmuir* **1996**, *12* (10), 2332–2333. https://doi.org/10.1021/la9515229.

(40) Lutton Cwalina, K.; Demarest, C. R.; Gerard, A. Y.; Scully, J. R. Revisiting the Effects of Molybdenum and Tungsten Alloying on Corrosion Behavior of Nickel-Chromium Alloys in Aqueous Corrosion. *Curr. Opin. Solid State Mater. Sci.* **2019**.

(41) Douglass. The Oxidation Mechanism of Dilute Ni-Cr Alloys. *Corros. Sci.* **1968**, *8* (9), 665–678.

(42) Takei, A.; Nii, K. The Growth Process of Oxide Layers in the Initial Stage of Oxidation of 80Ni-20Cr Alloy. *Trans. Jpn. Inst. Met.* **1976**, *17* (4), 211–219.

(43) Halem, Z.; Halem, N.; Abrudeanu, M.; Chekroude, S.; Petot, C.; Petot-Ervas, G. Transport Properties of Al or Cr-Doped Nickel Oxide Relevant to the Thermal Oxidation of Dilute

Ni-Al and Ni-Cr Alloys. *Solid State Ion.* **2016**, *297*, 13–19. https://doi.org/10.1016/j.ssi.2016.09.023.

(44) Luo, L.; Zou, L.; Schreiber, D. K.; Baer, D. R.; Bruemmer, S. M.; Zhou, G.; Wang, C. M. In-Situ Transmission Electron Microscopy Study of Surface Oxidation for Ni-10Cr and Ni-20Cr Alloys. *Scr. Mater.* **2016**, *114*, 129–132. https://doi.org/10.1016/j.scriptamat.2015.11.031.

(45) Luo, L.; Zou, L.; Schreiber, D. K.; Olszta, M. J.; Baer, D. R.; Bruemmer, S. M.; Zhou, G.; Wang, C.-M. In Situ Atomic Scale Visualization of Surface Kinetics Driven Dynamics of Oxide Growth on a Ni–Cr Surface. *Chem Commun* **2016**, *52* (16), 3300–3303. https://doi.org/10.1039/C5CC09165A.

(46) Dalvi, A. D.; Coates, D. E. A Review of the Diffusion Path Concept and Its Application to the High-Temperature Oxidation of Binary Alloys. *Oxidation of Metals*. 1972, pp 113–135. https://doi.org/10.1007/BF00610840.

(47) Bojinov, M.; Fabricius, G.; Kinnunen, P.; Laitinen, T.; Mäkelä, K.; Saario, T.; Sundholm, G. Mechanism of Transpassive Dissolution of Ni-Cr Alloys in Sulphate Solutions. *Electrochimica Acta* **2000**, *45*, 2791–2802. https://doi.org/10.1016/S0013-4686(00)00387-X.

(48) Oblonsky, L. J.; Ryan, M. P. In Situ XANES Study on the Active and Transpassive Dissolution of Ni and Ni-Cr Alloys in 0.1 M H_2SO_4. *J. Electrochem. Soc.* **2001**, *148* (10), B405–B411. https://doi.org/10.1149/1.1398276.

(49) Ter-Ovanessian, B.; Alemany-Dumont, C.; Normand, B. Electronic and Transport Properties of Passive Films Grown on Different Ni-Cr Binary Alloys in Relation to the Pitting Susceptibility. *Electrochimica Acta* **2014**, *133*, 373–381. https://doi.org/10.1016/j.electacta.2014.04.067.

(50) Ter-Ovanessian, B.; Mary, N.; Normand, B. Passivity Breakdown of Ni-Cr Alloys: From Anions Interactions to Stable Pits Growth. *J. Electrochem. Soc.* **2016**, *163* (8), C410–C419. https://doi.org/10.1149/2.0381608jes.

(51) Bojinov, M.; Fabricius, G.; Kinnunen, P.; Laitinen, T.; Mäkelä, K.; Saario, T.; Sundholm, G.; Yliniemi, K. Transpassive Dissolution of Ni-Cr Alloys in Sulphate Solutions - Comparison between a Model Alloy and Two Industrial Alloys. *Electrochimica Acta* **2002**, *47*, 1697–1712. https://doi.org/10.1016/S0013-4686(02)00018-X.

(52) Bojinov, M.; Fabricius, G.; Kinnunen, P.; Laitinen, T.; Makela, K.; Saario, T.; Sundholm, G.; Makela, K.; Saario, T.; Sundholm, G. Electrochemical Study of the Passive Behavior of Ni-Cr Alloys in a Borate Solution - a Mixed-Conduction Model Approach. *J. Electroanal. Chem.* **2001**, *504* (1), 29–44. https://doi.org/10.1016/S0022-0728(01)00423-5.

(53) Bojinov, M.; Galtayries, A.; Kinnunen, P.; Machet, A.; Marcus, P. Estimation of the Parameters of Oxide Film Growth on Nickel-Based Alloys in High-Temperature Water Electrolytes. *Electrochimica Acta* **2007**, *52*, 7475–7483. https://doi.org/10.1016/j.electacta.2007.06.002.

(54) Bojinov, M.; Kinnunen, P.; Sundholm, G. Electrochemical Behavior of Nickel-Chromium Alloys in a High-Temperature Aqueous Electrolyte. *Corrosion* **2003**, *59* (2), 91–103. https://doi.org/10.5006/1.3277550.

(55) Yu, X. X.; Gulec, A.; Sherman, Q.; Lutton Cwalina, K.; Scully, J. R.; Perepezko, J. H.; Voorhes, P. W.; Marks, L. D. Nonequilibrium Solute Capture in Passivating Oxide Films. *Phys. Rev. Lett.* **2018**, *121* (14), 145701.

(56) Sherman, Q. C.; Voorhees, P. W.; Marks, L. D. Thermodynamics of Solute Capture during the Oxidation of Multicomponent Metals. *Acta Mater.* **2019**, *181*, 584–594. https://doi.org/10.1016/j.actamat.2019.09.043.

(57) Wood, G. C.; Chattopadhyay, B. Transient Oxidation of Ni-Base Alloys. *Corros. Sci.* **1970**, *10* (7). https://doi.org/10.1016/S0010-938X(70)80032-4.

(58) Chattopadhyay, B.; Wood, G. C. The Transient Oxidation of Fe-Cr and Ni-Cr Alloys. *J. Electrochem. Soc.* **1970**, *117* (9), 1163–1171. https://doi.org/10.1149/1.2407761.

(59) Atkinson, A. Transport Processes during the Growth of Oxide Films at Elevated Temperature. *Rev. Mod. Phys.* **1985**, *57* (2), 437–470. https://doi.org/10.1103/RevModPhys.57.437.

(60) McCafferty, E. Graph Theory and the Passivity of Binary Alloys. *Corros. Sci.* **2000**, *42* (11), 1993–2011. https://doi.org/10.1016/S0010-938X(00)00038-X.

(61) McCafferty, E. Oxide Networks, Graph Theory, and the Passivity of Binary Alloys. *Corros. Sci.* **2002**, *44* (7), 1393–1409. https://doi.org/10.1016/j.corsci.2008.09.006.

(62) McCafferty, E. Relationship Between Graph Theory and Percolation Approaches in the Passivity of Fe–Cr Binary Alloys. *J. Electrochem. Soc.* **2008**, *155* (10), C501–C505. https://doi.org/10.1149/1.2958291.

(63) Blades, W. H.; Reinke, P. From Alloy to Oxide: Capturing the Early Stages of Oxidation on Ni–Cr(100) Alloys. *ACS Appl. Mater. Interfaces* **2019**, *10* (49), 43219–43229. https://doi.org/10.1021/acsami.8b15210.

(64) Marcelin, S.; Ter-Ovanessian, B.; Normand, B. Electronic Properties of Passive Films from the Multi-Frequency Mott-Schottky and Power-Law Coupled Approach. *Electrochem. Commun.* **2016**, *66*, 62–65. https://doi.org/10.1016/j.elecom.2016.03.003.

(65) Lutton Cwalina, K.; Ha, H. M.; Ott, N.; Reinke, P.; Birbilis, N.; Scully, J. R. In Operando Analysis of Passive Film Growth on Ni-Cr and Ni-Cr-Mo Alloys in Chloride Solutions. *J. Electrochem. Soc.* **2019**, *166* (11), C3241–C3253.

(66) MacDougall, B.; Mitchell, D. F.; Sproule, G. I.; Graham, M. J. Incorporation of Chloride Ion in Passive Oxide Films on Nickel. *J. Electrochem. Soc.* **1983**, *130* (3), 543–547. https://doi.org/10.1149/1.2119748.

(67) MacDougall, B.; Graham, M. J. Influence of Incorporated Cl-in NiO on the Pitting Susceptibility of Nickel. *J. Electrochem. Soc.* **1984**, *131* (4), 727–730. https://doi.org/10.1149/1.2115688.

(68) Seo, M.; Furuichi, R.; Okamoto, G.; Sato, N. Dissolution of Hydrous Chromium Oxide in Acid Solutions. *Trans. Jpn. Inst. Met.* **1975**, *16* (8), 519–525.

(69) Macdonald, D. D.; Sun, A.; Priyantha, N.; Jayaweera, P. An Electrochemical Impedance Study of Alloy-22 in NaCl Brine at Elevated Temperature: II. Reaction Mechanism Analysis. *J. Electroanal. Chem.* **2004**, *572* (2), 421–431. https://doi.org/10.1016/j.jelechem.2004.05.032.

(70) Hirschorn, B.; Orazem, M. E.; Tribollet, B.; Vivier, V.; Frateur, I.; Musiani, M. Constant-Phase-Element Behavior Caused by Coupled Resistivity Distributions in Films. *J. Electrochem. Soc.* **2010**, *157* (12), C424–C428. https://doi.org/10.1149/2.039112jes.

(71) Nečas, D.; Klapetek, P. Gwyddion: An Open-Source Software for SPM Data Analysis. *Cent. Eur. J. Phys.* **2012**, *10* (1), 181–188. https://doi.org/10.2478/s11534-011-0096-2.

(72) Biesinger, M. C.; Payne, B. P.; Grosvenor, A. P.; Lau, L. W. M.; Gerson, A. R.; Smart, R. S. C. Resolving Surface Chemical States in XPS Analysis of First Row Transition Metals,

Oxides and Hydroxides: Cr, Mn, Fe, Co and Ni. *Appl. Surf. Sci.* **2011**, *257* (7), 2717–2730. https://doi.org/10.1016/j.apsusc.2010.10.051.

(73) Werfel, F.; Minni, E. Photoemission Study of the Electronic Structure of Mo and Mo Oxides. *J. Phys. C Solid State Phys.* **1983**, *16* (31), 6091–6100.

(74) Moulder, J. F.; Stickle, W. F.; Sobol, P. E.; Bomben, K. D. Handbook of X-Ray Photoelectron Spectroscopy. **1992**, 261.

(75) Biesinger, M. C.; Payne, B. P.; Lau, L. W. M.; Gerson, A.; Smart, R. S. C. X-Ray Photoelectron Spectroscopic Chemical State Quantification of Mixed Nickel Metal, Oxide and Hydroxide Systems. *Surf. Interface Anal.* **2009**, *41* (4), 324–332. https://doi.org/10.1002/sia.3026.

(76) Strohmeier, B. R. An ESCA Method for Determining the Oxide Thickness on Aluminum Alloys. *Surf. Interface Anal.* **1990**, *15* (1), 51–56. https://doi.org/10.1002/sia.740150109.

(77) Cabrera, N.; Mott, N. F. Theory of the Oxidation of Metals. *Rep. Prog. Phys.* **1949**, *12* (1), 163–184. https://doi.org/10.1088/0034-4885/12/1/308.

(78) Samin, A. J.; Taylor, C. D. First-Principles Investigation of Surface Properties and Adsorption of Oxygen on Ni-22Cr and the Role of Molybdenum. *Corros. Sci.* **2018**, *134*, 103–111. https://doi.org/10.1016/J.CORSCI.2018.02.017.

(79) DorMohammadi, H.; Pang, Q.; Árnadóttir, L.; Burkan Isgor, O. Atomistic Simulation of Initial Stages of Iron Corrosion in Pure Water Using Reactive Molecular Dynamics. *Comput. Mater. Sci.* **2018**, *145*, 126–133. https://doi.org/10.1016/j.commatsci.2017.12.044.

(80) DorMohammadi, H.; Pang, Q.; Murkute, P.; Árnadóttir, L.; Isgor, O. B. Investigation of Chloride-Induced Depassivation of Iron in Alkaline Media by Reactive Force Field Molecular Dynamics. *Npj Mater. Degrad.* **2019**, *3* (1). https://doi.org/10.1038/s41529-019-0081-6.

(81) Pourbaix, Marcel. *Atlas of Electrochemical Equilibria in Aqueous Solutions*; National Association of Corrosion Engineers, 1974.

(82) Marks, L. Competitive Chloride Chemisorption Disrupts Hydrogen Bonding Networks: DFT, Crystallography, Thermodynamics and Morphological Consequences. *Corrosion* **2017**, *74* (3), 295–311.

(83) Quiambao, K. F.; McDonnell, S. J.; Schreiber, D. K.; Gerard, A. Y.; Freedy, K. M.; Lu, P.; Saal, J. E.; Frankel, G. S.; Scully, J. R. Passivation of a Corrosion Resistant High Entropy Alloy in Non-Oxidizing Sulfate Solutions. *Acta Mater.* **2019**, *164*, 362–376. https://doi.org/10.1016/J.ACTAMAT.2018.10.026.

(84) Lloyd, A. C.; Shoesmith, D. W.; McIntyre, N. S.; Noël, J. J. Effects of Temperature and Potential on the Passive Corrosion Properties of Alloys C22 and C276. *J. Electrochem. Soc.* **2003**, *150* (4), B120–B130. https://doi.org/10.1149/1.1554914.

(85) Zhang, X.; Shoesmith, D. W. Influence of Temperature on Passive Film Properties on Ni–Cr–Mo Alloy C-2000. *Corros. Sci.* **2013**, *76*, 424–431. https://doi.org/10.1016/J.CORSCI.2013.07.016.

(86) Ebrahimi, N.; Biesinger, M. C.; Shoesmith, D. W.; Noël, J. J. The Influence of Chromium and Molybdenum on the Repassivation of Nickel-Chromium-Molybdenum Alloys in Saline Solutions. *Surf. Interface Anal.* **2017**, *49* (13), 1359–1363. https://doi.org/10.1002/sia.6254.

(87) Zhang, X.; Shoesmith, D. W. Influence of Temperature on Passive Film Properties on Ni-Cr-Mo Alloy C-2000. *Corros. Sci.* **2013**, *76*, 424–431. https://doi.org/10.1016/j.corsci.2013.07.016.

(88) Huang, L.-F.; Hutchison, M. J.; Santucci, R. J.; Scully, J. R.; Rondinelli, J. M. Improved Electrochemical Phase Diagrams from Theory and Experiment: The Ni-Water System and Its Complex Compounds. *J. Phys. Chem. C* **2017**, *121* (18), 9782–9789. https://doi.org/10.1021/acs.jpcc.7b02771.

(89) Taylor, C. D.; Neurock, M.; Scully, J. R. First-Principles Investigation of the Fundamental Corrosion Properties of a Model Cu-38 Nanoparticle and the (111), (113) Surfaces. *J. Electrochem. Soc.* **2008**, *155* (8), C407. https://doi.org/10.1149/1.2926598.

(90) Horton, D. J.; Zhu, A. W.; Scully, J. R.; Neurock, M. Crystallographic Controlled Dissolution and Surface Faceting in Disordered Face-Centered Cubic FePd. *MRS Commun.* **2014**, *4* (03), 113–119. https://doi.org/10.1557/mrc.2014.23.

(91) Bland, L. G.; Gusieva, K.; Scully, J. R. Effect of Crystallographic Orientation on the Corrosion of Magnesium: Comparison of Film Forming and Bare Crystal Facets Using Electrochemical Impedance and Raman Spectroscopy. *Electrochimica Acta* **2017**, *227*, 136–151. https://doi.org/10.1016/j.electacta.2016.12.107.

(92) Huang, L.-F.; Rondinelli, J. Electrochemical Stabilities of Ni-Based Compounds from Bulk to Nanoscale Dimensions. *Bull. Am. Phys. Soc.* **2018**.

(93) Huang, L.-F.; Scully, J. R.; Rondinelli, J. M. Modeling Corrosion with First-Principles Electrochemical Phase Diagrams. *Annu. Rev. Mater. Res.* **2019**, *49* (1), annurev-matsci-070218-010105. https://doi.org/10.1146/annurev-matsci-070218-010105.

(94) McMahon, M. E.; Santucci, R. J.; Scully, J. R. Advanced Chemical Stability Diagrams to Predict the Formation of Complex Zinc Compounds in a Chloride Environment. *RSC Adv.* **2019**, *9* (35), 19905–19916. https://doi.org/10.1039/c9ra00228f.

(95) Tang, L.; Han, B.; Persson, K.; Friesen, C.; He, T.; Sieradzki, K.; Ceder, G. Electrochemical Stability of Nanometer-Scale Pt Particles in Acidic Environments. *J. Am. Chem. Soc.* **2010**, *132* (2), 596–600. https://doi.org/10.1021/ja9071496.

(96) Taylor, C. D.; Lu, P.; Saal, J.; Frankel, G. S.; Scully, J. R. Integrated Computational Materials Engineering of Corrosion Resistant Alloys. *Npj Mater. Degrad.* **2018**, *2* (1), 1–10. https://doi.org/10.1038/s41529-018-0027-4.

(97) Vetter, K. J. J.; Gorn, F. Kinetics of Layer Formation and Corrosion Processes of Passive Iron in Acid Solutions. *Electrochimica Acta* **1973**, *18* (4), 321–326. https://doi.org/10.1016/0013-4686(73)80036-2.

(98) H.-H. Strehblow; Marcus, P. Mechanisms of Pitting Corrosion. In *Corrosion Mechanisms in Theory and Practice*; 2012; pp 349–394.

(99) Sillen, L.; Society, A. M. Stability Constants of Metal-Ion Complexes. Suppl. No. 1; The Chemical Society, London, 1971.

(100) Löchel, B.; Strehblow, H. H. Breakdown of Passivity of Iron by Fluoride. *Electrochimica Acta* **1983**, *28* (4), 565–571. https://doi.org/10.1016/0013-4686(83)85043-9.

(101) Sakashita, M. Breakdown of Passivity of Nickel by Fluoride: I. Electrochemical Studies. *J. Electrochem. Soc.* **1984**, *131* (3), 522–529. https://doi.org/10.1149/1.2115620.

(102) Strehblow, H. H. Breakdown of Passivity of Nickel by Fluoride II. Surface Analytical Studies. *J. Electrochem. Soc.* **1984**, *131* (4), 713–723. https://doi.org/10.1149/1.2115678.

(103) Karmakar, P.; Mollick, S. A.; Ghose, D.; Chakrabarti, A. Role of Initial Surface Roughness on Ion Induced Surface Morphology. *Appl. Phys. Lett.* **2008**, *93* (10). https://doi.org/10.1063/1.2974086.

(104) Jensen, P.; Barabsi, A. L.; Larralde, H.; Havlin, S.; Stanley, H. E. Deposition, Diffusion, and Aggregation of Atoms on Surfaces: A Model for Nanostructure Growth. *Phys. Rev. B* **1994**, *50* (20), 15316–15329. https://doi.org/10.1103/PhysRevB.50.15316.

(105) Liu, H.; Lin, Z.; Zhigilei, L. V.; Reinke, P. Fractal Structures in Fullerene Layers: Simulation of the Growth Process. *J. Phys. Chem. C* **2008**, *112* (12), 4687–4695. https://doi.org/10.1021/jp0775597.

8.7 Supplementary Data and Supporting Information

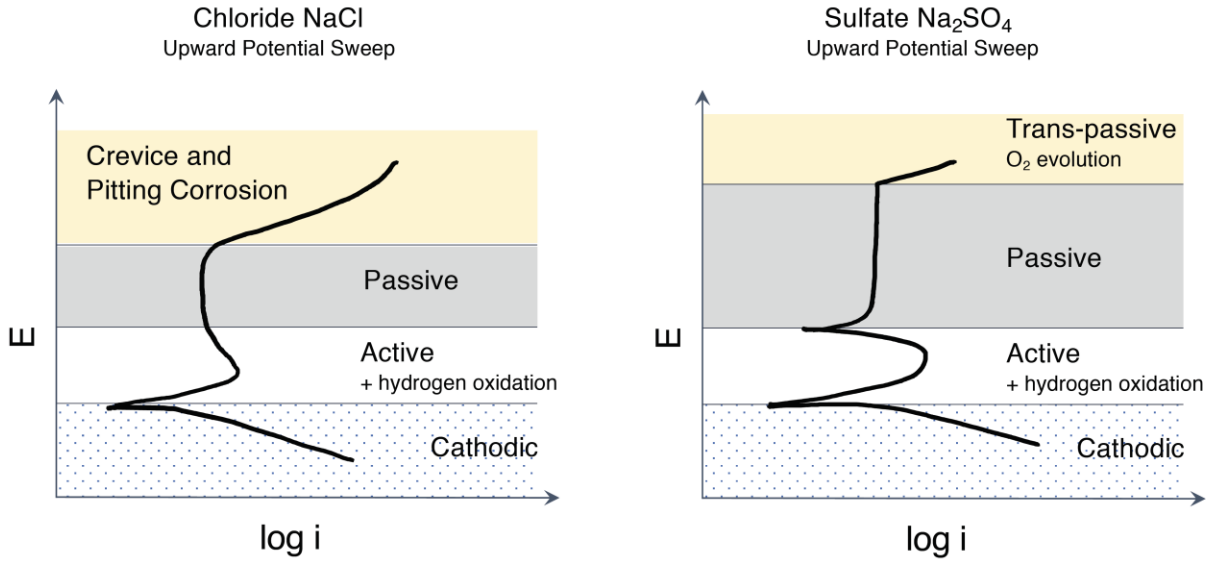

Figure 8-S1: Schematic illustration of the upward potential sweep in cyclic potentiodynamic polarization curves for chloride and sulfate solutions. The graphs show the general shape seen in the i versus E curves and serve as a visual guide to the interpretation of the experimental data presented in Figure 8-1. The passive region is marked in Figure 8-1 by arrows in the experimental data.

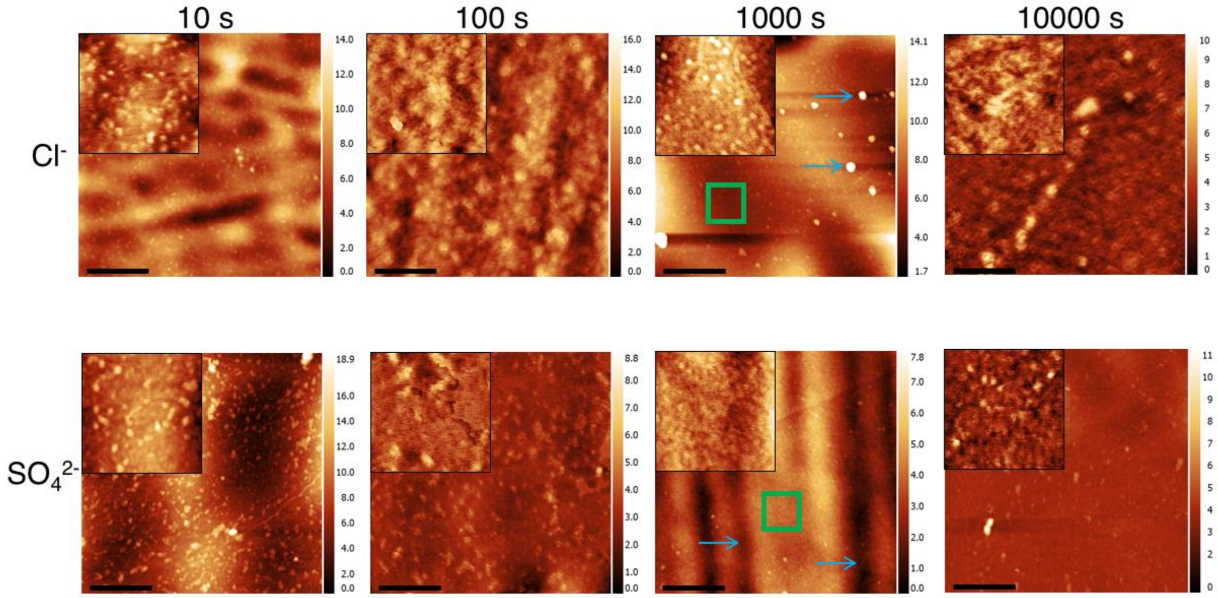

Height scale bar in [nm]

Figure 8-S2. Topography images taken with AFM after 10, 100, 1000, and 10000 seconds in both chloride and sulfate, labeled accordingly, with 500 nm^2 image insets. The insets are representative of a typical area use to take the oxide area, height, and RMS data from. For both the chloride and sulfate images at 1000s, the green boxes represent typical areas used to measure the RMS, while the blue arrows mark features (polishing residue and polishing grooves) that were excluded from the RMS. All scale bars are 500 nm and the vertical color bars are in units of nm.

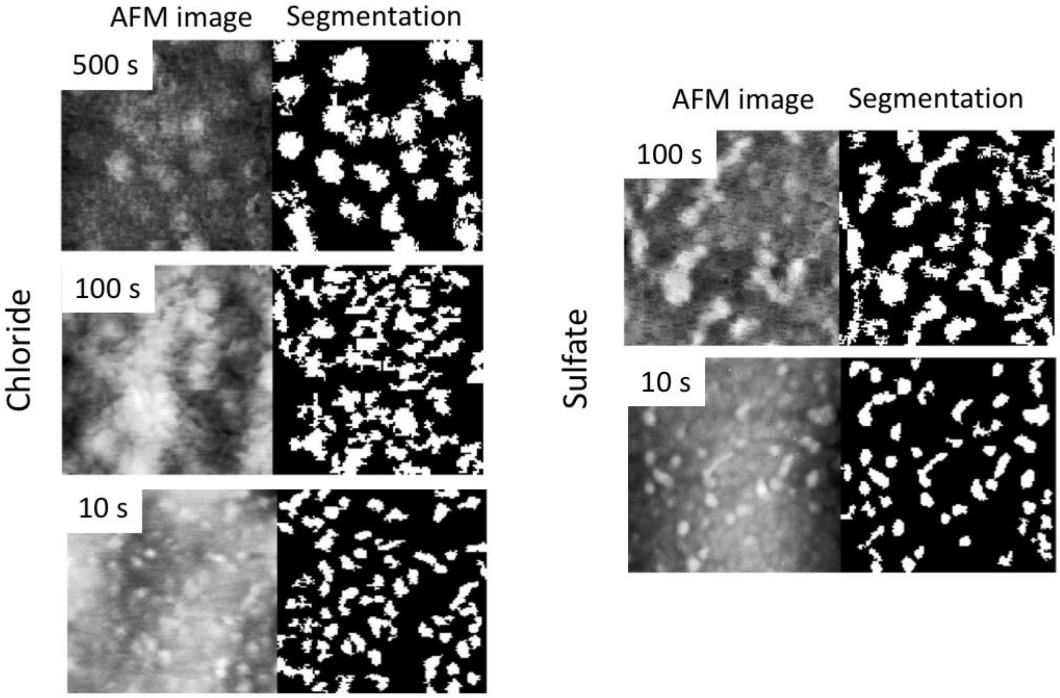

Figure 8-S3.1 AFM images before and after the segmentation process described in the Experimental Section of the manuscript for short passivation times for the chloride and sulfate data sets. The threshold is set at 50 +/- 5% of the maximum feature height for all images. The area distributions are obtained from the segmented images. The image size is 500x500 nm^2. The masking procedure was adapted through MATLAB version R2019a, and the areas taken and plotted as histograms in Igor (WaveMetrics, Lake Oswego, OR, U.S.A.).

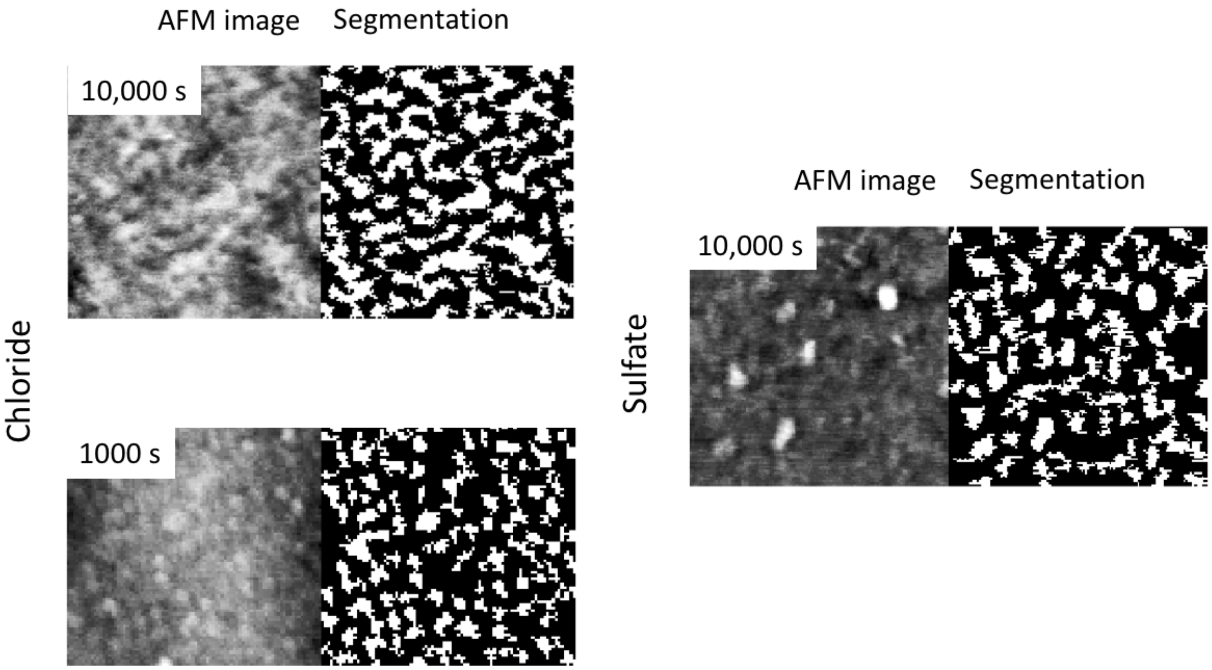

Figure 8-S3.2 AFM images before and after the segmentation process described in the Experimental Section of the manuscript for long passivation times. The threshold is set at 50 +/- 5% of the maximum feature height for all images. The area distributions are obtained from the segmented images, and the image size is 500×500 nm^2.

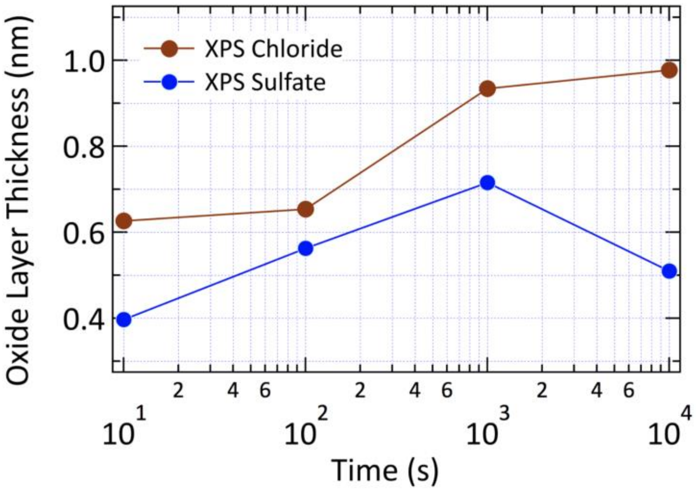

Figure 8-S4. Passive layer thickness calculated with the Strohmeier formula (B. R. Strohmeier, *Surf. Interface Anal.*, **15**, 51–56 (1990)) which assumes a layer-by-layer growth. For rough surfaces and island-growth the layer-by-layer values constitute a lower limit – the Strohmeier formula will underestimate the amount of material deposited on the surface. The general development of film thickness follows the trend shown in Figure 8-2 albeit the absolute numbers for the film thicknesses from the XPS measurements are smaller.

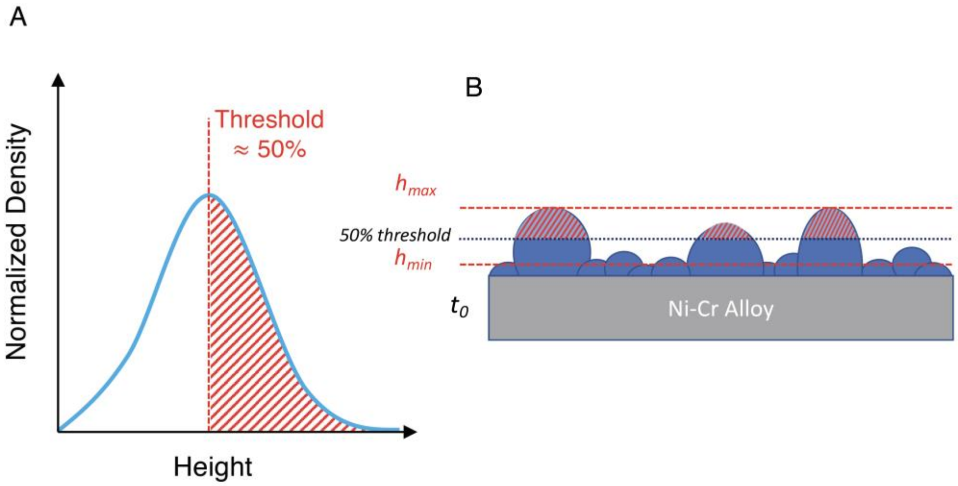

Figure 8-S5. Schematic illustration of the relation between height distribution (A) and area distribution (B). The height threshold for measuring area distributions was set at ~50% and the distributions therefore include all “islands” which contribute to the right-hand side of the height distribution. This threshold is chosen to avoid spurious contributions from unphysically small areas such as single pixels, and yielded the most consistent results in repeated analysis of the same image

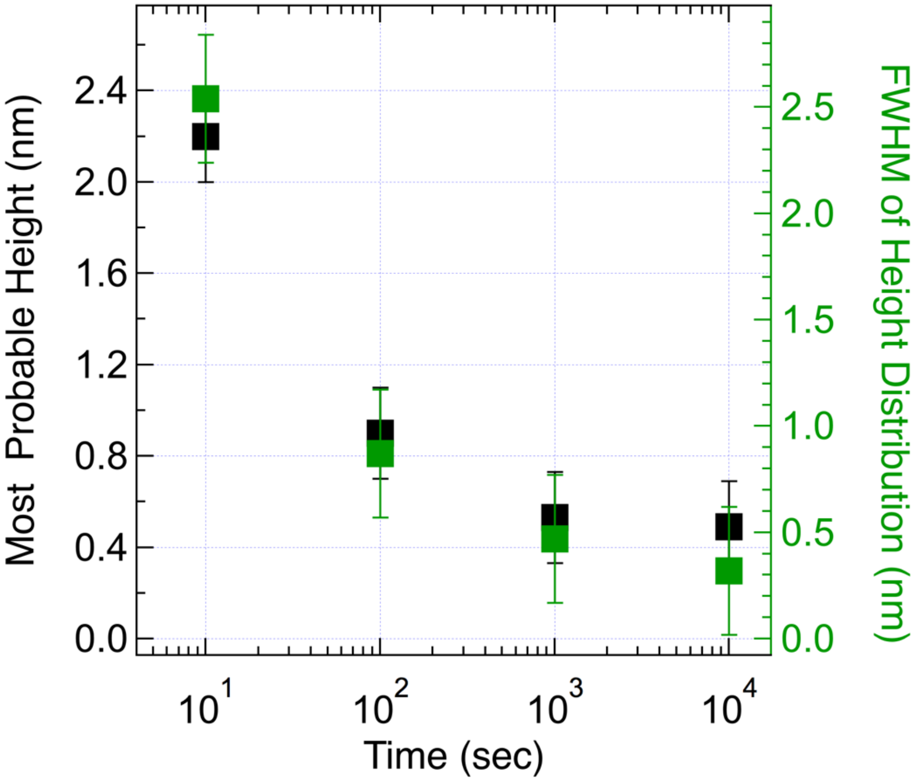

Figure 8-S6. Sulfate solution – **"**most probable height", and "full width at half maximum (FWHM)" for the height distributions shown in Figure 8-8. The distributions measured for chloride solution present a large variability due to the inherent spatial heterogeneity, and the comparison of the distributions themselves is more informative than a parameterized graph.